In Situ Measurements of Interfacial Concentration Enhancement in Solutions

Ruairidh Mackay

Department of Chemical and Process Engineering

A thesis presented to the Department of Chemical and Process Engineering, University of Strathclyde, in accordance with the requirements for the degree of Doctor of Philosophy.

October 2025

Declarations

This thesis is the result of the author's original research. It has been composed by the author and has not been previously submitted for examination which has led to the award of a degree.

The copyright of this thesis belongs to the author under the terms of the United Kingdom Copyright Acts as qualified by University of Strathclyde Regulation 3.50. Due acknowledgement must always be made of the use of any material contained in, or derived from, this thesis.

Signed: R. Mackay

Date: 9th October 2025

Abstract

Crystallisation is a widely used separation process for the purification of chemical and pharmaceutical compounds during manufacturing. Crystal nucleation is the first step in the crystallisation process and typically proceeds by means of a heterogeneous mechanism, where compounds originally dissolved in solution form a new crystal on surfaces such as vessel walls, impellers or particles suspended in solution.

However, comprehensive understanding of crystal nucleation is still lacking despite decades of investigation dedicated into elucidating various nucleation mechanism elucidation. Heterogeneous nucleation is also influenced by the presence of a surface. Molecular level solution behaviour at surfaces is not well understood and it is usually assumed that the solution composition at the surface is the same as in the bulk solution.

This thesis utilises surface measurement techniques, primarily surface plasmon resonance (SPR) spectroscopy, to conduct novel in situ measurements of aqueous solutions at solid interfaces and investigate the interfacial concentration enhancement when these solutions are in contact with a solid interface, which has been predicted in recent simulation studies.

A comprehensive workflow was developed for in situ SPR measurements, modelling of SPR spectra and fitting of experimental data to provide quantitative assessment of interfacial concentration enhancement in solutions.

The developed workflow was applied to undersaturated aqueous glycine and urea solutions on bare gold chips and on gold chips coated with an ultrathin polystyrene layer. The results showed a strong evidence of interfacial concentration enhancement at both gold and polystyrene surfaces for glycine and urea solutions at all concentrations investigated. The investigated solutions were undersaturated to allow for development and validation of experimental protocols in the absence of crystal formation. However, the experimental protocols and workflows introduced here can be used to study supersaturated solutions, where the interfacial concentration enhancement effect confirmed in this work is expected to play a significant role in heterogeneous nucleation.

Through systematic investigation of the effects of interfaces and solution concentrations on interfacial concentration enhancement in solutions, this work provides new insights into solution behaviour at interfaces and will help to develop better understanding of heterogeneous crystal nucleation phenomena.

Acknowledgements

There are a number of people without whom this thesis and my PhD experience as a whole would not have been possible. Firstly, my supervisors, Prof. Jan Sefcik and Dr. Aaron Lau. Your support, encouragement and guidance throughout my project have challenged and helped me to become a better researcher. Thank you, it has been a great experience.

I would also like to thank everyone at CMAC for their help in using the facilities, their support, and the informal chats about my research which were always helpful. You made the whole experience, both in and out of the lab, all the more enjoyable and I will always appreciate that.

I would like to thank my friends for their endless support and being there to listen to me talk about my PhD – you have the patience of saints! You have always been there to push me on and I couldn’t have done it without your support and the escape going out, watching the football or going up hills at the weekend with you all provided.

Finally, I would like to thank my family. Words do not do your unending support and encouragement justice, you are my biggest supporters and for that I am forever grateful.

I couldn’t have done it without you all - thank you!

Table of Contents

List of Figures

List of Tables

Chapter 1

1. Introduction

This thesis focuses on probing the behaviour of aqueous solutions when placed in contact with a solid interface. In order to assess how this behaviour underpins the formative stages of crystal nucleation, it is important to outline the fundamentals of crystal nucleation theory.

Crystallisation is an important separation process widely encountered in nature and in the industry. Whether it be the isolation of an active pharmaceutical ingredient (API) of interest in a pharmaceutical manufacturing process, the formation of ice in cold temperatures or production of salt from brine solutions, each process is linked by their dependence on a crystallisation process to yield the relevant crystal product.

Crystallisation takes advantage of the first order phase transition which exists between a solid and liquid to drive crystal growth, which arises from departing equilibrium conditions in a multicomponent system.[1] In industrial crystallisation processes, this is achieved by using a thermodynamically metastable solution to facilitate the formation of clusters of molecules into a new stable phase in solution- the crystalline phase.[2, 3] Altering process conditions, such as temperature, composition and pH leads to the generation of a supersaturated solution and thus the required driving force to facilitate crystal nucleation and subsequent growth from solution.

Although crystallisation processes are widely seen and used, the ability to employ selective control measures that consistently yield desirable molecular and particulate features, such as polymorph selectivity and particle size,[4] is not yet commonplace. This stems from the lack of comprehensive understanding of the initial stage in the crystallisation process, crystal nucleation, which marks the first step in transitioning from the supersaturated liquid phase in solution to the solid crystalline phase.[1]

This chapter introduces the two fundamental schools of thought on how crystal nuclei are generated with regards to the primary nucleation of crystals, where nuclei are generated from solution. The chemical and physical properties, such as the role of system thermodynamics and kinetics and how they in turn influence how nuclei are generated is detailed. This is then developed further through detailing the different nucleation mechanisms by which crystal nuclei are formed, including insight into how these processes occur, the main drivers in such processes and how experimental observations help to aid in understanding the key physical and chemical interactions which facilitate crystal growth.

Research which has been undertaken in the field of heterogeneous nucleation is reviewed and the connection to interfacial properties outlined, before the work presented in this thesis is introduced with respect to the way in which it rationalises crystal nucleation. The main theoretical concept is presented, along with areas it seeks to address which other established nucleation theories do not currently encompass with adequate detail. Current shortcomings of the theory are also discussed to highlight that further work in relation to better understanding crystal nucleation fundamentals is required to facilitate better understanding of the early stages of crystal growth across the field.

Surface plasmon resonance spectroscopy studies are introduced and the conventional application of the technique which can be observed in the literature, which differs from the application within this research. Other surface measurement techniques are discussed to give context on other methods by which interfacial properties can be probed, before outlining why SPR spectroscopy was selected for this research. Finally, the main aims and objectives of the research are presented.

1.1 Solubility, Supersaturation and Metastability

Solubility is a thermodynamic parameter defined as the maximum amount of solute capable of dissolving in a solvent at a given temperature and pressure. The resultant solution is said to be saturated upon arriving at this condition, referred to as the solubility point, whereby the chemical potential of both the solution (μ_L) and solid (μ_S) phases are equal. Consequently, the difference in chemical potential between the two distinct phases at equilibrium is zero, as shown in equation 1.1 below.

$$\Delta\mu = \mu_L - \mu_S = 0 \quad \text{(Eq. 1.1)}$$

Solubility is a key parameter when designing crystallisation processes, as knowing the solubility of a compound of interest in a prospective solvent system is necessary to subsequently tailor the process conditions to both facilitate and maximise crystal nucleation and growth. If the net difference between the chemical potentials of the solid and liquid phase is negative, this indicates that the solution is undersaturated. Crystallisation relies on a driving force to generate crystal nuclei from solution, which is obtained when the amount of solute added to the solution exceeds the solubility point.

A net positive difference in the chemical potential between the solid and solution phases in a system of interest generates the driving force for crystallisation - supersaturation.[5] Supersaturation can be expressed by one of two definitions; the supersaturation ratio (S) or relative supersaturation (σ). The supersaturation ratio is defined as follows:

$$S = \frac{c}{c^*} \text{ (Eq. 1.2)}$$

Where S is the supersaturation ratio, c is the solution concentration and c* is the equilibrium saturation at a known temperature, T.[3] Relative supersaturation, by contrast, is expressed as:

$$\sigma = \frac{c - c^*}{c^*} = S - 1 \text{ (Eq. 1.3)}$$

The influence of temperature and concentration on crystal growth are characterised by solubility phase diagrams, which provide valuable information to aid in the design of a crystallisation process. An example solubility phase diagram is shown in Figure 1.

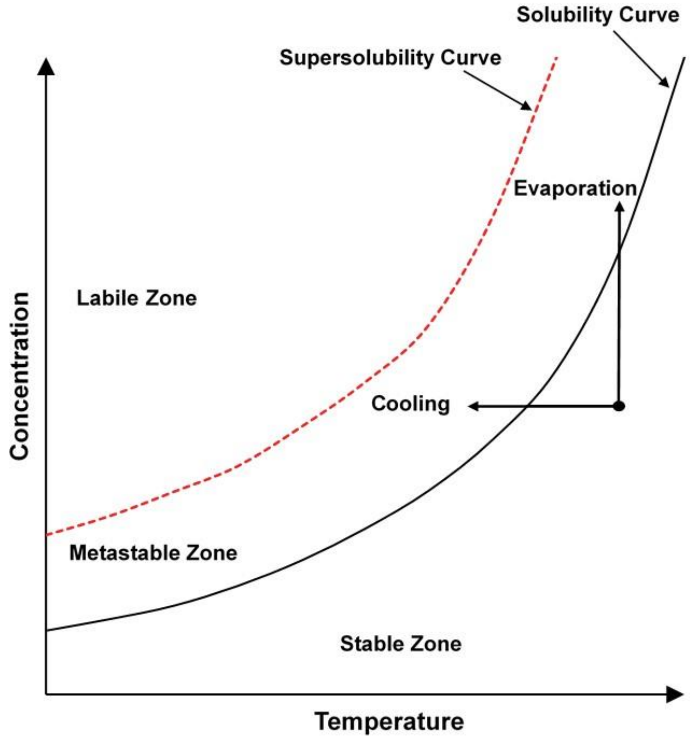

Figure 1: A general solubility curve, which shows the relationship between temperature, concentration and solubility, with key regions and features highlighted.

The solubility phase diagram is characterised by three distinct zones: the stable zone, metastable zone and labile zone. Within the stable zone, the observed solute concentration is lower than the equilibrium saturation at the given system temperature and therefore lies beneath the solubility line. As such, the solution is defined as undersaturated due the net negative difference in chemical potential between the solid and solution phase, which means that crystallisation will not be observed.[5]

Manipulation of the temperature and concentration of the system will alter its solubility, leading to supersaturation generation, the necessary thermodynamic requirement for crystallisation to occur. By contrast, nucleation and crystal growth are not governed by the same thermodynamic drivers. Rather, they are the result of kinetic processes. The region of supersaturation which exists above the solubility curve can be further defined as either the metastable zone or labile zone depending on the composition of the system.

The broken red line on the solubility curve represents the supersolubility curve, which is particularly sensitive to the speed at which solution supersaturation is achieved and how the process is attained, such as the involvement of solution agitation and foreign particles in solution which may act as trigger points for nucleation to occur. As a result, the exact position of the supersolubility curve is difficult to define precisely and thus will vary depending on real system properties.

The region which exists between both the solubility and supersolubility curves is the metastable zone, which forms because of the need for nuclei to form before crystal growth can proceed. Within this region, seed crystals will form but the spontaneous growth of crystals will not be observed by means of a primary homogeneous nucleation mechanism. This is due to insufficient supersaturation necessary to overcome the kinetic barrier for nucleation and crystal growth. Beyond the supersolubility curve lies the labile zone, within which spontaneous crystallisation becomes more likely.[5]

The ability to accurately distinguish the limits of the metastable zone and thus the nucleation behaviour of a system of interest allows for greater control of crystallisation processes, which is characterised by the metastable zone width (MSZW).[6] It is defined as the temperature difference which exists between the solution temperature where complete solute dissolution is observed and the temperature at which crystal formation is visually observed on decreasing the system temperature.[1] The metastable zone width indicates the limits within which a crystallisation process can be operated where careful control of crystal size and size distribution are possible.[7]

1.2 Crystal Nucleation Mechanisms

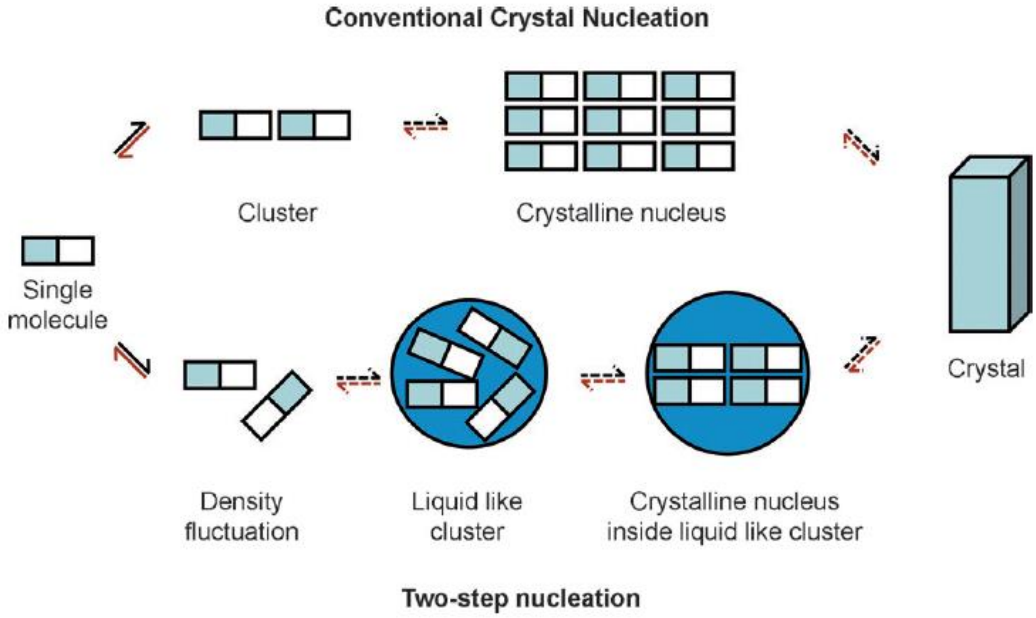

Figure 2: Schematic highlighting the pathways by which single molecules can nucleate and subsequently form crystal structures by following either conventional classical nucleation or two step nucleation pathways.[13]

As noted in the chapter foreword, there are two main theories by which crystal nucleation can be rationalised: classical nucleation theory (CNT) and non-classical nucleation theory (sometimes referred to as two step nucleation), as illustrated in Figure 2. Such nucleation systems are referred to as primary nucleation systems, as they do not contain any traces of crystalline material within the system from the outset.[5] These systems proceed by means of either a homogeneous or heterogeneous nucleation mechanism, so called based on the physical state of the nucleating solution they characterise.

Secondary nucleation, where nucleating solutions are “seeded” with crystals to accelerate the induction of crystal structures, will not be discussed as it is not relevant to this research.

1.2.1 Classical Nucleation Theory

CNT was developed as a result of work carried out in the early 1900’s by Gibbs, Volmer, Weber and a number of other researchers. For many years, CNT was the widely accepted as the definitive description of crystal nucleation and provides the foundation upon which ten Wolde and Frenkel went on to rationalise and propose that nucleation instead consists of two distinct steps in the late 1990’s.[4, 8]

Primarily based on the condensation of a vapour to generate a liquid, CNT formed the initial start point by which crystal nucleation from solution was rationalised.[5, 9] There were three main reasons which led to its adoption: the concept was easy to understand and translate to nucleation systems, there were few parameters required to physically describe the mechanism and it allowed for the nucleation rate to be calculated with relative ease as a result.[2] CNT is best explained by the mechanism which rationalises homogeneous nucleation. However, it can also be used to explain heterogeneous nucleation.

1.2.1.1 Homogeneous Nucleation

Homogeneous nucleation involves the spontaneous generation of nuclei from solution and is the foundation upon which CNT was adapted to explain crystal growth from nucleating solutions. Classical theories on homogeneous nucleation are aligned in the belief that the early growth of the nucleus is the result of reacting molecules or ions forming clusters[5].

However, these theories are not fully aligned on the degree of influence supersaturation, a main driver in crystal growth, influences the size of the critical nucleus. To fully understand CNT and the key physical quantities that influence this mechanism, it is important to consider both the thermodynamics and kinetics which underpin rationalising crystal nucleation in this way and the subsequent limitations it presents as a result.

Underlying Thermodynamics and Kinetics

CNT proposes that crystal growth stems from the clustering of small molecules to form a nucleus, the result of which is a change in the free energy of the system, ΔG.[10] When considering the thermodynamics that govern this phase transformation and the subsequent birth and growth of the crystal phase, the overall excess free energy of the system (ΔG) is determined to be the sum of two distinct free energy contributions: the surface (ΔG_S) and volume (ΔG_V) excess free energy.[5]

The excess free energy that exists between the surface and bulk of particles in solution, ΔG_S, favours the dissolution of clusters of molecules which would otherwise go on to form nuclei and gives rise to a positive free energy term.[5] This is generated because of the formation of the interface between the bulk solution and the newly formed crystal phase.[10] Therefore, by definition, it is the energy required to generate the solid structure from the nucleating solution.[9] This means that when small radii clusters exist in the solution, ΔG_S

is the dominant energy contribution to the free energy of the system, increasing ΔG and thus leading to their dissolution.

By contrast, the excess free energy that exists between an infinitely large particle (where radius r=∞) and solute in the solution, ΔG_V, is negative and characterises the phase change from liquid to solid in terms of intermolecular bonding which takes place.[9, 10] This is because the volume term favours the formation of nuclei as molecules aggregate, as the solid state is more stable than that of the liquid state.[4] This decreases the free energy of the system, in contrast to the surface term which favours dissolution of the nuclei and increases the free energy of the system. This relationship is expressed as follows:

$$\Delta G = \Delta G_S + \Delta G_V \text{ (Eq. 1.4)}$$

$$\Delta G = 4\pi r^2\gamma + \frac{4}{3}\pi r^3 \Delta G_v \text{ (Eq. 1.5)}$$

Where r is the radius of the growing nuclei (assumed to be an idealised spherical particle[10]), γ is the interfacial tension between the surface of the crystal and the solution which it is growing in and ΔG_v is the free energy change of the transformation per unit volume.[5] As a result, the processes of growth and dissolution are in direct competition with one another, which influences the degree to which nucleation occurs.

ΔG_S and ΔG_v, as can be seen in equation 1.4, do not have the same dependence on the radius of cluster r. This means that as a clusters size increases, the radius of the cluster approaches a maximum known as the critical radii, r_C, shown in Figure 3. This is the minimum size at which a nucleus is seen to be stable. When the cluster radius exceeds the critical radii, $r>r_C$, the system free energy decreases and thus nucleation is the most energetically favourable process, leading to the formation and growth of stable crystal nuclei.[5, 9]

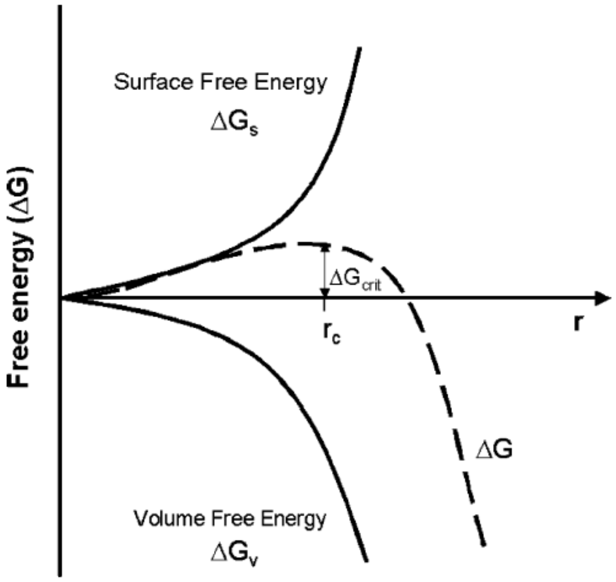

Figure 3: Diagram highlighting the observed free energy change in a supersaturated solution upon formation of a crystal nucleus with critical radii, r_{crit}. [5]

Differentiating equation 1.5 with respect to radius r and setting dΔG/dr =0 allows for the critical radius to be defined as follows:

$$\frac{d\Delta G}{dr} = 8\pi r\gamma + 4\pi r^2 \Delta G_v = 0 \text{ (Eq. 1.6)}$$

$$r_C = -\frac{2\gamma}{\Delta G_v} \text{ (Eq. 1.7)}$$

Rearranging r_C to solve for ΔG_V and substituting into equation 1.5 then determines the minimum energy requirement for a stable nucleus to form, the critical free energy, ΔG_{CRIT}:

$$\Delta G_v = -\frac{2\gamma}{r_C} \text{ (Eq. 1.8)}$$

$$\Delta G_{CRIT} = 4\pi r_c^2 \gamma + \frac{4}{3}\pi r_c^3 \left(-\frac{2\gamma}{r_C}\right) \text{ (Eq. 1.9)}$$

$$\Delta G_{CRIT} = \frac{12}{3}\pi r_c^2 \gamma - \frac{8}{3}\pi r_c^2 \gamma \text{ (Eq. 1.10)}$$

$$\Delta G_{CRIT} = \frac{4}{3}\pi r_c^2 \gamma \text{ (Eq. 1.11)}$$

The number of nuclei which form per unit time per unit volume defines the nucleation rate of the system, J. The nucleation rate is expressed as follows:

$$J = A\, exp\left(-\frac{B}{ln^2(S)}\right) = A \exp\left(-\frac{\Delta G_{CRIT}}{k_B T}\right) \text{ (Eq. 1.12)}$$

Where A and B are the pre-exponential and thermodynamic factors, which govern the molecular kinetics of nucleation and the free energy barrier for nuclei formation, S is the supersaturation ratio, k_B is the Boltzmann constant and T is the system temperature.[11] The nucleation rate, as seen in equation 1.12 above, has a non-linear relationship with the supersaturation ratio S. The supersaturation ratio is the main driver of the crystallisation process and is the ratio of system concentration with system solubility at a given time.[3]

When system concentration exceeds system solubility, this gives a positive S value which indicates the solution is supersaturated and that crystals present in the solution can grow. In contrast, when solubility exceeds concentration in a system, the solution is undersaturated and will lead to the dissolution of any crystals present, as mentioned in relation to the thermodynamic rationale.[3] Consequently, given the significance of the degree of supersaturation in the system on its kinetics, small changes in S lead to nucleation rates which can be increased or decreased by several orders of magnitude.[11]

1.2.1.2 Heterogeneous Nucleation

Although more applicable to homogeneous nucleation, CNT can also be applied to heterogeneous nucleation mechanisms, which proceed due to the presence of foreign particles or surfaces in the nucleating solution. The presence of such particles or surfaces leads to a reduction in the surface energy of clusters with critical radii (r_C) when they encounter them.[5] This leads to a lowering of the energy barrier required to pass the critical radius and facilitate the growth phase of crystal formation, meaning crystal formation is possible at lower supersaturation conditions.[12] The difference between heterogeneous and homogeneous nucleation and the way in which they generate crystal nuclei is highlighted in Figure 4.

Consequently, this means that heterogeneous nucleation is more energetically favourable and thus less energy intensive than homogeneous nucleation, with the difference shown in Figure 5. The relationship between the homogeneous and heterogeneous nucleation free energy barriers is as follows:

$$\Delta G'_{CRIT} = \varphi \Delta G_{CRIT} \text{ (Eq. 1.13)}$$

Where $\Delta G_{CRIT}'$ is the free energy barrier for heterogeneous nucleation and φ is an activity factor between zero and one.[1, 5] The activity factor is a scaling factor which accounts for the reduction of the interfacial energy between the solution and crystal due to its formation on the surface of the impurity or interface.[1]

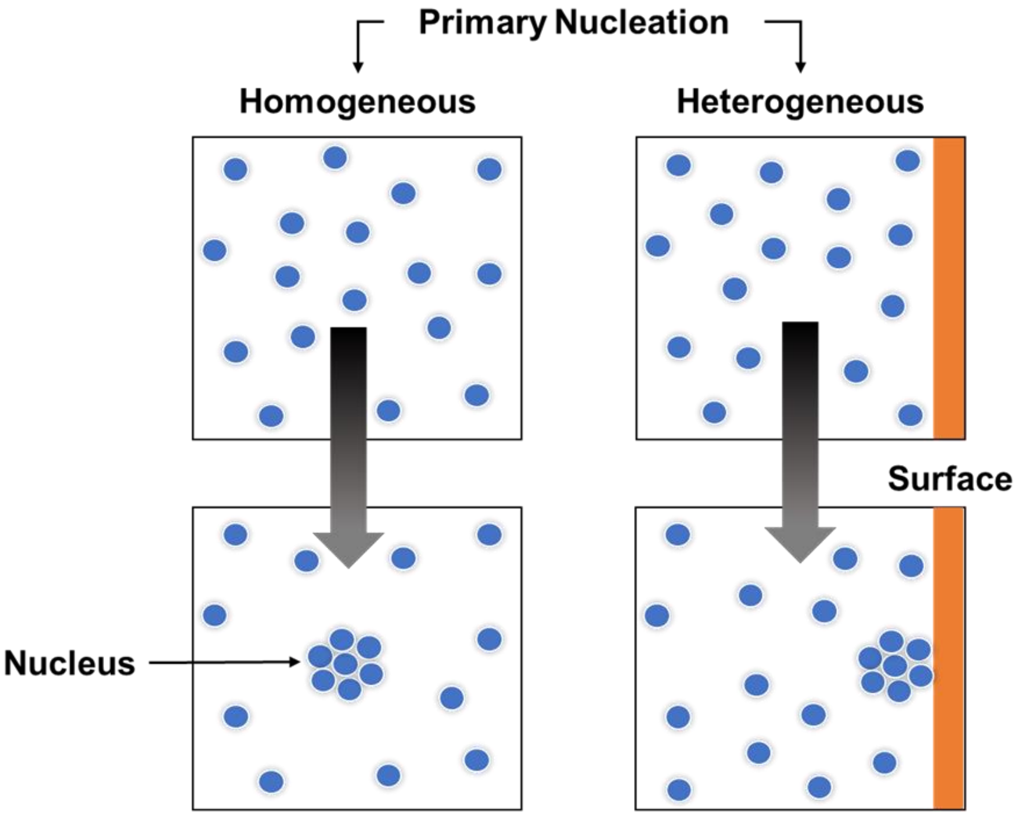

Figure 4: Schematic outlining the two pathways by which primary nucleation proceeds, either a homogeneous or heterogeneous nucleation mechanism.

Given that heterogeneous nucleation is concerned with nucleation on foreign surfaces and impurities, it is logical that the forces exerted between such surfaces and the nucleating solution will play a key role in the extent to which nucleation occurs. Specifically, the interfacial tensions (γ) between the growing cluster and the bulk solution, a foreign particle and the bulk solution and the foreign particle with the growing cluster play a key role in both the evolution and control of the crystal process over time.[1]

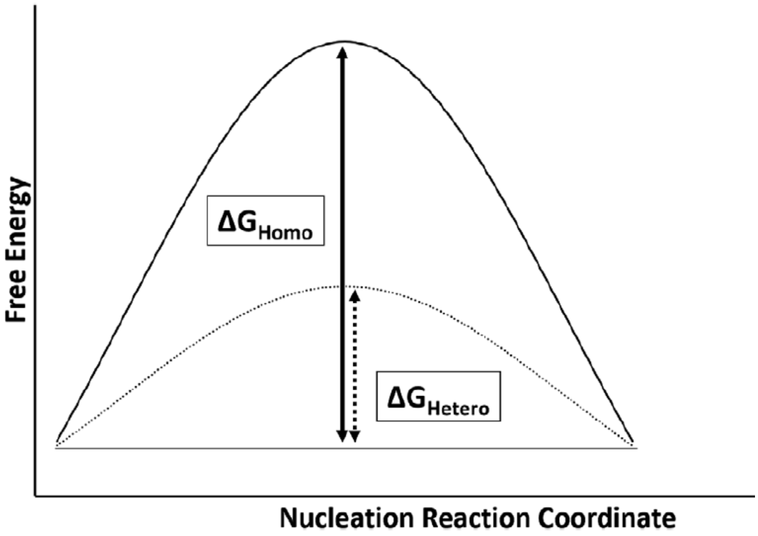

Figure 5: Visual representation of the difference in free energy barriers observed for homogeneous and heterogeneous nucleation to proceed. [4]

These parameters are given context by Figure 6, which illustrates the relationship between each respective interfacial tension to the system and highlights that the system kinetics are driven by the interaction of the interface with the bulk solution. Performing a force balance at the surface in the horizontal direction yields the following relationship:

$$\gamma_{CS} = \gamma_{CS} + \gamma_{CS} \cos\theta \text{ (Eq. 1.14)}$$

Where θ is the contact angle between the crystalline solid and the surface. The contact angle is related to the activity factor φ by means of the following equation, proposed by Volmer in 1939 [5]:

$$\varphi = \frac{(2+\cos\theta)\,(1-\cos\theta)^2}{4} \text{ (Eq. 1.15)}$$

This relationship allows for the activity factor to be determined based on the contact angle that exists between the growing face and the surface it is in contact with. As a result, the affinity the solution has for the surface and vice versa can be characterised. For example, when θ is equal to 180°, this would indicate that the crystal and the surface do not exhibit clear interactions with one another and that the free energy required for heterogeneous nucleation in this instance is equal to that of homogeneous nucleation.[2, 5]

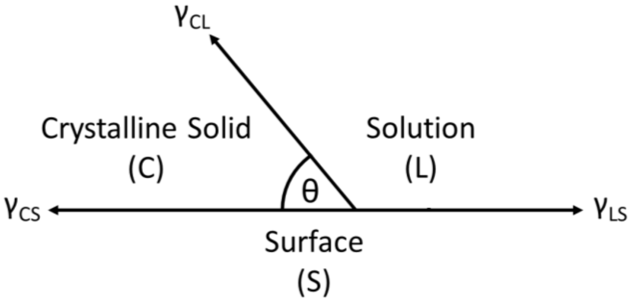

Figure 6: Interfacial tensions observed at the interface between a nucleating solution, solid surface in contact with the solution and a forming crystalline solid. (Adapted from [6])

By contrast, a contact angle of 0° shows that the surface and crystal have a clear affinity for one another and the free energy of the system is zero. This is characteristic of secondary nucleation, where a solution is seeded with crystals to induce crystal growth. As such, heterogeneous nucleation is facilitated within the region $0° < \theta < 180°$.[2, 5]

Underlying Kinetics and Thermodynamics

Heterogeneous nucleation and the rationale to how it proceeds classically is similar to that of homogeneous nucleation. Modelled on the formation of liquid droplets from the gaseous phase, a model system of which is shown in Figure 7, the theory proposes that crystal growth stems from the clustering of small molecules to form nuclei, which leads to a change in the free energy of the system, $\Delta G_{CRIT}'$.[10] The overall excess free energy ($\Delta G_{CRIT}'$) is the sum of the two distinct free energy contributions to the system: the surface (ΔG_S) and volume (ΔG_V) excess free energy.[5]

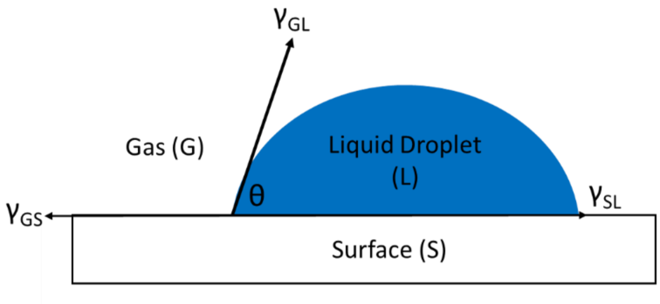

Figure 7: Interaction of a liquid droplet with a solid surface, the analogy by which heterogeneous crystal nucleation is rationalised.

To express the overall free energy of the system, the surface and volume terms must be appropriately scaled to represent the spherical cap which forms when a liquid droplet contacts the surface. The volume term, φ, is defined above and the surface term, α, is defined as follows [2]:

$$\alpha = \frac{1-\cos\theta}{2} \quad \text{(Eq. 1.16)}$$

The free energy of the system, accounting for the additional surface energy term arising from the interaction between the liquid and the surface, is expressed below:

$$\Delta G'_{CRIT} = \Delta G_V + \Delta G_{S1} + \Delta G_{S2} \quad \text{(Eq. 1.17)}$$

$\Delta G'_{CRIT} = \frac{4}{3}\pi r_c^3 \varphi \Delta G_V + 4\pi r_c^2 \alpha \gamma_{GL} + \pi(r_c^2 \sin\theta^2)(\gamma_{LS} - \gamma_{GS})$ (Eq. 1.18)

It is widely believed that the third term in equation 1.17, ΔG_{S1}, contributes less towards the overall free energy of the system than if the same surface area was exposed to the gaseous phase as is observed for ΔG_{S2}. This leads to the free energy of formation of the cluster being lowered and a reduction in the free energy barrier for nucleation because of this. The reason for this reduction is believed to be the surface tension between the cluster and the surface being decreased.[2] However, the precise explanation of the drivers behind this observation are not fully understood.

With regards to the kinetic description of the system where heterogeneous nucleation is facilitated, interaction with surfaces leads to a modification of the rate law used to characterise homogeneous nucleation. The modified kinetic relationship by which the nucleation rate is expressed for heterogeneous nucleation is as follows:

$$J_{HET} = A_{\ HET}\ exp\left(-\frac{B_{HET}}{ln^2(S)}\right) = A\exp\left(-\frac{\Delta G'_{CRIT}}{k_B T}\right) \text{ (Eq. 1.19)}$$

Where A_{HET} and B_{HET} are the kinetic and thermodynamic pre-factors accounting for heterogenous nucleation and $\Delta G_{CRIT}'$ is the free energy barrier for heterogeneous nucleation to occur.[1]

1.2.1.3 Effect of Interfacial Properties on Heterogeneous

Significant efforts have been made in the last century to better understand the key drivers which rationalise heterogeneous nucleation mechanisms in an attempt to better understand the system on the molecular level and translate this knowledge to practical control measures in crystallisation processes. The exact means by which heterogeneous nucleation proceeds can be rationalised by a number of well-developed schools of thought, which are extensively covered in published literature.

Such studies identify epitaxial crystal growth, the influence of surface topography and the role of surface functionality within the nucleating solution as key descriptors in the way the phenomenon is understood.

The proposed research aims to shed light on a recent discovery within the which assesses the role of Van der Waals forces on how heterogeneous nucleation Is both governed and rationalised, a point of discussion which has not made up a part of the standard knowledge in literature to date. The following assessment of the state of play within this area of research details these established schools of thought.

Epitaxial Crystal Growth Mechanism

Epitaxy is the process by which a material is deposited onto a substrate with similarities in both its functionality on the molecular scale and unit cell parameters.[13] These similarities result in the new solid phase being imparted with certain crystal orientations that lead to the functional groups on the substrate interacting with the solute molecules in a specific manner, in turn leading to molecular ordering of the new crystalline phase.[12, 13] The net result of the molecular ordering is the formation of ordered crystal lattices which match those of the substrate they were formed upon.

Warzecha et al. undertook a study where a templated two step nucleation mechanism was observed in the formation of olanzapine dihydrate from anhydrous olanzapine. [14] This work contributes to the body of evidence which has been developed over the last two decades rationalising the two-step nucleation mechanism and focused on assessing how surface topology, lattice matching and functionality all contribute to the successful two step mechanism.

It was observed that the surface played a key role in the outcome of the polymorphic outcome for olanzapine crystallisation, with the stable thermodynamic form selectively crystallising on the main face of the polymorphic form I of olanzapine by way of templating on the surface. Although this is clearly evidence of epitaxy, further analysis of the surface highlighted the significance that intermolecular interactions play in facilitating the epitaxial mechanism.

Ultimately, especially in the case of large-scale crystallisation, achieving such selectivity through epitaxy may not be uniformed across a surface due to the conflicting influence of the bulk system. As a result, further emphasis must be placed on the intermolecular interactions between the surface and the solute molecules in order to rationalise the early stages of nucleation and thus how epitaxy proceeds due to such interactions.

Influence of Surface Interactions and Functionality

As discussed previously, the presence of a surface lowers the free energy barrier for heterogeneous nucleation to take place and subsequently accelerates the rate at which crystals grow.[12] Having the ability to tune surfaces like these with precise characteristics that induce nucleation preferentially or quicker provides a key opportunity to gain greater control of crystallisation processes and subsequently manipulate conditions to suit desired specifications.

Diao et al. investigated the role which the surface chemistry and morphology of polymeric substrates have in the heterogeneous nucleation of aspirin. Using induction time and crystal orientation studies, they screened a range of substrates to assess which gave rise to the most effective crystal nucleation and the possible mechanistic drivers which play a part in this process, as well as probing how the surface chemistry influences the geometry of the crystals grown on respective surfaces.[15]

Specifically, polymers with significant polarity and an abundance of hydrogen bonding sites, such as acrylic acid and 4-acryloylmorpholine, were found to induce nucleation far more successfully that comparative polymer substrates that were less polar.

This is as would be expected, as large polarity differences between the substrate and the aspirin molecules would lead to the formation of favourable interactions and orientation of the aspirin molecules at the polymer surface. A particular observation of note was seen in the nucleation of aspirin both with and without 4-acryloylmorpholine present in the solution; as the polymer surface appeared to suppress bulk nucleation and enhance nucleation at the polymer-solution interface. This highlights the importance of correct polymer selection, as both surface polarity and the intermolecular interactions possible between the polymer and solution play a key role in determining the way liquid systems interact within the experimental setup.

Through assessment of the crystallisation of seven different API’s, Verma et al. assessed the impact of the presence and absence of a heterosurface (micro-crystalline cellulose, a common pharmaceutical excipient) and thus how heterogeneous nucleation depends on surface functionality.[16] The assembly of molecules at the solid-liquid interface is the result of selective and specific interactions, which were investigated using a combination of experimental and simulation work with the aim to investigate the impact of hydrogen bonding between the excipient and API on heterogeneous nucleation.

The study found two key factors which influenced the way crystallisation proceeded. The amount of time where a hydrogen bond was present between an API molecule and the surface is far greater than the time needed for API molecules to interact and bond to the growing crystal structure or interact with other API molecules in the bulk solution. This is due to the favourable energetics which result from formation of the stable crystalline phase, which encourages further crystal growth at the surface through interaction with further API molecules in the bulk solution.

In addition to this, hydrogen bond complementarity between the surface and API molecules was also found to play an important role in the crystallisation process. When a surface was present that had a wealth of hydrogen bond donor groups, this led to favourable interactions with acetaminophen and carbamazepine, both of which have hydrogen bond donor groups. This leads to preferential growth of clusters with this functionality as opposed to those with hydrogen bond accepting groups which could not move from the bulk solution to form complimentary interactions at the equivalent surface. This is an interesting insight, as the published results place a particular emphasis on the role of hydrogen bonding between the surface and API molecules as the key driver in the nucleation process, a stronger form of interaction than the Van der Waals forces other accounts believe have more significance in how molecules interact with heterosurfaces in the first instances.

Surface Topography

As well as the functionalisation of the surface, surface morphology (or topography) has been the focus of considerable research in recent years to assess how the structure of the surface upon which heterogeneous nucleation is induced may affect the degree of nucleation or indeed the selectivity of the crystal product which forms. This is significant as in-depth analysis at the nanometre scale sheds light on the activity of small molecules, which typically have a nucleus on the order of hundreds of angstroms in size. [12] Pores in surfaces intended for inducing heterogeneous nucleation are typically orders of magnitude larger and can subsequently give rise to molecular aggregation and similar events which promote nucleation at the surface.

Di Profio et al. have a number of studies which look to provide insight into the role of topography in heterogeneous nucleation. One such example was the investigation of how polymeric films affect the degree of nucleation of acetaminophen, acetylsalicylic acid and glycine, specifically the role the nanostructure of the films plays in driving or suppressing nucleation. [17] Solute-polymer interactions were found to dictate if a surface was an effective heteronucleants or not, while the roughness of the surface did not appear a definitive factor in the degree of nucleation observed.

In the case of glycine, nucleation activity was more apparent when hydrophilic polymer surfaces were employed rather than comparative use of hydrophobic surfaces. Given the acidic and basic functionality present within the structure of glycine, through carboxylic acid and amine functional groups, this meant that favourable acid-base interactions with the hydrophilic surface could be formed.

It was observed that some polymer surfaces, when the roughness of said surfaces were increased, led to slight enhancement of the nucleation rate. However, other surfaces assessed saw a reduction in the nucleation activity of the three molecules of interest. What this suggests is that while surface topography may play a part in affecting how nucleation proceeds, it is not the key driver.

Instead, the way in which the surface and solute interact at the interface would appear to be the dominant effect which in turn facilitates surface topography further enhancing nucleation. For example, while a porous surface morphology may promote active nucleation sites to enhance nucleation, this will be redundant if there is not favourable interaction between the surface and the solute molecules in solution. This is where the need to fully rationalise and understand these interfacial processes in great detail becomes more apparent.

Impact of Interfacial Effects on Nucleation

A further means by which heterogeneous nucleation can be rationalised is that of the interactions observed between the solute molecules within the nucleating solution and the surfaces with which it shares close proximity. The intermolecular interactions between adjacent atoms at the interface between the surface and solution, more commonly known as Van der Waals interactions, lead to directional alignment of the atoms based on their attraction or repulsion for one another. Research into whether or not this directional alignment can lead to preferential induction of nucleation or of the growth of more stable polymorphic forms of a molecule is ongoing and forms the background context within which the research proposed throughout is framed.

Given that water molecules are considerably smaller than the protein molecules used, they can interact more readily with the surface. The net result of this is that, depending on the affinity the surface and protein have for one another, crystallisation was either inhibited by the formation of a water depletion layer or preferred. In the case of a methyl functionalised SAM, the lack of hydrogen bond acceptors on the surface means that Van der Waals interactions between the protein and the surface are facilitated, leading to an increased concentration of proteins at the surface and thus a localised protein concentration increase.

Curcio et al. conducted a study in which six commercially available polymers were utilised as heteronucleants to assess how surface functionality regulates the rate of nucleation of acetaminophen (ACM).[18] The work identified that polymeric interfaces promote specific acid-base interactions and molecular reorganisation which enhance nucleation kinetics, while also demonstrating that surfaces which are unable to promote specific directional interactions between the polymer substrate and ACM inhibit its nucleation rate.

This study has relevance in relation to the nature of the polymeric substrates, which resemble the principle which would be followed in creating optical waveguide layers for OWS analysis. Being mindful of the material of construction and how its surface chemistry may interact with the model molecule of interest is important to ensure that promotion or inhibition of nucleation can be obtained. By trialling a variety of different polymer functionalities (including ester, aromatic and imide functionalities), this study provides insight into how ACM nucleation responds to different surfaces, from which the interactions observed can then be applied to this research to ensure that the polymeric surfaces created for experimental work are appropriate for the system of interest.

Zhang et al. investigated how the use of functionalised self-assembled monolayers (SAMs) affects the crystallisation of proteins from solution and how the insight gained may give rise to a new technique for controlled crystallisation. By functionalising a glass substrate with a range of different functional groups (including methyl, sulfydryl and amino groups) and assessing how the respective groups influenced the crystallisation of two model proteins (lysosome and glucose isomerase), the group identified that dispersion forces played an important role in whether protein crystallisation was enhanced or suppressed.[19]

The research identified that most crystals adhered to surface-water interfaces, which suggested that nucleation was specifically occurring at the interface. The range of functional groups selected and proteins (with lysosome being positively charged and glucose isomerase negatively charged) allowed for determining which SAM induced preferential nucleation of a particular proteins. In the solution, protein and water molecules were both capable of forming hydrogen bonds with the surface and as such were in direct competition to form surface interactions.

The work of Boyes et al. also investigated the nanoscale interactions which govern heterogeneous nucleation, by assessing how glycine solution crystallises when graphene is utilised as a template for selective polymorph growth with varying levels of oxidation.[20] By assessing graphene as both an additive and a substrate for the crystallisation of glycine, it was found that graphene led to preferential crystallisation of the metastable α-polymorph over the unstable β-polymorph and highlighted the importance of intermolecular interactions between the graphene surface and glycine molecules in directing selective polymorph formation.

1.2.1.4 Rationalising CNT and its Limitations

Given that CNT was developed initially from the model of vapour condensation to form a liquid, its validity in rationalising nucleation is underpinned by several predictions and assumptions. While helpful in explaining the underlying principles of the theory, these assumptions also mean that it is not widely applicable to most real systems, as they are based on ideal conditions not observed in real crystallisation processes.

This is not easily achievable though, as the assumptions made to simplify the system are also the reason that it deviates from observed experimental results for such nucleation systems, as no real system will ever be close to this degree of ideality.[21] For example, the assumption that nuclei structure (and by extension their surface tension) are the same as that of the new stable crystal phase which forms is a well-established idea in relation to CNT. However, a combination of computational and experimental work has since challenged its validity, which will continue as new experimental methods are utilised and direct measurement of the initial stages of crystal growth become more readily achievable with greater accuracy.

Furthermore, it is assumed that the localised density and surface tension at the surface of the cluster are equivalent to that of the bulk solution and of an equivalent solid-solution interaction at a planar surface, respectively.[9] This means that both parameters are negligible, when they play an important part in influencing the way crystallisation proceeds. These points are important to consider when rationalising primary homogeneous nucleation, given it is the most widely used theory to characterise this mechanism.

The key limitation of CNT though is that to be substantiated, it must be supported with quantitative experimental evidence. However, predictive nucleation kinetic models which are constructed based on CNT rationale do not generate nucleation rates reflective of observed nucleation kinetics from experimental studies. Small changes in system supersaturation can lead to nucleation rates that have orders of magnitude of difference between them.[11] To overcome this, the nucleation rate can be fitted to account for this discrepancy. However, this can lead to non-realistic physical parameters being predicted. The result is that neither approach can adequately capture system behaviour in the early stages of crystal nucleation.

One cause of this disagreement stems from the assumption of a steady state nucleation rate in CNT, which is calculated with the assumption that the size distribution of pre-nucleation clusters does not change with time.[9] This leads to a constant nucleation rate, which is not an accurate characterisation of the early stages of crystal nucleation, as a transition time is needed to establish such a steady state distribution of subcritical clusters. Within a real, physical system, this relaxation time varies from experiment to experiment and can outlast the lifetime of the supersaturated system of interest, meaning steady state nucleation does not occur.

To be able to more accurately model nucleation kinetics, less reliance on the traditional simplifications required by CNT are needed. CNT has challenges in accurately reflecting experimental data well due to the pre-exponential factor in the rate equation typically being orders of magnitude too small to see a good agreement. This difference stems from a theoretical overestimation of the number of molecules which actually attach to the growing crystal nucleus and an assumption to neglect cluster movement and treat it ideally as a stationary object.[9] The attachment of molecules to the cluster is a major source of uncertainty, as the dynamics of molecular attachment to the nucleus cannot be directly observed in experiments. The crystal growth rate can be measured though, which is sensitive to supersaturation (the thermodynamic driver of crystal nucleation).[22]

The pre-exponential factor (see equation 1.12) is related to the molecular kinetics of the nucleation process, namely the way in which molecules move in solution and in contact with pre-nucleation clusters. This is why CNT nucleation rates must be scaled through the application of a fit-adjustment to fall in line with experimentally obtained nucleation rates.[9] In addition to overestimating the attachment of molecules to the cluster, this could also be due to there being fewer active nucleation sites than theorised with CNT. [11]

1.2.2 Non-classical Nucleation Theory

Advances in nucleation research resulted in the proposal of an alternative, non-classical description of how crystal nucleation occurs. The findings, based on experimental observations, represented a departure from the widely accepted understanding rationalised by CNT. As such, non-classical explanations of nucleation theory are concerned with heterogeneous nucleation rather than homogeneous nucleation, the premise from which CNT was rationalised. However, the initial stages of crystal nucleation are still not fully understood and research continues to this day hoping to better understand the fundamentals of crystal growth.[23]

Two-step Nucleation Theory

First proposed by ten Wolde and Frenkel in 1999 using a simulation-based approach[8], two step nucleation theory postulates that solute molecules do not directly incorporate to form a cluster during the initial stages of nucleation. Through their work on homogeneous systems, they found that deviating from the liquid-liquid critical point in the system (such as the critical temperature) in turn led to simultaneous fluctuations in both the localised density and structure observed.[8] This observation agrees with that outlined by CNT. However, around the critical point, large density fluctuations were observed which led to identifying a new, two-step nucleation pathway.[9]

Such density fluctuations were believed to be the result of the free energy barrier for crystallisation being reduced, which would in turn increase the nucleation rate by several orders of magnitude. For example, at temperatures above the critical temperature, nucleation was observed to occur via crystal clusters being formed. Below the critical temperature, liquid clusters formed instead. The deduction from this observation indicated that for critical nuclei to form and facilitate crystal growth, a liquid-like droplet must first form which allows crystal nucleation to proceed.[8, 9]

Experimental evidence from such investigations has given rise to more qualitatively correct nucleation rates than those observed through CNT based modelling, providing insight on how nuclei form from solution during the initial stages of nucleation.[13]

An example of such research is seen in the work of Vekilov, who postulates that during the transition between the liquid and solid crystalline phase it is more energetically favourable to form a liquid-like cluster.[1] This was observed from both experimental and simulation work which also investigated protein crystallisation. The research found that the high-density liquid-like clusters suspended in the nucleating solution facilitated subsequent formation of crystal nuclei, as shown in Figure 8.[4]

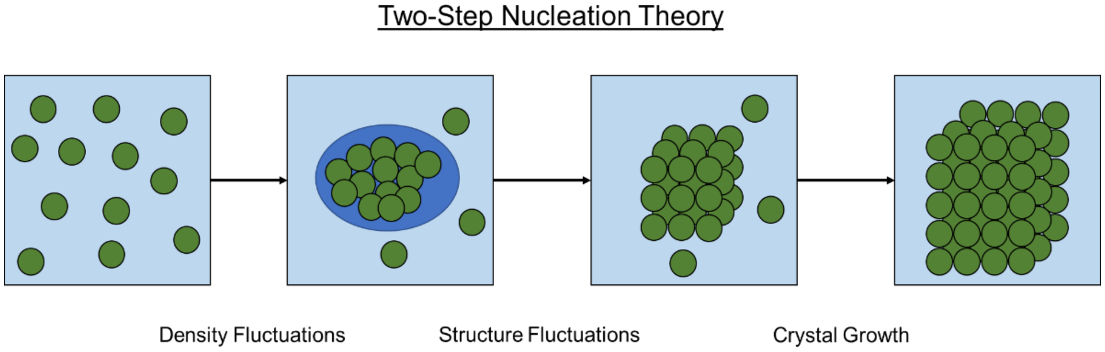

Figure 8: Key steps observed in the formation of crystals by means of a two-step nucleation pathway.

The mechanism was primarily investigated to better understand how the degree of supersaturation affected the nucleation rate of a model protein, lysosome. In doing so, key observations were made that challenged the assumptions of CNT. The observed nucleation rate was found to be several orders of magnitude less than the equivalent predicted nucleation rate when modelling based on CNT. Furthermore, temperature was found to have a significant impact on the nucleation rate also.

While reducing system temperature (thus increasing the degree of supersaturation) led to an exponential increase in the nucleation rate, in line with the observation of CNT, a deviation was observed where a maximum was passed and the nucleation rate went on to decrease with increasing temperature.[24] The maximum is reached when the quantity of the intermediate (in this case the cluster) is at its maximum, with the subsequent decrease due to the consumption of the intermediate to allow crystal growth to take place.[25] Assessing the kinetics of such systems in this manner allows for real time tracking of the progress on nucleation, which can help shed further light on key system parameters that influence the nucleation rate.

Given detailed imaging techniques were not available to directly quantify why such conditions were observed, it was rationalised that the effects were indeed the result of crystal nucleation occurring within metastable liquid clusters.[23, 24, 26] A subsequent modified nucleation rate was proposed, which is expressed as follows:

$$J = \frac{k\ C\ T\ \exp\left(-\frac{\Delta G_2^*}{K_B T}\right)}{\eta(C,T)\left[1+\frac{U_d}{U_f}\exp\left(\frac{\Delta G_C^*}{K_B T}\right)\right]} \text{ (Eq. 1.20)}$$

Where k is a constant and scales the nucleation rate of crystals within clusters, η is the viscosity within the cluster at a certain temperature and concentration, u_d and u_f are the effective rates of decay and formation respectively at a given concentration and temperature, ΔG_2^* is the nucleation barrier of crystals within the cluster and ΔG_C^* is the standard energy of the molecule within the cluster in excess to that of the surrounding solution in the system.[4]

The modified rate law indicates that the presence of surfaces or impurities in the nucleating solution, which trigger heterogeneous nucleation, does not lower the nucleation barrier to enable more molecular clusters to attain the critical size required for crystal growth. This is postulated for CNT, whereas for two step nucleation it is proposed instead that alteration of the nucleation rate facilitates the formation of stable clusters for crystal growth.[13]

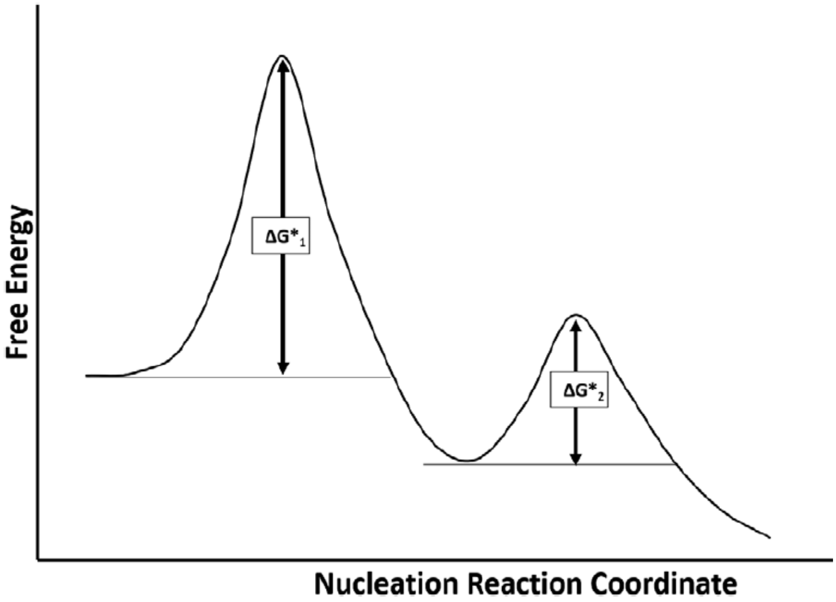

Figure 9: Difference in magnitude of the free energy requirements of the system for two-step nucleation to proceed and subsequent crystal growth to be observed. [4]

Generation of the initial dense liquid phase is a fast process, whereas the nucleation which then takes place within the cluster is comparably slower. As such, crystal nucleation is the rate determining step in the process. This gives rise to two distinct energy barriers, one for the liquid phase (ΔG_1^*) and the other for the solid crystalline phase (ΔG_2^*), both of which must be overcome for crystal growth to occur. These barriers are illustrated by the graph shown in Figure 9, which shows the comparative free energy requirements of the system as nucleation proceeds.

Although this non-classical rationalisation of crystal nucleation provides a more reasoned qualitative description of the process as a whole, it does not provide resolutions to the identified issues that are presented with the classical understanding of nucleation. A key area of contention lies in the rationalisation of the pre-nucleation solution behaviour as outlined by the non-classical nucleation theory.

While density fluctuations within the liquid cluster, subsequent ordering which yield critical nuclei with the same structure as that of the bulk crystal of interest and the aggregation of pre-nucleation clusters are all quite possible, it is important to acknowledge that this process is no different to liquid-liquid phase separation, often referred to as oiling out. Observed in the crystallisation of proteins and small molecules like glycine, this phase separation leads to a dispersion of concentrated drops of solution within a bulk solution of overall lower concentration.[11]

These drops offer an alternative environment to the bulk solution within which crystal nuclei can form but, importantly, do not lead to a different route by which crystallisation proceeds. As a result, the formation of the concentrated liquid droplets within the bulk solution simply represent the formation of an additional bulk phase within which nucleation can occur. This means that while qualitatively the theory describes crystal nucleation with a reasonable approach, it does not offer a deeper level of insight than that which classical nucleation theories have already established with respect to the early structure of the nuclei when forming.

Consequently, new ideas which challenge these well-established theories must be considered and subsequently tested in order to translate this to the design and optimisation of more efficient crystallisation processes.

1.3 Interfacial Concentration Enhancement and its significance in rationalising heterogeneous crystal nucleation

While CNT and non-classical nucleation theories have been the established schools of thought for many years, it is clear that more work is necessary to truly understand the key drivers behind this fundamental physical process. The work presented in this thesis seeks to contribute towards this furthering of understanding, challenging the established rationales with evidence that has not been previously considered.

It is well understood and widely accepted, based on the rationale posed by CNT, that the presence of a surface or interface within a solution prior to nucleation will stabilise the growing nucleus and lead to a reduction in the surface energy of the nucleus. The result of this is a lowering of the free energy barrier and a subsequent enhancement of the nucleation kinetics. CNT postulates that the solution concentration is equivalent throughout the system of interest, meaning that the concentration of the bulk solution is the same as at the interface between the solid surface and the solution phase. The question to pose in challenge to this belief is simple – is this truly the case?

A recent approach to investigate this theory, utilising a combined computational and experimental approach on solutions of aqueous glycine, identified a preferential orientation and subsequent enhancement of the nucleation kinetics of glycine at a solution-oil interface when contrasted with a solution-air interface.[27] Subsequent molecular dynamics simulations identified markedly different interfacial behaviour to that observed in the bulk solution, which was attributed to an effect that facilitates heterogeneous nucleation due to dispersion interactions between glycine molecules and the liquid interface.

The key thoughts upon which this rationale stands are grounded in considering the two key drivers of crystal nucleation – the thermodynamics and kinetics of the system. Although the behaviour observed at the interface was different, the chemical potential within the interfacial layer was believed to be equivalent to that of the bulk solution This is believed to be the result of an attractive potential between glycine molecules and the interface being in mutual equilibrium with the bulk solution. This behaviour aligns with observations from previous studies investigating the formation of mesoscale clusters of glycine molecules within aqueous solutions.[28]

It is therefore evident that if this interfacial effect does not stem from thermodynamic drivers of crystal nucleation, it must be the result of the kinetics directly influencing the local concentration at the solid-liquid interface. Specifically, it is the direct result of the attachment frequency of molecules to growing pre-nucleation clusters and the free energy barrier of the nucleus bound at the surface.

Nucleation occurs as the result of consecutive attachments and detachments of molecules to form differently sized clusters of the nucleating phase in solution. The kinetics of this process are governed by the frequency of those attachments, which are believed to be directly proportional to local concentration. As a result, the surface facilitates an enhanced frequency of this behaviour with respect to the bulk solution, an increase in the nucleation rate and a subsequent increase in the local concentration at the surface with respect to the bulk solution.

In addition to the influence of the relative attachment frequency on the local concentration at the surface, the energetics with respect to the free energy barrier for nucleation also play a part in driving this behaviour. CNT outlines that heterogeneous nucleation occurs at a faster rate due to a reduction in the crystal surface energy when close to a surface or interface, thus leading to a reduction in the energy barrier which must be overcome for nucleation to occur.

The activation energy necessary to facilitate nucleation depends on the nucleus' surface tension. Solute molecules within close proximity to a surface are less well bound to neighbouring molecules than those in the bulk solution, meaning the contribution they provide to the free energy of the new phase is greater. Consequently, exposure of the nucleus to a localised region of the solution with a higher concentration than that of the bulk solution results in a reduction in the surface energy. This is unexpected, as it would be expected that the surface free energy would increase in an attempt to destabilise the growing nucleus. Instead, the barrier to nucleation lowers due to the nucleation free energy barrier's joint dependence on both surface tension and solution composition.

The key question that stems from this is the need to consider how the solution behaviour differs from the region in direct contact with a nucleus, specifically the face not in contact with the interface, to that of the bulk solution. Surface energetics and molecular orientation can shed light on this effect and both offer plausible explanations for the drivers behind such behaviour. However, neither are directly investigated within this thesis.

Presently, neither classical nor non-classical rationalisations of crystal nucleation are able to comprehensively describe nucleation from both a qualitative and quantitative perspective. The work presented in this thesis does not provide immediate answers to the questions consistently leveraged at both schools of thought and further investigation will be needed to fully develop this understanding and rationale. However, it is clear that this reasoning must be accounted for when establishing new theories for the early stages of crystal nucleation due to the marked difference observed in interfacial behaviour when contrasted to that of bulk solution dynamics.

1.4 Surface Plasmon Resonance Spectroscopy

Significant research and development in the last forty years has seen advancements in optical sensing, more specifically surface plasmon resonance (SPR) sensing and its wide-ranging applications.[29] As such, this has seen SPR gain popularity and subsequently adoption in commercial applications, largely because of its label-free, highly sensitive range of detection to characterise biomolecular binding processes and interactions.[30, 31] [32]

SPR sensors are widely used as thin-film optical refractometers to detect changes in the refractive index of a sample medium of interest. By monitoring these shifts, SPR sensors can detect biomolecular interactions, chemical reactions, and environmental changes.[33] The ability of such sensors to perform highly sensitive measurements through the detection of changes in the refractive index at the surface of thin metal films without molecular labelling makes them incredibly useful,[34] especially when considering the behaviour of solutions prior to crystal nucleation in contact with different interfaces.

Example processes include antigen-antibody interactions for immunosensing, genetic analysis through assessment of protein-DNA interactions and cancer biomarker detection, all of which can be undertaken through the application of SPR spectroscopy. This is extremely beneficial to patients, as it facilitates early disease detection and the ability to develop drugs to treat diseases at an increased rate.[29]

Although widely applied to biosensing, SPR spectroscopy is not limited to biomolecular sensing. It is also an incredibly useful technique for application in chemical sensing, such as in the real-time detection of hazardous chemicals and gases by measuring changes in their refractive index. For example, SPR can be used to monitor hydrocarbons, aldehydes and alcohols in vapours through the use of polyethylene glycol thin films.[29] SPR sensors also see application in food safety and environmental monitoring applications, using the enhanced sensitivity for the detection of contaminants and toxins. This includes, but is certainly not limited to, the detection of pesticides in water and the detection of heavy metals (such as copper and lead) in water when coupled with anodic stripping voltammetry.[29]

1.5 Other Surface Measurement Techniques

Although the surface selectivity of SPR spectroscopy makes it an interesting proposal for assessing surface-solution interactions, there are other means by which these interactions could be investigated. Atomic force microscopy, spectroscopic ellipsometry and optical waveguide spectroscopy are examples of other techniques utilised for the measurement of surfaces, which are outlined below.

Atomic Force Microscopy

Atomic force microscopy (AFM) is a high-resolution scanning probe microscopy technique used in the analysis of surfaces at the nanoscale. AFM provides real time microscopy by way of its method of data acquisition, whereby a sharp tip is mounted on a cantilever over a sample. The tip is then moved in three dimensions, with a laser beam reflected from the cantilever to a photodiode detector. [35] The deflection of the cantilever then provides height information about the sample through the monitoring of laser reflection, which can be related to atomic-scale morphological information about the given sample.

There are two main methods by which AFM can be performed: contact or non-contact (dynamic) mode. In contact mode, the most commonly applied AFM measurement method, the tip remains in continuous contact with the sample surface and deflection of the cantilever is monitored to construct high-resolution topological images of the surface. The tip can also be placed in tapping mode, where the cantilever instead oscillates at its resonance frequency, periodically tapping the sample surface. This is generally more applicable for use in the study of biological material or polymers.[36]

In non-contact mode, the tip oscillates just above the sample surface, which in turn leads to the detection of interactions such as van der Waals forces. This method benefits from being able to provide high resolution images without physical contact being made between the tip and sample surface. The schematic in Figure 10 below shows the difference between the two measurement modes.

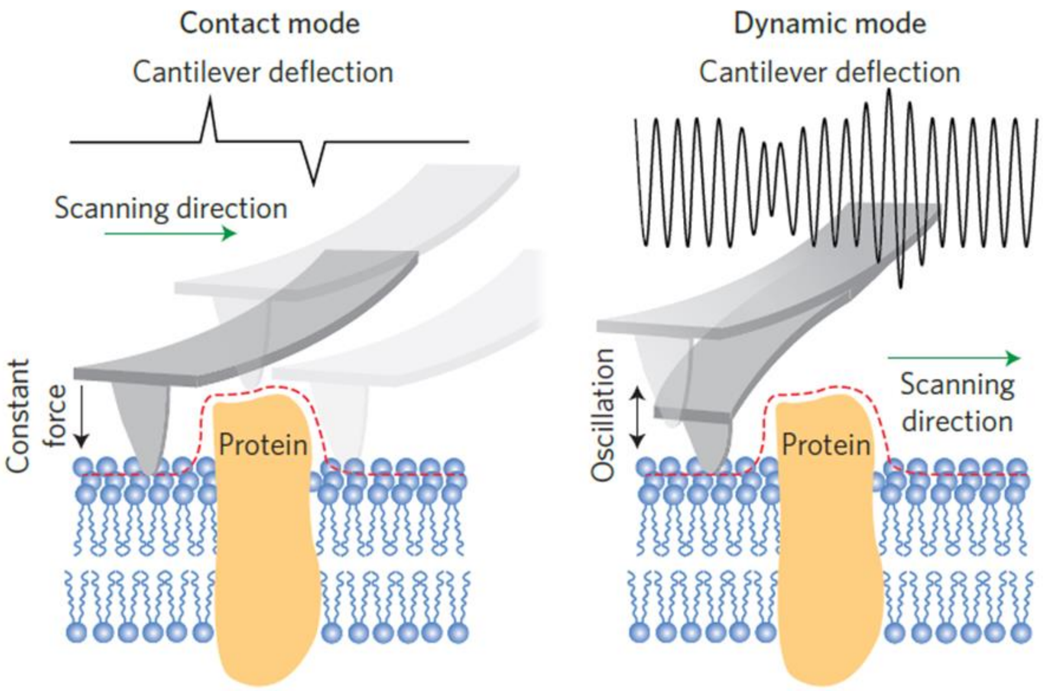

Figure 10: Examples of the two main methods of operation for atomic force microscopy: contact and dynamic mode. [36]

AFM is widely used for the characterisation of thin films, nanoparticles and nanostructures given its ability to provide real time imaging. Additionally, it can be used to measure mechanical properties of a surface, such as the Young's modulus of soft materials like biomolecules. As a result, AFM sees widescale use in material science and biomolecular research, nanotechnology and metallurgy, where precise information about the nanoscale characteristics of a surface are essential.

Spectroscopic Ellipsometry

Spectroscopic ellipsometry is a commonly used and effective means by which to measure ultrathin films. It is a highly sensitive technique, with the ability to measure transparent films down to a thickness limit of one angstrom and repeatable measurements of a material's dielectric properties.[37]

A non-destructive technique, ellipsometry relies on the changes to the polarisation state of an incident light source, typically ultraviolet-visible (UV-Vis), upon striking a thin film sample through the use of polarisers, with the light reflected indirectly from the sample.[38, 39] A schematic of a commonly used spectroscopic ellipsometer, a rotating analyser spectroscopic ellipsometer, is shown in Figure 11 below.

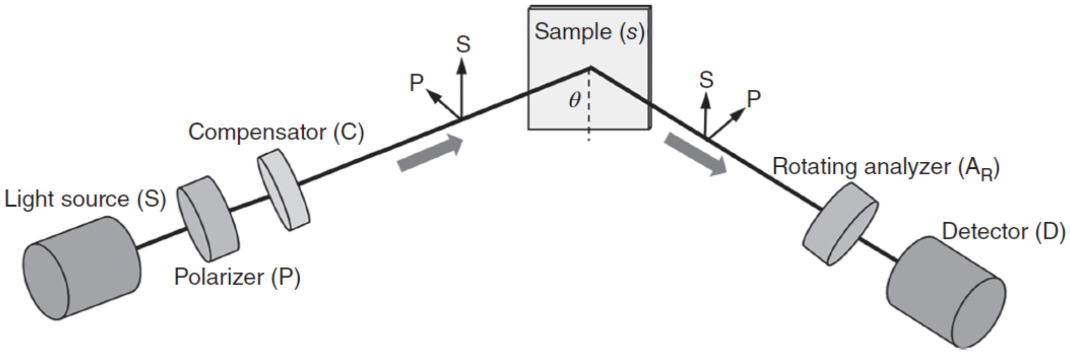

Figure 11: Schematic diagram of a spectroscopic ellipsometer, with a rotating analyser configuration. [37]

Like SPR spectroscopy, ellipsometry is unable to directly measure film thickness and relies on the deployment of models to characterise experimental data. This means that for ex-situ measurements, characterisation of a wide range of film properties, such as; layer thickness surface roughness and composition can be determined.

Conversely, in-situ measurements can be used to determine nucleation and growth parameters of thin films as they are formed on a surface.[38] While the technique offers a fast, non-destructive analytical technique, the mathematical analysis which is required to extract optical properties from the raw data is not straightforward. [39]

Furthermore, it is best suited to samples which are homogeneous and of sufficient thickness, meaning that application to heterogeneous systems requires approximations which may lead to non-realistic optical parameters.

Optical Waveguide Spectroscopy

In addition to SPR spectroscopy, optical waveguide spectroscopy (OWS) can also be employed for analysis of interfacial processes through the excitation of surface plasmons. The underlying principles of the technique are similar to that of the Kretschmann configuration employed for SPR sensing under ATR conditions and as such can offer at least comparable levels of sensitivity in the measurements which can be obtained. The following section outlines the fundamental principles behind the utilisation of optical waveguides (OWG) and the configurations and methods of construction employed to generate them.

Deposition of a coating layer onto a glass substrate with a refractive index equal to that of the glass prism used in the experimental setup [40], such as thin layer of high refractive index waveguiding material,[41] gives rise to additional film resonances which can be observed when performing angular reflectivity scans of a sample. Such resonances are characterised by narrow dips in the system response and are the result of the incident light source exciting guided optical modes within the deposited film.[40]

In order to ensure that there are no breaks in the media the incident light source passes through to reach the waveguide-metal interface, specifically between the prism and the glass substrate, refractive index matching oil is applied to the prism surface to ensure optical consistency in the system and minimise inaccuracy in the recording of measurements.

As a result of the way in which the system is configured, incident light propagates exclusively within the structure of the deposited waveguide.[42] These resonances propagate as bound electromagnetic waves and have a characteristic evanescent tail, which decays exponentially away from the metal-waveguide interface into both the waveguide and sample being analysed, exciting surface plasmons at the outer boundary of the metal layer.[34, 40, 42] A typical experimental setup and the response such a system produces is shown in Figure 12 below, which is an example of the most commonly utilised waveguide configuration in optical sensing, a planar OWG:

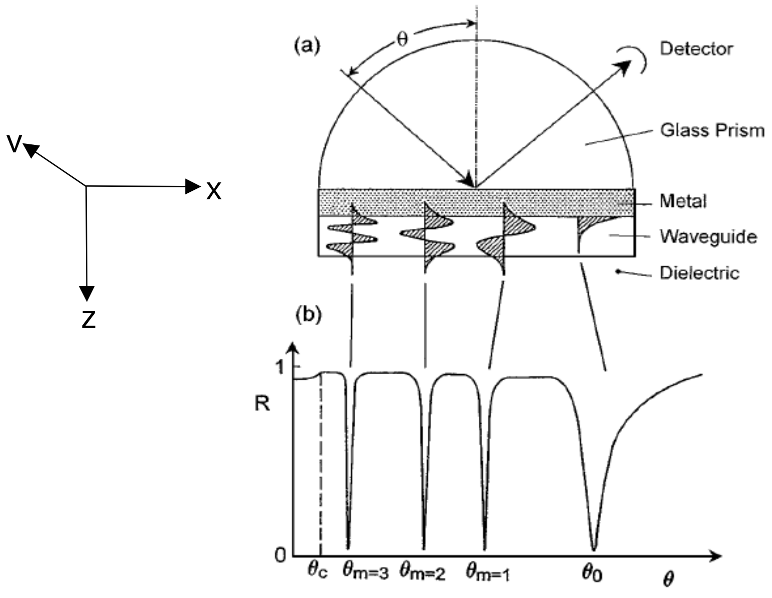

Figure 12: Experimental configuration and resultant angular response curve of a typical OWG experimental setup. [40]

The momentum of these guided electromagnetic modes in the x direction of travel is greater than that of the corresponding photons in free space, hence the need to couple the light source, as is the case for the Kretschmann configuration of the SPR sensor, using a high refractive index glass prism to ensure momentum matching of the bound waves and the incident photons.[40]

As shown in Figure 12, a waveguide with a set thickness has a number of modes, with their corresponding positions in the angular reflectivity scan dependant on both the wavelength of the incident light source and the respective refractive indexes observed in the experimental system. Changes in the conditions at the surface of the OWG structure change the refractive index, which in turn lead to minor shifts in the coupling angle.[42] Comparison of such changes can be used to determine key information about the system characteristics, such as the concentration of the sample at the interface or the thickness of a layer if molecules have adsorbed at the metal-dielectric interface.

Typically, OWG are produced from polymeric materials by spin coating layers of polymer onto the glass substrate to produce an OWG of the desired thickness. Examples include polystyrene[43], poly(methyl methacrylate) (PMMA), polycarbonate (PC) and polyurethane (PU).[44]

Generation of the bound electromagnetic waves that give rise to the sensing effect is not possible without total internal reflection occurring at both the prism-waveguide and metal waveguide-interfaces.[40] For total internal reflection to occur, the refractive index of the OWG must exceed the refractive indexes of both the glass prism and dielectric medium.

This scenario is shown in Figure 13; where n_1, n_2 and n_3 are the refractive indexes of the glass prism, OWG and dielectric medium, respectively. Consequently, $n_1<n_2>n_3$ satisfies the required conditions for total internal reflection to occur, which traps the light within the waveguide film and generates the guided electromagnetic mode that give rise to the sensing effect.[40, 44]

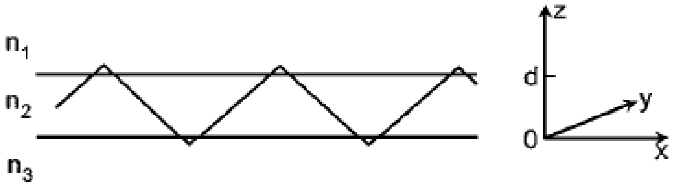

Figure 13: Geometry of an OWG, indicating the three regimes of differing refractive index the incident light passes through. [40]

Justification for use of SPR Spectroscopy

SPR spectroscopy is capable of probing interfacial behaviour as a result of its sensitivity directly at the solid-sample interface, which gives the ability to measure the thickness of a layer of molecules bound at the solid surface without detecting possible artefacts in the signal response caused by bulk solution measurement artefacts.

Consequently, SPR spectroscopy facilitates selective characterisation of this region relative to the properties of the bulk medium. For example, in an aqueous solution of glycine, SPR spectroscopy can be applied to sense localised concentration differences at the solid-liquid interface relative to the composition of the bulk solution. If the refractive index of the bulk solution is known, a representative model system can be built to determine the thickness of this interfacial layer of molecules.

Conversely, if the refractive index of the layer is unknown, a layer thickness can be assumed that facilitates quantification of the refractive index of the interfacial layer and subsequently the density of the layer. Due to the direct relationship between refractive index and concentration, this gives an indication of the solution density within this interfacial layer with respect to the bulk solution density. Neither measurement is entirely conclusive though, as each carries an associated degree of error by either assuming a layer thickness or refractive index. The result is a trade-off which the user must assess to establish which parameter is of more importance for characterisation. It was decided that based on this enhanced selectivity, SPR spectroscopy would be utilised in this research.

Furthermore, application of top down techniques such as ellipsometry and reflectometry were not considered, as they required looking through a sample cell as opposed to sensing within the cell as is the case for SPR spectroscopy. The inherent risk of sensitivity results caused by this top down approach were deemed undesirable given the level of sensitivity the proposed measurement in this research require.

1.6 Research Aims and Objectives

The work presented within this thesis can be can be briefly summarised as aiming to achieve the following high level aims:

- Determine whether SPR spectroscopy has the required sensitivity to detect interfacial concentration enhancement in situ.
- Probe interfacial effects in undersaturated solutions of aqueous pharmaceuticals on gold surfaces.
- Assess whether functionalisation of gold surfaces with a hydrophobic interface leads to a change in interfacial solution behaviour.

In Chapter 3, total internal reflection reflectometry and surface plasmon resonance spectroscopy are utilised sequentially to probe whether the experimental setup developed for this work has the necessary sensitivity to be able to accurately determine bulk solvent properties (critical angle for total internal reflection and solvent relative permittivity) and interfacial properties (SPR coupling angle minima). These metrics are key to probing interfacial concentration enhancement and therefore establishing how precisely they can be characterised is a key foundation upon which the work is based upon.

In Chapter 4, the critical angle and SPR coupling angle minima are utilised to capture interfacial concentration enhancement in situ. This is achieved through comparison of refractive index matched aqueous glycine solutions, with solvent reference measurements of binary solvent systems (1-propanol – methanol mixtures) and pure component solvents (ethanol).

In Chapter 5, this work is extended to solutions of aqueous urea, which has a higher solubility in water than glycine. This allows for a wider range of pure component solvents to be probed as reference solvents for refractive index matched urea solutions.

In Chapter 6, using the findings of Chapters 4 and 5 as a basis, gold chips are functionalised with ultrathin polystyrene layers on their surface before again performing measurements of solvent reference mixtures and pure component solvents, alongside the refractive index matched concentrations of aqueous glycine solutions. In doing so, the aim was to assess the influence of ultrathin hydrophobic interface on interfacial concentration enhancement and whether the enhanced hydrophobicity with respect to bare gold chips would lead to a change in the degree of interfacial concentration enhancement observed in situ.

Chapter 2

2. Materials and Methods

2.1 Introduction

In this chapter, the model compounds utilised in this research are outlined and described briefly to highlight why they were selected for use. The fundamental theory of both total internal reflection and surface plasmon resonance is then detailed, along with a description of surface plasmon resonance spectroscopy.

The spectrometer setup is outlined in detail for both the Total Internal Reflectometry (TIR) and Surface Plasmon Resonance (SPR) Spectroscopy configurations utilised to measure pure solvents, binary solvent mixtures and aqueous solutions of glycine and urea, along with the practicalities of operating the experimental setup to perform such measurements. The Winspall program, used to develop model representation so experimental measurements, is also detailed in how it operates and its limitations.

Additionally, the standardised experimental procedures utilised for contact angle microscopy (used to assess macroscale surface-solution interactions) and optical microscopy (used to assess the macroscale surface environment upon which solvents and solutions were placed into contact with) are also detailed.

2.2 Materials

2.2.1 Glycine

The small molecule glycine is primarily utilised in this work as a model compound to study interfacial interactions at solid-liquid interfaces. Glycine is a simple, non-essential amino acid which plays an important physiological role in mammals, supporting metabolic processes, as well as neurological function and immune response within the human body.[45, 46] In addition to its importance to physiological processes, glycine is also widely applied to pharmaceutical research as an ideal model system. This is due to glycine's molecular simplicity, ease of handling, known physical forms and low cost, all of which make it especially useful for when trying to better understand crystallisation processes. The structure of glycine and its relevant zwitterion, the form it adopts in neutral solutions, can be seen in Figure 14 below.

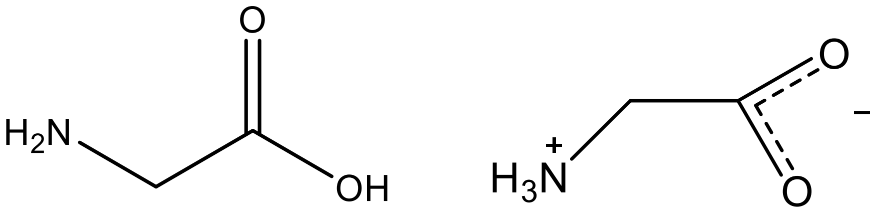

Figure 14: Chemical structure (left) and zwitterionic form (right) of glycine.

Glycine is a polymorphic molecule and consequently forms three distinct polymorphs under ambient conditions; alpha (α), beta (β) and gamma (γ). Of these three forms, the γ form is the most thermodynamically stable polymorph, with α and β forming metastable polymorphs, where the β form is least stable.

Each polymorph can be preferentially formed depending on the crystallisation method selected. For example, α-glycine is the dominant polymorph observed in cooling crystallisation processes, where crystals form from pure aqueous solution and can transform to the stable gamma form by way of a solution-mediated polymorphic transformation. [47, 48] However, for antisolvent crystallisation processes, β-glycine becomes the dominant polymorph formed and can be seen to transform to the more stable α form due to solution mediated polymorphic transformation. [48, 49] With regards to the formation of γ-glycine, crystallisation processes where solution pH is altered to yield acidic or basic conditions have been found to preferentially yield the stable γ-polymorph.[50, 51]

2.2.2 Urea

In addition to the use of glycine, urea was also utilised to probe solid-liquid interfacial interactions. Urea is a white, colourless crystalline organic solid, [52] with uses in fertilizers, feed supplements and as a precursor for polymers and resins. It is synthesised industrially from the reaction of both ammonia and carbon dioxide at high temperature and pressure.[53] Much like glycine, its molecular simplicity, in combination with both fast nucleation and growth kinetics, means that urea has been extensively studied. This makes it an attractive small molecule for the research of crystal nucleation fundamentals. The structure of urea is shown in Figure 15 below.

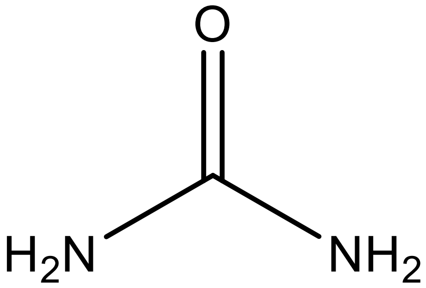

Figure 15: Chemical structure of urea.

Upon crystallisation from aqueous solution, urea forms long, needle-like crystals. There are three extensively characterised polymorphs - Form I (the most stable under ambient conditions), Form III & Form IV (both of which are high pressure forms)- with up to five known polymorphs observed in the literature. [54, 55]

2.2.3 Polystyrene

Polystyrene is a commonly used polymer in materials science research, primarily due to its well-defined surface chemistry when deposited upon a surface of interest, chemical inertness and hydrophobicity, weak electron donor phenyl rings and absence of polar functional groups. This makes it especially useful for the investigation of surface-liquid interfacial interactions. The monomer structure is shown in Figure 16 below.

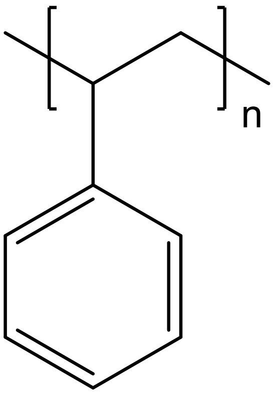

Figure 16: Chemical structure of polystyrene.

Numerous studies in literature have observed that the presence of a polystyrene interface in induction time measurements will enhance primary nucleation kinetics of various active pharmaceutical ingredients, making it especially relevant when trying to establish the key drivers behind such enhanced nucleation rates. [15, 18, 56] Ultrathin polystyrene films can be produced using spin coating, whereby polystyrene is dissolved in toluene, pipetted onto a surface of interest and then dispersed across the surface at a set spin speed. Polymer concentration and spin speed variation will yield thicker or thinner films as desired.[57, 58]

2.3 Experimental Methods

The following section outlines the fundamental theory behind the spectroscopic methods utilised in this work, as well as the experimental methods used for in situ surface-solution measurements, representative model systems used to rationalise these measurements and the imaging tools used for macro scale investigation of surface-solution interactions.

2.3.1 Total Internal Reflection

When light travels from one medium to another, both the speed and wavelength of the light source change but its frequency remains constant. Therefore, for a light source of a fixed wavelength, the change in speed that occurs when light moves into the new medium leads to refraction of the light at the interface between these two media. Measuring the angle at which the incident light source strikes, normal to the interface, allows for the angle of transmitted light to be determined by Snell's law, given in Equation 2.1 below and visually displayed in the schematic in Figure 17.

$$n_1 sin\theta_1 = n_2 sin\theta_2 \quad \text{(Equation 2.1)}$$

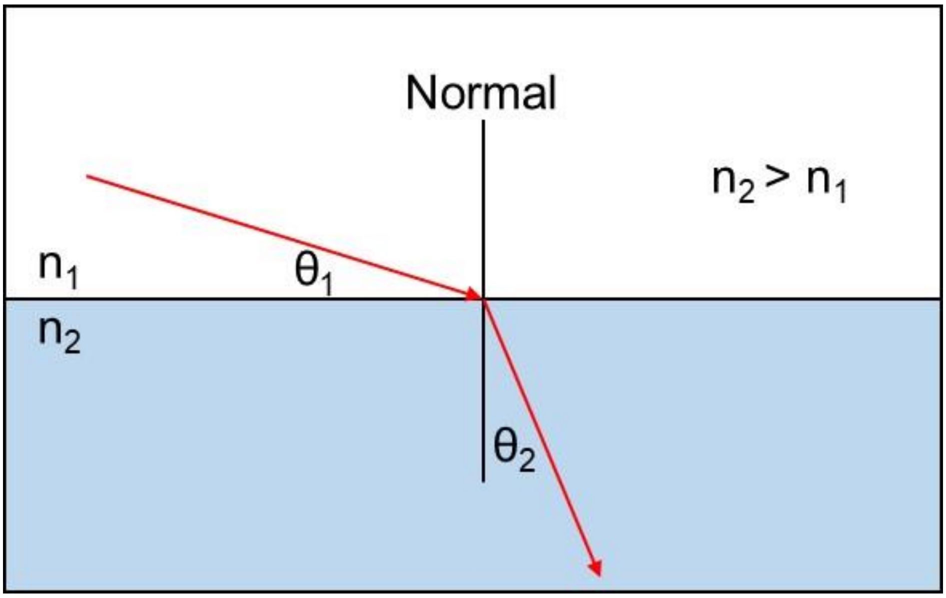

Figure 17: Schematic detailing the refraction of an incident light source on moving from a material of lower refractive index n_1 to one of a higher refractive index n_2.

Figure 16 shows that when light moves from the medium with refractive index n_1 (e.g. air) to the medium with refractive index n_2 (e.g. glass), the light bends towards the normal. Contrastingly, were the light to move from glass to air, the light would bend away from the normal. As a result, an angle exists at which light travelling from a lower refractive index material to one with a higher refractive index will be refracted at 90°. This is the critical angle for total internal reflection, which is shown in Figure 18.

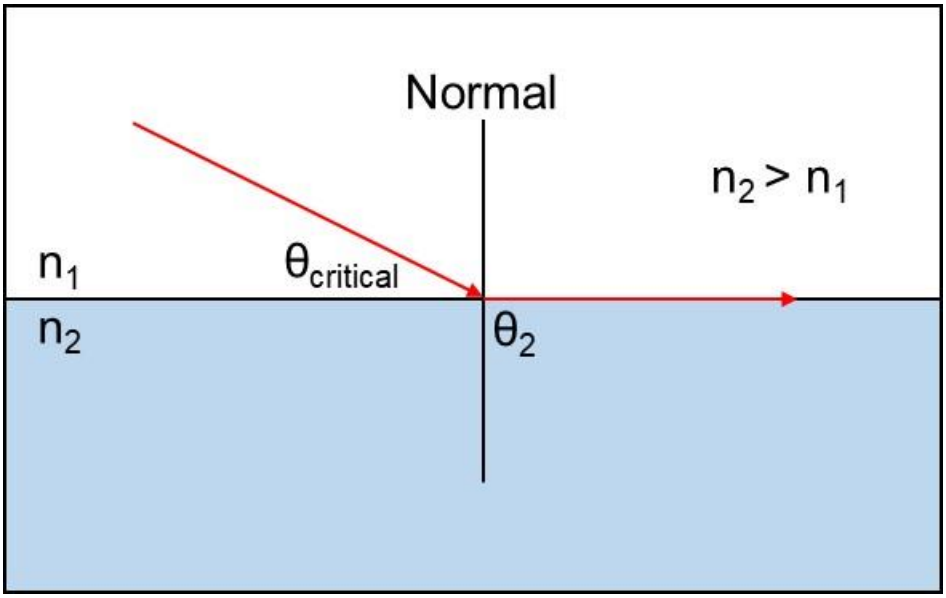

Figure 18: Critical angle for total internal reflection, where incident light is refracted along the interface between the two media.

Using Snell’s Law, where the angle of the refracted light is 90°, it is possible to calculate the critical angle for total internal reflection, shown below in Equation XX.

$$\theta_{Critical} = sin^{-1}\left(\frac{n_2}{n_1}\right) \text{ (Equation 2.2)}$$

If the angle of incidence were to exceed this critical angle for total internal reflection, this would lead to the sine of the refracted light being greater than one, which cannot be solved. Consequently, in this scenario, the incident light source is reflected off the interface in its entirety, thus obeying the law of reflection.

2.3.2 Surface Plasmon Resonance & Evanescent Waves

SPR is surface sensitive because the technique is able to excite the coherent oscillation of free outer electrons on a metal surface with an incident light source under momentum-matching conditions. This is possible under attenuated total internal reflection conditions (ATR) and backside illumination,[29] where the incident light travels through a semi-transparent metal layer deposited on a glass substrate and excites surface plasmons oscillations (SP) on the other side of the metal layer (i.e., “top” surface) that is exposed to the dielectric medium directly above it.[59]

The resulting SP propagates along the surface of the metal film and is a mode of guided evanescent electromagnetic field.[34] A metal film is necessary because coupling of the incident light into SPs requires a higher propagation constant in the metal layer than in the outside dielectric medium. Moreover, attenuated total reflection using a prism constructed from high refractive index glass is employed so that the incident light can acquire a sufficiently high wavevector for SP coupling at relatively low incident angles, to facilitate measurement acquisition.[34]

This configuration is shown in Figure 19, where the generated electromagnetic waves, bound at the interface between the metal and dielectric medium, propagate along its surface in the z-direction. These waves are TM-polarized (transversal magnetic or p-polarised).[29] Referred to as evanescent waves, they are generated when an optical reflection takes place and serve as the means by which light identifies the surrounding environment it is passing through.

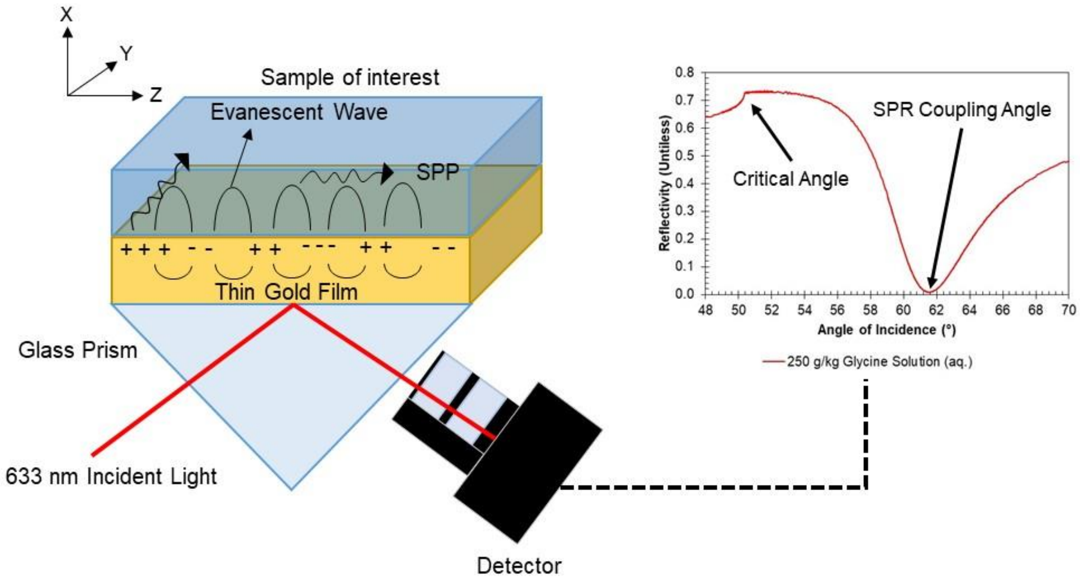

Figure 19: Schematic diagram detailing how evanescent waves are generated within an SPR sensor configuration. The light reflected back from the metal surface, when collected by a photodiode detector, gives rise to the characteristic SPR spectral response shown on the right ride of the figure. These spectra are characterised by two key figures of merit – the critical angle of total internal reflection and the SPR coupling angle minima.

Evanescent waves propagate in the z-direction, as seen in Figure 19, across the surface of the thin metal film at its interface with a dielectric medium (such as a liquid sample of interest). A further component of the wave travels in the x-direction of travel, where it penetrates the dielectric medium and its intensity decays exponentially with increased distance from the metal surface. It is this component of the wave that facilitates real time sensing of the region directly above the metal film. The interface is illuminated selectively, with the wave intensity decreasing as it moves towards the bulk system and subsequently not probing the bulk medium with the same selectivity as at the interface.

2.3.2.1 SPR Sensor Configuration and Operation

Surface plasmon resonance sensors, as explained above, are optical sensors which utilise the excitation of surface plasmons to conduct accurate small-scale measurements.[34] Of the coupling methods commonly used to directly induce SP excitation, the use of high refractive index glass prisms is most widely seen in literature. Specifically, the Kretschmann configuration is viewed as the “go to” geometry to adopt, due to its experimental simplicity.

The Kretschmann Configuration

The Kretschmann configuration is a commonly used setup for conducting SPR experiments. It consists of a thin metal film layer, typically gold or silver due to their stability and optical properties,[29] which is deposited on the surface of a glass substrate. The glass surface and low loss metal layers do not have a strong adhesion for one another, though this is typically overcome through the deposition of a thin layer of chromium on the glass substrate upon which the thin metal film can be deposited.[60]

The thickness of the typical metal film, whether it is gold or silver, is of particular significance due to the nature of the evanescent wave from which the information about the system of interest is obtained. Careful optimisation of this layer in necessary to maximise the sensitivity of the sensor’s response, as too thick a layer will dampen the observed signal. Within the literature for this field of research, the common convention is for the metal layer to be approximately 50 nm in thickness.[29, 61]

With regards to operation of the sensor in this configuration, a monochromatic light source, such as a He/Ne laser beam, is passed through the high refractive index glass prism and the glass substrate upon which the metal layer is deposited.[29, 40] A refractive index matching oil is applied to the surface of the prism prior to addition of the gold chip, to ensure that the light source has constant optical contact between the two surfaces. Upon striking the chip surface, the light source is reflected at the interface between the substrate and the metal layer. Upon contacting the metal layer, the light source excites SPs, which generate evanescent waves as they oscillate. As noted in Section 2.1.1.1, evanescent waves exhibit an exponential energy decay with increasing distance from the metal surface and into the liquid sample of interest.[29, 30, 40] The light which penetrates the liquid sample senses changes in the refractive index distribution at the metal-dielectric interface, which leads to a change in the effective refractive index of the dielectric.[34, 60] This process only occurs at a certain angle of incidence, referred to as the resonance angle (θ_{SPR}).

A detector is placed in contact with the glass prism, which identifies the intensity of light which is bounced back from the metal surface. The electrical signal detected is then amplified and presented as an SPR response curve, which plots reflectivity against the incident angle of the laser source with the metal-prism interface.

The generated spectrum has two key features which are of importance for analysing an experimental system; the critical ($\theta_{critical}$) angle and θ_{SPR}, which were highlighted in Figure 19. As the angle of incidence of the incident laser source is cycled through the specified angle range of the user, a portion of the incident light is reflected. This can be due to either reflection of the light at the interface between the metal and the glass prism or by total internal reflection of the light, where the angle of incidence exceeds the critical angle.[34]

The position of $\theta_{critical}$ depends solely on the difference between the dielectric constants of the metal surface and the liquid sample directly above it. This makes the critical angle an important means by which comparisons can be made against standard measurements. Changes to the liquid sample system that occur at the sensor surface also result in a change in θ_{SPR}. The characteristic dip in the spectrum, observed as the intensity minima in Figure 19, is generated by the coupling of light with surface plasmons.[62] The interaction between the surface plasmons and the incident light leads to the intensity of the reflected light approaching a minimum, at which point the surface plasmons are excited by the incident light where the reflected light is close to zero (θ_{SPR}).

The observed surface conditions at the metal-dielectric interface also change how the SPR response is characterised. This is represented by the SPR response curve shifting left or right due to changes in the refractive index of the liquid sample, linked to the dielectric constant by the following relationship:

$$\varepsilon = n^2$$

For example, if an experimental system is used such as the one illustrated in Figure 19, typically a solution of interest will be pumped into the flow cell by exchanging it with a pure solvent to distinguish between the different regimes.[60] In turn, this will lead to the observed θ_{SPR} being shifted, which can be tracked in real time by means of repeated scans of the system response. This is referred to as angle tracking and will form an integral part of the experimental work conducted in this research.

Measuring the difference between such measurements allows for determination of the local concentration at the metal-dielectric interface and adsorption or interaction of molecules with the metal surface, which drives this change in the detected optical conditions.

2.3.2.2 Minimising system limitations through sensitivity and selectivity enhancement

Although SPR sensors are both highly effective and incredibly useful, they are not without their limitations. A variety of factors, if not carefully optimised, can lead to a reduction in the sensitivity of the instrument and the measurement it generates. In a theoretically idealised SPR experimental setup, there are no losses in signal intensity due to chip preparation or spectrometer setup. The generated SPR curves from such a setup would show well resolved spectra, where the critical and coupling angles have a high signal to noise ratio and thus can be clearly distinguished.

Although it is possible in an experimental setup to achieve high quality SPR curves with well resolved spectral features, this can only be done by utilising a range of tools to minimise any potential external influences on the quality of the SPR curves generated by the setup as far as practicable. Ultimately, improvements to the experimental setup and preparation of gold chip substrates are the key means by which system sensitivity can be improved.

With regards to chip preparation, employing measures to minimise substrate roughness, having an awareness of how changes in the relative dielectric constants of the metal and the liquid sample influence the response and selecting the optimal thickness of the metal film are key considerations. The thickness of the thin metal film, which can be considered as both the adhesive chromium layer and the gold film itself, play a significant role in the level of response generated by the SPR spectrometer when performing measurements.

If not selected carefully, all key characteristics of the SPR response used to determine interfacial enhancement in the liquid sample, such as the minimum reflectivity observed and the sensitivity of the sensor, are diminished.[63] Consequently, optimisation of the metal layer is a key means by which sensitivity enhancement can be obtained.

As previously noted, a surface adhesion layer exists between the glass prism and the gold film to stabilise it.[61] Ekgasit et al. (2005) conducted a study whereby they looked to investigate the influence of the metal film thickness on the experimentally generated SPR response, identifying that the resonance angle increases slightly as the thickness of the metal film increases and the reflectance observed depends strongly on the thickness of the metal film.[61]

The study found that while the sensitivity of the observed reflectance changes decreased when employing thicker chromium layers and thinner gold film layers, the sensitivity of the measurement of θ_{SPR} was unaffected by these variations in the thickness of the metal film. An important point to note though is that while the position of the θ_{SPR} may be unchanged, the sharpness of the minima will be reduced due to this change in layer thickness. This, coupled with an excessively noisy experimental response, could lead to a less accurate quantification of θ_{SPR}.

Reflectivity changes play an important part in inferring valuable information about the experimental system, such as local concentration and chip layer thickness. As such, it is important to ensure careful optimisation of the metal film to attain highly sensitive reflectivity data about the system.

A further consideration which can be altered to maximise sensitivity is assessing the degree of roughness which is observed on the metal surface, which stems from the chip preparation process. If the surface of the gold layer is excessively rough, this will lead to the SPs scattering upon striking the surface in different directions.[63]

The result of this unwanted scattering is a broadening of the dip observed in the SPR response, the minima around θ_{SPR}. Furthermore, in the context of this research, defects on the metal surface may act as ideal nucleation sites from which nuclei could form and subsequently induce crystal growth. As such, ensuring the surface is as smooth as possible is important to ensure as clear a response as possible is obtained and that unwanted side processes at the metal-dielectric interface are minimised.

Alongside improvements to chip preparation, sensitivity can be further improved with refinements to the experimental setup itself. One such example is the obtainable angle resolution of the instrument and how repeatable the alignment of the glass prism is, as this will influence the instruments sensitivity. If the critical and coupling angles cannot be accurately quantified by the experimental setup, or there is considerable scattering of the signal response in these regions, this will limit the precision with which these parameters can be determined. However, attention must also be paid to the solution being analysed to minimise background noise during signal processing which may hide key system features.

To mitigate potential inaccuracies in measurements or excessive background noise when sampling, there are techniques and examples of good practice available which can enhance both the selectivity and sensitivity of SPR sensors and the experimental sensitivity which can be obtained from the instrument. Hardware changes to the system such as the use of a lock in amplifier, which processes the generated response signal and recovers signals buried within the noise of the system or the use of an improved detector with a larger active surface area are practical alterations which can lead to additional significant improvements in the degree of sensitivity attainable by the sensor system. Incorporating these methods into the operation of SPR sensor operation is a worthwhile practice, as it enables closer inspection of chips in contact with liquid samples and thus the inference of further information about the system of interest.

In combination with the influence metal film thickness and morphology have on these surface measurements, the sample solution in contact with the surface also plays a key role in determining the degree of sensitivity with which measurements can be made. In the context of this research, an emphasis is placed on assessing interfacial processes, which are typically observed at the nanoscale.

Excessive noise from the bulk solution can lead to a dampening of the signal received from the detector in analysing the experimental system, which can interfere in identifying the finer details within a given SPR response. A practical alteration can be the choice of solvent within which the compound of interest (glycine in this instance) is dissolved to form a solution. This is important as failing to consider such a step would mean not recognising the need to reduce the amount of background noise in the experimental system as much as possible.

Selection of a solvent system with optical properties similar to that of the solution of interest means that the optical response can be calibrated prior to measurement, then exchanged with the solution of interest to perform the desired measurement. Comparison of the response of each system identifies noise present in the bulk solution and thus makes rationalising the information present in angular reflectivity scans less troublesome.

2.3.3 Gold Chip Preparation

The application of gold layers to the LASFN9 glass slides was undertaken at the Molecular Sciences Research Hub (MSRH), Imperial College London.

Prior to chromium and gold layer deposition, LASFN9 slides were thoroughly cleaned using a Hellmanex washing procedure. Slides were first wiped with an ethanol-soaked Kim wipe to remove residue, before being placed into a polypropylene Coplin staining jar and covered with a 1% Hellmanex-water solution and sonicated (10 minutes). The solution was discarded and the jar flushed repeatedly with water, before being filled with water and sonicated (10 minutes). Slides were then removed from the jar and rinsed with ethanol, before being dried under a stream of nitrogen gas and stored in plastic slide tubes ready for deposition.

2.3.4 SPR Spectrometer Setup

The experimental setup consists of a monochromatic, 632.8 nm laser source (He/Ne, R-30989, Research Electro Optics Inc, Colorado, USA) directed towards a high refractive index glass prism through an optical chopper (SR540, Stanford Research Systems, California, USA). The chopper was utilised to modulate the intensity of the output beam from the light source. Further modulation of the light intensity being directed towards the prism was achieved down line from the chopper through use of a sequence of mirrors and polarisers. (Thorlabs Inc., New Jersey, USA)

The glass prism was held in a 3D printed holder and mounted upon a rotation stage (Hans Huber AG, Germany), which allows for the incident light source to strike the glass prism across a range of incident angles. The intensity of the light reflected back from the prism was detected through use of a large area silicon biased photodetector, equipped with a 50 Ω BNC terminator and two convex N-BK7 glass lenses, used to direct the reflected beam spot from the prism to the centre of the detector's active area (all produced by Thorlabs Inc., New Jersey, USA).

The detector setup is utilised in combination with a lock-in amplifier (SR350, Stanford Research Systems, California, USA). Temperature was monitored through use of an HH309A Data logger thermometer (Omega Engineering, Manchester, U.K), with one thermometer probe monitoring laboratory temperature and a further probe monitoring the temperature as close to the chip surface as was practicable. An image of the experimental setup is shown in Figure 20 below.

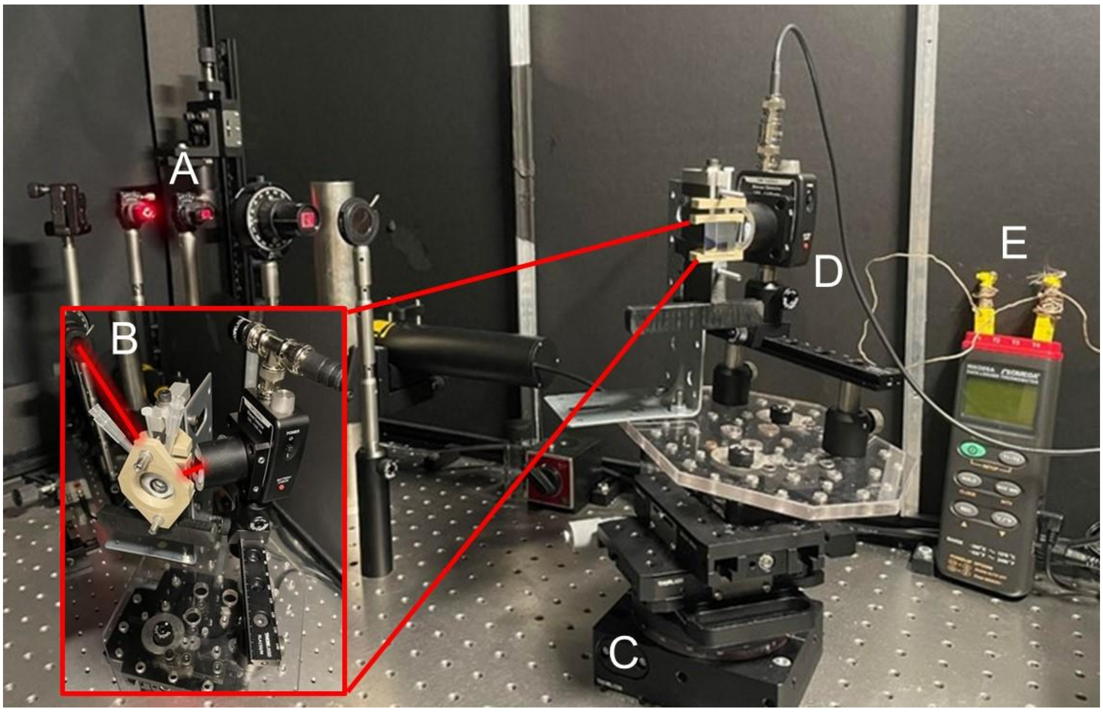

Figure 20: Image of the experimental setup utilised for surface measurements in this research. Section A shows the optical setup components, which include the laser source and a number of polarisers and mirrors which are used to direct the light towards the glass prism and modulate the intensity of the incident light. The inset, denoted "B", shows the prism with the PTFE flow cell and plastic endcap in position for measurement acquisition and the path of the incident light to the prism face and on to the photodiode detector. "C" denotes the optical stage upon which the glass prism sits, "D" the photodiode detector and "E" the data logger thermometer.

A 3D printed Polytetrafluoroethylene (PTFE) flow cell with inlet and outlet injection ports was placed on the chip and an airtight seal was formed by placing a transparent microscope slide on top of the flow cell. The configuration was secured by screwing a plastic cover piece onto the top of the glass slide and placed on the goniometer stage. The configuration was aligned to the incident laser beam at a range of angles in air (20, 45- and 60-degrees angle of incidence) to ensure generation of accurate reflectivity spectra, after which measurements could be obtained. A schematic diagram of the experimental setup is shown in Figure 21 below.

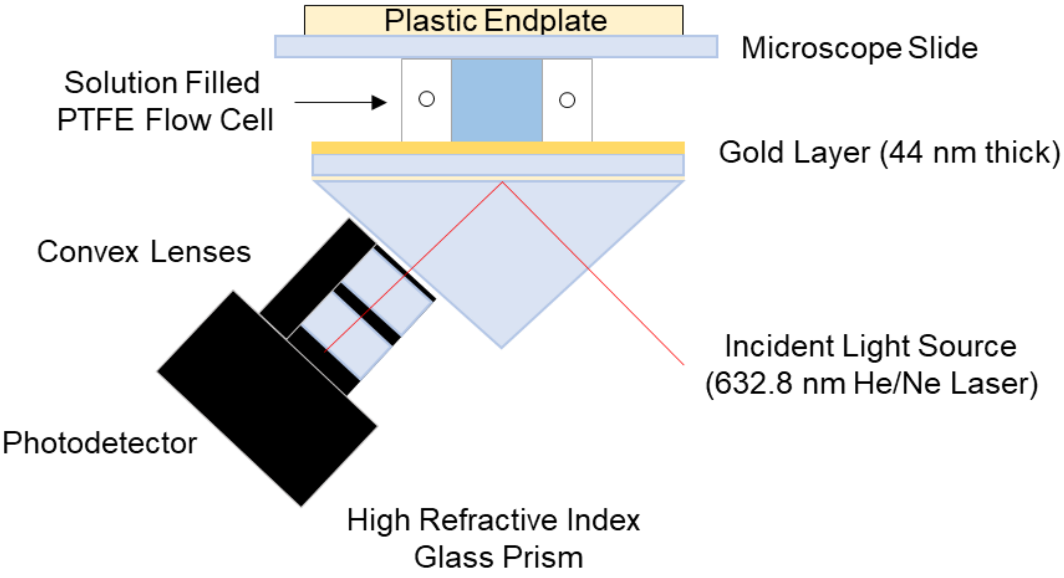

Figure 21: Schematic detailing the experimental configuration adopted for SPR measurements of pure solvents, binary solvent mixtures and aqueous solutions of glycine and urea, respectively.

2.3.5 Model System Generation

To analyse the data generated by the spectrometer, representative model systems were generated using the Winspall program. Developed by the Max Planck Institute, Winspall implements a standard transfer-matrix calculation of the light propagating through the experimental system of interest, thus solving the Fresnel equations for light transmission and reflectance at an interface. [64] The Fresnel equations assume perfectly flat interfaces between layers of uniform thickness and optical properties, meaning that this idealised condition is a limitation inherent in using Winspall models. Winspall provides a means by which the Fresnel equations can be solved, layer thicknesses can be determined and subsequent relative permittivity values can be calculated. The procedure followed to generate such model systems for both TIR reflectivity and SPR spectroscopy scans is outlined as follows.

Model systems for TIR measurements of solvents begin with fixing the glass prism dielectric constant. The prism dielectric constant is fixed and kept constant for each individual set of measurements, having confirmed the prism refractive index through repeated measurement of the prism in air. Experimental measurements are then imported to Winspall and the bulk solvent permittivity is fitted to the TIR scan of the respective solvent, thus determining the critical angle of the solvent also.

In the case of SPR scans, a model system of the gold chip in air is first generated. Prior to model development, the glass prism dielectric constant is fixed and kept constant throughout for each set of measurements, having confirmed the prism refractive index through repeated measurement of the prism in air. The experimental measurement of the chip in contact with air is then imported to Winspall and the gold and chromium layer thicknesses are measured and fixed.

The real and imaginary components of the chromium refractive index are fixed, with the real and imaginary components of the gold refractive index fitted. The fitting procedure yields an idealised, representative model of the experimental data, as well as both the thickness and refractive index of each layer which achieve the best available fit to the experimental measurement. As such, the representative thicknesses of gold and chromium can be accurately characterised.

Having accurately characterised the gold chip of interest, model systems are generated for water, pure solvents, binary solvent mixtures or aqueous solutions of glycine or urea, respectively. This is achieved by fitting the bulk solution refractive index and real and imaginary components of the gold layer refractive index to the respective experimental measurement of interest.

2.3.6 Contact Angle Measurements

Contact angle measurements were performed using a Krüss DSA30 Contact Angle Measuring System as a way by which the properties of bare gold chips and chips coated with ultrathin polystyrene layers could be assessed for their influence on aqueous glycine solutions of varying bulk glycine concentration. The theory and importance of critical angles with respect to heterogeneous nucleation are covered in Section 1.2.1.2.

Contact angles are specific to given liquid systems in contact with a respective solid surface and determined from the interactions observed between the solid, liquid and gaseous phase when a droplet is placed in contact with a surface. They are typically measured by depositing a drop of liquid on a given solid surface using a syringe filled with a liquid of interest. The instrument, through use of a camera and accompanying software will then capture and analyse the shape of the liquid droplet placed in contact with the surface of interest. This method of contact angle determination is known as the sessile method, where the droplet sits on the surface and the three-phase boundary is stationary.

The wetting capacity of a surface is related to the contact angle. For example, as the contact angle decreases below 90°, a surface exhibits increasingly more hydrophilic behaviour. By contrast, the contact angle exceeding 90° is characteristic of a “super hydrophobic” surface. An image of the experimental setup is shown in Figure 22.

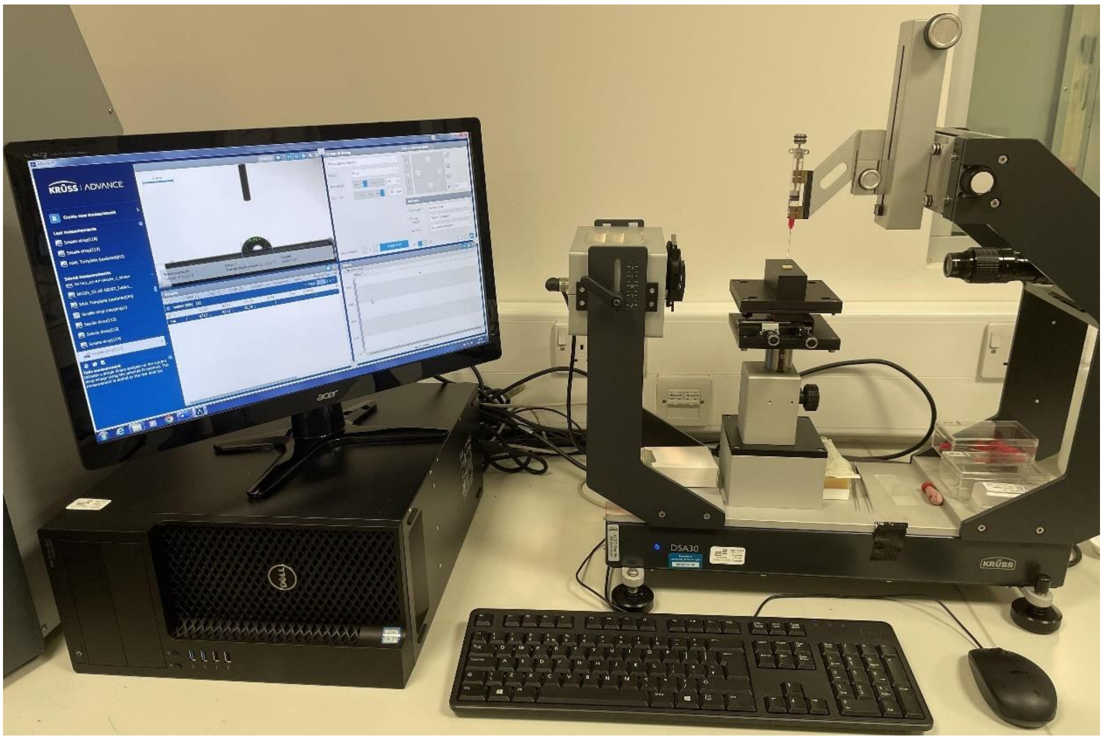

2.3.6 Optical Microscopy

Optical microscopy was performed using the Leica DM6000M 1 and M165 CM optical microscopes, equipped with 5x, 10x, 50x and 100x magnification objective lenses respectively, to examine gold chip surfaces prior to and following the addition of ultrathin polymer layers to qualitatively assess thiol and polystyrene layer heterogeneity respectively.

Chapter 3

3. Refractive Index Measurements of Pure Component Solvents Using TIR Reflectivity and SPR Spectroscopy

3.1 Introduction

The refractive index of a substance is a characteristic physical property by which it can be described. In the case of liquids, the refractive index will depend on the temperature of the liquid, wavelength of the light source passing through it and the presence of a dissolved solute in solution. Each of these factors influence the bulk system refractive index and as such must be precisely known.

One such example can be found in process monitoring, where there is the potential need to monitor concentration as a reaction or process progresses. Measuring the refractive index over time allows for real time concentration measurements to be obtained, allowing users to make more intuitive decisions when controlling a process. Consequently, the refractive index is a powerful metric by which a liquid or solution can be both characterised and further analysed.

Within the context of this research, determination of the refractive index is the fundamental metric by which data is to be interpreted in the first instance. To probe interfacial interactions at solid-liquid interfaces, experimental techniques with the necessary degree of sensitivity to observe such processes are required. SPR spectroscopy provides such an opportunity to probe these interactions.

In this work, measurements were performed in the first instance without the presence of a gold layer on a glass prism (TIR reflectometry) to establish how accurately the critical angle of bulk liquids could be characterised in isolation. In doing so, the consistency of these measurements both internally and with literature sources was compared and the key instrument parameters which influence their sensitivity investigated.

Having assessed bulk liquid characterisation, surface measurements were performed with pure component solvents on a gold surface topped prism (SPR spectroscopy) to assess the accuracy with which the SPR coupling angle minima, which is used to characterise solid-liquid interfacial interactions, and critical angle could be determined. In the case of both the TIR and SPR measurements, performing such measurements helped to better understand the key instrumental parameters which control these spectral features.

Key experimental system metrics, such as critical angle, bulk solvent permittivity and SPR coupling angle minima were then compared against simulated responses generated using gathered literature data to assess how the experimental setup compares for acquiring precise measurements. Pure solvents served as a means by which the optical response could be initially calibrated, to facilitate progression to aqueous glycine solutions of varying concentrations in contact with gold surfaces. We expect that the pure component solvents and aqueous glycine solutions should give rise to similar optical responses.

3.2 Materials & Methods

3.2.1 Materials

Water (HPLC Plus Grade, Sigma Aldrich), Ethanol (Absolute, Fisher Scientific), 1-Propanol (HPLC Grade, 99.9%, Sigma Aldrich), Isoamyl Alcohol (98%), Propylene Carbonate (99.5%, Acros Organics) and Dimethyl Sulfoxide (Reagent Grade, >99.9%, Honeywell) were purchased and used as received.

3.2.2 TIR Reflectivity Measurements

A 3D printed flow cell with inlet and outlet injection points was placed on a high refractive index glass prism, before an airtight seal was formed by placing a glass slide on top of the flow cell. The configuration was secured by screwing a plastic cover piece specific to the configuration onto the top of the glass slide and placed on the stage of the goniometer, before sealing the outlet injection point with a pipette tip. The sample cell was then calibrated to the incident laser beam by aligning the glass prism beneath it at a range of angles in air (20, 45 and 60 degrees) to ensure a complete reflectivity scan would be generated. The experimental setup is shown in Figure 23 below.

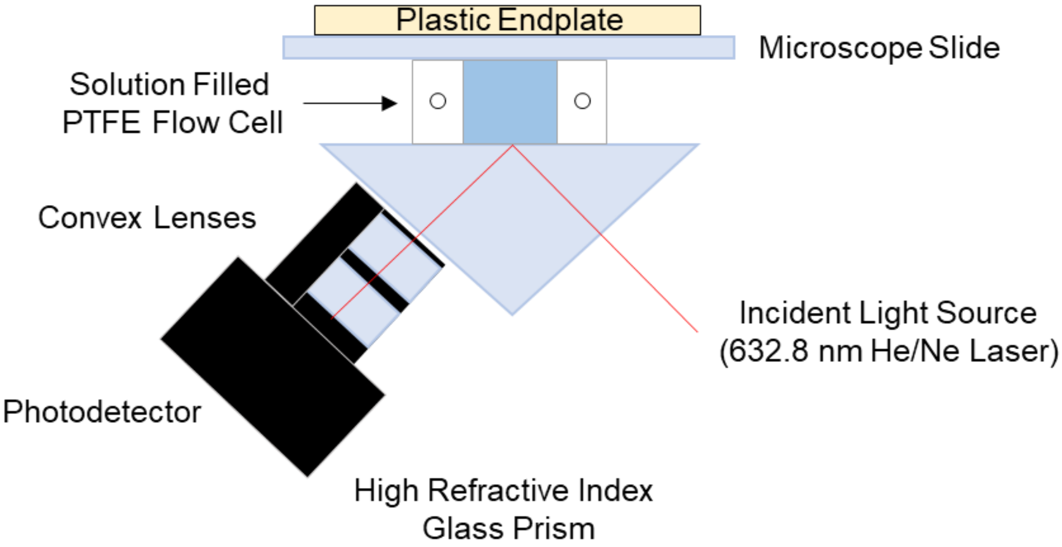

Figure 23: Schematic detailing the experimental configuration adopted for TIR reflectivity measurements of pure solvents.

For each solvent analysed, an aliquot of the respective solvent (269 µL) was then injected into the flow cell using a syringe and the inlet injection point was sealed using a pipette tip.

To generate a complete dataset in one run of experiments, the solvent range was worked through in terms of each solvent's miscibility in one another. This ensured that each solvent could be measured in one run of experiments, with the order in which solvents were measured as follows: Water, Ethanol, Isoamyl Alcohol, an ethanol flush and finally 1-Propanol.

To prevent residual solvent in the cell when transitioning between solvents impacting the accuracy of the critical angles measured, it was decided that the flow cell would be flushed out three times with the solvent next in the sequence for measurement before injection of the aliquot of liquid for use in obtaining a measurement. The representative experimental protocol workflow is shown in Figure 24 below.

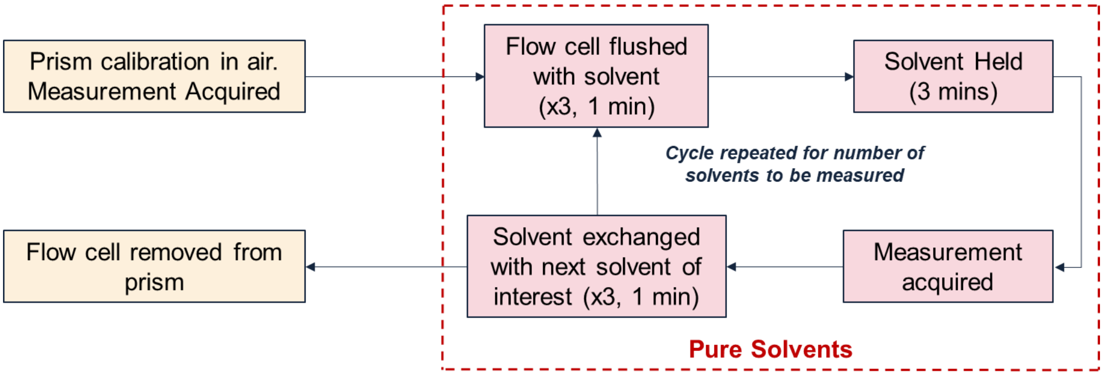

Figure 24: Experimental procedure developed for the TIR measurements of pure solvents on a bare glass prism.

3.2.3 SPR Measurements

The experimental setup is prepared in a defined sequence to facilitate SPR measurements of pure component solvents, which is explicitly covered in Section 2.3.4. Gold Chips were prepared per the procedure outlined in Section 2.3.3. A schematic diagram of the configuration of the spectrometer for SPR measurements is shown in Figure 25 below.

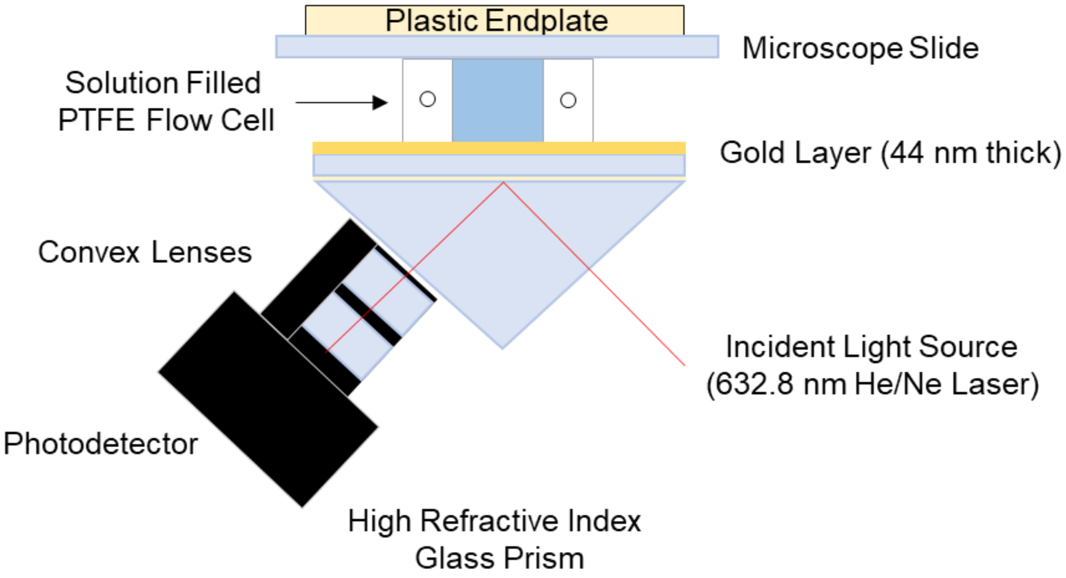

Figure 25: Schematic detailing the experimental configuration adopted for SPR measurements of pure solvents.

Pure component solvents were placed in contact with the gold chip by injection to the 3D printed flow cell for steady state measurements. For each sample analysed, an aliquot of liquid (269 μL) was injected into the flow cell using a syringe, with the injection points sealed using pipette tips. Temperature readings were collected throughout the data acquisition process through use of the datalogger thermometer. The same sequence of liquids as was used for TIR measurements of pure solvents was also followed for all SPR measurements obtained.

Following calibration, the measurement of pure solvents was undertaken. The flow cell was first flushed out with the sample of interest in triplicate to ensure only the sample of interest was present in the flow cell, before being held in the flow cell (3 minutes). A measurement was then acquired, with the flow cell flushed out three times with the next liquid of interest, as shown in the experimental procedure detailed in Figure 26.

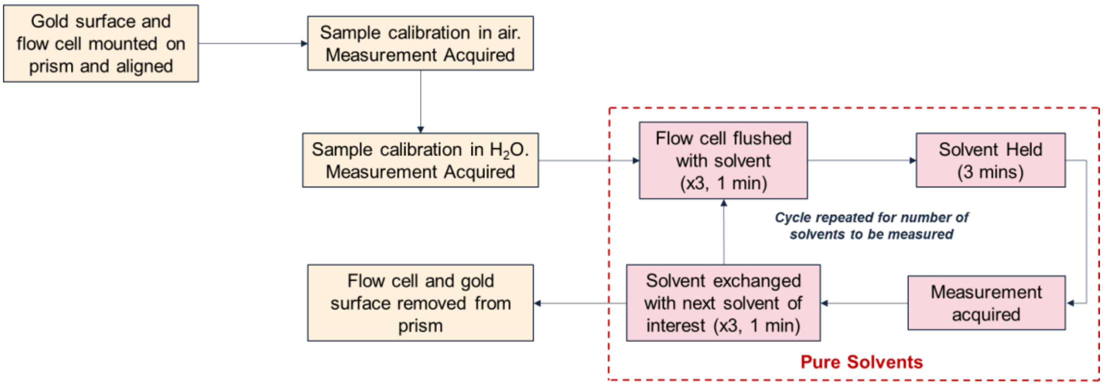

Figure 26: Experimental procedure developed for the SPR measurements of pure solvents on a gold chip.

Experimental scan data for measurements on both the bare glass prism and on gold chips was acquired through a user interface utilising the LabVIEW software platform. This interface allows for reflectance scans to be generated (which plot angle of incidence versus reflectance detected by photodiode detector), which can then be imported into the Winspall program for further analysis.

3.2.4 Model System Generation

To analyse the data generated by the spectrometer, representative model systems of the experimental schematics shown in Figure 23 and 25 were generated using the Winspall program, as outlined in Section 2.3.5.

3.3 Results & Discussion

In this section, we outline how TIR reflectivity measurements and SPR spectroscopy can be employed for the precise measurement of pure solvent refractive indexes. Section 3.3.1 details the collection of pure solvent refractive index data from literature and the difficulty in finding accurate refractive index data to utilise as a benchmark for the experimental data generated in this work.

The TIR reflectivity study is then presented in Section 3.3.2, whereby model systems are implemented to analyse raw experimental data generated for each pure solvent measured. This is achieved through use of a representative model of the prism-solvent of interest- multi-layer system for individual measurements, which is used to quantify the bulk solvent permittivity and subsequently the critical angle for total internal reflection.

This is further developed in section 3.3.3, whereby SPR measurements on gold chips are presented. After measurement acquisition, representative model systems of the prism-gold chip-solvent of interest multi-layer system for an individual gold chip are generated to assess how accurately key SPR spectral features can be quantified. In doing so, we can provide an estimate of the sensitivity capabilities the experimental setup is capable of as a reference point to progress and subsequently probe interfacial interactions in solutions of aqueous glycine at solid-liquid interfaces using SPR spectroscopy.

Both the experimental and literature data are then brought together and critically assessed in section 3.3.4, to establish how each differs from one another and the contributing factors which play a role in this. In doing so, comparisons or adjustments can be made to see the key influences on critical angle and bulk solvent refractive index.

3.3.1 Literature search for solvent refractive index data

To make informed decisions regarding solvent selection when shortlisting potential options for measurements, reported refractive index data for aqueous glycine solutions from literature was required to establish a working refractive index range within which solvent bulk refractive indexes must fall. [65]

Aqueous glycine refractive index data is particularly sparse across the solubility range of glycine in water, with available data being obtained at low concentrations. As such, it was necessary to apply an empirical fit to reported data and then extrapolate this fit to higher glycine concentrations to give an initial estimate of expected refractive indexes for solvent selection. Such an extrapolation is given with the accompanying refractive index data in Table 1.

Table 1: Corresponding glycine dielectric constants for aqueous glycine solutions spanning a concentration range of 100-500 g/kg, reported by Soto et. al (1999) and extrapolated to 500 g/kg. [65]

Fitting equation utilised: y = $-4 \times 10^{-7}x^2 + 0.0005x + 1.7756$		
Glycine Solution Concentration (g/kg)	Refractive Index (Unitless)	Relative Permittivity (Unitless)
100	1.3497	1.82156
200	1.3637	1.85956
300	1.3746	1.88956
400	1.3826	1.91156
500	1.3877	1.92556

Aqueous urea refractive index data was also searched for in the literature, but was found to be even more sparse than that of aqueous glycine data. Data was obtained from TIR measurements of aqueous urea solutions between 200-1000 g/kg and is shown in Table 2 below.

Table 2: Aqueous urea relative permittivity data generated internally using TIR reflectometry measurements, per the protocol outlined in Section 3.2.2.

Urea Solution Concentration (g/kg)	Refractive Index (Unitless)	Relative Permittivity (Unitless)
200	1.3549	1.83567
400	1.3737	1.88710
600	1.3875	1.92520
800	1.3997	1.95907
1000	1.4093	1.98623

Based on the anticipated refractive indexes to be expected when carrying out experiments, the range within which a chosen solvents refractive index was required to fall was 1.35-1.41. As a first reference point, a chart detailing the physical properties of commonly used solvents (including their refractive index at 20°C) was sourced from Merck (Sigma Aldrich) and shows several solvents which have refractive indexes at 20°C.[66] Solvents were selected on the basis that their refractive index fell within the range for undersaturated aqueous glycine and urea solutions. Methanol has a lower refractive index than water, so does not match an aqueous solution. Rather, it was used as a means by which binary solvent mixtures with a refractive index equivalent to that of aqueous glycine solutions could be prepared to span the water to ethanol solvent refractive index range. Having taken this into consideration, the following solvents were selected for use in this study: water, ethanol, 1-propanol and isoamyl alcohol. Details of the sources of this data and the reported light wavelength they were captured at are shown in Table 3 below.

Table 3: Literature sources of solvent refractive index data found as an initial reference point for obtaining TIR and SPR measurements. The source of the data and light wavelength at which the refractive index was captured (if specified) are detailed

Solvent	**Refractive Index Data Source and light wavelength captured at**
Methanol	Aralaguppi [67], Iglesias [68]
Water	Tilton & Taylor [69] (633 nm)
Ethanol	Marsh [67], Ortega [70] (λ not Specified) Rodriguez [71], Aralaguppi [67], and Kumari [72]
1-Propanol	Marsh [67], Ortega [70] (λ not Specified) Aralaguppi [67], Kumari [72] (589 nm) O'Brien [73] (633 nm), Iglesias [68]
Isoamyl Alcohol	O'Brien [73] (633 nm) Ikeda [74] (λ not Specified)
Ethyl Acetate	Resa [75], Aminabhavi [76]
1-Butanol	Aralaguppi [67], Kumari [72] (589 nm), O'Brien [73] (633 nm)

Having sourced literature data for each solvent of interest, the reported data was plotted as master series for each solvent. An empirical fit was then applied through each solvent set to generate a representative line of best fit. The equation for each line of best fit across their reported temperature range was then used to calculate solvent permittivity at temperatures which mirror those observed experimentally, as shown in Figure 27.

This enabled the generation of representative model systems for each literature source using the same prism dielectric constant as observed with corresponding experimental measurements, as well as the solvent permittivity at the same temperature as that of data from this work. This ensures that the model systems are as closely comparable as practicable to experimental data when looking to make comparisons between each measurement case.

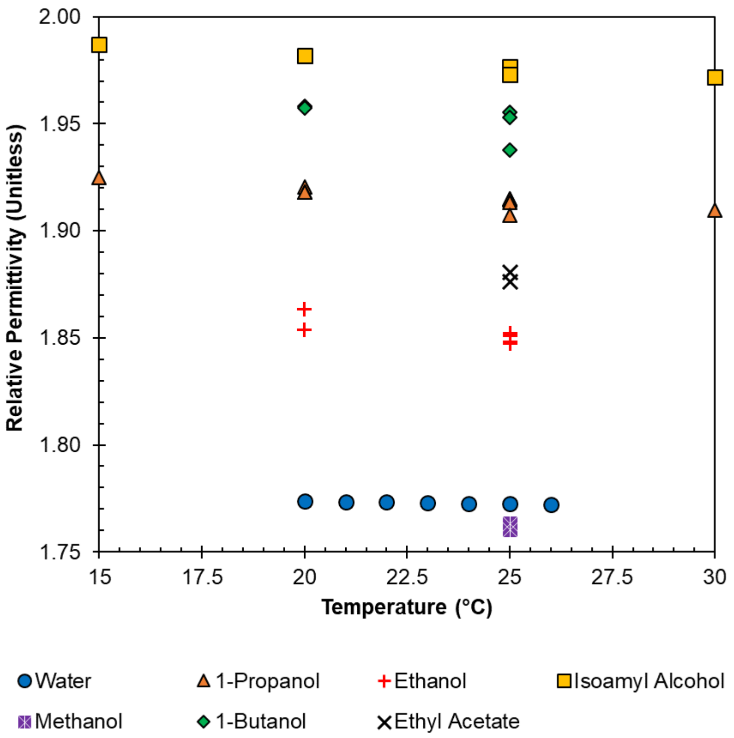

Figure 27: Master plot combining all literature sources for each respective solvent identified for use in this research.

3.3.2 TIR measurements on bare prism

Having shortlisted solvents of interest for use in this study, TIR reflectivity measurements were performed on the bare glass prism using a 633 nm light source in the first instance to assess how accurately the solvent bulk permittivity's (and by extension their critical angles) could be determined. This was achieved following the protocol outlined in section 3.2.2, with the raw angular reflectivity data for four solvent measurements shown in Figure 28 below, alongside the calculated reflectivity measurements to match the experimental measurements, generated in Winspall.

We see that qualitatively, the measured critical angles for each solvent are sharp, with minimal noise to the spectral response. This makes accurate determination of the critical angles a possibility, with the critical angle able to be characterised to within 0.01° in the experimental setup. Representative data is shown in Table 4, which shows the observed relative permittivity and critical angles for the respective solvents shortlisted, along with the temperature at which the data was acquired.

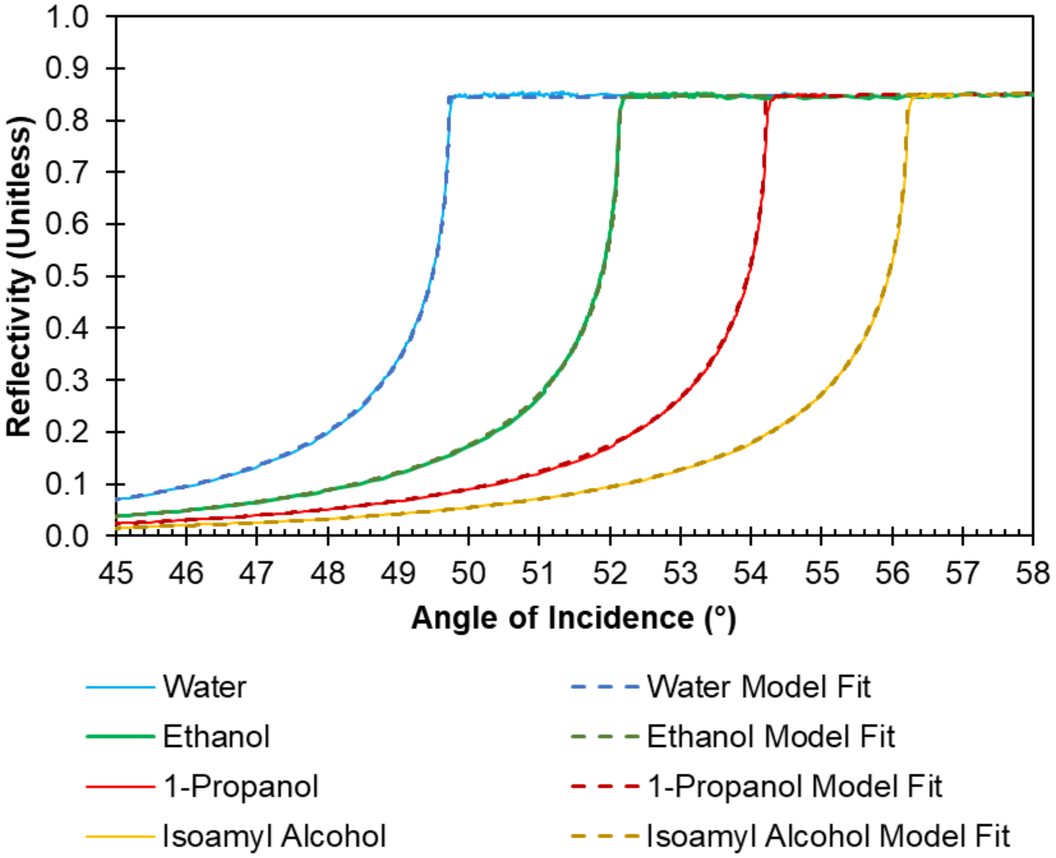

Figure 28: Raw spectral responses for TIR measurements of water, ethanol, 1-propanol and isoamyl alcohol in contact with a bare glass prism, alongside the calculated reflectivity to match the experimental response.

Table 4: Observed relative permittivity and critical angle for each solvent of interest, with the accompanying temperature at which each measurement was acquired at.

Solvent	Temperature (°C)	Relative Permittivity (Unitless)	Critical Angle (°)
Water	21	1.7734	49.71
Ethanol	21	1.8515	52.04
1-Propanol	21.1	1.9144	54.12
Isoamyl Alcohol	21.1	1.9765	56.20

Having assessed the raw experimental data, each set of experimental measurements was then compared against the expected literature response at the same temperature, using the empirical fits established in section 3.3.1. This was achieved through utilisation of the Winspall program, with models generated for this work and the expected response based on permittivity data from literature sources. To make an effective comparison, the literature solvent data was modelled in contact with the equivalent prism dielectric constant that had been determined prior to measuring solvent relative permittivity's.

When comparing the expected literature response against the experimental measurements taken in this work, a slight disagreement was seen between experimental data and the model developed using literature data, specifically for ethanol, 1-propanol and isoamyl alcohol. This was consistently observed for each of the six sets of measurements taken, with an example highlighted for ethanol in Figure 29.

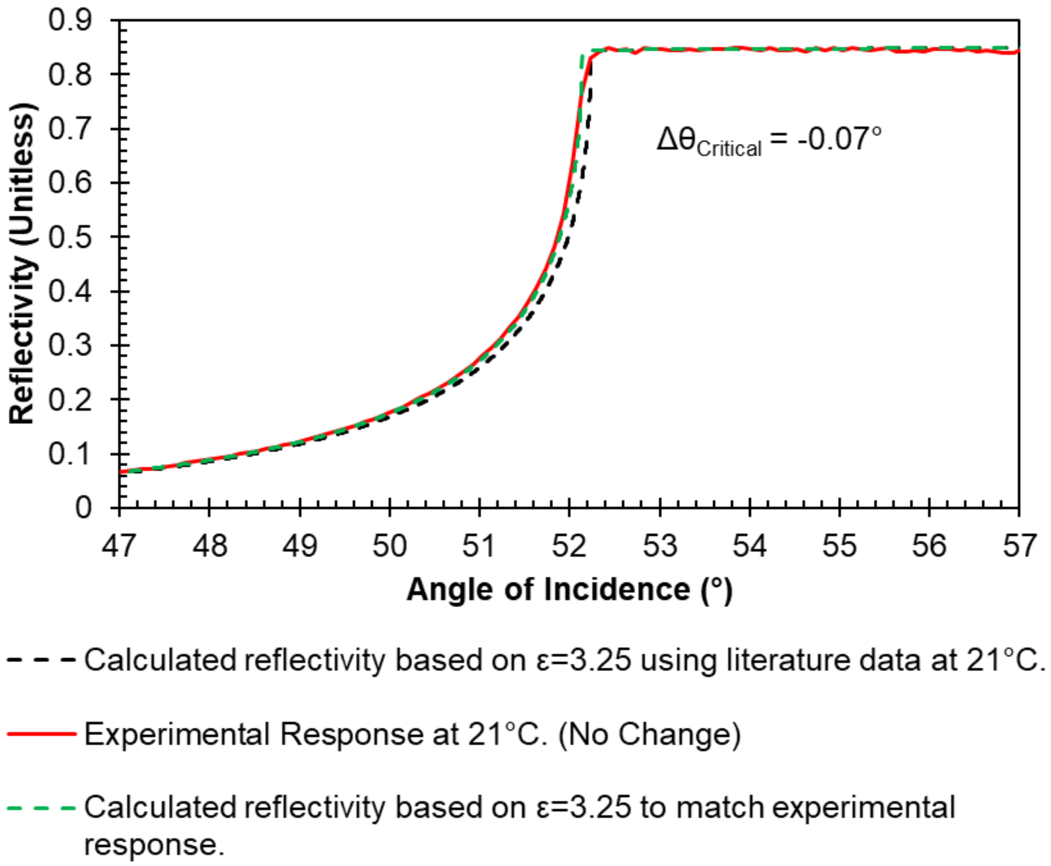

Figure 29: Comparison of an experimental measurement of ethanol with the corresponding simulated response using permittivity data sourced from literature at the same temperature and the calculated reflectivity to match the experimental response. The mismatch in critical angle between this work and those in literature is clearly evident.

In the case of ethanol, as shown in Figure 29, a difference in critical angle of 0.07 degrees corresponds to a difference in relative permittivity of 0.0025 a.u. There are a number of factors which could contribute to the consistent offset observed between the literature permittivity and measured permittivity values. The key factors which influence the bulk permittivity of a liquid include the measured permittivity of the glass prism upon which the measurement has been performed, the temperature of the experimental system and the wavelength of light used to capture the experimental data.

In the case of Figure 29 above, the simulated response uses literature data at the same temperature and with an identical glass prism permittivity. As such, the light wavelength at which the data is captured at is the key difference between this work and that in literature for ethanol permittivity data. The influence of temperature and wavelength are discussed in Section 3.3.4 in greater detail.

The significance of the glass prism permittivity on determination of the critical angle is also a key factor which must be considered. Through the course of successive measurements and data acquisition, it was observed that the glass prism upon which in situ measurements were performed in this work influenced the bulk permittivity observed when measuring liquid samples of interest. The glass prism upon which early measurements were performed in this project was ordered specifically for use, with an anti-reflective coating on the prism face which faces the photodiode detector to mitigate back reflections of light into the prism that may lead to unnecessary noise in spectral responses.

It was found that the dielectric constant of the prism, when measured prior to solvent measurements, was different from alignment to alignment in the experimental setup, even though the experimental procedure used to mount and subsequently align the prism was consistent. The result of this difference was that bulk solvent measurements had a range of different critical angles observed for any given system which were far larger than could be attributed to the temperature difference observed from measurement to measurement. One such example is given in Figure 30 below, which shows six measurements of water from six prism alignments and the resultant difference in critical angle position.

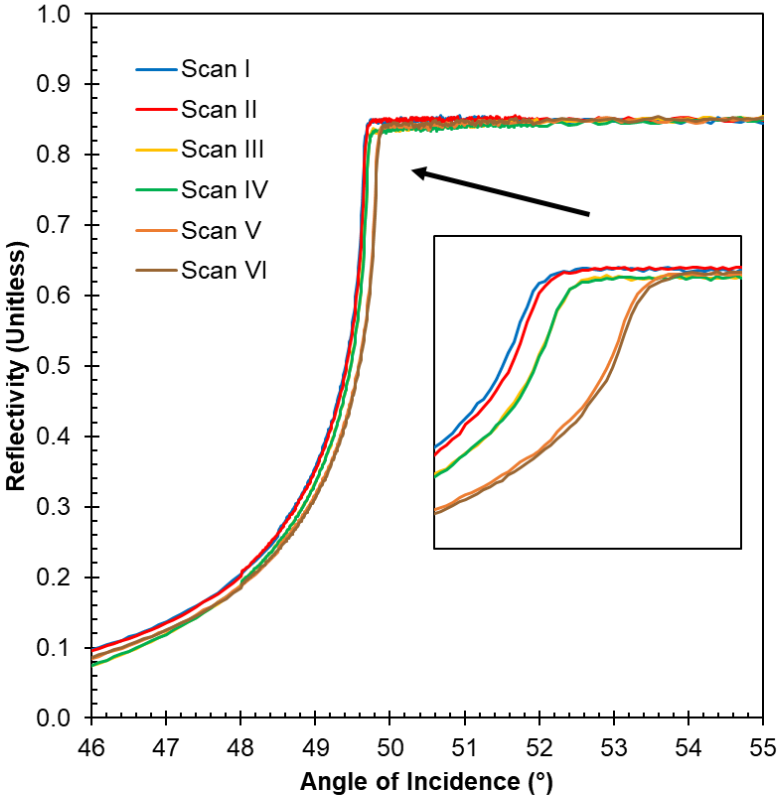

Figure 30: Six independent measurements of water with respective alignments of the glass prism. This highlights how prism alignment can play a major role in the position of the critical angle for a given system of interest. Scans refer to independent sequences of measurements performed across the shortlisted solvents

It was observed that each of the six measurements has a clear difference in the critical angle position, with the six sets clustering in groups of two measurements. Scans I and II have critical angles of 49.65 and 49.66 degrees respectively, whereas those of scans V and VI have critical angles of 49.81 and 49.82 degrees. This is a considerable difference in critical angle for the same solvent being measured in the same manner with the same wavelength of light and cannot be attributed to temperature effects, as the temperature difference observed is at most 0.7°C between measurements.

Consequently, the variation in the observed prism dielectric constant can be attributed to the glass prism being miscut and as such not to the expected specification that was first thought. This is clearly highlighted in Table 5 below, which highlights the difference in the refractive index and by extension relative permittivity of the glass prism when measured in air. This may not appear significant without prior knowledge of the influence this variation leads to but it is clear from Figure 30 that this is a considerable issue when considering the application for which the prism was intended for use.

Table 5: Measured refractive index and relative permittivity of the glass prism observed for each respective prism alignment.

Scan	Measured Prism Refractive Index (Unitless)	Measured Prism Dielectric Constant (Unitless)
I	3.254	1.8039
II	3.253	1.8036
III	3.25	1.8028
IV	3.25	1.8028
V	3.244	1.8011
VI	3.243	1.8008

The measurements presented in this work are reliant on high precision surface measurements for which repeatability of procedure is essential. In order to achieve this, issues such as a prism for which repeatable measurements cannot be obtained is not ideal and introduces an unnecessary degree of uncertainty to the measurements being performed. This is observed when comparing expected literature solvent critical angle positions against those obtained in the experimental setup, as shown in Figure 31.

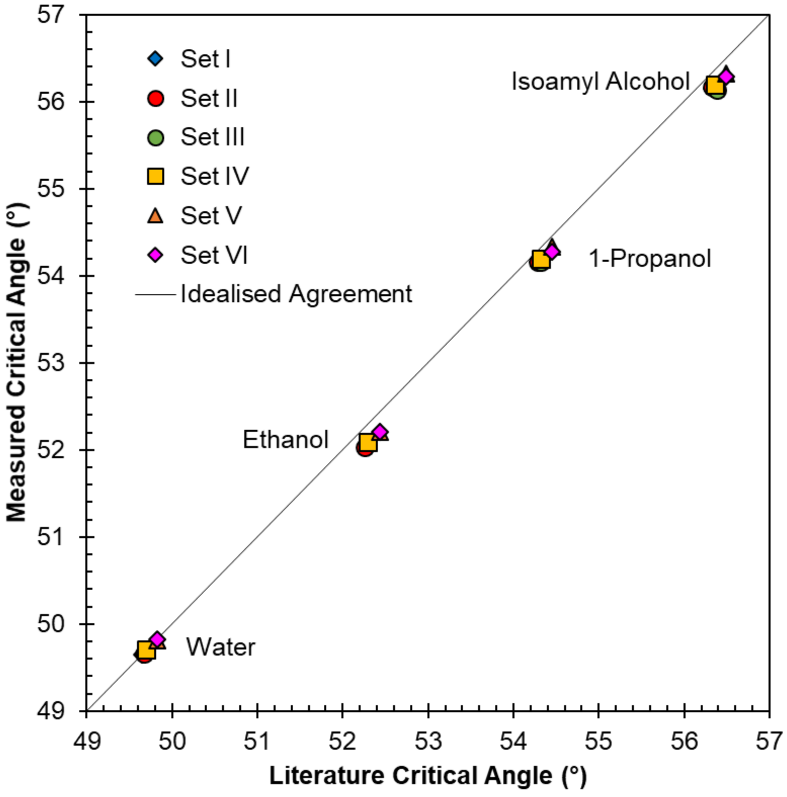

Figure 31: Comparison of critical angle position for each of the assessed solvents measured against the comparative literature response modelled using literature permittivity data.

For each solvent measured, there is a degree of scattering to the agreement between the measured critical angle and that which would be observed based on data sourced from literature. The discrepancy between the six data sets highlights that use of a prism for which the relative permittivity is not consistent with repeat measurements leads to an inaccurate representation of the system. As such, the validity of the critical angles being observed can justifiably be called into question.

To mitigate the chance for such sources of error, the glass prism was replaced with a glass prism used in the experimental setup prior to this work. The experimental analysis was repeated on this glass prism, outlined in Section

3.3.2, to assess whether it led to an improvement in the degree of attainable precision and accuracy from the experimental setup.

Using the alternative glass prism resulted in a far more precise determination of solvent critical angles than was possible with the prism used in the first instance. To better understand how significant the difference between the reported data in literature and the experimental data captured in this work, a representative comparison plot for measured solvent relative permittivity versus reported literature data was generated and is seen in Figure 32 below. It can be seen that while the experimental data is in good agreement with the reported literature data for water, as mentioned previously there is a slight disagreement for the remaining three solvents measured.

The experimental setup, based on this data, is capable of achieving greater sensitivity than Abbe refractometers used in the literature data presented in Section 3.3.1 for determination of pure solvent and aqueous glycine solution refractive index data. Relative permittivity accuracy can be quantified to give a refractive index value of up to five decimal places, compared with the four decimal places presented in literature sources. This level of precision is essential for subsequent probing of surface level concentration profiles in both aqueous glycine and urea solutions, as such measurements cannot be facilitated without an accurate quantification of the bulk solution of interest’s properties.

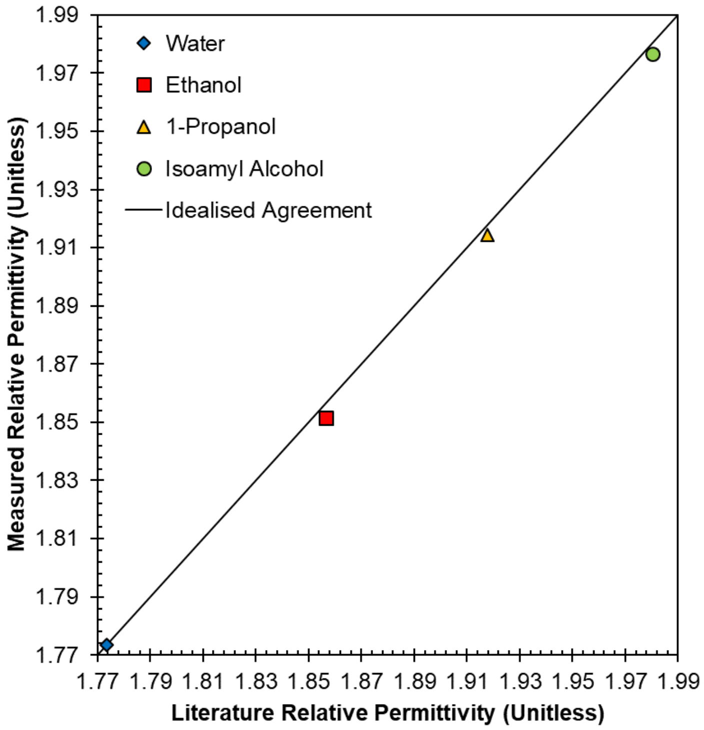

Figure 32: Comparison of mean relative permittivity for each of the assessed solvents measured against the comparative literature response modelled using literature permittivity data.

3.3.3 SPR measurements on gold chips

Following the completion of TIR reflectivity measurements of the shortlisted solvents, which identified the sensitivity of the experimental setup for critical angle determination, SPR measurements were then undertaken to assess how accurately the SPR coupling angle minima could be characterised. This is of particular importance for this research, as the SPR coupling angle minima is the key metric by which we can assess solid-liquid interfacial interactions at the gold chip surface.

Figure 33 below shows the SPR measurement of a bare gold chip in contact with air, the first measurement performed as a calibration method prior to the measurement of solvent relative permittivity. Also shown is the modelled response calculated in Winspall, which is used to generate a model of the experimental response.

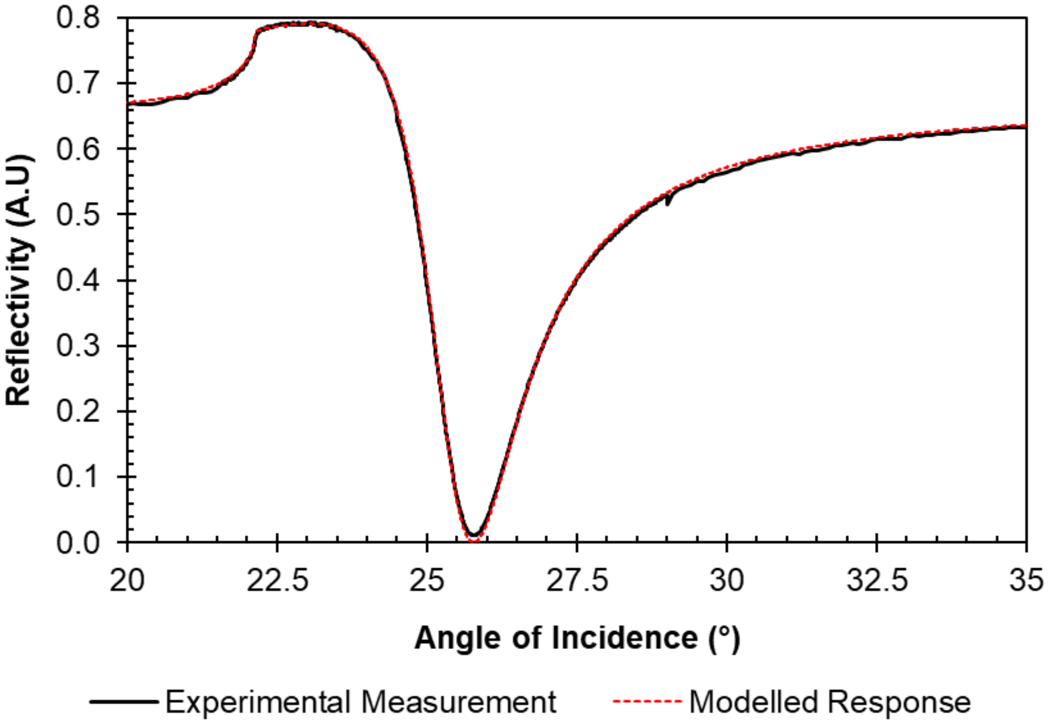

Figure 33: Experimental measurement and corresponding Winspall model generated for the measurement of air in contact with a gold chip. The gold chip had a 0.1 nm Chromium layer and 46 nm thick gold layer.

It can be seen from the comparison of the experimental and modelled response that an excellent agreement can be attained for characterisation of the gold chip by use of Winspall. The experimental curve is clear, with a sharp and well resolved critical angle and coupling angle minima. This can be extended to the measurement of solvents, as shown in Figure 34, where methanol, water, ethanol and 1-propanol are measured and the subsequent Winspall models are generated for their responses.

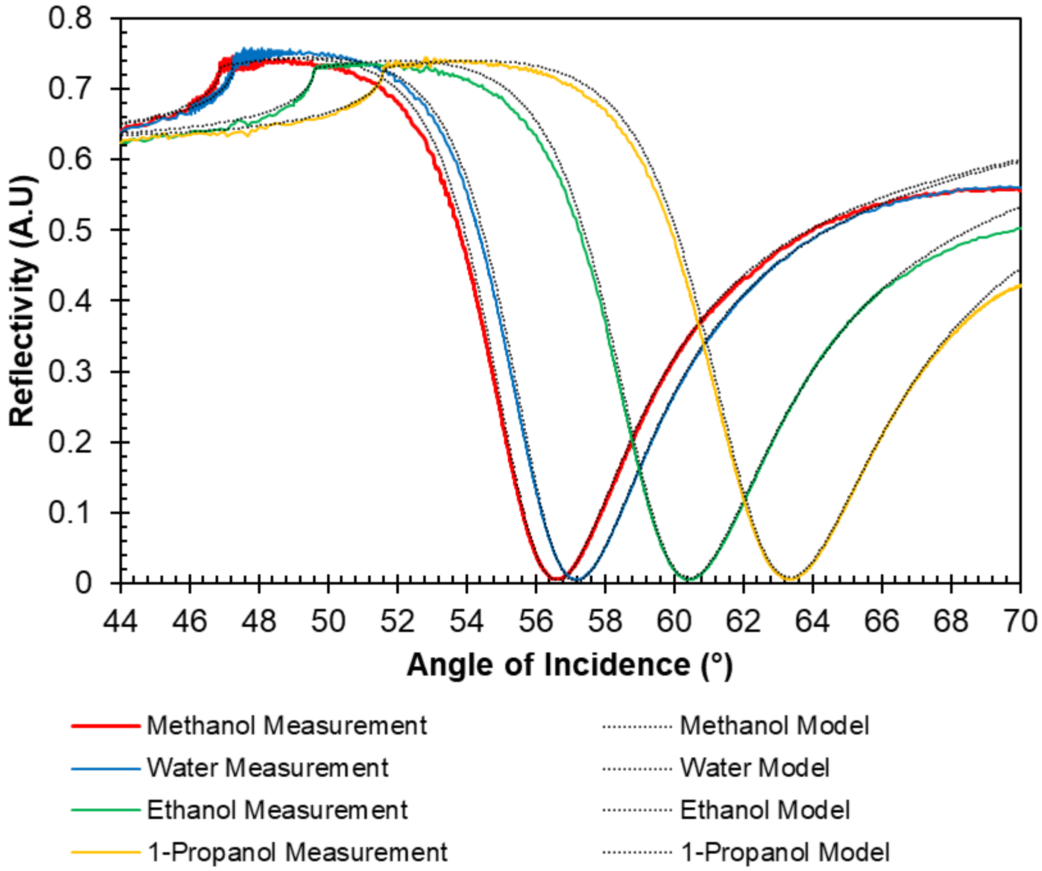

Figure 34: Experimental measurements of methanol, water, ethanol and 1-propanol. These measurements were performed on the gold chip characterised in Figure 32, with a 0.1 nm Chromium layer and 46 nm Gold layer, respectively. The experimental measurements are shown alongside there corresponding Winspall models.

As was the case for the measurement of the gold chip in air, the measurements of solvents in contact with the gold chip and their representative model systems generated in Winspall show excellent agreement with one another. The real and imaginary components of the gold layer relative permittivity in contact with air and each of the measured solvents are shown in Table 6 below.

Table 6: Real and imaginary components of the relative permittivity of the gold layer of the gold chip (46 nm, with 0.1 nm Chromium layer) when in contact with air, methanol, ethanol and 1-propanol, respectively.

Sample	Gold Layer ε_{Real} (Unitless)	Gold Layer $\varepsilon_{Imaginary}$ (Unitless)
Air	-11.48	1.42
Methanol	-12.1317	1.64
Water	-12.0616	1.59
Ethanol	-12.1792	1.7
Propanol	-12.228	1.7

It is clear from the data presented in table six that both the real and imaginary components of the relative permittivity of the gold layer do vary with respect to the sample they are in contact with, as a starker contrast is observed between air and liquid systems. This is expected though, given that the sharpness of the coupling angle minima is not as high for solvent measurements as for those in air. The variation observed between solvents is minimal, and purely relates to the tuning of the fit of these parameters in Winspall to ensure the model has an equivalent SPR coupling angle minima to that of the experimental measurements.

The measured critical angles and fitted solvent permittivity with repeated measurements of water are shown in Table 7 below, which shows that repeated measurements yield consistent values for each parameter that do not change for a given media. Table 8 contains the mean SPR coupling angle minima for the repeated measurement of each solvent and the standard deviation per solvent. This highlights the difference in the SPR coupling angle minima from solvent to solvent, but that repeated measurements of a given solvent are not subject to such variability.

Table 7: Measured relative permittivity and critical angles for six repeat measurements of water.

Measurement	Measured Relative Permittivity (Unitless)	Measured Critical Angle (°)
1	1.77322	47.25
2	1.77322	47.25
3	1.77322	47.25
4	1.77322	47.25
5	1.77322	47.25
6	1.77322	47.25

Table 8: Mean SPR coupling angles for repeated solvent measurements on given gold chip's and the observed standard deviation.

Solvent	Mean SPR Coupling Angle (°)	Standard Deviation (°)
Water	56.910	0.025
Ethanol	60.214	0.004
1-Propanol	63.071	0.010
Isoamyl Alcohol	66.037	0.020

Table 9 below shows the variation in relative permittivity of the gold layer parameters for water measured on a range of different gold chips, given that, water was used as a calibrant prior to measuring different solvents per the experimental procedure outlined in Section 3.2.3.

Table 9: Measured relative permittivity and gold layer parameters observed for SPR measurements of water on a range of different gold chips.

Measured Relative Permittivity (Unitless)	Cr Thickness (nm)	Au Thickness (nm)	Gold Layer ε_{Real} (Unitless)	Gold Layer $\varepsilon_{Imaginary}$ (Unitless)
1.773	1	43.4	-12.0378	1.44
1.7731	1	43.4	-12.1256	1.53
1.77304	1	43.4	-12.2677	1.65
1.77304	1	43.4	-12.2996	1.61
1.7731	1	43.4	-12.2335	1.46
1.77311	1	43.4	-12.2559	1.46
1.77322	1.3	51	-12.3785	1.4
1.77322	1.3	51	-12.3187	1.4
1.77322	1.3	51	-12.3207	1.4
1.77322	1.3	51	-12.3111	1.4
1.77322	1.3	51	-12.2988	1.4
1.77322	1.3	51	-12.3037	1.4
1.77314	0.1	46	-12.42	1.62
1.77322	0.1	46	-12.0978	1.65

1.77311	0.1	46	-12.0616	1.59
1.77322	0.15	45	-12.1912	1.66
1.77324	0.1	46	-12.1925	1.37
1.77324	0.1	46	-12.1548	1.69
1.77319	0.1	46	-11.9456	1.7

The data presented in Table 7 shows SPR measurements of water for a range of different gold chips and at different temperatures. For chips of the same thickness specifications, it is clear that there is a degree of variation within these sets of measurements for both the real and imaginary components of the gold layer permittivity. It is important to note that if there are any defects in the gold layer for solvent molecules to enter, the measured gold permittivity will change as solvents are cycled through.

Moreover, due to the gold layer being so thin, any polarizability changes induced in the skin layer of the film by the solvent environment (expected to be in the nanometre range) will be a non-negligible part of the permittivity response which is measured. As a result, it is not unusual to measure minor changes in the gold permittivity from measurement to measurement, even though the bulk properties of the solvent remain consistent. This variation is then clearer when comparing between chips of different gold layer thicknesses. However, the standard error of the mean for both the real and imaginary component permittivity’s across all measurements in Table 7 are 0.028 and 0.027, respectively. This identifies an inherent variability in the gold layer parameters from gold chip to gold chip, which although small in magnitude, must be considered when performing such measurements.

The reason as to why these parameters vary from chip to chip lies in the fact that the deposition of gold and chromium onto the glass slide will never be exactly the same. Typical values which can be expected for a 50 nm thick gold layer with no chromium deposited are -12.45 and 1.3 for the real and imaginary permittivity components respectively. [64] Given the varying thicknesses of gold and chromium seen across different gold chips, the data reported in Table 7 on the same order of magnitude. As a result, the variability observed is not expected to impact the performed measurements' model representations, as they are simply characterising the given gold chip upon which measurements are undertaken.

This can be verified by using the example of measurements of methanol and water, which have a similar relative permittivity (ε ~1.76 for methanol and ε ~1.77 for water). The data shown in Table six shows the difference in the real and imaginary component of the gold layer relative permittivity between methanol and water measurements. Figure 35 below shows how the water model fit for the experimental measurement would compare to a model fit for water which was calculated using the gold layer properties of a methanol measurement's model fit.

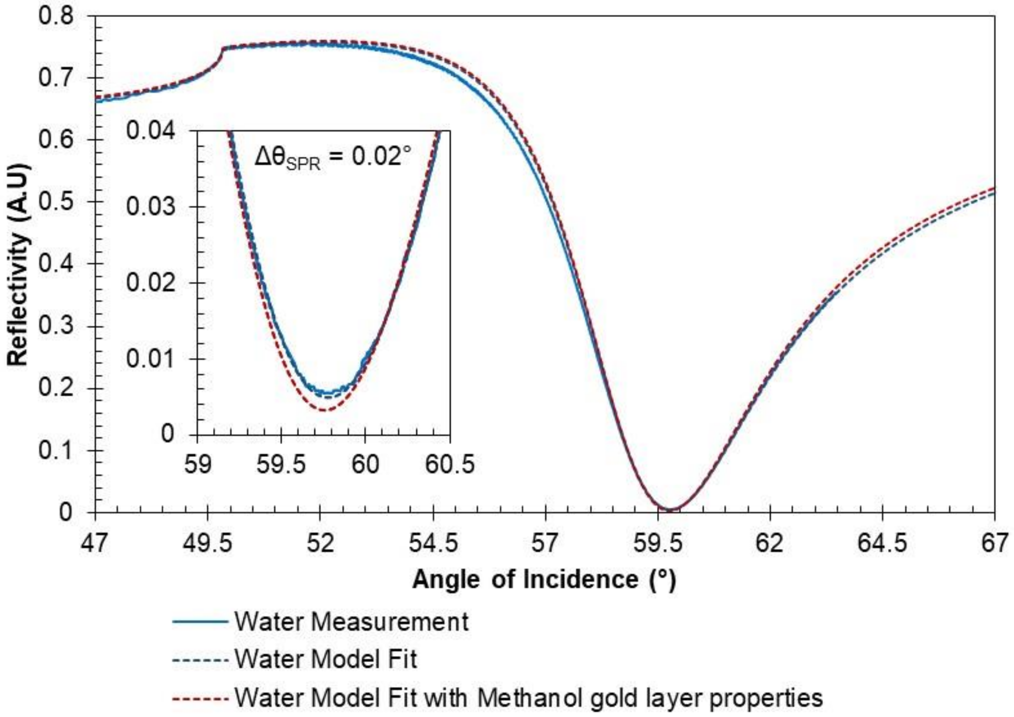

Figure 35: Observed change in the SPR coupling angle minima if the gold permittivity for methanol was used when fitting the data measured in water, rather than that of the water measurement itself.

Given that methanol has a lower relative permittivity than water, it would be expected that using the gold layer properties of methanol to fit to a water measurement would lead to a mismatch in the SPR coupling angle minima, where the model would have a lower coupling angle position than the water measurement. This is indeed the case, with the water measurement in Figure 35 having an SPR coupling angle minima of 59.772° (the water model fit being equivalent to this) and the water model fit using the methanol measurement gold layer properties yielding an SPR coupling angle minima of 59.752°. This is a difference of 0.02°, which highlights that bulk liquid environments with similar relative permittivity's will yield different coupling angle minima from one another that do not scale linearly with increasing relative permittivity.

Having verified that the representative models generated by Winspall were accurate and captured the key experimental parameters effectively, measurements of water, ethanol, 1-propanol and isoamyl alcohol could be undertaken to determine the sensitivity of the experimental setup. Raw SPR spectral data is presented in Figure 36 below for the solvent set assessed.

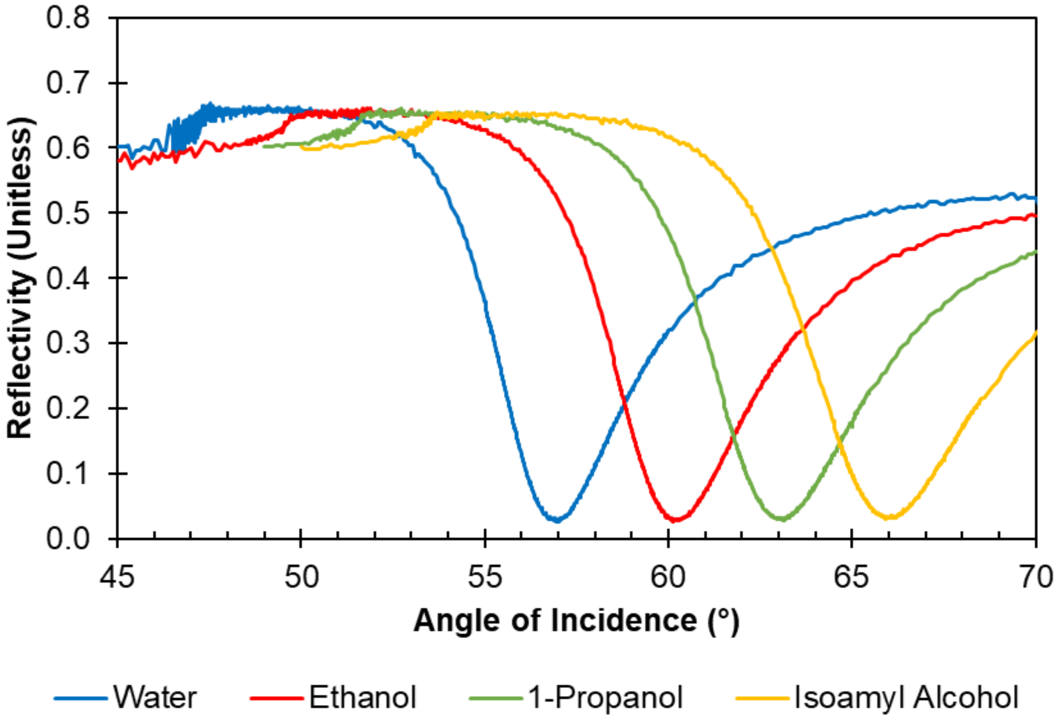

Figure 36: Raw spectral responses for SPR measurements of water, ethanol, 1-propanol and isoamyl alcohol in contact with a gold chip.

The resultant spectra have clearly distinguishable SPR characteristics and as such allow for precise determination of both the critical angle and SPR coupling angle minima. All solvents are captured without manipulation of the physical elements of the experimental setup. In the case of the water measurement, the detector position was non-optimal for the region between 45-48°, which results in the more scattered spectra when contrasted with the other solvent spectra shown here.

As was the case with TIR reflectometry data, experimental measurements were then used to generate models' systems for further in-depth comparative analysis. Table 10 below summarises the observed critical angles, coupling angle minima and relative permittivity measurements for four solvent measurements, along with the system temperature at the time of the measurement being acquired.

Table 10: Observed relative permittivity, critical angle and SPR coupling angle minima for each solvent of interest, with the accompanying temperature at which each measurement was acquired at.

Solvent	Temperature (°C)	Relative Permittivity (Unitless)	Critical Angle (°)	SPR Coupling Angle Minima (°)
Water	21.7	1.7732	47.25	56.858
Ethanol	21.7	1.8505	49.66	60.209
1-Propanol	21.9	1.9133	51.63	63.051
Isoamyl Alcohol	21.8	1.9725	53.50	66.000

Experimental data was once again compared against reported permittivity data from literature through the generation of representative models using the Winspall program. The key difference with models of SPR measurements, when compared with those of TIR measurements, is the modelling of the gold surface on which the solvents are placed in contact within the flow cell. This was modelled by importing a measurement of the gold surface in contact with air and then fitting the thickness of gold and chromium layers, as well as the real and imaginary components of the gold layer dielectric constant. The real and imaginary components of the chromium layer dielectric constant were fixed at constant known values.

In order to assess how accurately the solvent relative permittivity's were able to be determined when measuring SPR spectra, a comparison was made against the relative permittivity's observed for the same solvents on the bare glass prism, as outlined in section 3.3.2. The resultant relationship between the two experimental configurations measured relative permittivity data is shown in Figure 37 below.

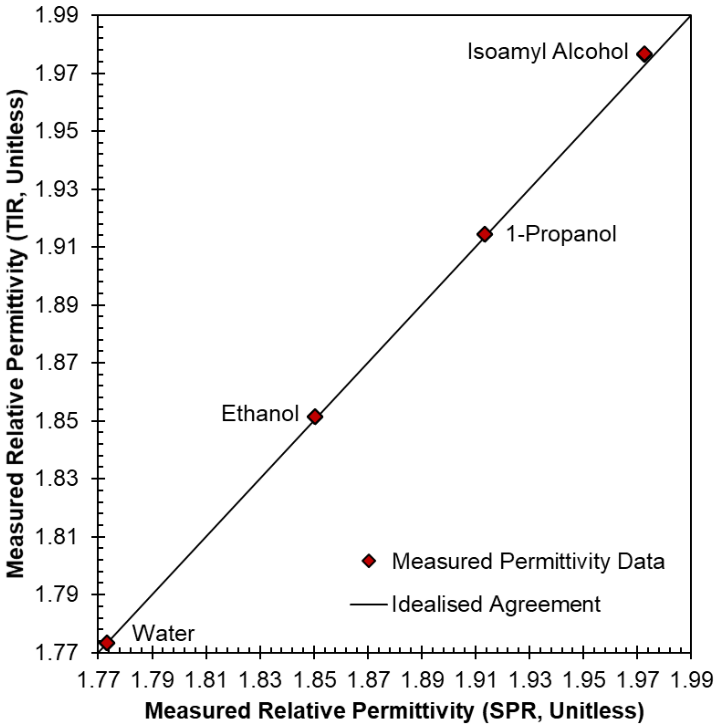

Figure 37: Comparison of measured permittivity values for each solvent of interest in both TIR and SPR experimental configurations. It is observed that the agreement between both configurations is excellent, further highlighting the precision with which measurements can be obtained from the experimental setup.

The measured permittivity values for both the TIR and SPR measurements given in Figure 36 show excellent agreement with one another. In the case of isoamyl alcohol, the permittivity observed in TIR measurements appears to be slightly higher than those for the SPR measurements. This can be attributed to the temperature of the respective measurements, which have a difference of 0.7°C, with the solvent samples for SPR measurements being captured at higher temperatures than those of the TIR measurements. Relative permittivity is influenced by temperature, decreasing with increasing temperature. As a result, this difference is to be expected.

Overall, this highlights the accuracy possible from the experimental setup and confirms that precise surface measurements can be performed using the setup through determination of both the critical angle and SPR coupling angle minima.

3.3.4 Overview of Refractive Index Sensitivity and Dependency on Temperature and Wavelength

To establish why such a difference in the position of solvent critical angles was observed when comparing measurement data acquired in this work against relative permittivity data sourced from literature, further investigation was required. Specifically, the influence of temperature and light wavelength on the bulk solvent properties, in order to assess the significance of each factor in contributing towards the difference in critical angle being observed.

In the absence of a wide field of reported refractive index data for the solvents of interest and additionally for aqueous glycine when first shortlisting solvents of interest, pure water was utilised as a suitable approximation. Figure 38 below details a variety of literature sources of data on the relative permittivity of water and its dependence on temperature, as well as data from literature sources detailing glycine relative permittivity data for 0 g/kg solutions (pure water).

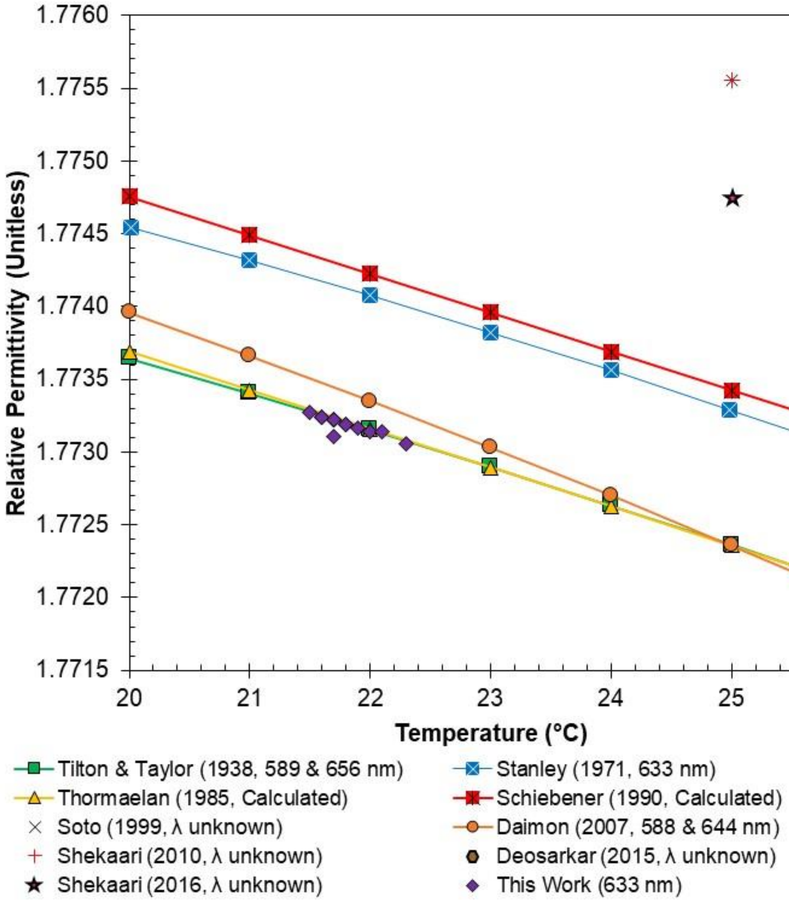

Figure 38: Comparison of gathered literature data for the permittivity of water against experimental measurements performed in this work, along with the reported permittivity of water in studies were the permittivity of aqueous glycine solutions was performed. There is a clear discrepancy between the literature data reported for water in published glycine data and that of pure water permittivity measurements.

It is evident from the plot that there is a significant difference between the relative permittivity of water being reported for literature sources of glycine permittivity data and that of pure water, ranging from 0.0007 to 0.0012 at 25°C.

This magnitude of difference is of the same order of magnitude as would be observed for a six-degree temperature increase and is closer in value to refractive indexes for lower temperatures.

An encouraging observation from the plot is that the permittivity data being reported for internal experimental work is consistent with that of reported literature sources. Given the magnitude of the difference between experimental data and that of the data reported in literature for sources of glycine permittivity data, this suggests that temperature is not the sole contributing factor to the difference between the permittivity of water reported by literature sources investigating glycine and those assessing pure water solely.

Having confirmed that temperature alone was not driving the significant difference in critical angle position being observed, the role of light source wavelength was investigated. The experimental setup utilises a 633 nm monochromatic He/Ne laser. However, data sourced from literature did not always state the light wavelength at which refractive index measurements were obtained. This highlighted some ambiguity in terms of how accurately such literature data reflected the experimental setup and subsequently the value of making comparisons between the two.

As such, a further literature search was necessary to determine the method by which all glycine and water refractive index data had been obtained and the corresponding wavelength of light which had been used to capture the reported data. The results of this search are summarised in Table 11 below.

Table 11: Literature sources of water permittivity data, the light wavelength at which they were acquired and temperature range assessed. In addition, the method of data acquisition is noted, whether it be instrument based or calculation through use of fundamental relationships.

Literature Source	Wavelength Data was obtained at	Data Acquisition Method	Temperature Range Assessed (°C)
Tilton & Taylor (1938) [69]	Linear Interpolation between 589 and 656 nm	Spectrometer and glass prism.	0-60
Stanley (1971) [77]	633 nm	Interferometer	1-60
Thormaelan (1985) [78]	Linear Interpolation between 405 and 707 nm	Equation based on the electromagnetic theory of light	-10 to 500
Scheibener (1990) [79]	633 nm	Equation based on the electromagnetic theory of light	0-500
Daimon (2007) [80]	Linear Interpolation between 587 and 656 nm	Goniometer spectrometer	19, 21.5, 24
Soto (1999) [65]	Not specified	ATAGO RX-1000 refractometer.	25
Shekaari (2010) [81]	LED, 589 nm	ATAGO-AR1 refractometer	25
Deosarkar (2015) [82]	Not specified	Refractometer from Amkette analytics	26
Shekaari (2016) [83]	LED, 589 nm	ATAGO-AR1 refractometer	25

When initially searching for accurate permittivity data for pure water that could be used as a reference point when performing similar experiments in the experimental setup, a variety of sources which reported R.I data at different light wavelengths were found. The experimental setup uses a 633 nm wavelength He/Ne laser, as such the focus was on obtaining literature sources that capture the permittivity of water at this wavelength. Most significant of these is the sources of glycine refractive index data, as this means that direct comparisons cannot instantly be made between future measurements in this work and references in the literature.

A thorough search of the literature yielded a variety of data sources, capturing the relative permittivity of water using different methods and wavelengths (refractometer/spectrometer, 633 nm or a wide range of wavelengths). For sources which presented the permittivity across a range of wavelengths, this meant determining the permittivity at 633 nm through use of linear interpolation between the two wavelengths either side of 633 nm (source dependent) to produce a range of permittivity’s for temperatures which may be experienced in the laboratory, where the temperature could range between 20-25°C.

This was necessary for Tilton & Taylor (1938), Thormaelan (1985) and Daimon (2007). The interpolations, when plotted, all follow the same trend and have slopes of the same magnitude. However, when adding the data reported at a single excitation wavelength (Stanley (1971) and Scheibener (1990)), it became apparent that there was a banding of the data sources into two groups of three sources; those for which linear interpolation was required to obtain the refractive indexes over the required temperature range and those with absolute values across that range.

The data being obtained experimentally in the lab aligned with that of Tilton & Taylor’s work, with all experimental data obtained sitting alongside the interpolated data. This seemed strange to see such a margin of difference between some of the literature sources and the experimental data generated in the laboratory. However, the fact that the internally generated data was aligned with reported sources in literature was positive.

Figure 39 below shows the data from this work presented against the interpolated data of Tilton & Taylor between 589 nm and 656 nm, with reported data points at each wavelength shown in the figure, respectively. The interpolation was conducted across the temperature range of interest for this work (20-25°C, with measured values in the laboratory typically falling within a range of T=21-23°C) to be able to make an effective comparison, and highlights the alignment between this work and the literature.

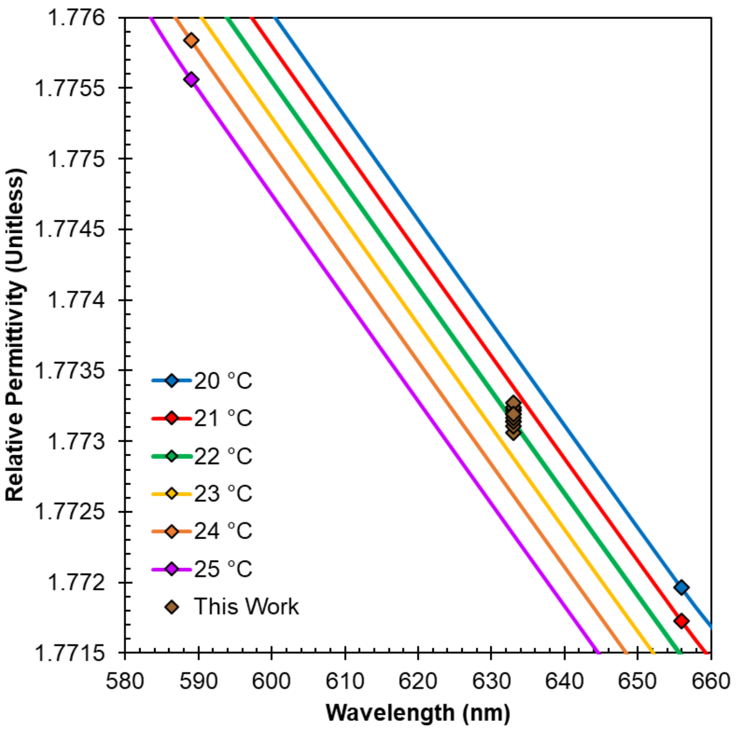

Figure 39: Dependence of relative permittivity on light wavelength, highlighted using data sourced from Tilton & Taylor for water [50]. The measurements acquired from this work (measured using a 633 nm light wavelength) in order to highlight how the fall within the expected range of values.

The difference observed between internal data and that sourced from the literature was emphasised when looking solely at pure water. The reported refractive index of 0 g/kg aqueous glycine solution (i.e. pure water) was markedly higher than both interpolated water data from literature and internally generated experimental data, ranging between n = 1.3322 – 1.3325 at 25°C. This is a difference of n = 0.001 from the experimental values obtained consistently in repeat scans of water performed in the laboratory.

The key conclusion when looking at how literature data varied so significantly from source to source was that given the range of reported permittivity data in literature and alignment of this work to data at the corresponding light wavelength of 633 nm, that internal consistency of measurement was to be accepted as the go to metric by which to compare repeat measurements of solvents and aqueous solutions alike, rather than direct comparison with literature. When looking to compare with literature data, acknowledgement of the factors which lead to differences and the impact they have is key in the interests of transparency.

This is a known effect which is covered extensively in the literature, as this overview looks to highlight for the example of water. Given that this research uses aqueous solutions extensively, the aim was to assess this effect and its magnitude in order to understand the magnitude of such effects which we could expect in the work undertaken in Chapters 4-6.

3.4 Conclusions

In conducting both TIR and SPR measurements of pure solvents, it has been possible to establish that highly sensitive measurements of single component liquid systems are possible with the experimental setup available for use in the laboratory. The protocol and experimental setup established can generate clear spectra from which key spectral features can be precisely quantified, with critical angle and SPR coupling angle minima determination possible to within to 0.01°. Having observed differences between the permittivity data presented in this work and that published in the literature, it is important to be mindful of the role temperature and light wavelength have on a liquids relative permittivity when performing such measurements and be able to account for this when comparing internally generated data against that reported in the literature.

Chapter 4

4. Capturing interface induced concentration enhancement in glycine solutions in situ using SPR spectroscopy

4.1 Introduction

Many processes involving liquid solutions are driven by what is happening at solution interfaces. For example, primary nucleation of crystalline solids from solution typically proceeds via heterogeneous mechanisms, where the presence of interfaces in contact with the solution facilitate the birth of crystal nuclei. The surface energy of crystallites in contact with such interfaces is reduced and this decreases the size of the smallest stable (or critical) nucleus.[5] However, here it is conventionally assumed that solution composition at the interface is the same as in the bulk solution and thus the solute attachment rates and the surface energy of the nucleus-solution interface correspond to conditions encountered in bulk solution.

Interfacial effects, based either on surface crystal structure or topography [3-4] or else on surface chemical properties [5-8] had been extensively considered in previous studies of crystal nucleation. However, previous investigations of effects of surface chemical properties have focused on specific functional groups attached to surfaces rather than the properties of materials which were in contact with solutions. For example, the effects of surface chemical functionality of graphene on nucleation of glycine polymorphs were recently investigated .[20]

However, recent studies have reported that glycine nucleation is rapidly accelerated at solid (PTFE) and liquid (tridecane) hydrophobic surfaces in contact with aqueous glycine solutions.[27, 84, 85] These surfaces do not have any specific functional groups that would be expected to have specific affinity with glycine. It has been proposed that these unexpected observations are due to non-specific dispersion (van der Waals) interactions. These interactions in turn lead to the formation of a concentrated interfacial layer of glycine at hydrophobic interfaces, which has been seen in molecular dynamics (MD) simulations.[27] Furthermore, this novel insight has challenged the widely held assumption within the classical nucleation theory, which assumes a uniform solution composition throughout the solution.[5] Consequently, it is of particular importance to provide a direct experimental confirmation of the interface induced concentration enhancement effect.

Through the use of an in-situ surface measurement technique, surface plasmon resonance spectroscopy (SPR), this work has aimed to probe the solution interfacial region. In SPR spectroscopy, an incident light source is directed towards a thin gold film, in order to excite a surface plasmon. Plasmon oscillation results in the generation of a bound electromagnetic wave, known as an evanescent wave, which exhibits exponential energy decay with increasing distance from the gold film surface [29, 30, 40] and thus the surface plasmons enable extremely sensitive measurements through the detection of changes in the refractive index within the nanoscale solution region adjacent to the gold film surface. [34] SPR measurements can also be performed for gold films coated with nanolayers of other materials, including oxides or polymers, so that solutions in contact with these surfaces can also be investigated. As a result, SPR sensors are widely used in biomolecular and nanoparticle research, [32] where they are typically used for highly dilute aqueous solutions.

In this work, we provide for the first time a direct experimental confirmation of the interface induced concentration enhancement effect, which has been seen in previous molecular dynamics (MD) simulations in slightly undersaturated glycine solutions interacting with a model Lennard-Jones surface. SPR measurements were undertaken for a series of pure solvents and their binary mixtures to provide reference spectra, as well as for a range of undersaturated glycine solutions at gold and polystyrene interfaces.

4.2 Materials & Methods

In this section, the experimental setup (a custom-built refractive index sensor based on an SPR spectrometer setup) is described, along with the procedures used to prepare both the binary solvent mixtures and aqueous solutions used in this study. The acquisition procedure utilised for carrying out SPR measurements of pure component solvents, solvent mixtures and aqueous solutions of glycine respectively is also outlined, along with the procedure followed to develop representative models of respective experimental measurements for further analysis.

4.2.1 Solution Preparation

Water (HPLC Plus Grade, Sigma Aldrich), Methanol (99%, VWR), Ethanol (Absolute, Fisher Scientific), 1-Propanol (HPLC Grade, 99.9%, Sigma Aldrich)

1-Dodecanethiol (≥98%, Sigma Aldrich), Polystyrene (Mw 34,300 g mol^{-1}, Polymer Source Inc.), Toluene (Laboratory Reagent, ≥99.3%, Sigma Aldrich) and Glycine (Fisher Scientific, 98.5%) were purchased and handled as received.

Aqueous glycine solutions were prepared ranging from pure water to 250 $g_{glycine}/kg_{water}$ (which will be denoted as g/kg throughout) by combination of glycine powder and water within glass vials. Prior to solution preparation, vials were washed and subsequently rinsed with HPLC grade water, before drying under a stream of nitrogen gas. Solutions were prepared by weighing the required mass of glycine powder into a vial, followed by the corresponding mass of water to obtain the desired solution concentration. Vials were then sonicated in an ultrasonic bath for up to 10 minutes, until dissolution was confirmed by visual inspection, and then they were left to thermally equilibrate with their surroundings for at least 1 hour.

Pure solvents and their binary mixtures were prepared through matching refractive indices of respective aqueous glycine solutions in order to provide reference SPR spectra. Binary solvent mixtures were prepared using methanol ($\varepsilon = 1.76$) and 1-propanol ($\varepsilon = 1.91$) with the relevant compositions for binary solvent mixtures (with a total mixture volume of 2 mL) shown in Table 12 below.

The relative permittivity of the mixtures is calculated from the sum of the volume fraction of each pure component multiplied by the relative permittivity of the pure component solvent, with the measured values utilised for analysis in the generation of SPR models. Refractive indices of aqueous solutions, pure solvents and their mixtures were obtained from the critical angle in the measured SPR spectra which were in good agreement with corresponding values reported in the literature.

Table 12: Relevant volumes of methanol and 1-propanol, respectively, utilised to prepare representative binary solvent mixtures for aqueous glycine solutions with concentration between 50-250 g/kg.

Reference Concentration (g/kg)	Volume Methanol (μL)	Volume 1-Propanol (μL)	Ideal $\varepsilon_{\text{binary mixture}}$ (unitless)	Mean Measured $\varepsilon_{\text{binary mixture}}$ (unitless)
50	1479	521	1.799	1.802
100	1219	781	1.819	1.815
125	1108	892	1.828	1.826
150	952	1048	1.839	1.833
200	689	1311	1.858	1.856
250	473	1527	1.875	1.871

4.2.2 Gold Chip Preparation

Gold chips were prepared per the protocol outlined in Section 2.3.3.

4.2.3 SPR Spectrometer Setup

The SPR experimental setup is outlined in Section 2.3.4, with a schematic given in Figure 40 below.

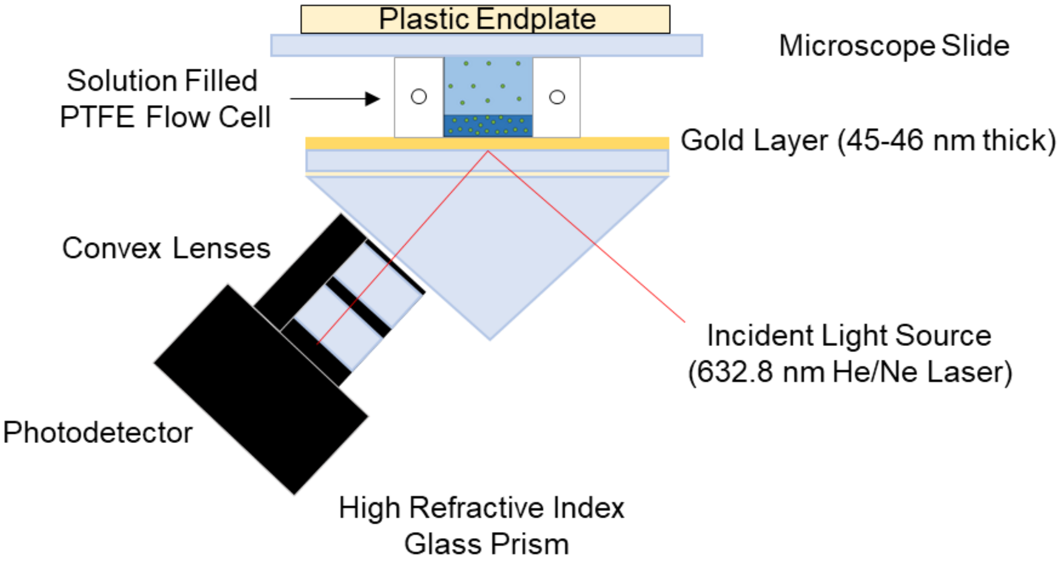

Figure 40: Diagram detailing the key components of the SPR setup.

4.2.4 SPR Measurement Procedure

SPR measurements of the gold chips were performed in air, water, pure solvents, solvent mixtures and aqueous glycine solutions. For each liquid sample analysed, an aliquot of liquid (269 μL) was injected into the flow cell using a syringe, with the injection points sealed using pipette tips. The flow cell was flushed out with the sample of interest in triplicate, before being held in the flow cell (3 minutes). A measurement was then acquired, with the flow cell flushed out three times with the next sample of interest.

Measurements were obtained in sets following a defined sequence, whereby pure solvent and solvent mixture measurements were undertaken prior to aqueous glycine solutions measurements. The flow cell was flushed out with water three times before addition of the next liquid sample of interest. Temperature readings were collected throughout the data acquisition process using the datalogger thermometer. Upon completing a set of measurements, the gold chip and flow cell were then removed from the prism and cleaned by immersion in 1% Hellmanex-water solution and rinsed with water to ensure the setup was free of contaminants.

The experimental procedure is summarised in Figure 41 below, which details the procedure that was followed for SPR performing measurements.

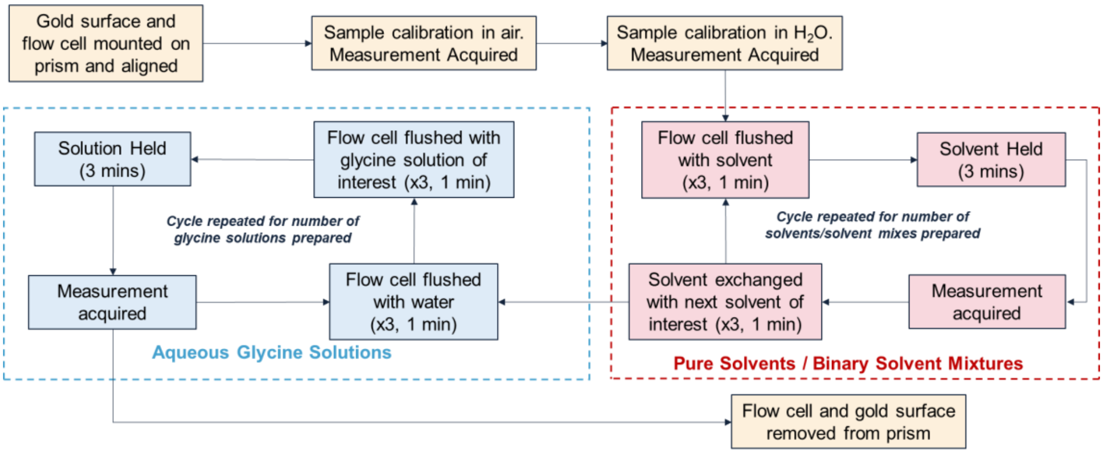

Figure 41: Experimental procedure developed for SPR measurement of aqueous glycine solutions, pure solvents and binary solvent mixtures.

4.2.5 SPR Model Generation and Data Analysis

To analyse experimental SPR spectra, representative SPR models were generated using the Winspall program developed by the Max Planck Institute [64]. Winspall implements standard transfer-matrix calculations of the light propagating through the experimental system of interest, solving the Fresnel equations for light transmission and reflectance at an interface. Such calculations assume infinite layers with perfect interfaces and provide excellent agreement with experimental data for layered assemblies such as Langmuir-Blodgett assembled layers [86, 87]. Light propagation through a relevant multilayer system (see Figure 42) depends on each layer thickness and its relative permittivity (or dielectric constant) ε (which is the refractive index squared). The dielectric constant of air is assumed to be equal to one.

Figure 42: Schematic diagram outlining the constituent parts of the experimental system used to generate the representative SPR model. All gold chips contain glass prism, chromium and gold layers. Pure liquids only contain bulk, but solutions can also include a separate interfacial layer.

A model system of the gold surface in air is first generated. Prior to model development, the glass prism dielectric constant is fixed and kept constant throughout, having confirmed the prism refractive index through repeated measurement of the prism in air. The experimental measurement of the surface in contact with air is then imported to Winspall and the gold and chromium layer thicknesses are measured and fixed. The real and imaginary components of the chromium refractive index are fixed, with the real and imaginary components of the gold refractive index fitted. The fitting procedure yields an idealised, representative model of the experimental data, as well as both the thickness and refractive index of each layer which achieve the best available fit to the experimental measurement. As such, the representative thicknesses of gold and chromium can be accurately characterised.

Having accurately characterised the gold surface of interest, model systems are generated for water, pure solvents and solvent mixtures. This is achieved by fitting the bulk solution refractive index and real and imaginary components of the gold layer refractive index to the respective experimental measurement of interest. This leads to the generation of reference models with which aqueous glycine solutions of the same bulk refractive index can be compared against.

For a given reference model, the relevant aqueous glycine solution is imported into the model and the glycine solution measurement is compared against that of the corresponding solvent reference measurement. The bulk refractive index of the solvent system model is then matched to that of the aqueous glycine solution if not an ideal match by adjustment of the bulk solution refractive index, such that an exact match is achieved. From this adjustment, a qualitative observation can be made of the mismatch in the position of the coupling angle minima of the solvent reference model to that of the experimental aqueous glycine measurement.

To remove this mismatch, an interfacial layer of solution with thickness of one nanometre is modelled between the gold layer and that of the bulk solution. The refractive index of the interfacial layer is then subsequently fitted to observe that the model coupling angle minima is equal to that of the experimental aqueous glycine solution coupling angle minima. This gives a known value for the interfacial region permittivity, which can be subsequently used to determine the concentration of glycine at the solid-liquid interface.

The data analysis procedure is summarised in the workflow given in Figure 43 below.

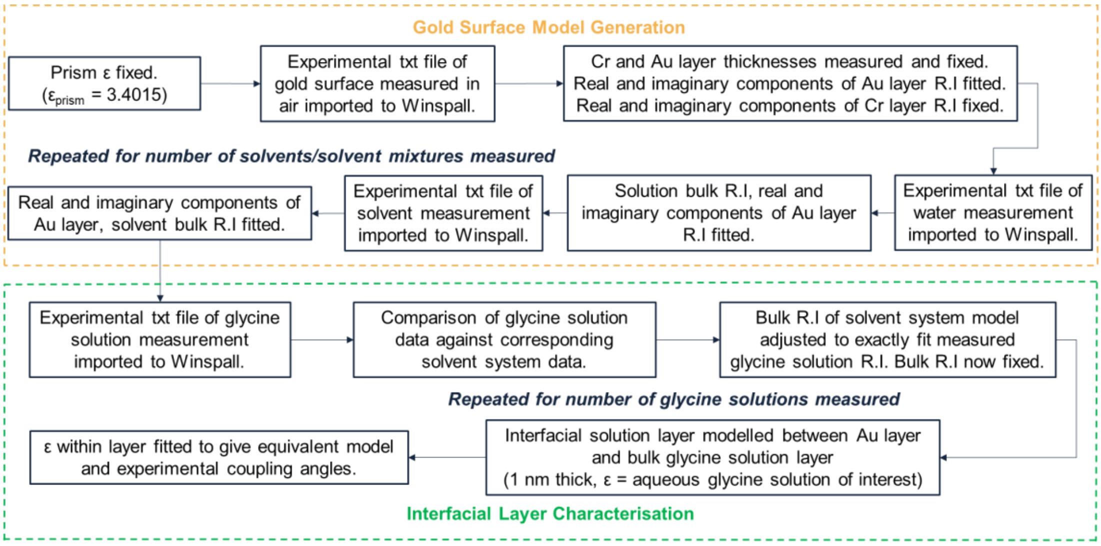

Figure 43: Data analysis procedure followed for the development of representative SPR models for interfacial layer characterisation.

4.2.6 Calculation of surface concentration from relative permittivity measurements

Through use of empirical models, best estimates were made as to how to accurately quantify this degree of oversaturation at the interface in terms of interfacial glycine concentration, to then compare this behaviour against that observed in the bulk solution.

Having set basis for the calculation, the following key assumptions are made. We are assuming ideal mixing of the aqueous glycine solutions between pure water and pure glycine and that the molecular polarizability of glycine is constant, irrespective of state. As such, we generate an idealised solution density by taking the sum of each pure component density multiplied by its respective mass fraction for a given aqueous glycine solution concentration, thus giving solution density data to span the region from which experimental data was not captured.

$$Solution\ Density\ (kg\ m^{-3}) = \sum(\rho_{water}x_{water}) + \left(\rho_{glycine}(1 - x_{water})\right)$$

This density calculation facilitates calculation of estimates as to what the interfacial region permittivity of the measured aqueous glycine solutions can be. This is achieved through use of the Clausius Mossotti equation, which is shown below.

$$\frac{\varepsilon_r - 1}{\varepsilon_r + 2} = \sum \frac{N_i\ \alpha_i}{3\ \varepsilon_0}$$

Where ε_r is the relative permittivity, N_i is the number density of the respective pure component, α_i is the molecular polarizability of the respective pure component and ε_0 is the permittivity of free space. The equation is used typically to determine the permittivity of a substance based on known fundamental physical properties, whereas its application here is to determine permittivity data given the assumption of ideal mixing.

To determine the permittivity across the x = 0-1 mass fraction range, molecular polarizability values for pure water and glycine are required. For these to be determined though, permittivity values for each pure component are also required. We use experimental permittivity data for pure water and literature data for that of pure glycine respectively to determine each component's molecular polarizability. Density and permittivity data of both pure (i.e., solid) and aqueous glycine [65, 81-83, 88] has been compiled from literature to compare experimental data against literature data for reference. This data is then compared against the idealised solution densities to see how they compare and if they are a good estimate of the true solution's physical behaviour.

The pure component number densities of water and glycine are then determined, allowing for the right side of the Clausius Mossotti equation to be calculated and thus the relative permittivity at mass fractions between pure water and pure glycine to be determined.

$$N_i = \frac{\rho_i \times N_A}{M.W_i}$$

Where ρ_i is the pure component density, N_A is Avogadro's number and $M.W_i$ is the pure component molecular weight. We can then use the pure component number densities to determine the component number densities for each mass fraction of glycine in solution within the assessed concentration range (glycine mass fraction = 0-1).

To contextualise the measurements performed in this work, the Clausius Mossotti equation is once again used. In this instance, the equation is calculated to solve for the molecular polarizability of pure glycine. This is achieved through use of aqueous glycine solution density data from the literature and the relative permittivity data obtained from SPR measurements. This allows for experimental measurements to be fitted to the equation and thus determine surface concentrations which lie beyond the limit of undersaturated glycine solution permittivity data.

4.3 Results & Discussion

In this section, we outline how SPR spectroscopy has been used as a unique means to directly measure concentration enhancement effect at the solid-liquid interface. Section 4.3.1 details the collection of SPR measurements for pure component solvents and binary solvent mixtures and how these can be used to yield reference measurements for comparison against SPR measurements of aqueous glycine solutions.

We then present the implementation of a light propagation model for analysis of measured SPR spectra in section 4.3.2, where we utilise a representative model of the prism-gold surface-solution of interest, to quantify the increase in interfacial layer permittivity with respect to the permittivity of the bulk solution. This analysis provides a quantitative representation of the concentration enhancement observed at the solid-liquid interface. This is further developed in section 4.3.3; whereby repeat measurements of individual gold chips are presented. We observe a degree of variability in the degree of glycine concentration enhancement observed at the solid-liquid interface. This variation is rationalised to give context to why such variation is observed and the contribution, if any, it may have towards the observed surface concentration enhancement of glycine. In doing so, we can provide an estimate of the interfacial concentration enhancement at the solid-liquid interface and provide context to the findings observed in section 4.3.4.

4.3.1 Raw Angular Reflectivity Measurements

To probe solution composition at the solid-liquid interface, measurements of pure (single component) solvents and binary solvent mixtures in contact with the gold surface were carried out in the first instance. In the case of pure component solvents, there is no competition with other molecules in the liquid phase to interact with the solid surface due to the liquid homogeneity. Each solvent sample has a known refractive index and as such, a characteristic SPR response.

The bulk refractive index is characterised by the position of the critical angle in the SPR spectra, whereas the SPR coupling angle depends on both the bulk refractive index and local refractive index variation in the liquid adjacent to the solid interface. We can therefore take these two angles and utilise both when looking to capture the interfacial concentration enhancement effect in situ. As a result, such solvent systems can be utilised as a reference measurement to compare measurements of aqueous glycine solutions against, where both glycine and water molecules are interacting at the interface.

If we assume that local compositions of aqueous glycine solutions are not influenced by contact with solid interfaces, we can expect that a glycine solution with the same refractive index as that of a pure solvent should elicit an identical SPR response. This assumption can be tested by refractive index matching glycine solutions, through adjusting their glycine concentration, to pure solvents, so that the two systems have identical critical angles. If there is no significant compositional difference between composition in the bulk solution and at the solid-liquid interface, then the SPR coupling angles of both the pure solvent and aqueous glycine solution should be the same.

However, if this is proved not to be the case and there is in fact a shift in the coupling angle to a higher angle than the observed coupling angle for the solvent reference measurement, then this can be rationalised as the concentration of glycine molecules in the vicinity of the gold surface exceeding that in the bulk solution, with its corresponding refractive index exceeding the bulk solution refractive index. As such, this would suggest the qualitative evidence of interfacial effects which arise due to non-specific surface interactions at the solid-liquid interface.

In order to ensure a refractive index match of a glycine solution to a pure solvent, we need to establish accurate data for refractive index dependence on the glycine solution concentration in aqueous solutions. The respective relative permittivity data for aqueous glycine solutions assessed, along with data sourced from the literature, is highlighted in Figure 44 below.

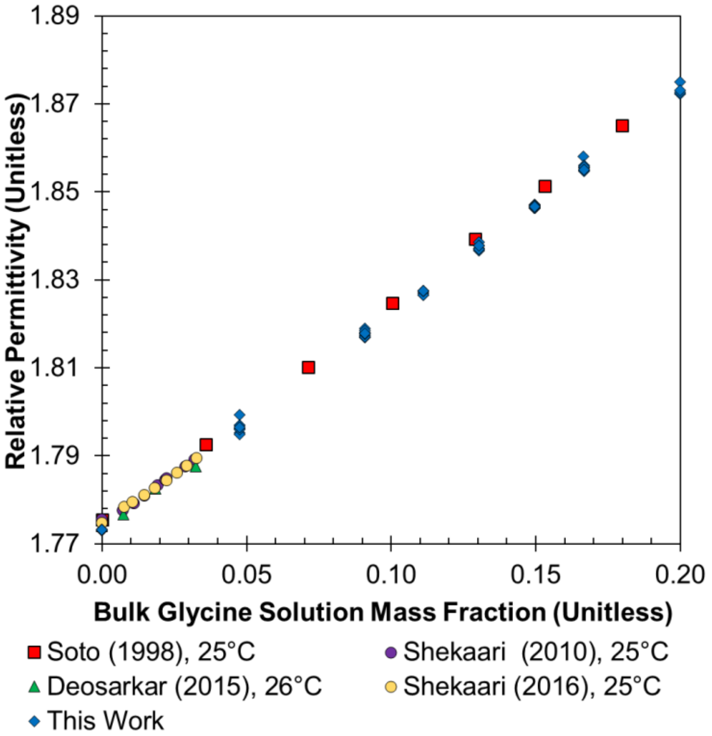

Figure 44: Comparison of measured permittivity values for aqueous glycine solutions against those reported in literature.

It is seen from the comparison of permittivity data generated in this work with reported literature data that there is a good agreement between each. However, it should be noted that reported literature data is either captured using a lower light wavelength (589 nm) or with no reported light wavelength due to the instrumentation used, whereas this work utilises a 632.8 nm light source. Consequently, we note the influence that both temperature and light source wavelength have on bulk solution refractive index properties and thus account for this.

Raw SPR spectra of aqueous glycine solutions are shown across the solubility range of glycine in water in Figure 45 below.

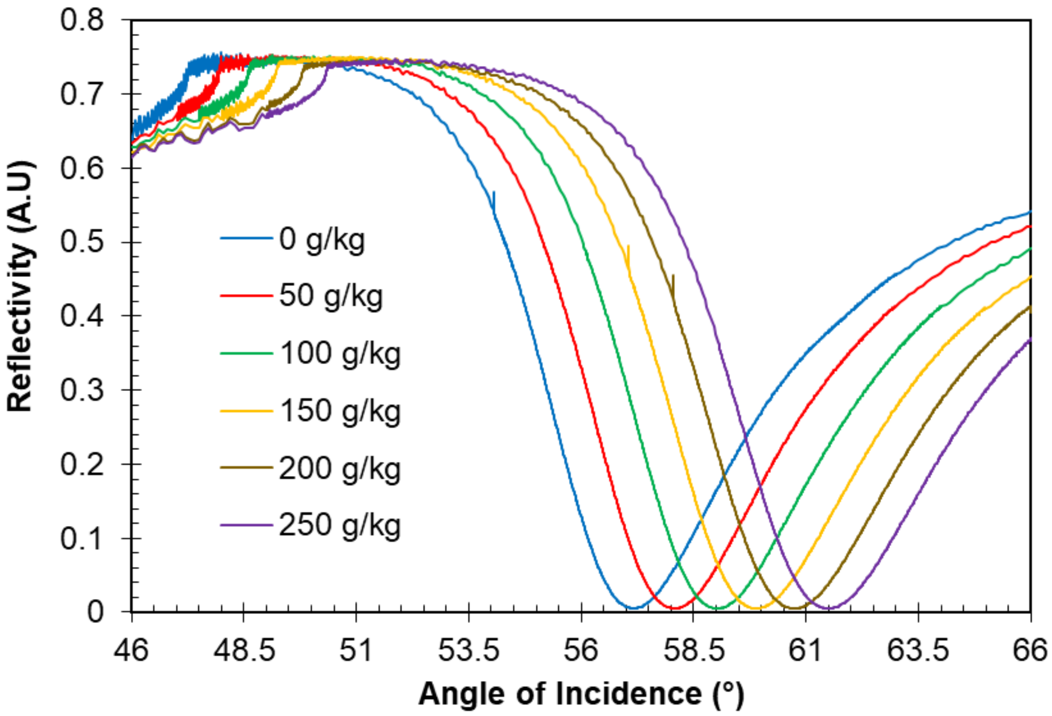

Figure 45: Raw SPR spectra of aqueous glycine solutions across the solubility range of glycine in water (g/kg basis) measured on gold chip 2.

Figure 46 below shows a comparison between an aqueous glycine solution and solvent measurement. The raw SPR spectra of an aqueous glycine solution (176 g/kg), the concentration which yields a refractive index matched to ethanol, is compared against an SPR scan of pure ethanol. As can be seen from the inset on the left of the figure, the refractive index of both solutions is equivalent by way of their critical angle being the same. This means that the SPR coupling angle, the metric by which we confirm the existence of surface concentration enhancement, is the appropriate metric of interest.

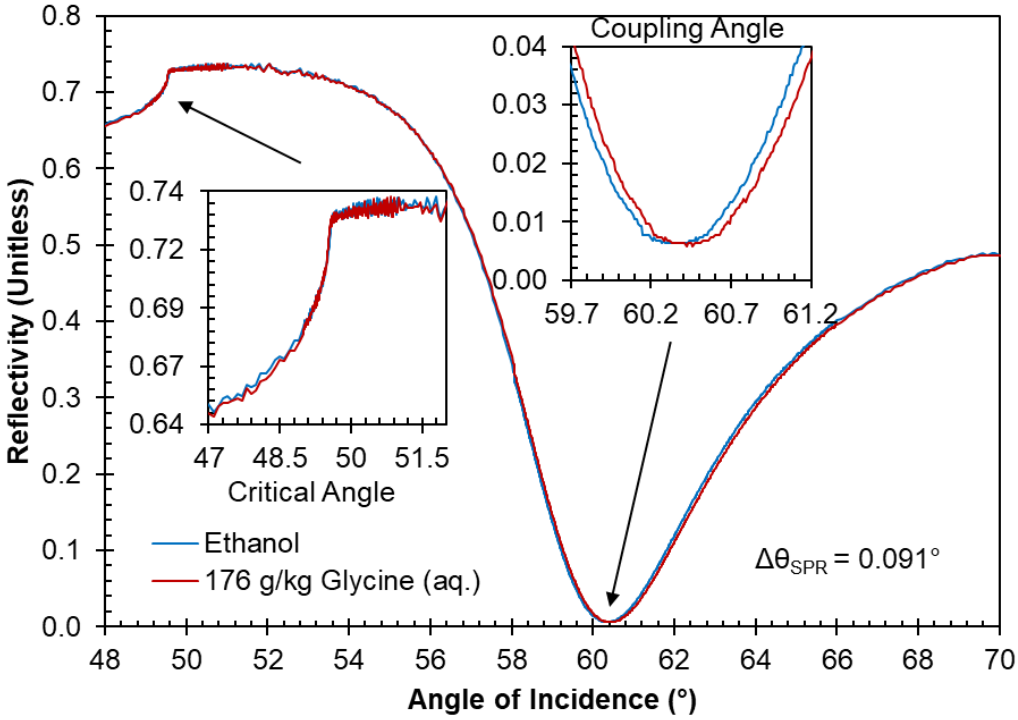

Figure 46: Raw SPR reflectivity scan data for pure ethanol and 176 g/kg glycine (aq.). Figure shows that when a glycine solution is refractive index matched to a reference solvent (ethanol), the position of the SPR coupling angle is at a larger angle than that of

When comparing the SPR coupling angles of both the ethanol and glycine solutions, it is quite apparent that the angles are not the same. This shows that the aqueous glycine solution does not behave as a homogeneous system, as this would require each system’s coupling angle to be the same. This means that we have qualitative observation of concentration enhancement of the solution localised at the gold-solution interface, something which has not previously been assessed or directly observed.

As outlined in section 4.2.3, the order in which solvents and glycine solutions were injected into the flow cell for measurement acquisition was explicit, with solvents entering the cell first in series (based on their miscibility with one another), followed by aqueous glycine solutions in order of increasing bulk solution concentration. As such, it was uncertain whether the order by which liquid is injected into the cell and contacts the gold surface could play a role in the degree of enhancement of the interfacial region permittivity being observed. Consequently, a sensitivity analysis study involving repeat measurements of both ethanol and the corresponding refractive index matched aqueous glycine solution – 176 g/kg bulk solution concentration – was undertaken to challenge both the repeatability and robustness of the measurement procedure and whether it plays any part in the observations made.

Different experimental scenarios were trialled to assess the degree of influence (if any) they had on the position of the SPR coupling angle for both the ethanol and the aqueous glycine solution, as highlighted in Figure 47. This included repeated measurements of ethanol followed by repeated measurements of 176 g/kg glycine (aq.) solution, measurement of ethanol in contact with the gold surface before aqueous glycine solution before alternating between the two solutions and finally placing glycine solution in contact with the gold surface prior to ethanol being injected and then alternating between measurements of each solution. Chip 9 shows repeated measurements where ethanol was placed in contact with the gold surface prior to aqueous glycine solution, whereas Chips 8 and 10 correspond to the addition of glycine solution before ethanol to the flow cell on different gold surfaces.

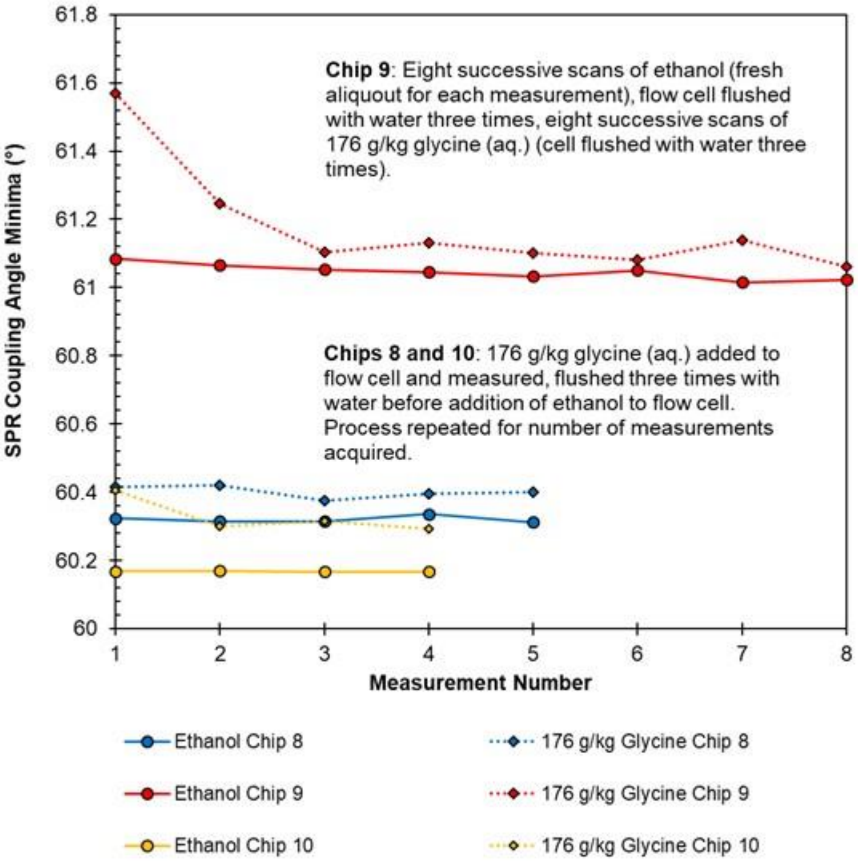

Figure 47: Sensitivity analysis study of repeat measurements of ethanol and 176 g/kg aqueous glycine solution.

Within each respective scenario there was a degree of variation from measurement to measurement. However, irrespective of the order in which ethanol or glycine solution were introduced to the flow cell, the SPR coupling angles of the aqueous glycine solution consistently exceeded that of the ethanol reference measurements SPR coupling angles, thus further substantiating our belief that this difference in SPR angles is solely the result of interfacial concentration enhancement. Furthermore, the minimal variation across trialled scenarios allows us to conclude that the overall order of measurements being changed does not provide any additional effect beyond that which already exists when measuring on different gold surface chips.

4.3.2 Model generation for interfacial layer permittivity determination

Having qualitatively observed interfacial concentration enhancement, models of the experimental system were developed and deployed to provide supporting quantitative evidence. The models were utilised to characterise each respective system measured and provide an estimate as to the difference in interfacial solution layer relative permittivity between solvent systems used as a baseline reference measurement and aqueous glycine solutions which span a 0-250 g/kg concentration range. All experimental measurements performed were modelled using Winspall generated light propagation models. The refractive index of the bulk solution and of the interfacial solution layer were determined by using these models to fit the measured critical angle and SPR coupling angle for each individual experiment.

As noted in section 4.3.1, we see that the SPR coupling angles observed for aqueous glycine solutions do not align with those of a model response for a homogeneous system. However, upon modelling an interfacial layer of glycine solution between the gold surface and the bulk solution with a thickness of 1 nm, we can match the SPR coupling angle of the model system to that of the experimental glycine measurement by increasing the relative permittivity within the 1 nm layer of solution. This then gives a value for the permittivity within the 1 nm interfacial layer which can be attributed to the increased concentration of glycine molecules at the solid-liquid interface relative to the bulk solution.

SPR measurements and corresponding models were then generated for each individual gold chip and relative permittivity's of interfacial solution layers were determined. Repeat measurements of ethanol and its index matched aqueous glycine solution bulk concentration (176 g/kg) are presented in Figure 48 below, whereby comparison of solvent reference measurements and glycine solution measurements in terms of their bulk and interfacial layer permittivity can be performed.

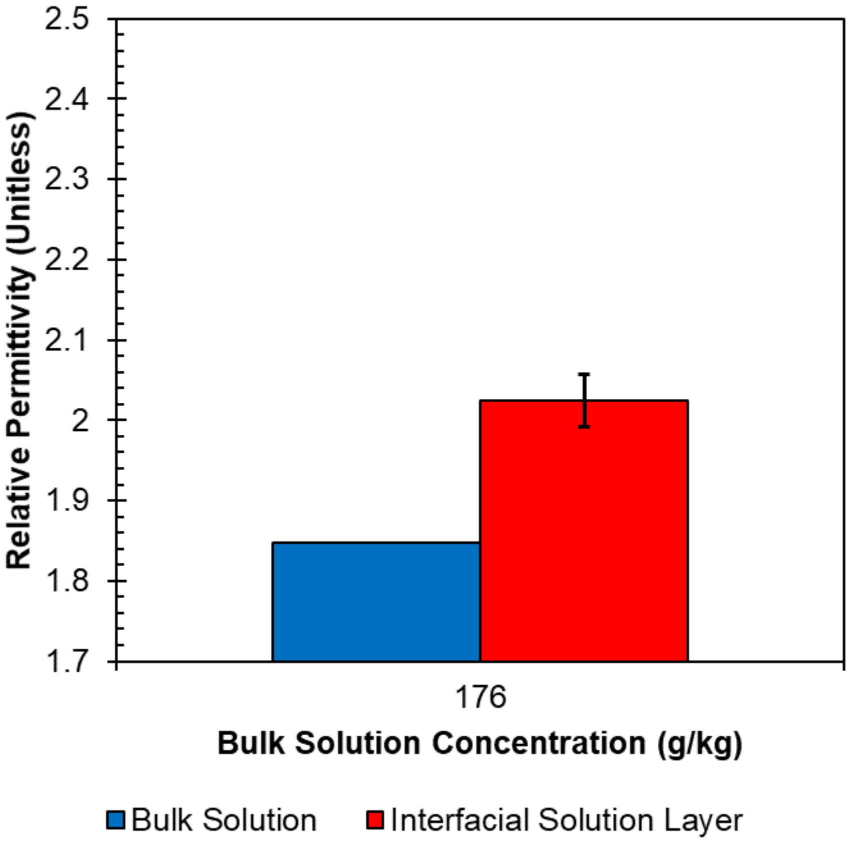

Figure 48: Average surface permittivity observed on gold chip 8, with error bars signifying one standard deviation from the mean. Here, only 176 g/kg aqueous glycine solutions were measured with the corresponding reference solvent – ethanol. The sequence of measurements was five successive measurements of water, followed by five successive measurements of ethanol and finally five successive measurements of aqueous glycine solutions.

Performing repeat measurements on a single gold chip allow us to quantify the degree of variability which could be observed across multiple stages of flushing the flow cell and the influence which repeated measuring of the same solution had on the estimated interfacial layer permittivity. Figure 48 indicates that there is no major influence from the experimental procedure or instrument on the degree of concentration enhancement observed at the solid-liquid interface.

By fitting linear regressions through both the measured bulk solution permittivity and the interfacial layer permittivity values determined through use of the representative model systems, it is possible to quantify the difference in bulk and interfacial solution behaviour by means of their regression slopes. Figure 49 shows one example of such measurements across the solubility range of glycine in water. We can see that the permittivity within the 1 nm interfacial layer clearly exceeds that of the pure bulk solution at isolated concentrations and subsequently the SPR coupling angles has exceeded that of the reference solvent measurement SPR coupling angles. Moreover, this uplift in interfacial layer permittivity with respect to bulk solution permittivity is consistently observed over repeat measurements. This provides clear quantitative evidence for the glycine concentration enhancement at the gold surface.

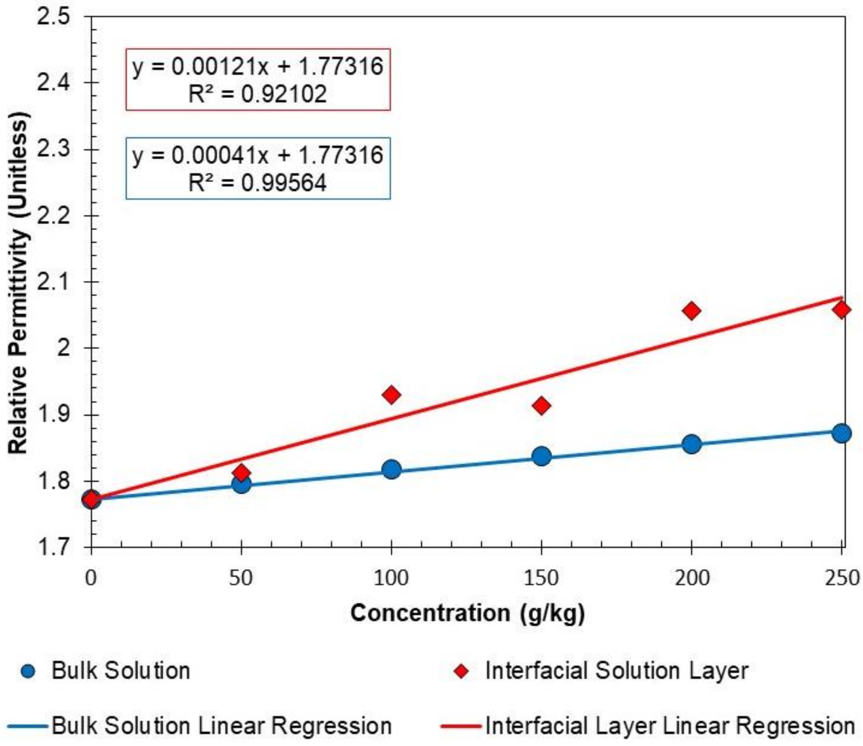

Figure 49: Respective measurements of both the bulk solution and interfacial region for a range of aqueous glycine solutions on gold chip 5.

4.3.3 Chip to chip variability

Having established the presence of a solution region at the solid-liquid interface with permittivity exceeding that of the bulk solution permittivity across a wide range of undersaturated bulk glycine solution concentrations, the next step was to confirm that this effect would be consistently observed across different individual gold chips. Figures 50-60 show the bulk solution permittivity and corresponding interfacial layer permittivity values obtained for gold chips one to eleven, where measurements were either performed once on given solution concentrations across the nominal concentration range, repeated to yield two measurements of a given concentration on a chip, or repeat measurements at given solution concentrations.

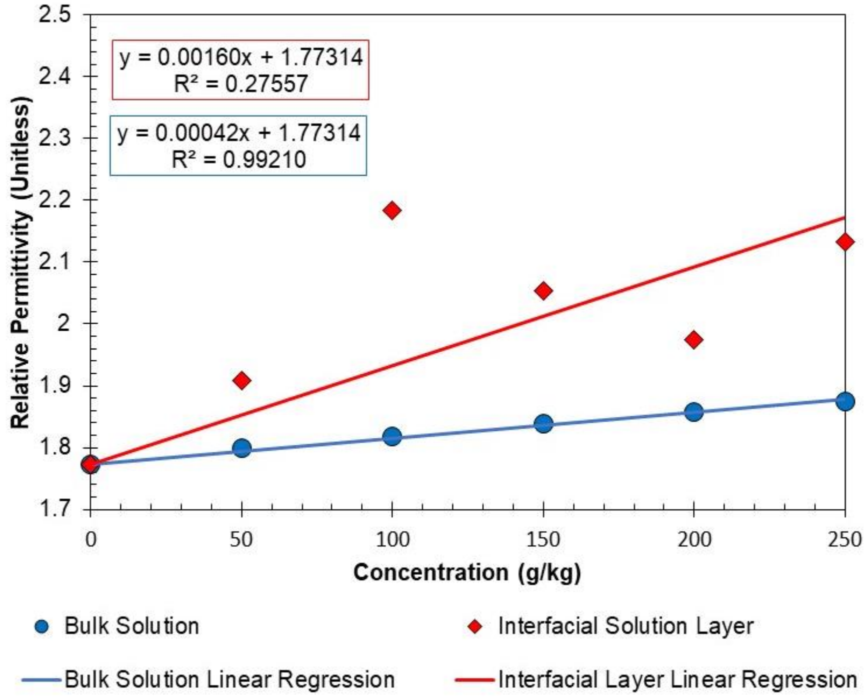

Figure 50: Gold Chip 1, 46 nm gold layer.

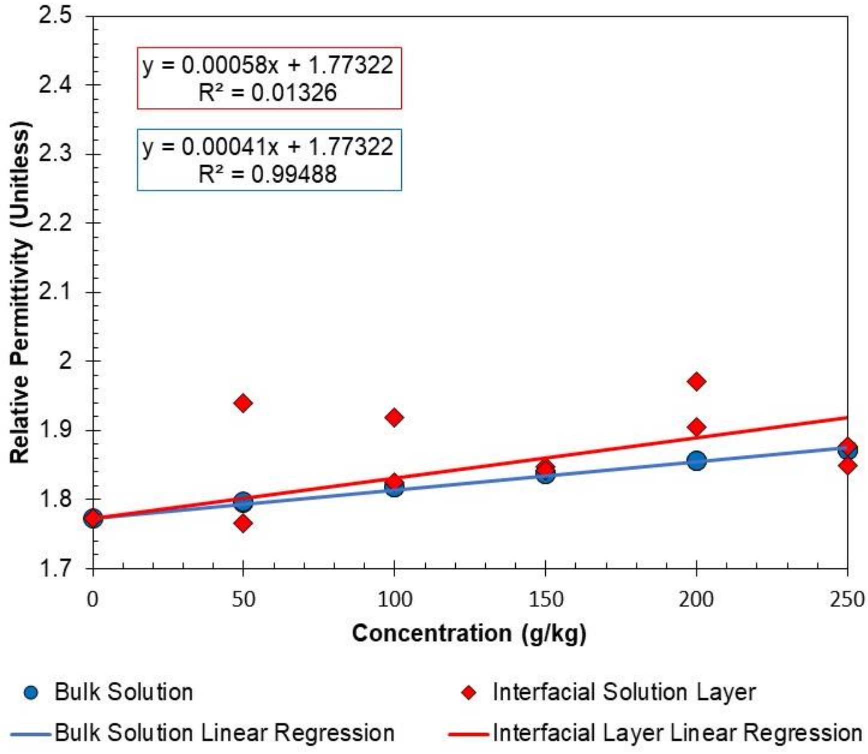

Figure 51: Gold Chip 2, 46 nm gold layer.

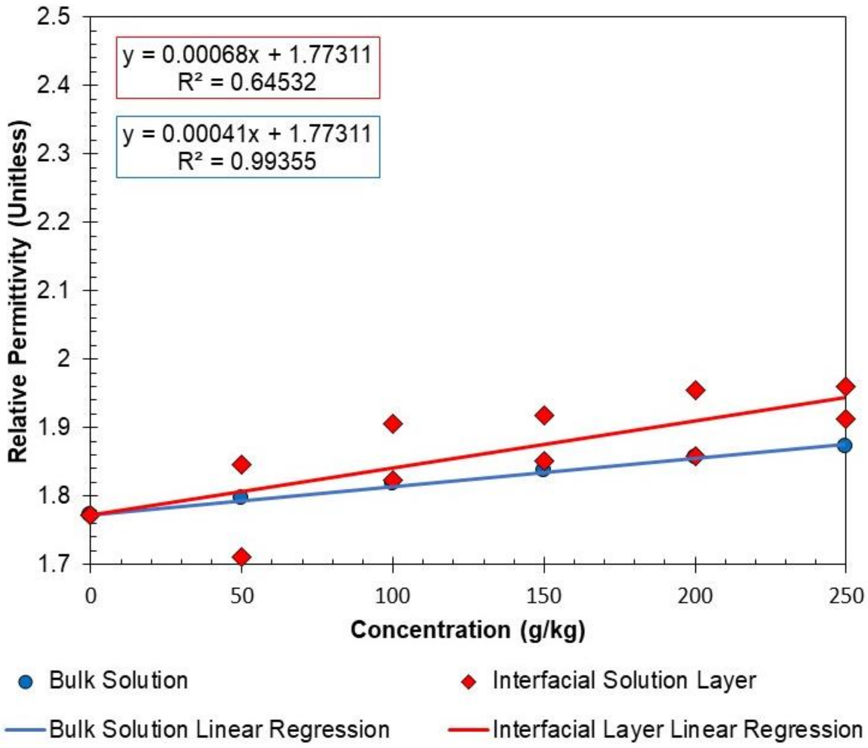

Figure 52: Gold Chip 3, 46 nm gold layer.

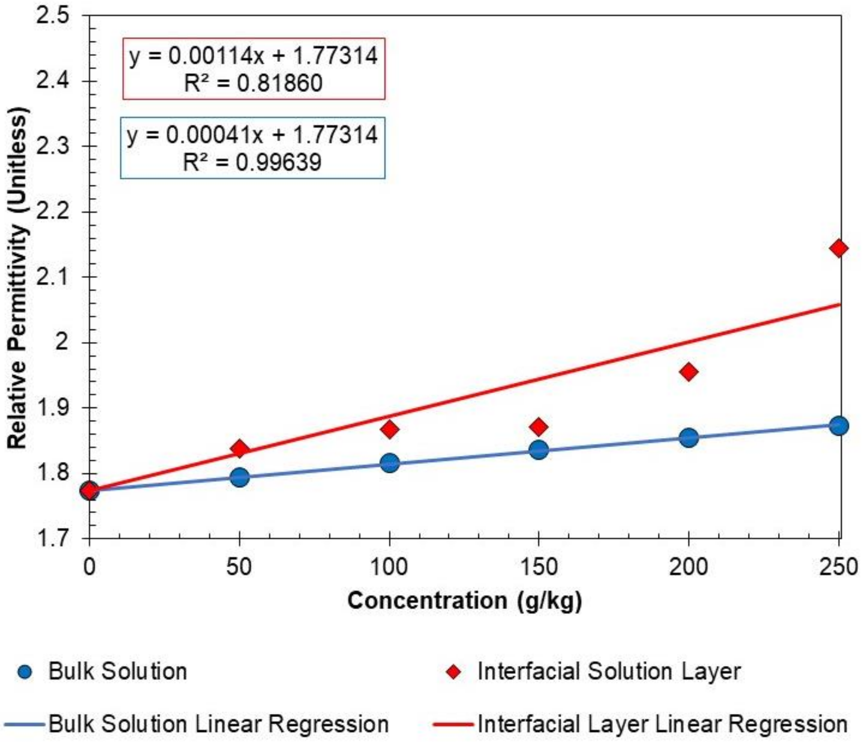

Figure 53: Gold Chip 4, 45 nm gold layer.

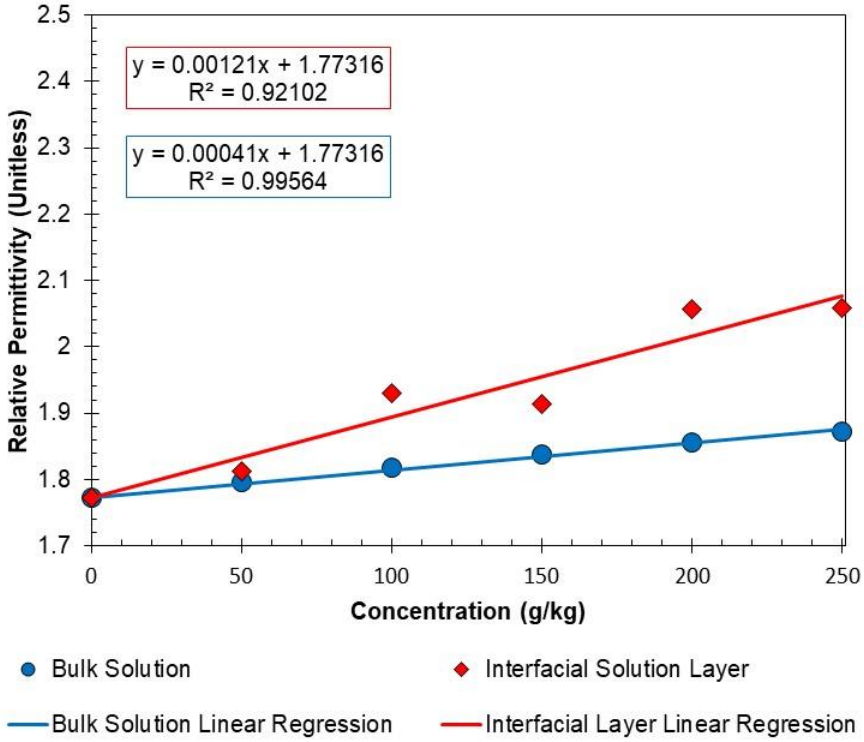

Figure 54: Gold Chip 5, 45 nm gold layer.

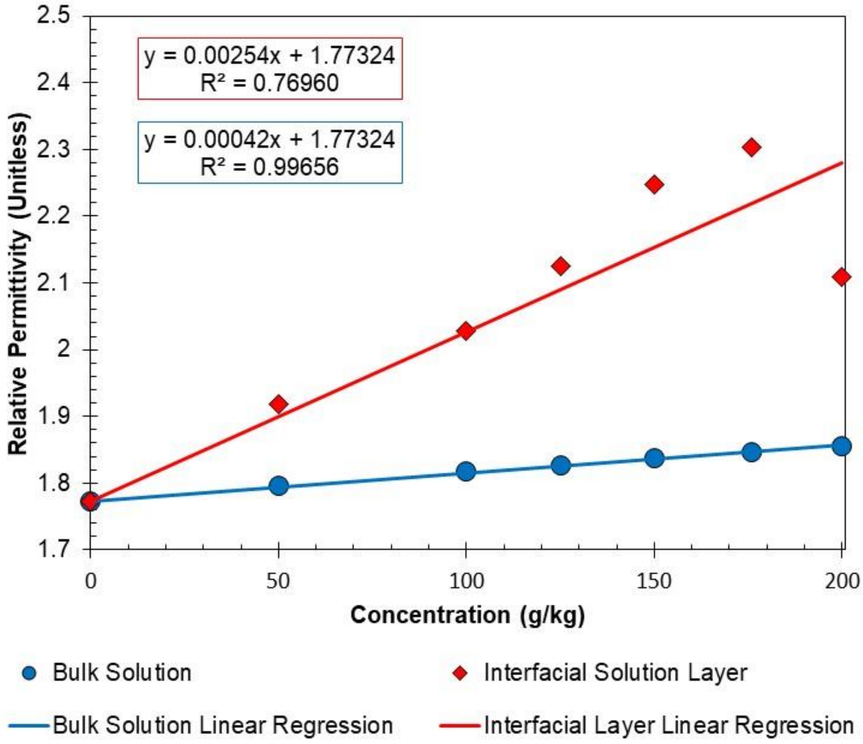

Figure 55: Gold Chip 6, 46 nm gold layer.

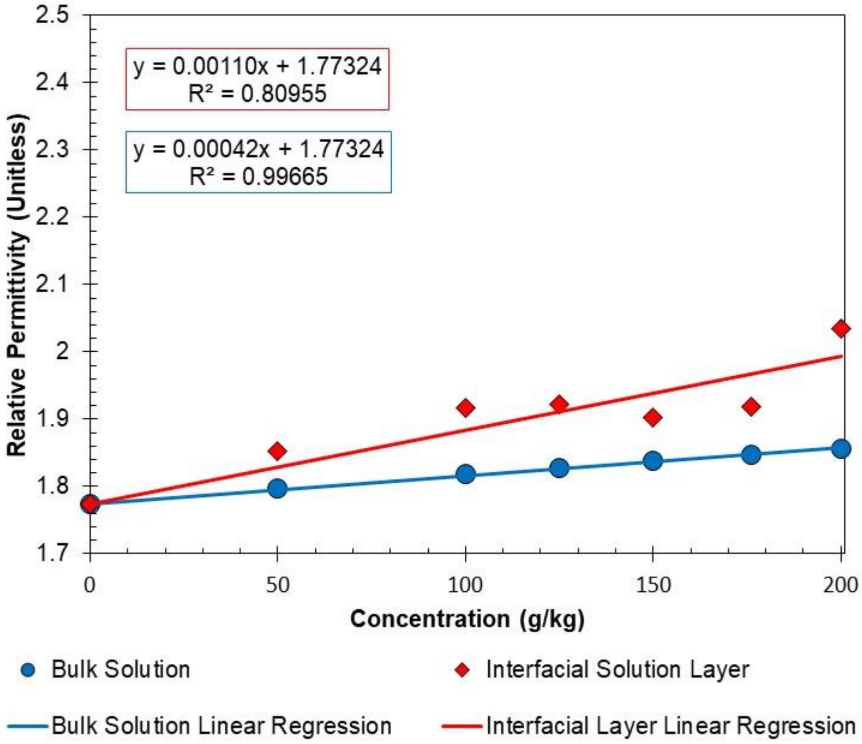

Figure 56: Gold Chip 7, 46 nm gold layer.

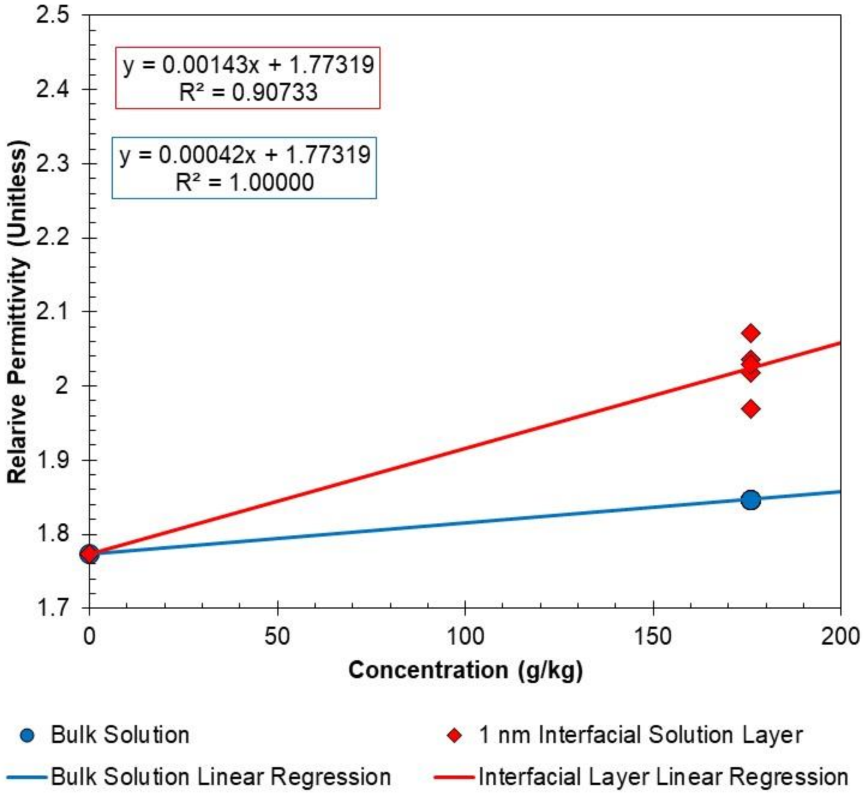

Figure 57: Gold Chip 8, 46 nm gold layer.

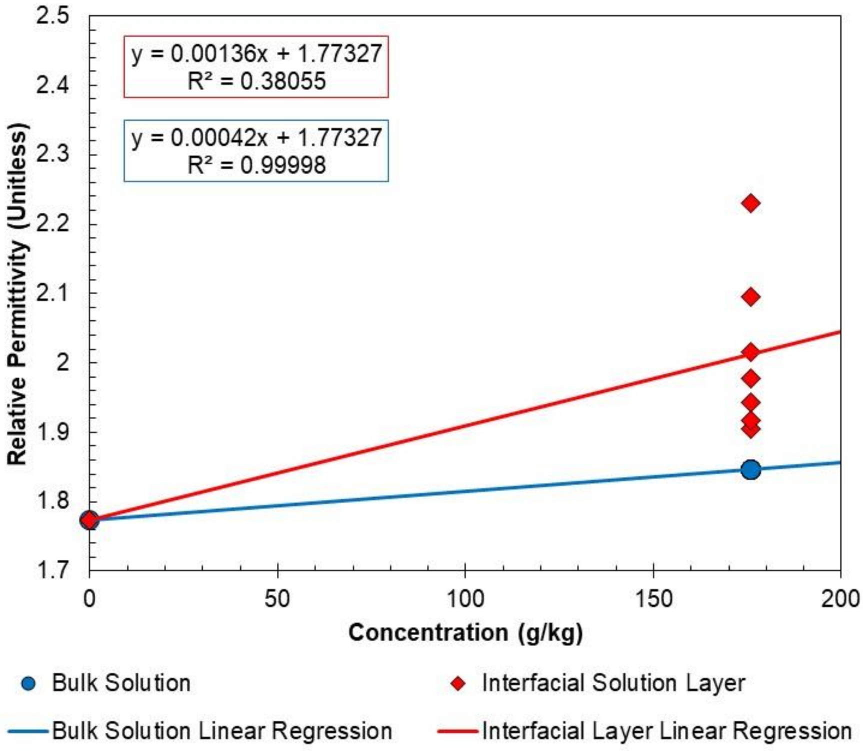

Figure 58: Gold Chip 9, 46 nm gold layer.

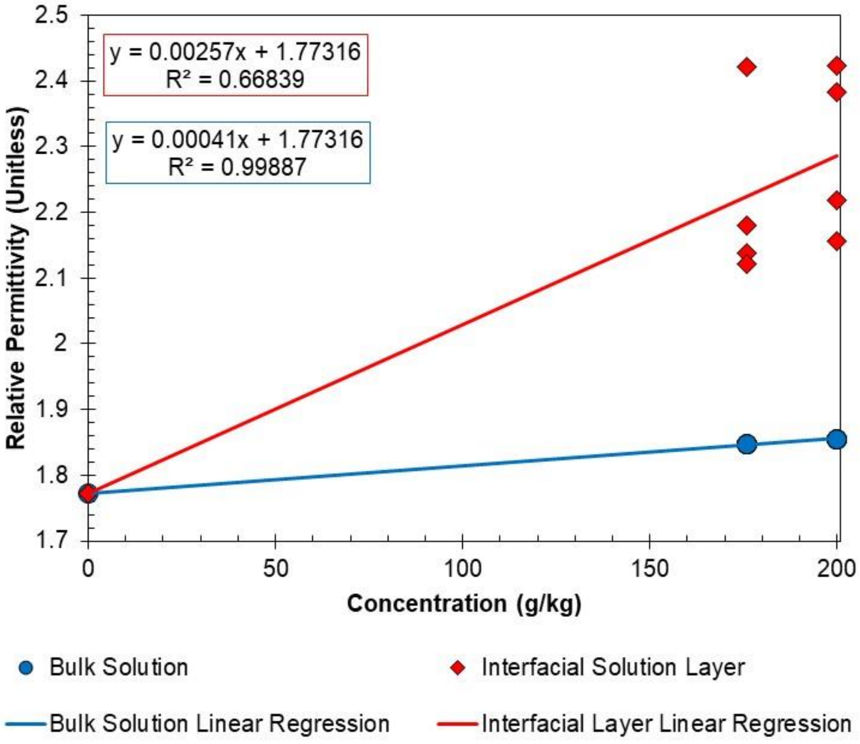

Figure 59: Gold Chip 10, 46 nm gold layer.

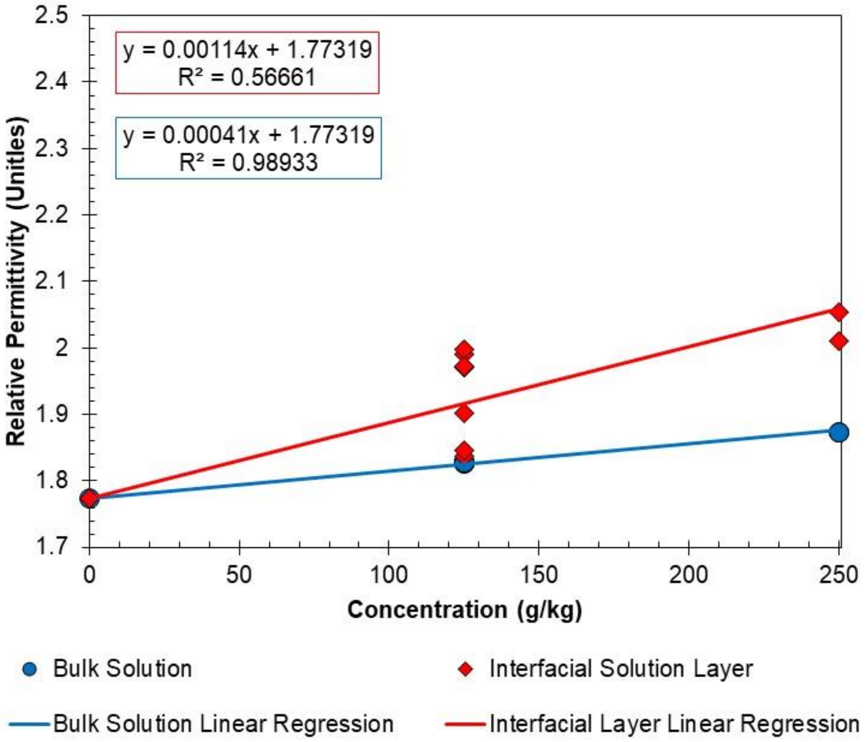

Figure 60: Gold Chip 11, 46 nm gold layer.

Figure 61 shows all recorded measurements across the eleven gold chips of bulk solution permittivity, along with the interfacial solution layer permittivity. In order to collectively analyse the data generated for each gold chip, the slopes of both the bulk solutions and interfacial solution layers can be plotted together, as shown in Figure 62.

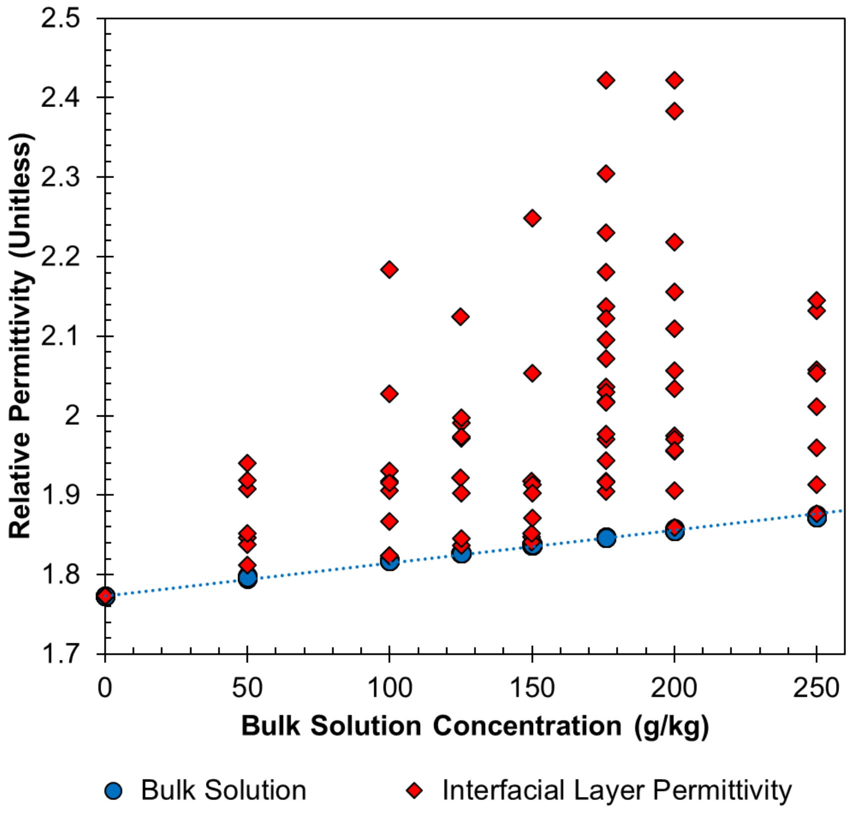

Figure 61: All measurements of aqueous glycine on bare gold chips, with the accompanying interfacial permittivity for a 1 nm interfacial solution layer.

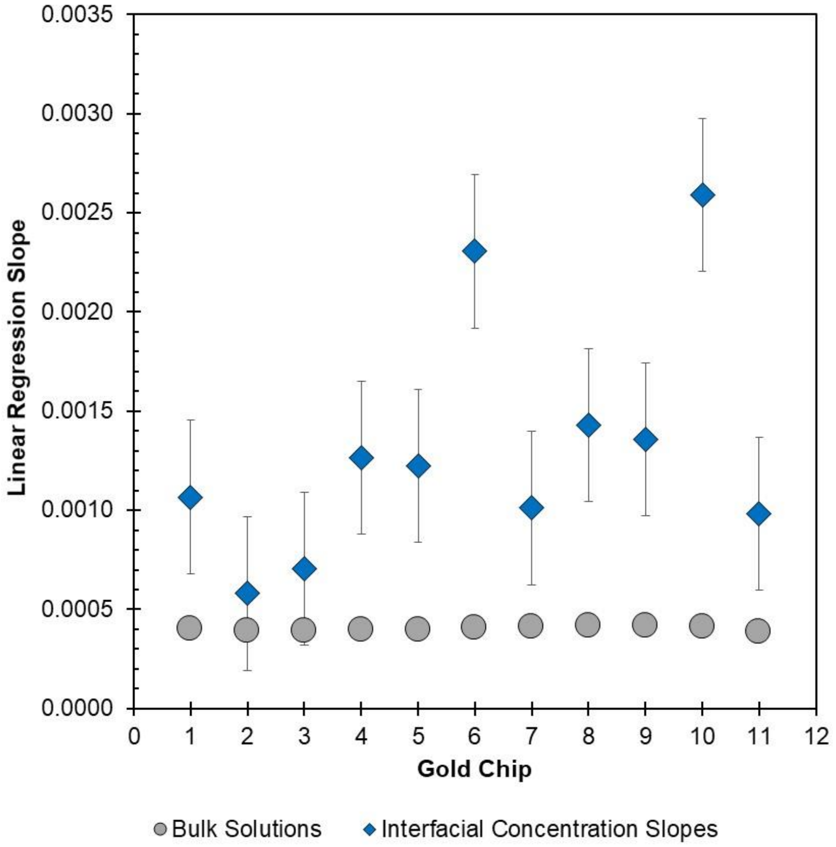

Figure 62: Comparison of bulk glycine solution slopes against slopes for interfacial solution layers. The slopes for bare gold chips are shown, with the error bars signifying the 95% confidence intervals.

Here, it is clear that the slope of each interfacial solution layer consistently exceeds that of the bulk solution measurements for the given gold chips, with the error bars on the interfacial layer slopes indicating the 95% confidence interval on the respective values presented. These statistics are summarised in Table 13 below and further emphasise the presence of the interfacial layer when contrasted with bulk solution measurements.

Table 13: Bulk and interfacial regression slopes for each bare gold chip utilised in this study. Also included are the upper and lower bound 95% confidence intervals.

Chip	Bulk Solution Slope	Interfacial Layer Slope	Upper C.I. (95%)	Lower C.I. (95%)
1	0.00040	0.00107	0.00145	0.00068
2	0.00039	0.00058	0.00097	0.00019
3	0.00039	0.00071	0.00109	0.00032
4	0.00040	0.00127	0.00165	0.00088
5	0.00040	0.00122	0.00161	0.00084
6	0.00041	0.00231	0.00269	0.00192
7	0.00041	0.00101	0.00140	0.00062
8	0.00042	0.00143	0.00182	0.00104
9	0.00042	0.00136	0.00174	0.00097
10	0.00041	0.00259	0.00298	0.00221
11	0.00039	0.00098	0.00137	0.00060

This is one way in which the inherent chip to chip variability of the interfacial solution layer magnitude can be visualised, whereby all measurements on a given chip are collectively grouped by the magnitude of the linear regression slopes. However, it is also possible to describe the variability by presenting the mean relative permittivity measurement for given aqueous glycine solution concentrations across all chips measured.

In Figure 63 we can see that the mean permittivity of the interfacial solution layer across multiple gold chips is higher than the bulk solution permittivity at all glycine solution concentrations. The corresponding statistics are summarised in Table 14. There is a significant chip-to-chip variability in estimated interfacial layer permittivity values, which can be due to microheterogeneity of gold thin layers caused by local defects at grain boundaries. Nevertheless, there is a statistically significant effect in terms of enhancing glycine concentration in the interfacial layer of glycine solutions in contact with gold surface.

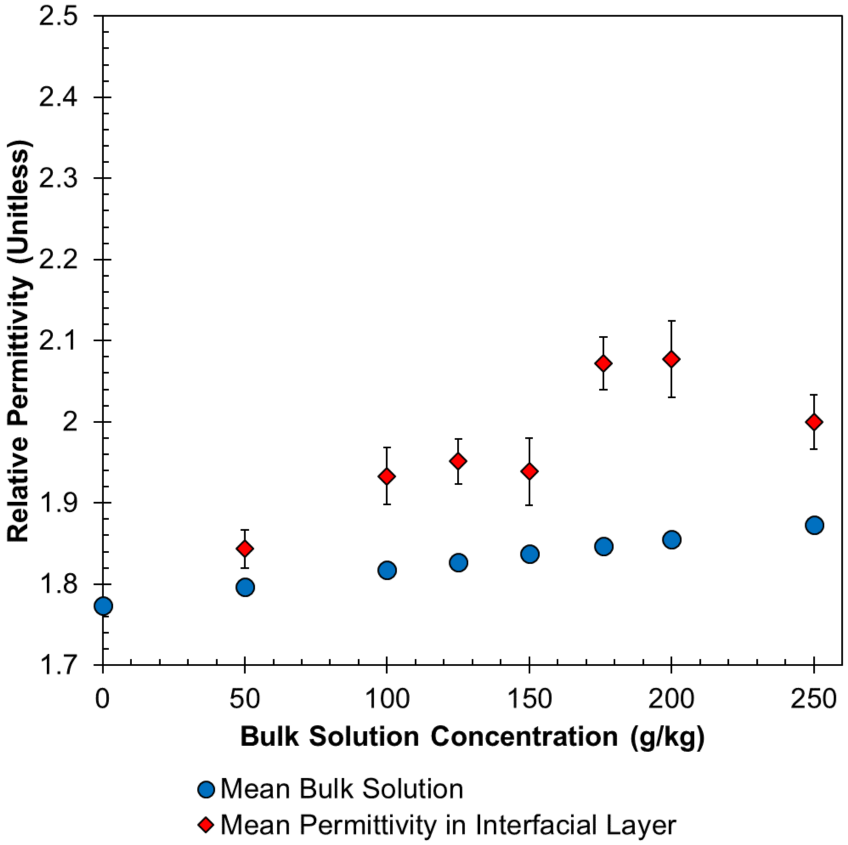

Figure 63: Mean bulk solution measurements across the measured concentration range, along with the mean permittivity within the interfacial layer when L=1 nm. The error bars represent the standard error of the mean.

Table 14: Mean concentration, interfacial layer permittivity, standard deviation and standard error of the mean for measurements of aqueous glycine in contact with a bare gold surface.

$\bar{X}$ Concentration (g/kg)	$\bar{X}$ Bulk Solution ε (Unitless)	$\bar{X}$ Interfacial Layer ε (Unitless)	σ Interfacial Layer	$\sigma_{\bar{X}}$ Interfacial Layer	n
0.000	1.773	1.773	0.000	0.000	10
49.988	1.797	1.843	0.070	0.023	9
99.968	1.818	1.933	0.106	0.035	9
125.074	1.827	1.952	0.083	0.028	9
149.945	1.837	1.939	0.125	0.042	9
175.977	1.847	2.058	0.129	0.031	18
199.993	1.855	2.077	0.169	0.047	13
249.958	1.873	2.000	0.101	0.034	9

The key conclusion is that while variation in the magnitude of interfacial layer permittivity is observed across the gold chips used in this study, there is a clear trend of interfacial layer permittivity exceeding bulk solution permittivity across all solutions concentrations investigated here.

4.3.4 Relating interfacial layer permittivity to concentration

Following both qualitative and quantitative assessment of the interfacial region, the next step is to quantify the interfacial layer concentration with respect to that of the bulk solutions. Given the limited data in the literature for relative permittivity of aqueous glycine solutions and glycine crystal solid forms, a combination of empirical relationships and fundamental physical relationships were utilised to estimate the interfacial layer glycine concentration using the interfacial layer permittivity estimates gathered from SPR measurements reported in section 4.3.3. The steps involved in these calculations are detailed in section 4.2.5.

Through use of the Clausius Mossotti equation, relative permittivity values were estimated for water-glycine mixtures containing solely water (glycine mass fraction of zero) and solely glycine (glycine mass fraction of one). This allowed for a theoretical relationship between glycine mass fraction and relative permittivity to be established from which interfacial layer permittivity values estimated from experimental measurements could be converted to interfacial layer concentrations. The resulting relationship is shown in Figure 64, with a comparison of solution permittivity measurements from this work fitted to the Clausius Mossotti equation and glycine crystal solid form permittivity values reported in previous literature.

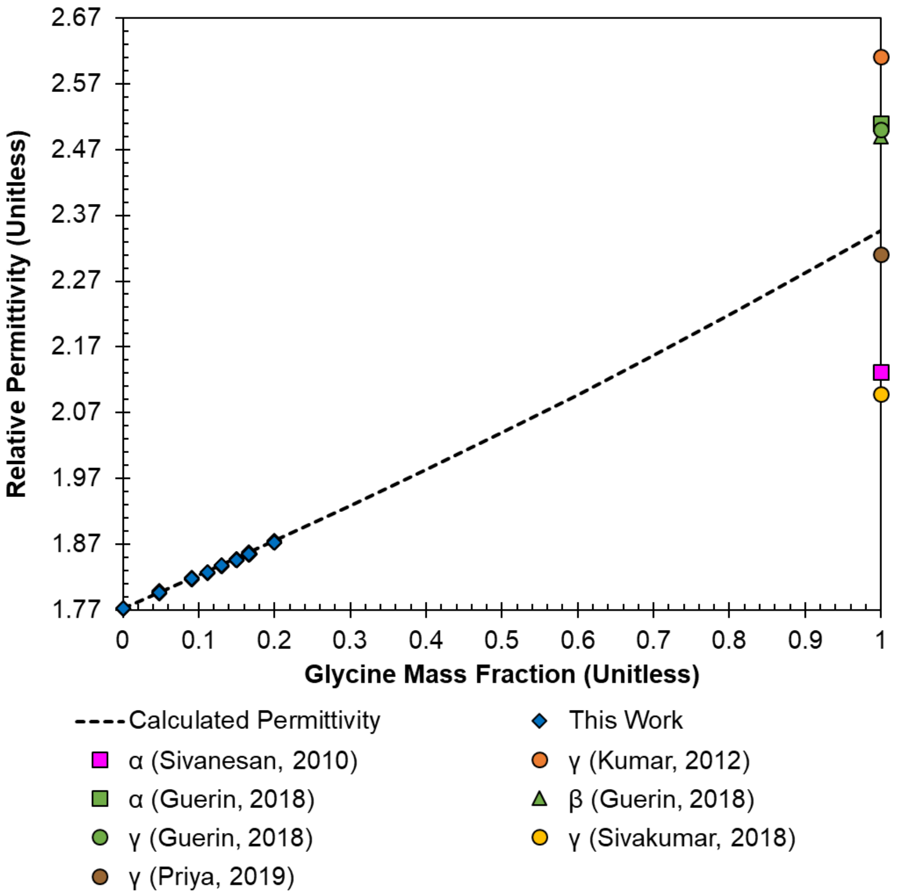

Figure 64: Comparison of idealised permittivity values determined from Clausius Mossotti relationship versus calculated permittivity values based on fitting this work to the Clausius Mossotti equation. Literature data for pure glycine crystal permittivity is also presented for comparison.

A thorough literature search for crystalline glycine permittivity data was undertaken to provide a representation of the solid form when looking to extrapolate from undersaturated glycine solutions to the region where an aqueous solution would be supersaturated. However, the literature values seen in Figure 64 indicate a significant degree of variation in the reported values. (see also Table 15). In addition to the conflicting values reported, it is unclear which solid form would best represent the experimental data and be suitable for extrapolation from undersaturated measurement data. This highlights the need to use the fitted value for pure glycine determined using the Clausius Mossotti equation for interfacial layer concentration estimations.

Table 15: Reported literature values for the relative permittivity of crystalline glycine in its different polymorphic forms.

Source	Polymorphic Form	Relative Permittivity (Unitless)
Sivanesan [89]	α	2.13
Guerin [90]	α	2.51
Guerin [90]	β	2.49
Guerin [90]	γ	2.50
Priya [91]	γ	2.31
Kumar [92]	γ	2.61
Sivakumar [93]	γ	2.10

Through use of the empirical fit from experimental glycine mass fraction versus permittivity data shown in Figure 64, determined using the Clausius Mossotti equation, the corresponding mass fractions for the permittivity values estimated for interfacial layer width of 1 nm across x=0-1 glycine mass fraction range were then determined. A simple conversion then allows for the concentration within the interfacial layer to be calculated on a g/kg concentration basis. Figure 65 shows the resulting representation of interfacial layer concentration versus bulk solution concentration of glycine, highlighting the magnitude of the concentration increase at the solid-liquid interface in contrast to the of the bulk solution.

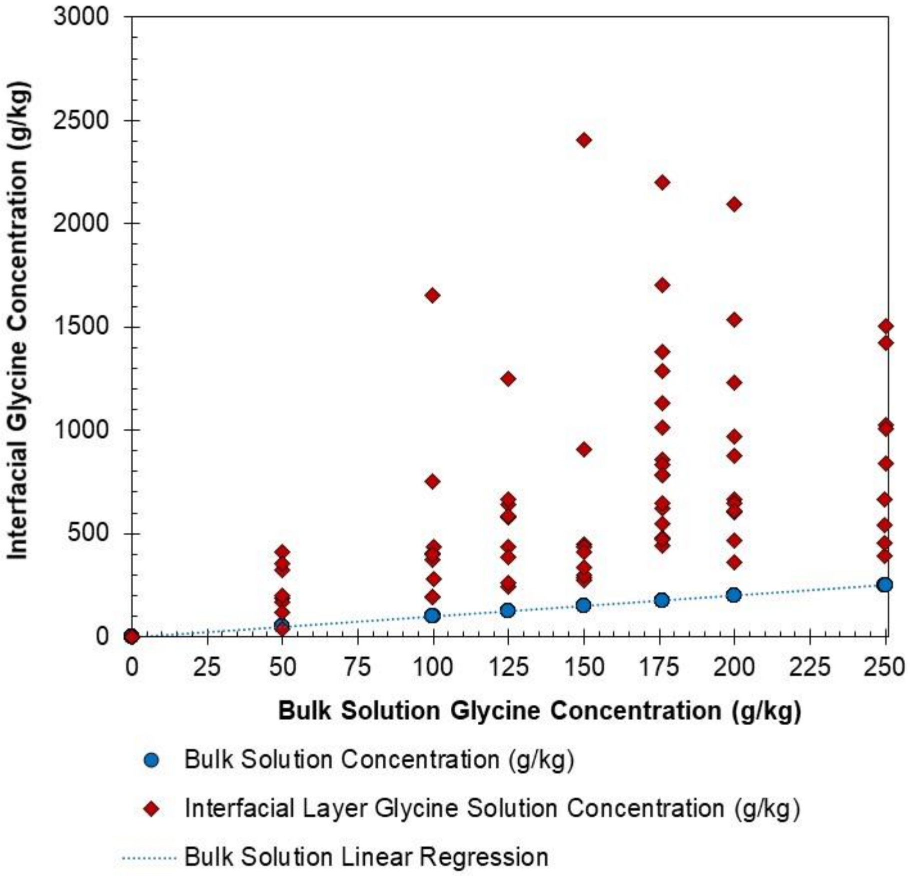

Figure 65: Estimated interfacial layer concentrations for gold chips 1 to 11.

In Figure 66 we can see that the mean concentration of the interfacial solution layer across multiple gold chips is higher than the bulk solution concentration at all glycine solution concentrations. The corresponding statistics are summarised in Table 16.

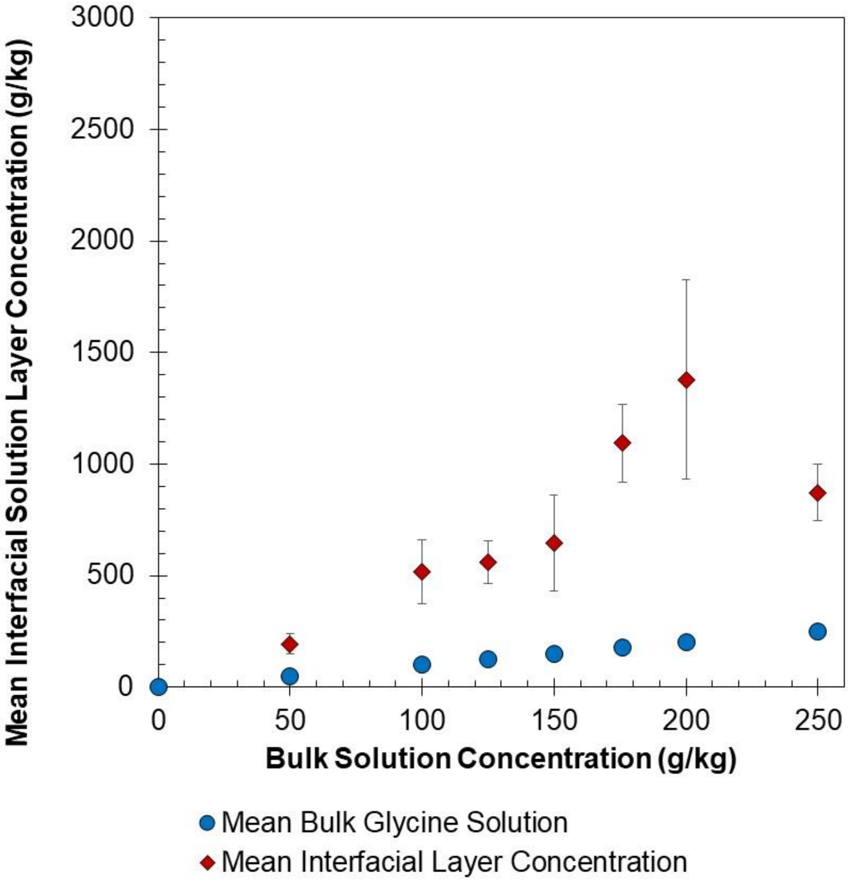

Figure 66: Mean bulk solution concentrations and mean calculated interfacial layer concentrations when L=1 nm. The error bars represent the standard error of the mean.

Table 16: Mean concentration, interfacial layer concentration, standard deviation and standard error of the mean for measurements of aqueous glycine in contact with a bare gold surface.

$\bar{X}$ Concentration (g/kg)	$\bar{X}$ Interfacial Layer Concentration (g/kg)	σ Interfacial Layer (g/kg)	$\sigma_{\bar{X}}$ Interfacial Layer (g/kg)	n
0.000	0.000	0.000	0.000	10
49.988	194.402	140.775	46.925	9
99.968	519.139	430.255	143.418	9
125.074	560.270	285.212	95.071	9
149.945	646.454	648.631	216.210	9
175.977	1094.373	740.697	174.584	18
199.993	1378.616	1609.550	446.409	13
249.958	871.581	380.953	126.984	9

The estimates outlined in Figure 66, while useful in giving an indicative range of expected interfacial region solution concentrations across the assessed bulk solution concentration range, must be viewed with the following key points in mind. The degree of variation for reported interfacial layer permittivity values across gold chips results in considerable uncertainty in the estimates of interfacial layer permittivity, irrespective of the statistical significance these values are shown to have. This uncertainty, when coupled with the uncertainty in the conversion of permittivity to a concentration basis observed through the varied reported literature values for the relative permittivity of pure crystalline glycine, means that the presented results give an indicative range within which the true concentration is expected to lie. However, confidence in the magnitude of the effect presented quantitatively should not be the key takeaway of this representation. Rather, the method by which permittivity estimates are handled and converted to yield an interfacial concentration in this manner shows a means by which the two key uncertainties can be handled currently to yield a qualitative assessment of the interaction between the solution and the solid interface.

These results have a qualitative agreement with molecular simulations that have sought to simulate the interfacial solution layer and its behaviour with both the solid interface and bulk solution layer. However, it is not currently possible to draw a direct quantitative comparison between these results and the work outlined in this chapter due to the uncertainty in estimating the interfacial concentration based on the outlined surface measurements.

4.4 Conclusions

In this work, we have shown how in situ measurements using surface plasmon resonance spectroscopy can be utilised to better understand the behaviour of aqueous glycine solutions when placed in contact with a solid gold surface. By doing so, we aimed to better understand the behaviour of glycine at solid-solution interfaces which is crucial for fundamentals of heterogeneous nucleation.

Through the development of a novel experimental procedure, we have been able to both qualitatively and quantitatively verify a region of enhanced glycine concentration at a solid gold-aqueous glycine solution when comparing this against reference measurements of pure solvents and binary solvent mixtures. This new insight can be rationalised as being due to glycine molecules exhibiting greater dispersion forces when interacting with the gold surface than those exhibited by water molecules.

When performing SPR measurements of aqueous glycine solutions and determining their SPR coupling angle position, this angle is consistently at a higher angle than reference measurements of corresponding reference solvents or their mixtures. This angle difference is indicative of a region at the interface which has a concentration higher than that of the bulk solution upon which measurements are being performed. This can be expressed in terms of the interfacial solution enhancement in a solution region of a certain thickness (e.g. 1 nm) at the solid-liquid interface.

We can represent interfacial concentration enhancement in terms of the relative permittivity within this hypothetical 1 nm thick interfacial solution layer. We can also go further and quantify the glycine concentration within the 1 nm interfacial layer.

When looking at measurements on individual gold chips collectively, a degree of variation is observed in the interfacial solution layer permittivity. We postulate that this is primarily the result of secondary effects which vary on a chip-to-chip basis, such as the polycrystalline nature of gold and the respective surface morphology and topography of individual gold chips on the nanoscale. Irrespective of the degree of variation observed because of such secondary effects, the clear trend shows that interfacial concentration exceeds that of the measured bulk solution concentration across gold chips and bulk glycine solution concentrations assessed. As a result, this work shows that it is possible to probe such interfacial solution layers in situ and to capture interfacial concentration enhancement in solutions, providing new insight into the behaviour of solutions at solid interfaces.

Chapter 5

5. In situ measurements of interface induced concentration enhancement in aqueous solutions of urea

5.1 Introduction

Having observed interfacial concentration enhancement in glycine aqueous solutions in contact with a gold surface outlined in Chapter 4 and finding that it can be both qualitatively identified and quantitatively characterised, these findings were then extended to urea aqueous solutions with the work outlined in this chapter.

The approach used in Chapter 4 was applied to urea aqueous solutions in contact with bare gold chips, to assess how the magnitude of concentration enhancement at the interface may compare to that of glycine solutions for another small molecule system of interest. However, urea has greater solubility in water compared to glycine, which allows for the probing of higher bulk solution concentrations.

Furthermore, the wider solubility range encompasses more pure solvents with a relative permittivity to match urea aqueous solutions for comparative analysis. To achieve this comparison, surface measurements of pure solvents and refractive index matched solutions of aqueous urea were undertaken to generate SPR spectra. Model systems were then generated to assess the degree of enhancement in surface urea concentration being observed with respect to the bulk solution concentration.

5.2 Materials & Methods

5.2.1 Materials

Water (HPLC Plus Grade, Sigma Aldrich), Ethanol (Absolute, Fisher Scientific), Ethyl Acetate (ACS Reagent, ≥99.5%, Sigma Aldrich), 1-Propanol (HPLC Grade, 99.9%, Sigma Aldrich), 1-Butanol (ACS, 99.4+%, Alfa Aesar), Isoamyl Alcohol (98%) and Urea (Reagent Grade, 99.0-100.5%, Fisher Scientific) were purchased and used as received.

5.2.2 Aqueous Urea Solution Preparation

Aqueous urea solutions were prepared across a pure water (hereafter referred to as 0 g_{urea}/kg_{water}) to 878 g_{urea}/kg_{water} concentration range, which will be denoted as g/kg throughout, by combination of urea and water respectively directly within glass vials. The preparation method for each respective aqueous solution was the same.

Prior to solution preparation, vials were washed and subsequently rinsed with HPLC grade water, before drying under a stream of nitrogen gas to exclude the presence of contaminants within the liquid sample. Solutions were then prepared by directly weighing the required amount of urea into a sample vial, followed by the corresponding mass of water to obtain the desired bulk solution concentration.

Sample vials were then sonicated until dissolution in an ultrasonic bath, which was confirmed by visual inspection, before the vials were left to equilibrate with their surroundings. Table 17 below shows the ideal masses of water and urea required to prepare the target bulk solution concentrations necessary for measurements to be performed and the corresponding pure solvent refractive index match for each respective urea solution.

Table 17: Urea solution compositions used in this work along with the accompanying solvent match for each respective concentration, based on their relative permittivity.

Solvent Match	Target Concentration (g/kg)	Target Mass Urea (g)	Target Mass Water (g)
Ethanol	246	2.46	10
Ethyl Acetate	355	3.55	10
1-Propanol	514	5.14	10
Butan-1-ol	727	7.27	10
Isoamyl Alcohol	878	8.78	10

5.2.3 SPR Measurement Procedure

Gold chips, prepared per the protocol outlined in Section 2.3.3, were first mounted on the high refractive index glass prism and fitted with a flow cell configuration for liquid injection to the chip surface. A 3D printed Polytetrafluoroethylene (PTFE) flow cell with inlet and outlet injection points was placed on the prism, before an airtight seal was formed by placing a transparent quartz slide on top of the flow cell. The configuration was secured by screwing a plastic cover piece specific to the configuration onto the top of the glass slide and placed on the stage of the goniometer.

The configuration was aligned to the incident laser beam at a range of angles in air (20, 45- and 60-degrees angle of incidence) to ensure a complete and accurate reflectivity scan was able to be generated and then subsequent calibration SPR measurements were performed on the surface in air (no liquid present in the flow cell) and water.

Pure component solvents and aqueous urea solutions were placed in contact with the gold surface by injection to the 3D printed flow cell for steady state measurements. For each sample solution analysed, an aliquot of liquid (269 μL) was injected into the flow cell using a syringe, with the injection points sealed using pipette tips. Temperature readings were collected throughout the data acquisition process through use of the datalogger thermometer.

Following calibration, measurements of pure solvents were performed. The flow cell was first flushed out with the sample of interest in triplicate to ensure only the sample of interest was present in the flow cell, before being held in the flow cell (3 minutes). A measurement was then acquired, with the flow cell flushed out three times with the next liquid of interest. Having completed measurements on pure solvents and binary solvent mixtures, the flow cell was flushed out with water before measurements of aqueous glycine solutions were acquired. Following acquisition of a solution on interest, the flow cell was flushed with water three times before addition of the next solution of interest.

Experimental measurements were obtained in a defined sequence based on the above description, whereby pure solvent measurements on gold surfaces were undertaken prior to the introduction of aqueous urea to the flow cell for measurements to be carried out. Upon completing a set of measurements, the glass slide and flow cell were then removed from the prism and cleaned by immersion in 1% Hellmanex-water solution and rinsed with water to ensure the setup was free of contaminants.

Experimental scan data was acquired through a user interface utilising the LabVIEW software platform. This interface allows for reflectance scans to be generated (which plot angle of incidence versus reflectance detected by photodiode detector), which can then be imported into the Winspall program for analysis. The procedure is summarised in Figure 67.

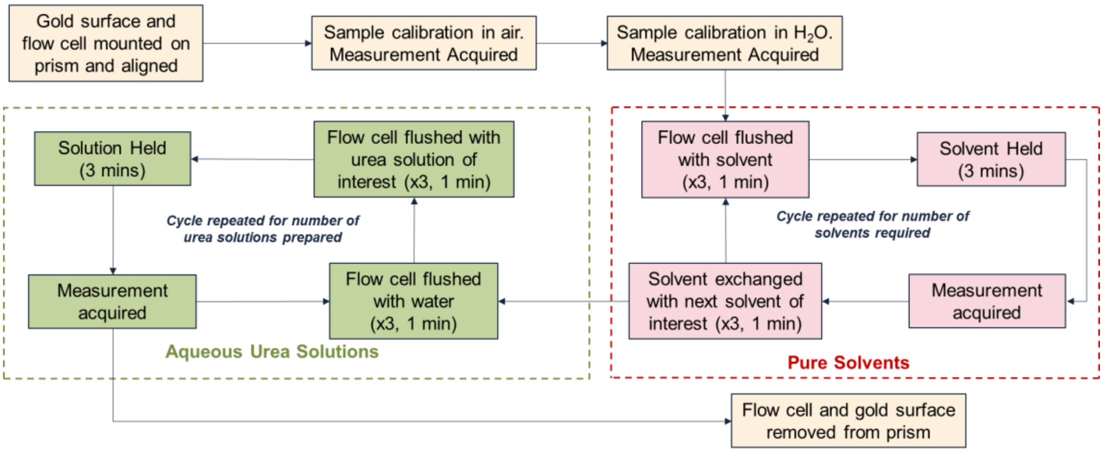

Figure 67: Experimental workflow developed for SPR measurement of both pure solvents and aqueous urea solutions in contact with a bare gold chip.

5.2.4 SPR Model Generation

The procedure followed to generate representative model systems for both pure solvent measurements and aqueous urea solutions is identical to that of the glycine measurements described in Chapter 4.2.5, with the difference being the use of aqueous urea as opposed to aqueous glycine solutions.

A step-by-step schematic outlining the procedure followed to generate representative SPR models is shown in Figure 68 below.

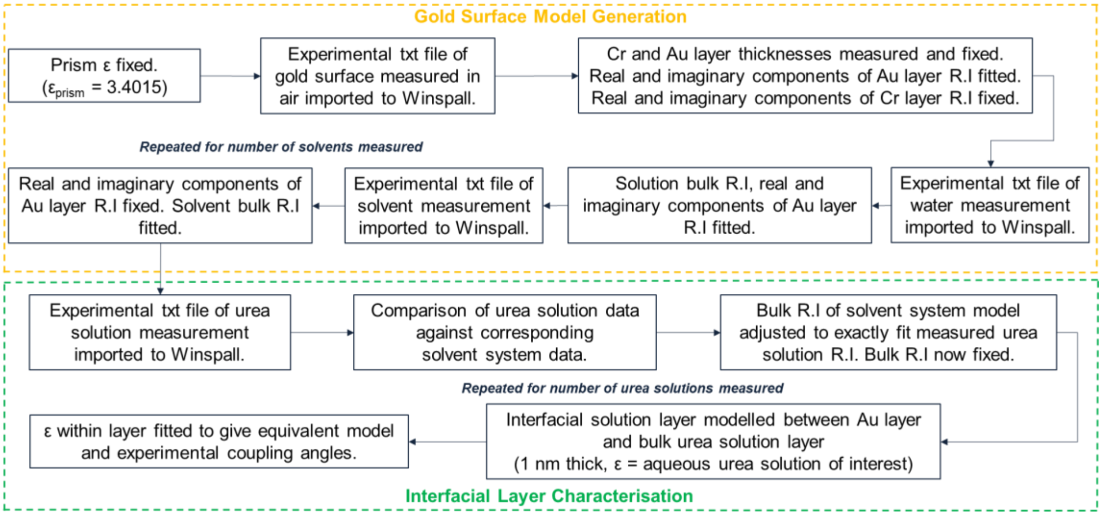

Figure 68: Workflow protocol followed to generate representative SPR models for experimental measurements in order to characterise the interfacial layer permittivity with respect to that of the bulk solution.

5.3 Results & Discussion

5.3.1 Raw Angular Reflectivity Measurements

In order to establish a working concentration range for in situ measurements of urea to be performed within, an extensive literature search was first performed in order to obtain concentration-relative permittivity data.[94-96] The sourced data then served as a comparison by which this work could be assessed to determine if the permittivities being observed for set concentrations at a given temperature fell in line with other work which has been published in the literature, as shown in Figure 69 below.

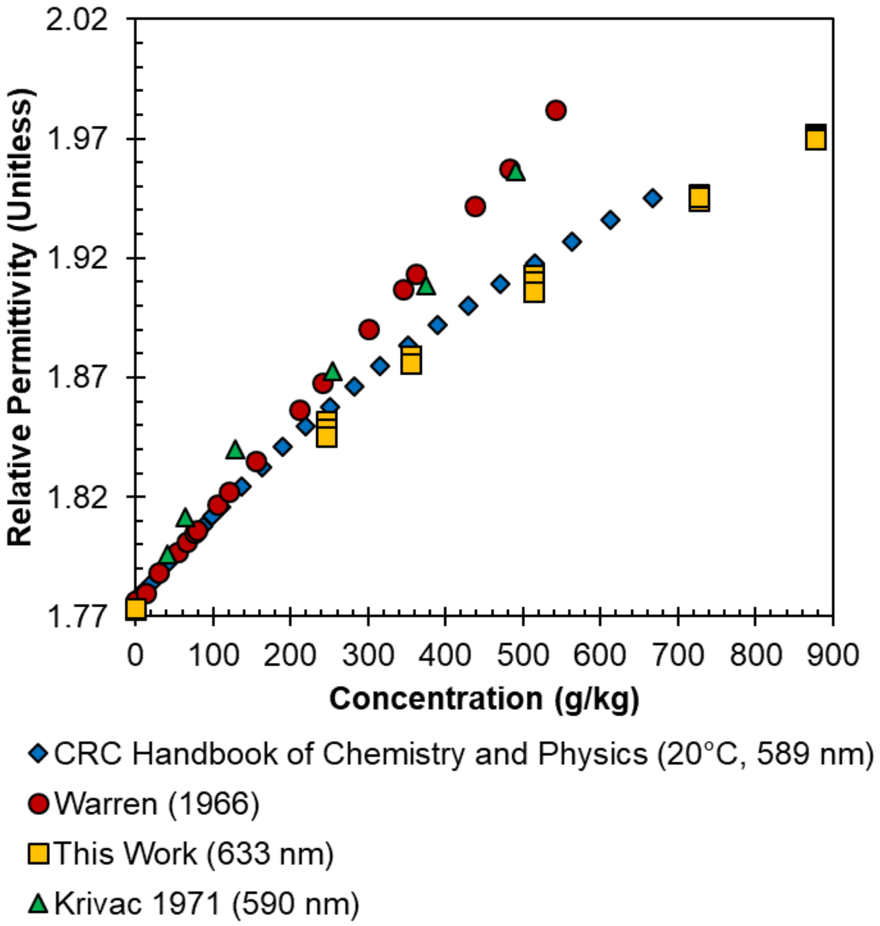

Figure 69: Comparison of permittivity measurements made in this work against those sourced from literature. Literature data is split into two groupings, which have markedly different permittivity values as shown in the magnified plot.

It is seen from the comparison of permittivity data generated in this work with reported literature data that there are conflicting reports of what the true relative permittivity may be across urea solubility limit in water. It should be noted that the reported literature data is captured using a lower light wavelength (589 or 590 nm) or with no reported light wavelength, whereas this work utilises a 632.8 nm light source. As a result, it is again important to be mindful of the influence this has on the generated permittivity data.

However, the conclusions of chapter three highlighted that while light wavelength and temperature can impact the observed bulk solution permittivity, the observed contradiction between the two bandings of permittivity data in Figure 69 far exceeds the difference which may be likely to observe as a result of data captured at different experimental conditions. As such, the permittivity data collected in this work and its internal consistency is deemed appropriate. Raw SPR spectra of aqueous urea solutions are shown across the solubility range of urea in water in Figure 70 below.

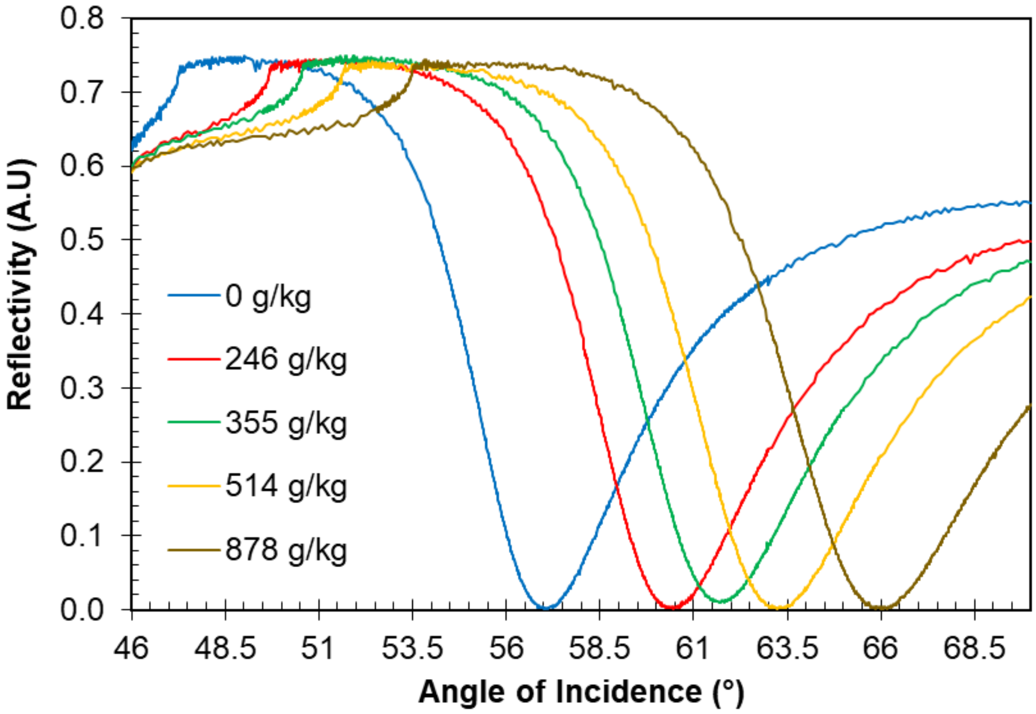

Figure 70: Raw SPR spectra of aqueous glycine solutions across the solubility range of glycine in water (g/kg basis) measured on gold chip 2.

Having compared measurements of aqueous urea solution against literature data, solvent reference measurements and measurements of aqueous urea solutions were performed. These measurements were then compared to assess whether interfacial concentration enhancement was being qualitatively observed by means of a difference in the SPR coupling angle minima. Figure 71 shows the raw SPR spectral responses of an aqueous urea solution (246 g/kg, the concentration which yields a refractive index matched to ethanol) compared against an SPR scan of pure ethanol, with Table 18 showing the relevant critical angles and coupling angle minima.

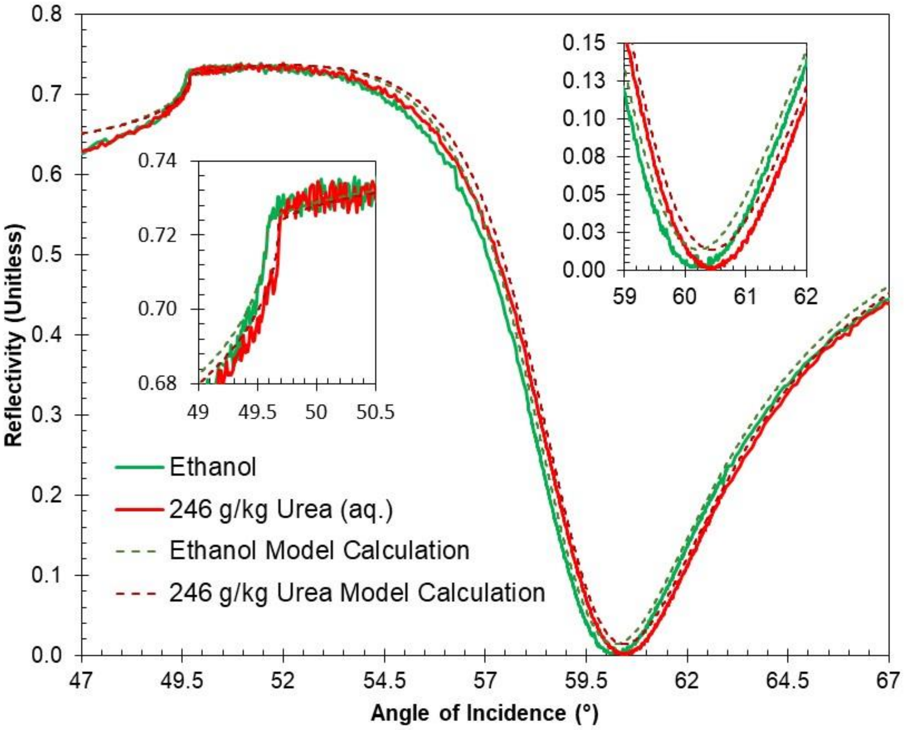

Figure 71: Raw SPR reflectivity scan data for pure ethanol and 246 g/kg urea (aq.). Figure shows that when a urea solution is refractive index matched to a reference solvent (ethanol), the position of the SPR coupling angle is at a larger angle than that of the reference measurement.

Table 18: Measured and calculated relative permittivity, critical angle and SPR coupling angle minima for ethanol and 246 g/kg aqueous urea, and the difference between the observed variables

Parameter/Measured System	Ethanol	246 g/kg Urea	Difference
Measured Relative Permittivity (Unitless)	1.8481	1.851	0.003
Measured Critical Angle (°)	49.59	49.67	0.080
Measured SPR Coupling Angle (°)	60.22	60.44	0.220
Calculated Critical Angle (°)	49.59	49.68	0.090
Calculated SPR Coupling Angle (°)	60.22	60.44	0.220

Figure 71 shows an example for which the relative permittivity of the prepared aqueous urea solution was slightly mis-matched from the ethanol reference measurement at the time of measurement. This difference in relative permittivities was explicitly included in the Winspall model and therefore it does not have any influence on the difference in coupling angles, which are also shown in Table 18. Ranges were added to the inset graphs. However, this highlights that SPR angle shifts are not the result of uncertainty in the measured gold permittivity values or bulk solvent permittivity, as the SPR coupling angle minima for urea would still exceed the ethanol reference measurement if they were equivalent.

When comparing the SPR coupling angle minima of both the ethanol and urea solutions, the angle minima are not the same. This observation qualitatively confirms that the concentration of urea at the solid-liquid interface differs from that of the bulk solution. This supports the findings highlighted in chapter four for aqueous glycine solutions, whereby interfacial concentration enhancement can be highlighted due to the coupling angle minima mismatch between reference solvent measurements and urea measurements.

5.3.2 Chip to chip variability

Following qualitative confirmation of interfacial concentration enhancement, representative models were generated in order to quantitatively determine the uplift in interfacial region permittivity with respect to that of the bulk solution permittivity. Models were generated for each of the six gold chips upon which measurements were performed, with the observed bulk and interfacial region permittivity values presented in Figure 72 below.

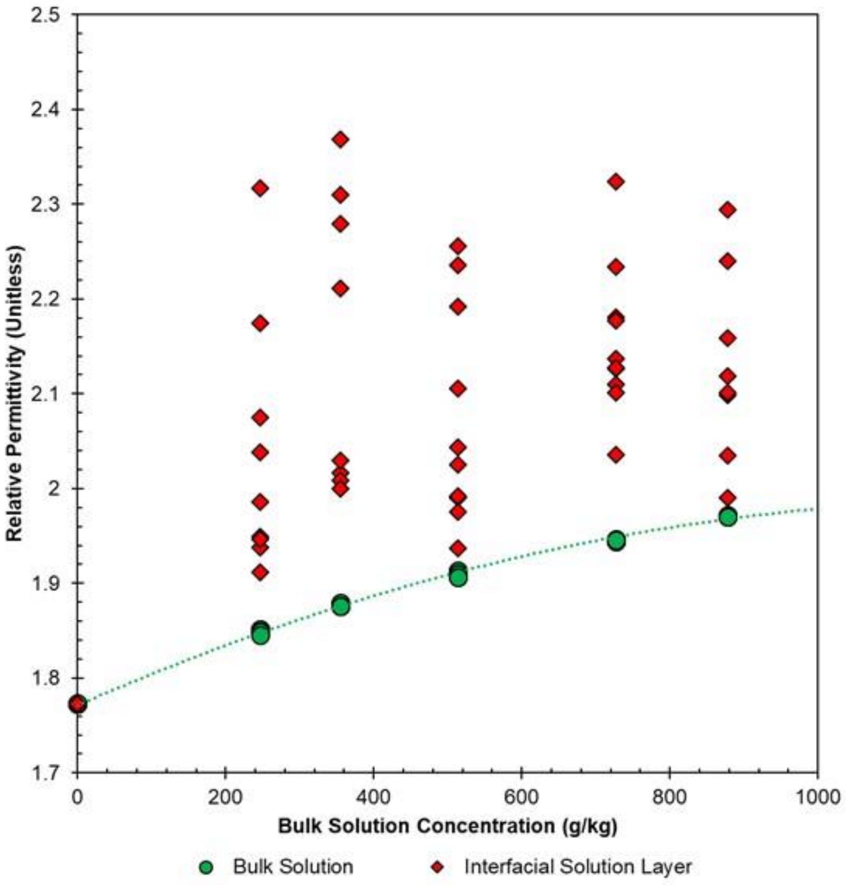

Figure 72: All measurements of aqueous urea solutions and corresponding interfacial region permittivity observed across all six chips utilised.

When looking at the measurements collectively from all chips utilised, we see a large spread of interfacial region permittivity values, with no clear trend beyond the fact that interfacial region permittivity exceeds that of bulk solution permittivity. Consequently, the influence of chip to chip variability, as was encountered in chapter four, must again be looked at in order to rationalise these observations with greater certainty.

Figures 73-77 show the bulk solution permittivity and subsequent interfacial region permittivity values obtained using model systems for chips one to five, upon which a range of urea solutions were measured. Chips 1,2 and 3 all appear to have similar observed interfacial region permittivity values, with chips 2 and 3 being particularly similar.

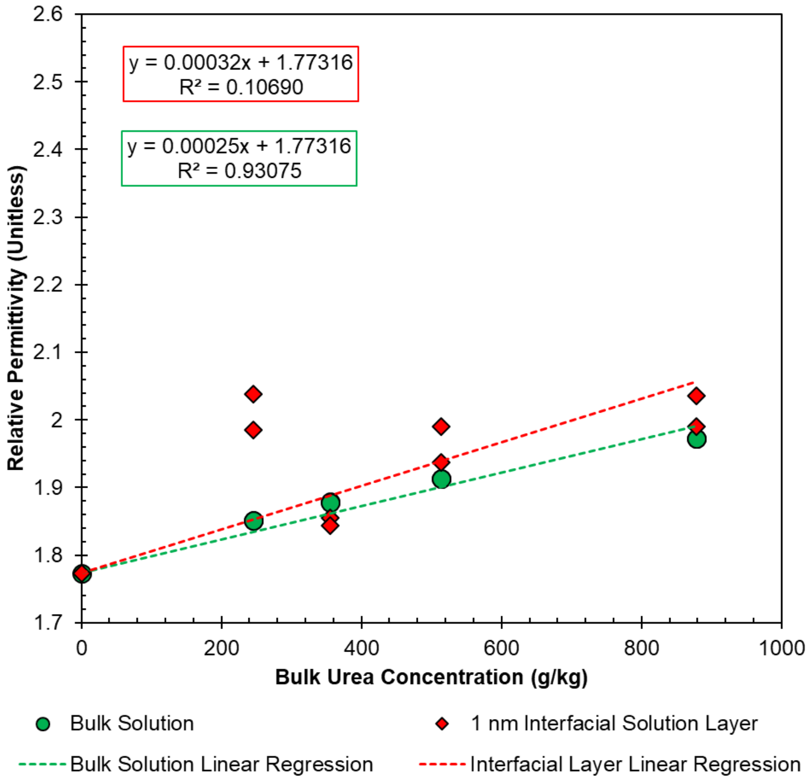

Figure 73: Gold chip 1, 46 nm thick gold layer.

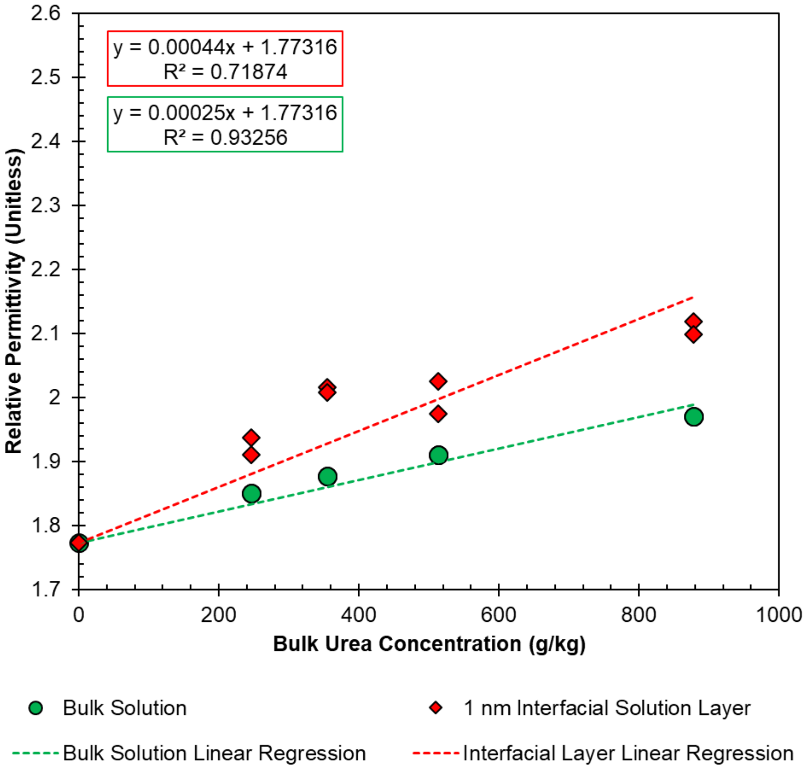

Figure 74: Gold chip 2, 58 nm thick gold layer.

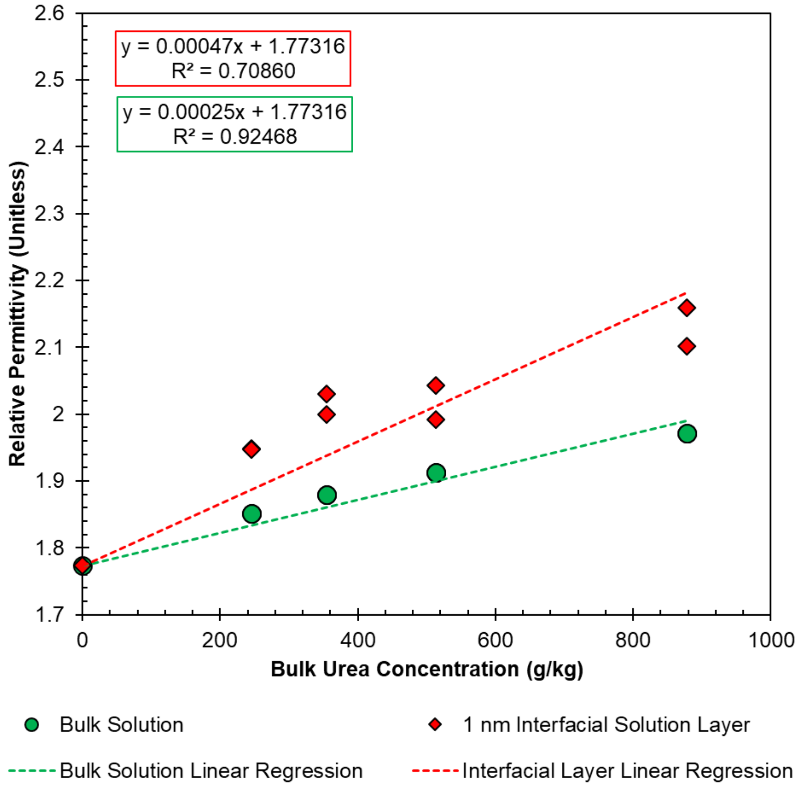

Figure 75: Gold chip 3, 58 nm thick gold layer.

On first inspection, this similar level of enhancement may appear to have a causal link, as chips 2 and 3 have the same gold layer thicknesses (58 nm) as one another. However, chip 4 has the same gold layer thickness as these chips and the observed enhancement is greater, which suggests that gold layer thickness does not directly influence the degree of surface urea enhancement with respect to the bulk solution concentration. Chip 5, similarly to chip 4, sees a higher interfacial region permittivity across the concentration range of interest in contrast to chips 1 to 3.

Instead, the variability is most likely the result of multiple factors inherent to the measurement technique, while probing significant concentration changes in high concentration solutions.

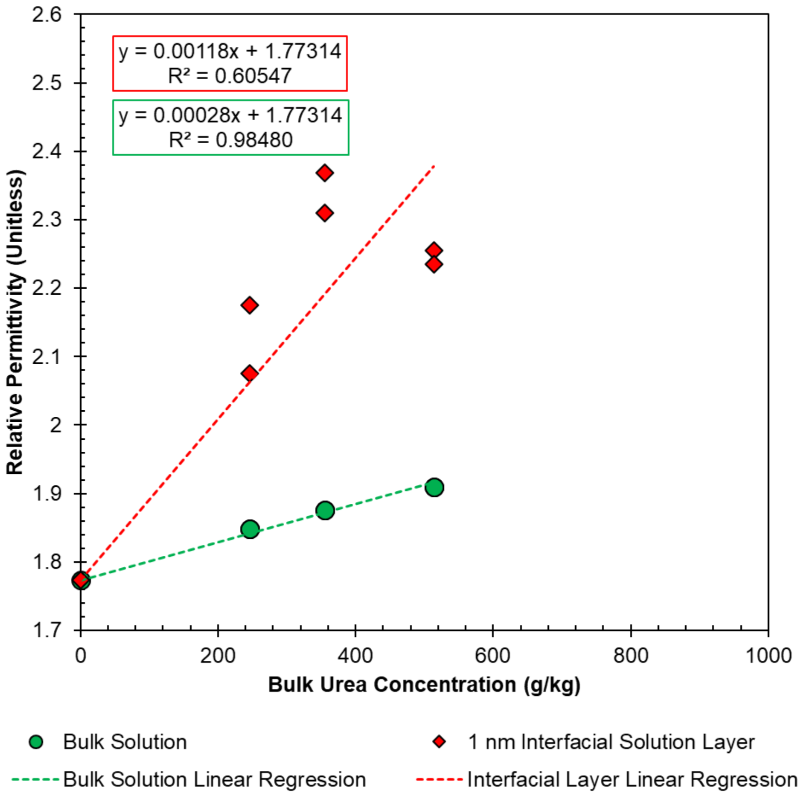

Figure 76: Gold chip 4, 58 nm thick gold layer.

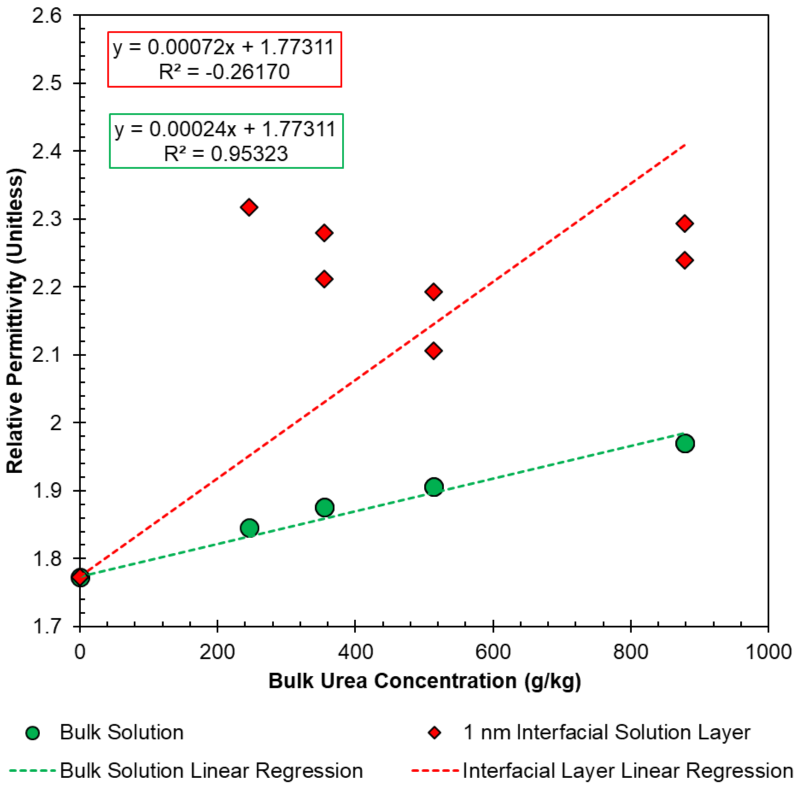

Figure 77: Gold chip 5, 61 nm thick gold layer.

Having highlighted in chapter four that chip to chip variability in the degree of interfacial region permittivity is prevalent across all measurements performed, the degree of variability for measurements of aqueous urea solutions was assessed. A comparison of all chips collectively is possible by comparing the magnitude of the slope for each line of best fit against the respective bulk solution slope. This can then be extended to compare all chips in order to establish the degree of variability observed. Figure 78 provides such a representation, with the error bars signifying the 95% confidence interval for the slopes of the interfacial permittivity fits and associated statistics shown in Table 19.

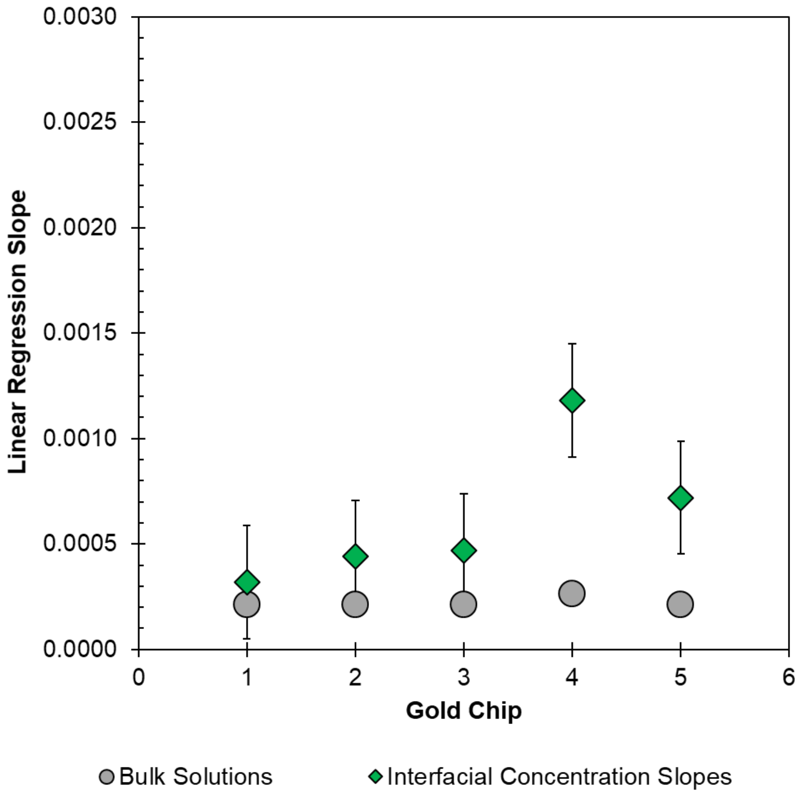

Figure 78: Comparison of bulk urea solution slopes against slopes for interfacial solution layers. The slopes for bare gold chips are shown, with the error bars signifying the 95% confidence intervals.

Table 19: Bulk and interfacial regression slopes for each bare gold chip utilised in this study. Also included are the upper and lower bound 95% confidence intervals.

Chip	Bulk Solution Slope	Interfacial Layer Slope	Upper C.I. (95%)	Lower C.I. (95%)
1	0.00025	0.00032	0.00060	0.00005
2	0.00025	0.00044	0.00071	0.00017
3	0.00025	0.00047	0.00074	0.00020
4	0.00028	0.00118	0.00145	0.00091
5	0.00024	0.00072	0.00099	0.00045

The magnitude of the interfacial slope across four of the five chips is broadly of the same magnitude, with chip four appearing to be an outlier with regards to the rest of the dataset. However, this can be explained as likely being due to the measurements on this chip only covering four of the five urea solution concentrations measured on the four other gold chips. Had measurements of 878 g/kg urea solutions been performed on this chip, it may be the case that the magnitude of the slope decreases to a level resembling the other chips assessed.

Irrespective of this, the key observation from this representation is that interfacial region permittivity again exceeds bulk solution permittivity, as was the case for aqueous glycine solutions, across the gold chips used in this study. While the degree of enhancement varies from chip to chip, it is observed consistently and thus cannot be disregarded.

The sixth gold chip was used to confirm, as was the case in chapter four with measurements of aqueous glycine, how much variation can be observed with repeat measurements of urea on a given gold chip. In this instance, ten successive measurements of 727 g/kg urea solution were performed after ten successive measurements of butan-1-ol, the solvent with which 727 g/kg urea solution is a refractive index match. The average interfacial region permittivity observed is shown in Figure 79 below.

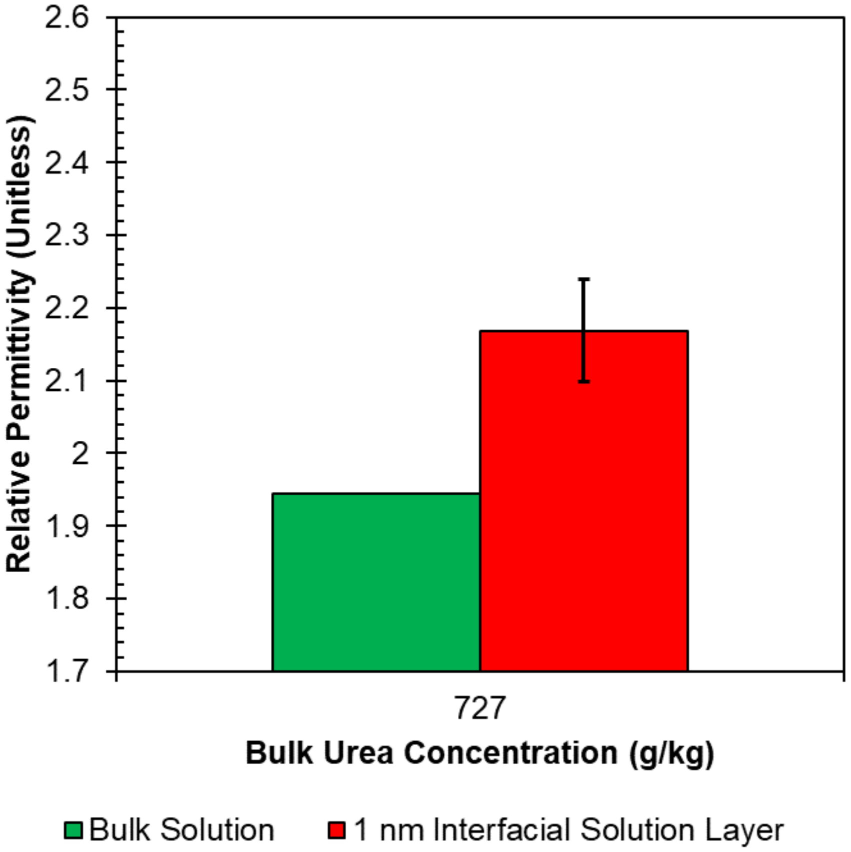

Figure 79: Gold chip 6, upon which ten repeat measurements of 727 g/kg urea solution and isoamyl alcohol were performed to establish the uncertainty in performing such in situ measurements. The error bars signify one standard deviation from the mean value of the ten measurements performed.

As noted in chapter four, the alternative presentation which can be utilised to highlight the degree of chip to chip variability observed in the given measurements is through presenting the mean bulk solution and interfacial solution layers concentrations for each bulk solution concentration assessed on all gold chips. This is shown below in Figure 80, with the associated statistics outlined in Table 20.

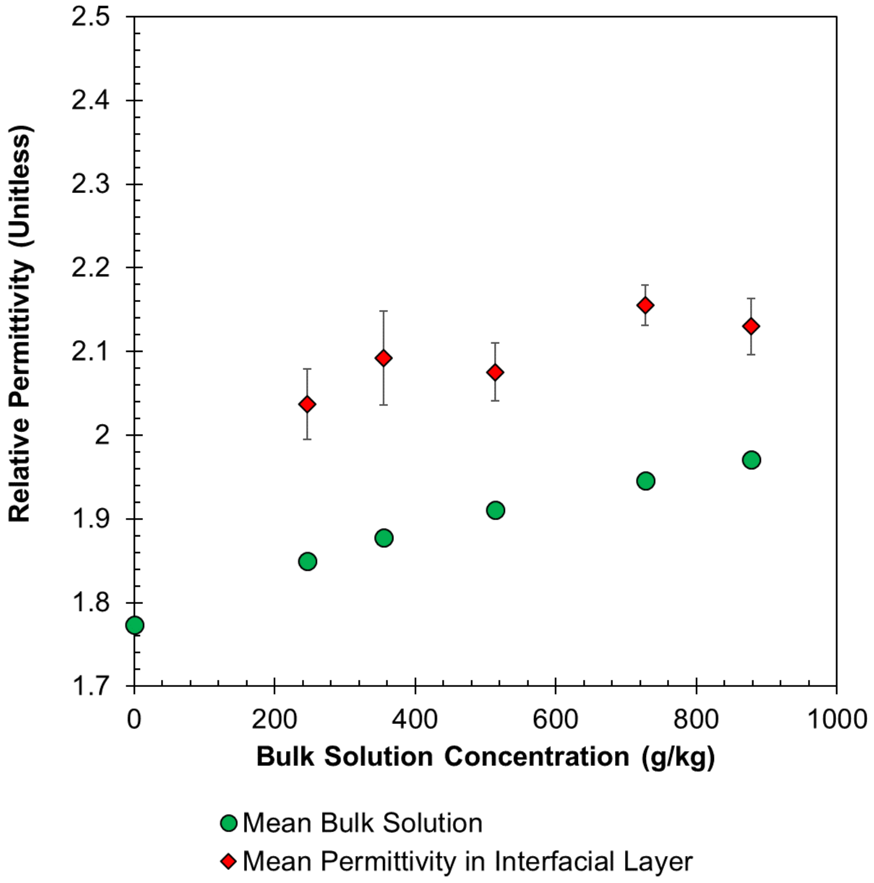

Figure 80: Mean bulk solution permittivity across the measured concentration range, along with the mean permittivity within the interfacial layer when L=1 nm. The error bars represent the standard error of the mean.

Table 20: Mean concentration, interfacial layer permittivity, standard deviation and standard error of the mean for measurements of aqueous urea in contact with a bare gold surface.

$\bar{X}$ Concentration (g/kg)	$\bar{X}$ Bulk Solution ε (Unitless)	$\bar{X}$ Interfacial Layer ε (Unitless)	σ Interfacial Layer	$\sigma_{\bar{X}}$ Interfacial Layer	n
0.000	1.773	1.773	0.000	0.000	9
246.055	1.850	2.037	0.126	0.042	9
354.772	1.877	2.092	0.178	0.056	10
513.430	1.910	2.075	0.109	0.035	10
726.834	1.945	2.155	0.075	0.024	10
877.747	1.971	2.130	0.094	0.033	8

Figure 79 highlights that irrespective of the degree of variability observed from chip to chip in the magnitude of the interfacial region permittivity, the reported values have statistical significance, further supporting the findings outlined in chapter four and highlighting that this interfacial phenomenon is observed with consistent measurements.

5.3.3 Relating interfacial layer permittivity to concentration

Having established that interfacial solution region permittivity exceeds bulk solution permittivity when assessing urea solutions, permittivity values were then converted to a concentration basis so that a comparison could be made with bulk solution concentrations. This comparison was made through use of the Clausius Mossotti equation, as outlined in chapter four, which provided a means to relate expected permittivity values to urea mass fraction for higher urea concentrations.

In order to utilise the equation, pure component number densities and molecular polarizabilities are calculated for both water and urea, which are then proportionally scaled for given mass fractions of urea. This provides an idealised permittivity value at a given mass fraction, which can be used to attribute a mass fraction to the interfacial layer permittivity values being observed through use of the SPR measurement models. These values are dependent on the literature value selected for crystalline urea as higher or lower values for the relative permittivity of pure urea will proportionally scale the magnitude of the permittivity value observed at a given urea mass fraction.

The permittivity of pure urea is not extensively reported in literature and in fact only one value was found in the literature. This introduces a degree of uncertainty as to whether the values calculated are an accurate representation of what the expected permittivity may be at a given urea mass fraction. To minimise this uncertainty, the measurements in this work were subsequently fitted to the Clausius Mossotti equation in order to determine how relative permittivity varies with increasing urea mass fraction. The comparison of each scenario is presented in Figure 81 below.

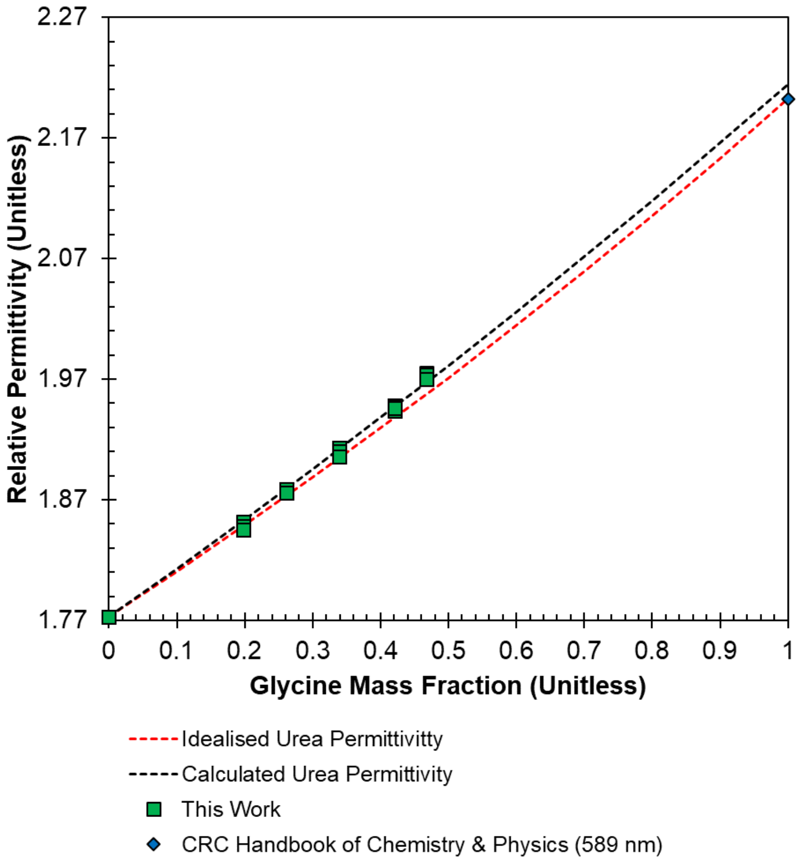

Figure 81: Comparison of idealised permittivity values determined from Clausius Mossotti equation using permittivities of pure water and pure urea from literature and those calculated by fitting Clausius Mossotti equation to permittivity data measured in this work are plotted.

The idealised permittivity-mass fraction relationship based on the Clausius Mossotti equation using permittivities of pure water and pure urea form literature appears to slightly underestimate the measured values of urea permittivity at higher urea concentrations. The fitted values determined using this work are subsequently utilised to calculate urea concentrations in the interfacial solution layer.

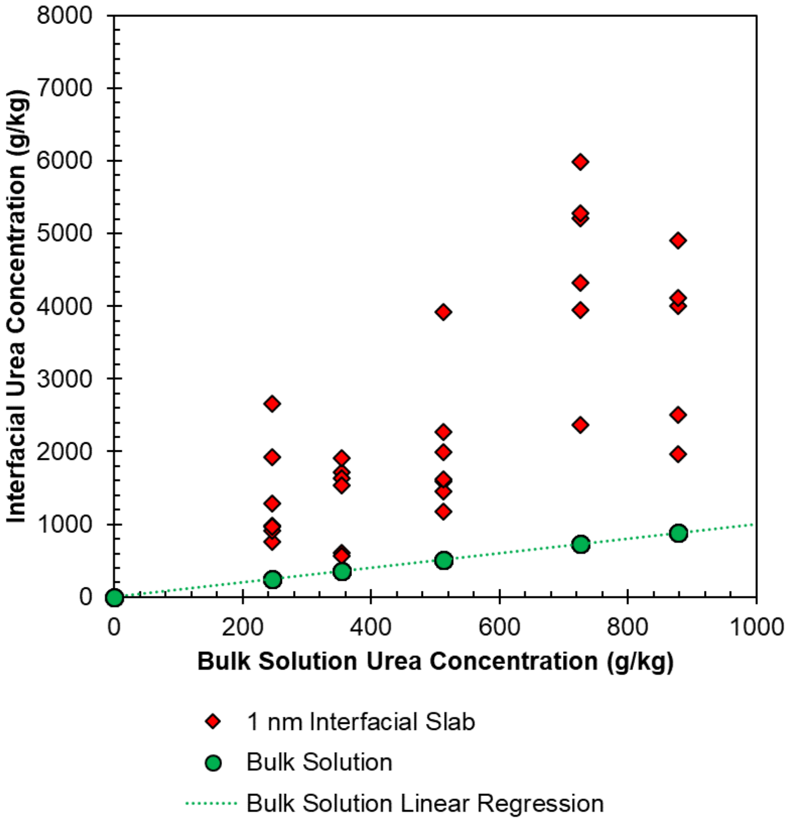

Figure 82: Estimated urea concentrations in the interfacial solution region for the six gold chips utilised in this work.

The results of this calculation are presented above in Figure 82, which shows the spread in interfacial region concentrations observed across the six gold chips. The observed concentration enhancement appears to increase slightly with increasing bulk solution concentration of urea aqueous solutions, similar to what was observed for glycine aqueous solutions.

5.4 Conclusions

In conclusion, in situ measurements of aqueous urea solutions and pure solvents have been undertaken in order to establish whether a localised concentration increase of urea molecules at the solid-liquid interface is observed when urea solutions are placed in contact with a gold chip surface.

When performing SPR measurements for aqueous urea solutions, it was found that the SPR coupling angle was consistently higher than for reference measurements of corresponding reference solvents. Through use of SPR measurement models, it has been confirmed that the solution permittivity in the interfacial region was higher than that in the bulk solution, across all chips used. This is very significant as it extends the results for aqueous glycine solutions outlined in chapter four to aqueous area solutions and provides further validation to the presence of an interfacial solution layer with localised concentration enhancement being observed at the solid-liquid interface.

Again, chip to chip variability is observed in relation to the degree of concentration enhancement being observed at the interface, which can be attributed to differences between chips, such as gold layer thickness, polycrystallinity of the gold film upon application and surface level defects in chips. Irrespective of these influences, this is an important indication and validation of this interfacial enhancement effect.

Chapter 6

6. In situ measurement of interface induced concentration enhancement in aqueous solutions of glycine in contact with polystyrene surfaces

6.1 Introduction

It is widely accepted that crystal nucleation primarily occurs by means of a heterogeneous mechanism, whereby the presence of surfaces in contact with solution lowers the energy requirement for nucleation and thus promotes faster nucleation. Consequently, gaining a greater understanding of how such surfaces can either promote or suppress crystal nucleation is important if more efficient crystallisation processes are to be developed in the future.

This chapter uses the findings of chapters four and five as a foundation from which interfacial concentration enhancement effects are further probed through the application of hydrophobic polystyrene layers to gold chips. Solutions of aqueous glycine were placed in contact with these chips to assess how the magnitude of concentration enhancement at the polystyrene-solution interface may compare to that of glycine solutions in contact with a bare gold chip.

Polystyrene is a hydrophobic polymer, with weak electron donor phenyl rings, where interactions of solution molecules with the polymer surface are driven by dispersion interactions.[15] Previous studies have been carried out in literature with use of polystyrene layers for induction time studies to assess crystal nucleation at the polymer-solution interface. [15, 18] Polystyrene was utilised in this thesis for its chemical inertness and ability to form smooth polymer layers as a control substrate.

This is of interest when looking to investigate the role of non-specific dispersion interactions at the solid-liquid interface, hence the utilisation of polystyrene in this study. Gold chips were prepared though the deposition of dodecanethiol monolayers on the gold chips in the first instance as a foundation onto which stable ultrathin polystyrene layers can be spin coated. A schematic diagram outlining the constituent elements of the experimental system is presented in Figure 83.

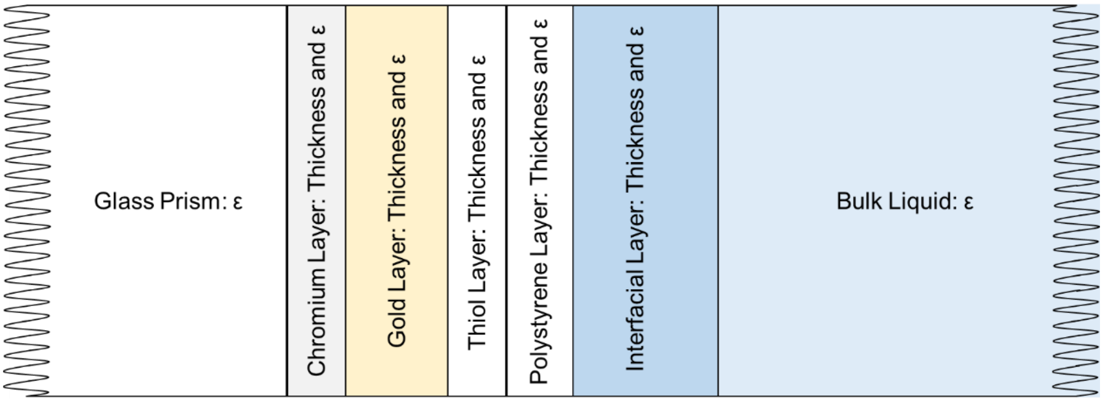

Figure 83: Schematic diagram outlining the constituent parts of the experimental system used to generate the representative SPR model for polystyrene coated gold chips. All chips contain glass prism, chromium, gold and polystyrene layers. Pure liquids only contain bulk, but solutions can also include a separate interfacial layer.

To investigate glycine solution-polystyrene interfacial region, SPR measurements of pure solvents and refractive index matched solutions of aqueous glycine were undertaken on gold chips spin coated with ultrathin polystyrene layers to generate SPR spectra. To analyse the SPR data, representative model systems of the experimental system shown in Figure 83 were generated using the Winspall program, to assess the degree of enhancement in glycine concentration in the interfacial solution region with respect to the bulk solution concentration.

Contact angle goniometry measurements were performed for a range of aqueous glycine solution concentrations in contact with bare gold chips and polystyrene coated gold chips. Determination of the contact angle provided a means by which the solution behaviour observed at the solid-liquid interface in SPR measurements could be related to macroscale behaviour of liquid droplets on polystyrene coated chips.

6.2 Materials & Methods

6.2.1 Materials

Water (HPLC Plus Grade, Sigma Aldrich), Methanol (99%, VWR), Ethanol (Absolute, Fisher Scientific), 1-Propanol (HPLC Grade, 99.9%, Sigma Aldrich), 1-Dodecanethiol (≥98%, Sigma Aldrich), Polystyrene (Mw 34,300 g mol^{-1}, Polymer Source Inc.), Toluene (Laboratory Reagent, ≥99.3%, Sigma Aldrich) and Glycine (Fisher Scientific, 98.5%) were purchased and handled as received.

6.2.2 Dodecanethiol and polystyrene layer deposition on gold surfaces

Prior to thiol layer addition, bare gold chips, prepared per the protocol outlined in Section 2.3.3, were oxygen plasma cleaned to remove any potential contaminants from the surface, before examination under an optical microscope (Leica M165 CM Microscope) to determine if there were any defects or deformations on the surface. All glassware used was cleaned using a Hellmanex (1% Hellmanex-water solution) washing procedure.

1-Dodecanethiol was added to a known volume of ethanol to prepare a stock solution (1 mM). The desired number of gold chips were then submerged in the solution (1 hour). The solution was then exchanged with fresh ethanol in triplicate, followed by water, before the chips were removed and dried under a stream of nitrogen gas. The thiol coated chips were then stored in a sealed container prior to use. The resultant thiol layer was examined under an optical microscope for qualitative confirmation of surface coverage prior to layer characterisation using SPR spectroscopy.

Polystyrene (250 mg, Polymer Source Inc., 34,300 g mol-1,) was dissolved in toluene (5 mL) to prepare a stock solution (50 mg mL^{-1}, 5.8 % w/v). A 1 % w/v polystyrene solution was prepared using aliquots of stock polystyrene solution and toluene (867 µL 5.8 % w/v polystyrene (l), 4133 µL Toluene). Polystyrene solutions (0.3, 0.5 and 0.75 % w/v respectively) were then prepared from the 1 % w/v solution, with the corresponding volumes given in Table 21.

Table 21: Volumes of 1 % w/v polystyrene solution and toluene used to prepare polystyrene solutions for spin coating.

Polystyrene Concentration (% w/v)	Volume 1 % w/v Polystyrene Solution (µL)	Volume Toluene (µL)
0.3	600	1400
0.5	1000	1000
0.75	1500	500

Spin coating of gold chips was undertaken using a spin coater (KW-4A, Chemat Technology). To coat gold chips, a given chip was placed on the chuck within the spin coater unit and the vacuum switched on to fix the chip to the chuck surface. An aliquot of polystyrene solution (50 μL) was then pipetted onto the surface of the chip and the spin cycle was started. Following the completion of the spin cycle (60 seconds, 1500 rpm), the chip was removed from the chuck and stored in an airtight container to dry (24 hours), ready for characterisation using SPR spectroscopy to determine layer thickness and optical microscopy to qualitatively assess layer uniformity across the gold chip. The experimental protocol followed to form both the thiol and polystyrene layers is shown in Figure 84.

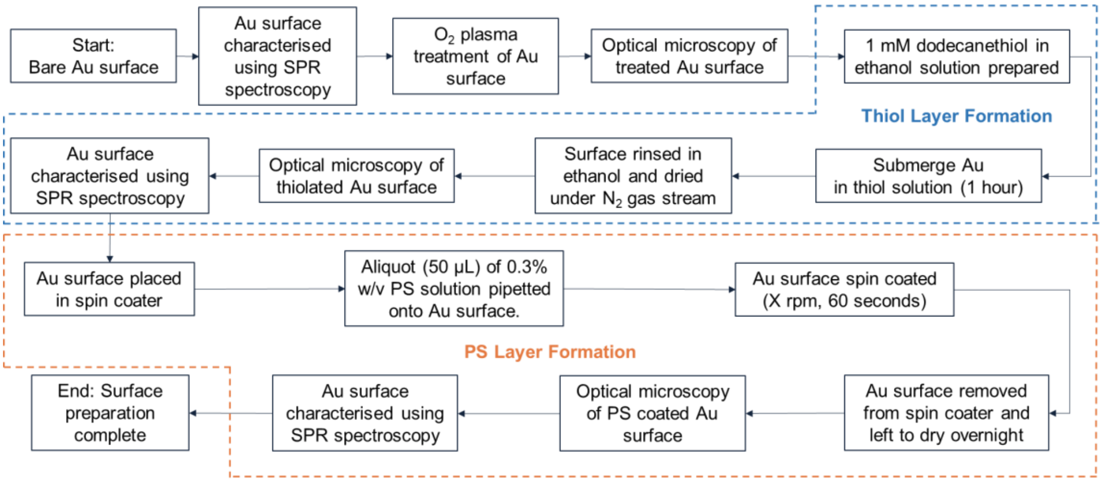

Figure 84: Experimental procedure followed in order to prepare PS spin coated gold chips for use in SPR measurements of aqueous glycine solutions.

6.2.3 Solution Preparation

Pure solvents and their binary mixtures were prepared to produce reference spectra across the range of refractive index values of aqueous glycine concentration assessed. Each pure solvent's refractive index was first determined, along with the refractive index of the aqueous solution of interest. The refractive index data was then used in combination with a target volume of solvent mixture to determine the necessary solvent ratios required to produce a binary system, which was refractive index matched to that of the aqueous solution of interest.

Aqueous glycine solutions were prepared according to the procedure outlined in Chapter 4.2.1 across a pure water (hereafter referred to as 0 $g_{glycine}/kg_{water}$) to 250 $g_{glycine}/kg_{water}$ concentration range, which will again be denoted as g/kg throughout. by combination of glycine and water respectively directly within glass vials.

6.2.3 SPR Measurement Procedure

Gold chips with spin coated polystyrene layers were mounted on the high refractive index glass prism and fitted with a flow cell configuration for liquid injection to the chip surface. The measurement acquisition procedure was identical to that outlined in Section 4.2.4.

6.2.5 SPR Model Generation

To analyse SPR measurements of both solvents and aqueous glycine solutions alike on polystyrene coated gold chips, representative SPR models were generated for analysis through use of the Winspall program following the procedure outlined in Chapter 4.2.5.

Having first characterised the bare gold chip per the workflow, the addition of a dodecanethiol layer is then incorporated into the model. Using the initial bare gold chip model, the real component of the thiol layer dielectric constant is fixed based on a value obtained from literature.[97] The layer thickness of the thiol layer is fitted to ensure that the model and experimental coupling angle minima are equivalent.

Following thiol layer addition, an ultrathin polystyrene layer is spin coated onto the thiolated gold chip and a subsequent model is needed to characterise the system. Using the model for the thiolated gold chip, the real component of the polystyrene layer dielectric constant is fixed based on a value obtained from literature.[98] The layer thickness of the polystyrene layer is fitted to ensure that the model and experimental coupling angle minima are equivalent.

Having accurately characterised the gold chip of interest following the addition of thiol and polystyrene layers, models are generated for water, pure solvents and solvent mixtures in line with the procedure outlined in Chapter 4.2.5. This resultant workflow for generating models for polystyrene coated gold chips is summarised schematically in the data analysis workflow outlined in Figure 85.

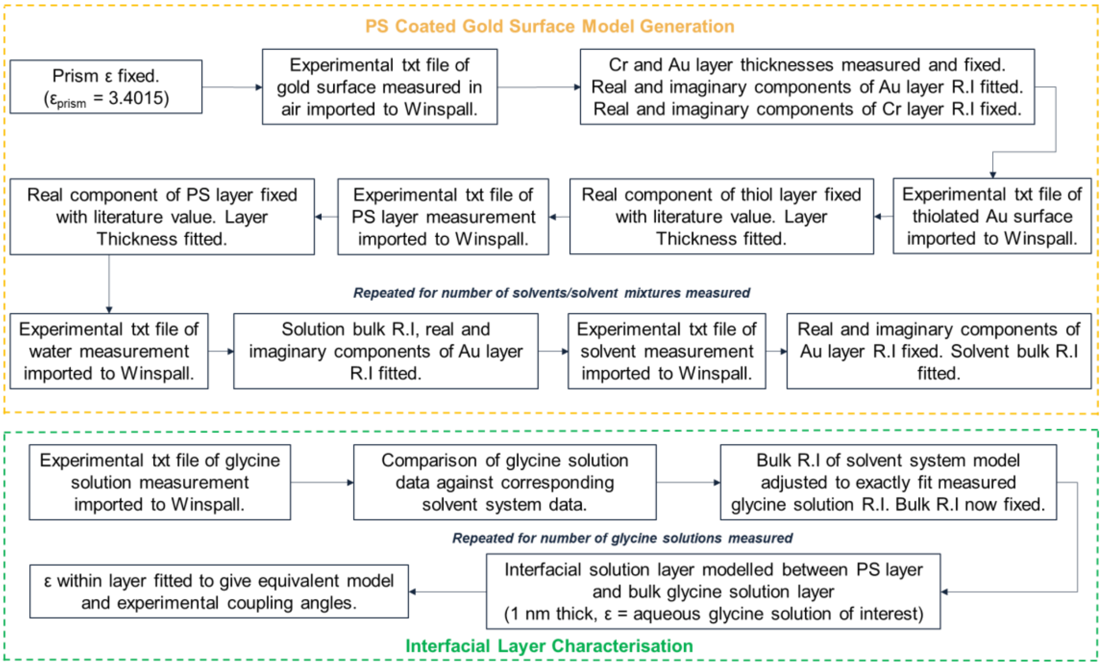

Figure 85: Workflow developed for generating representative SPR models for polystyrene coated gold chips and subsequent measurements of solvents and aqueous glycine solutions.

6.2.4 Contact Angle Goniometry Measurements

To further probe the influence of the polystyrene surface on aqueous glycine solutions, advancing, static and receding contact angle measurements were performed using a Krüss DSA30 goniometer, in combination with a syringe pump (New Era Pump Systems, Inc.). An image of the experimental setup is shown below in Figure 86, with a close up of the gold chip and needle given within the inset image.

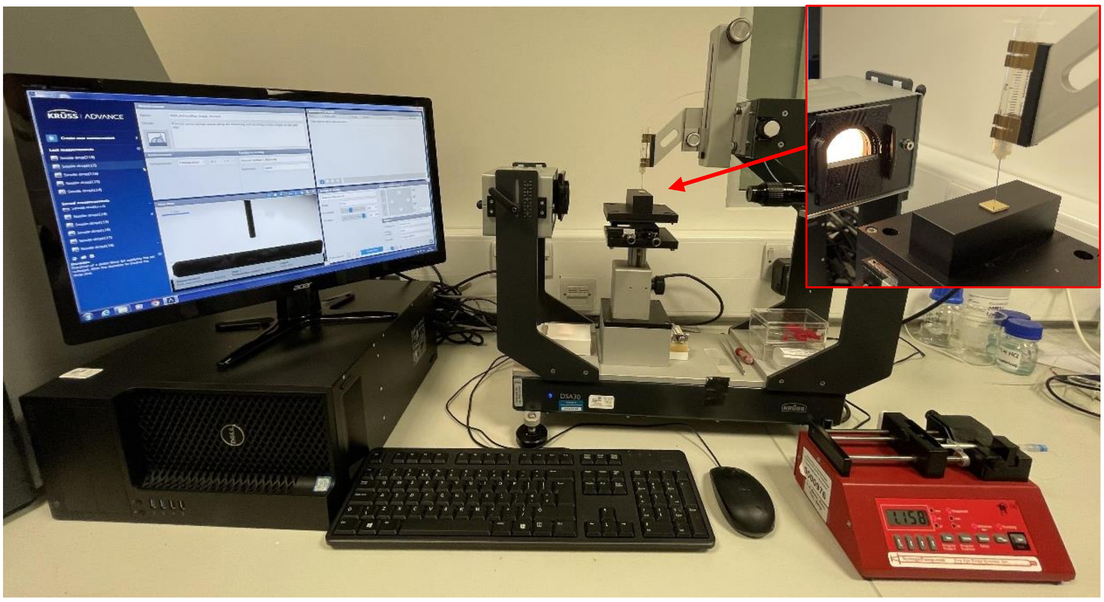

Figure 86: Image showing the experimental setup utilised for contact angle measurements of aqueous glycine solutions on bare gold and PS coated gold chips. The inset shows a magnified image of the optical stage and needle.

Using four bare gold chips as a control and four polystyrene coated gold chips as a test surface, the intention was to probe the influence of such surfaces on a macroscopic scale (along the surface) in contrast previously assessed impact on the solution at the nano scale (in the normal direction to the surface). Polystyrene coated gold chips were prepared following the procedure outlined in section 6.2.2, with aqueous glycine solutions prepared following the protocol outlined in 6.2.3.

Gold chips (coated and uncoated) were grouped for measurements with specific concentrations of glycine solution, as shown in Table 22. The solution of interest was pumped into the syringe pump, with care taken to avoid the presence of air bubbles in the connecting tubing between the needle and syringe. With the syringe filled and ready for use, the needle tip and surface baseline were calibrated through use of the in-built software in the instrument.

A droplet was then pumped from the syringe (0.015 mL min^{-1}), with a video recording of the surface started after droplet formation. The droplet was then brought into contact with the gold chip of interest, before the needle tip was moved to the back of the formed droplet, with the pump restarted to increase the size of the droplet (20 seconds, 0.015 mL min^{-1}). The now larger droplet was left to equilibrate with the environment (30 seconds), before withdrawing the droplet from the surface. The video recording was stopped at this point, signifying the end of a respective measurement.

This protocol was repeated a further three times to produce four measurements per chip at the glycine solution concentration of interest, using different parts of each gold chip surface for each respective measurement. Between measurements of different glycine solution concentrations, the tubing and syringe were flushed with water in triplicate to ensure no residual material from the previous measured solution remained in the system. Videos were analysed using the Krüss software to determine the advancing, static and receding contact angles.

Table 22: Gold chips used for respective aqueous glycine solutions on chips A-G.

Chip	Target Glycine Solution Concentration (g/kg)	Actual Glycine Solution Concentration (g/kg)
A, E	0	0.0000
B, F	100	99.970
C, G	176	175.55
D, H	250	249.95

6.3 Results & Discussion

In this chapter the aim is to assess and quantify an interfacial concentration enhancement in glycine solutions at polystyrene-solution interfaces. This section details the steps needed to establish this and the findings observed at each respective stage when working through each of the workflows outlined in Section 6.2.

The addition of thiol layers and polystyrene layers to bare gold chips is first discussed, in order to establish how the addition of such layers atop the gold chip influences the resultant SPR spectra. Optical microscopy is utilised to qualitatively verify that the gold surfaces are being coated with a uniformed layer at each point in the procedure.

After qualitative confirmation of the presence of polystyrene layers on the gold surface, the influence of such layers is then tested through comparison of glycine solutions in contact with a polystyrene surface against corresponding solvent reference measurements. Model systems are then implemented in order to analyse SPR spectra to assess how interfacial region permittivity compares with that of the bulk solution permittivity for each of the six gold chips utilised for this work.

The interfacial region permittivity determined through use of the model systems is then converted to concentration using the Clausius Mossotti equation, as was performed for chapters four and five, in order to estimate the magnitude of enhancement at the interface with respect to the bulk glycine solution concentration.

Finally, through use of contact angle measurements, we look to relate these nanoscale interfacial concentration enhancement observations to those at the macroscale for the contact angle for aqueous glycine solutions (0-250 g/kg) on bare gold chips and gold chips coated with ultrathin polystyrene layers.

6.3.1 Functionalisation of Bare Gold Chip Surface

To form ultrathin polystyrene layers upon the gold chip surfaces, a number of steps were followed in sequence as outlined in the procedural workflow shown in Section 6.2.2. Having measured the corresponding gold chip layer thicknesses using SPR spectroscopy, a dodecanethiol layer was deposited on the surface of gold chips.

The addition of the thiol layer prior to polystyrene spin coating was undertaken in an attempt to promote better dispersion of the polymer film and also to prevent de-wetting of the film upon application to the gold chips surface. Given that gold and polystyrene do not have a strong affinity for one another, not utilising alkanethiol chemistry would result in dewetting of the polymer film on spin coating. This would result in the formation of a film that is not uniform and smooth, which is necessary for such precise surface measurements, and SPR spectra with poorly resolved coupling angle minima.

Formation of the Au-S bond from immersion of the chip in alkanethiol solution facilitates a better dispersion of the polystyrene solution on spin coating, in turn yielding a smooth and well dispersed film. Raw SPR spectra for each step in the chip preparation process for Chip 1 are shown in Figure 87 below, with the corresponding layer thicknesses shown in Table 23.

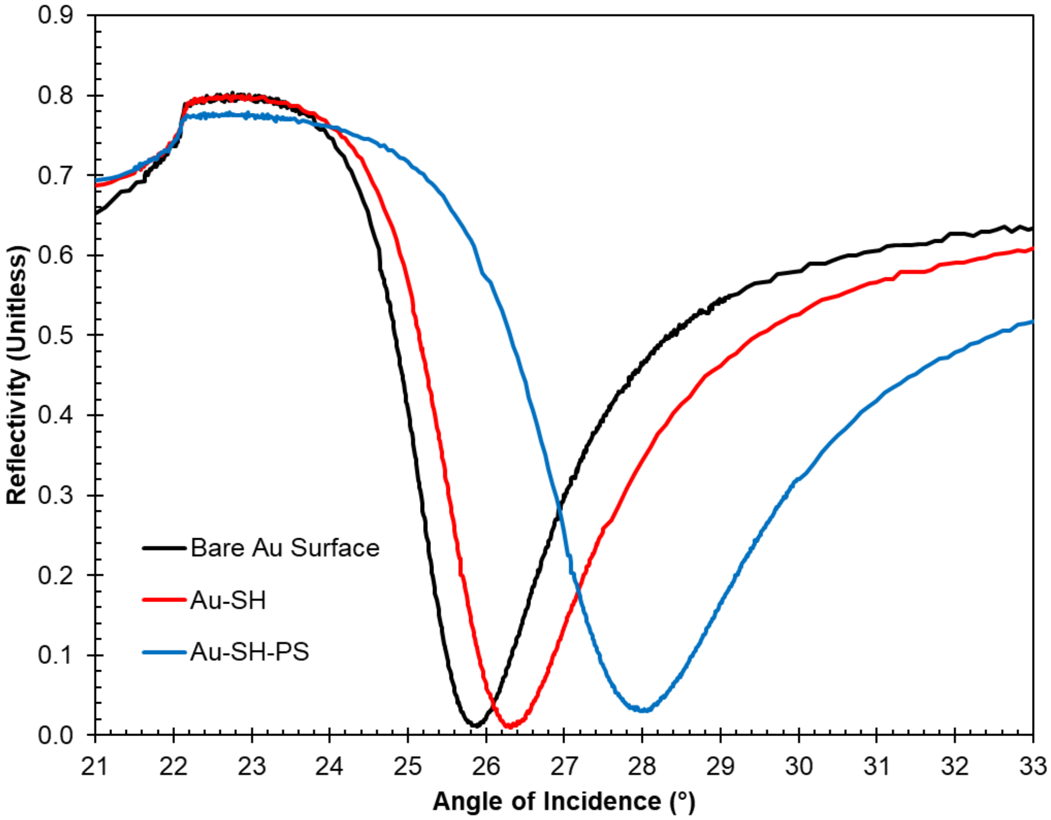

Figure 87: Raw spectral responses of each stage in chip preparation, measured in air. It is seen that with each layer application, the SPR coupling angle minima shifts to a higher angle of incidence than that of the bare gold surface, indicative of increasing layer thickness above it.

Table 23: Gold chip compositions by layer thickness (nm).

Chip Number	Cr Layer (nm)	Au Layer (nm)	SH Layer (nm)	PS Layer (nm)
1	0.1	46	2.825	7.2500
2	0.1	46	2.600	8.7000
3	0.1	46	1.584	8.6800
4	0.1	46	1.232	7.9900
5	3.2	59.5	1.640	14.235
6	3.3	57.5	1.595	13.520

Qualitatively, the successive shift of the SPR coupling angle minima to higher angles of incidence is indicative of layer formation at the gold-air interface. The measured polystyrene layers, when looked at across all six chips, agree with the visual inspection of the raw spectra, whereby thicker polystyrene layers have larger SPR coupling angle minima. Furthermore, the acquired spectra have sharp spectral features, which show that the layers formed are able to be measured in the experimental setup.

When assessing all of the six chips collectively, disregarding spectral differences which arise from different gold and chromium layer thicknesses, we can see that not all chips (2, 5 and 6) have reflectivity values at SPR coupling angle minima which are near zero, as is the case for chips 1,3 and 4) as would be expected. This suggests macroscopic uniformity issues on the chip surface which were encountered during polystyrene layer formation, as shown in Figure 88 as gold layers of this thickness have a reflectivity value at the coupling angle minimum close to zero.

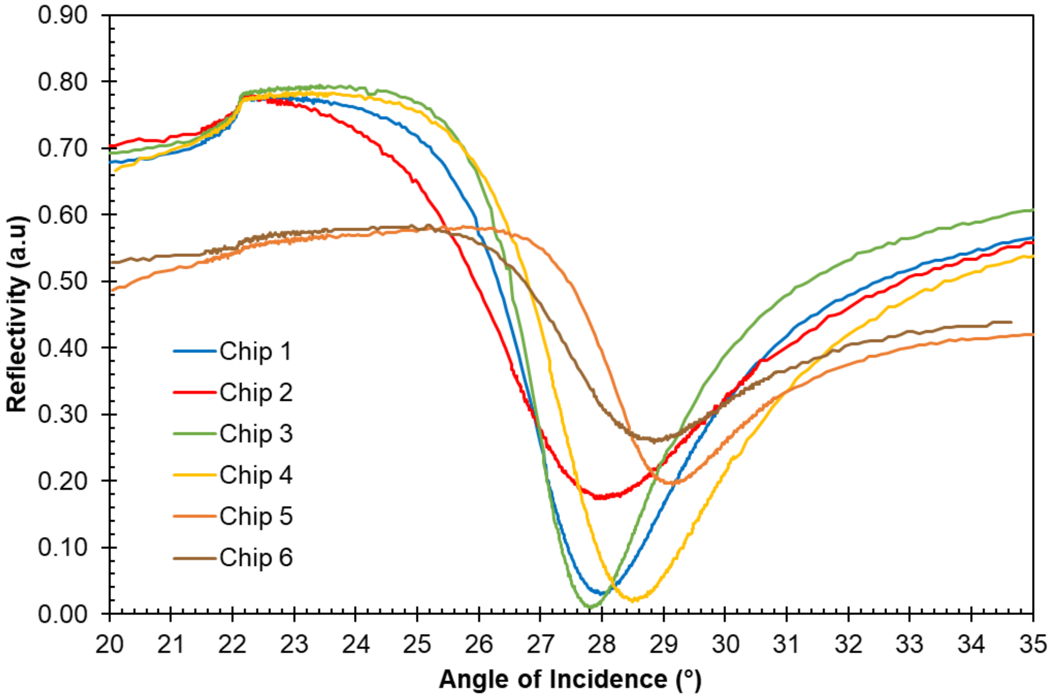

Figure 88: Raw SPR spectral responses for each of the six PS coated gold chips utilised in this study, measured in air.

Optical microscopy was used to visually confirm the presence of thiol and polystyrene layers in the first instances through imaging of bare gold chips and then successive images at each addition stage of chip preparation, as well as providing a means by which the chips could be visually inspected for layer disturbances.

Figure 89 shows such images for gold chip 1. In the case of chips 1 and 2, it was suspected that defects in the gold layer are at play when measuring thiol layer thickness and this is why they are larger than feasibly possible. This is also aiding in explaining why the thiol and polystyrene layers on these gold chips appear non-uniform, evidenced by the blotchy like appearance of small dots under the light microscope. This appearance is likely to be the result of a macroscale issue at the surface and hence why the coupling angle minima of these chips does not go to zero, as shown in Figure 88.

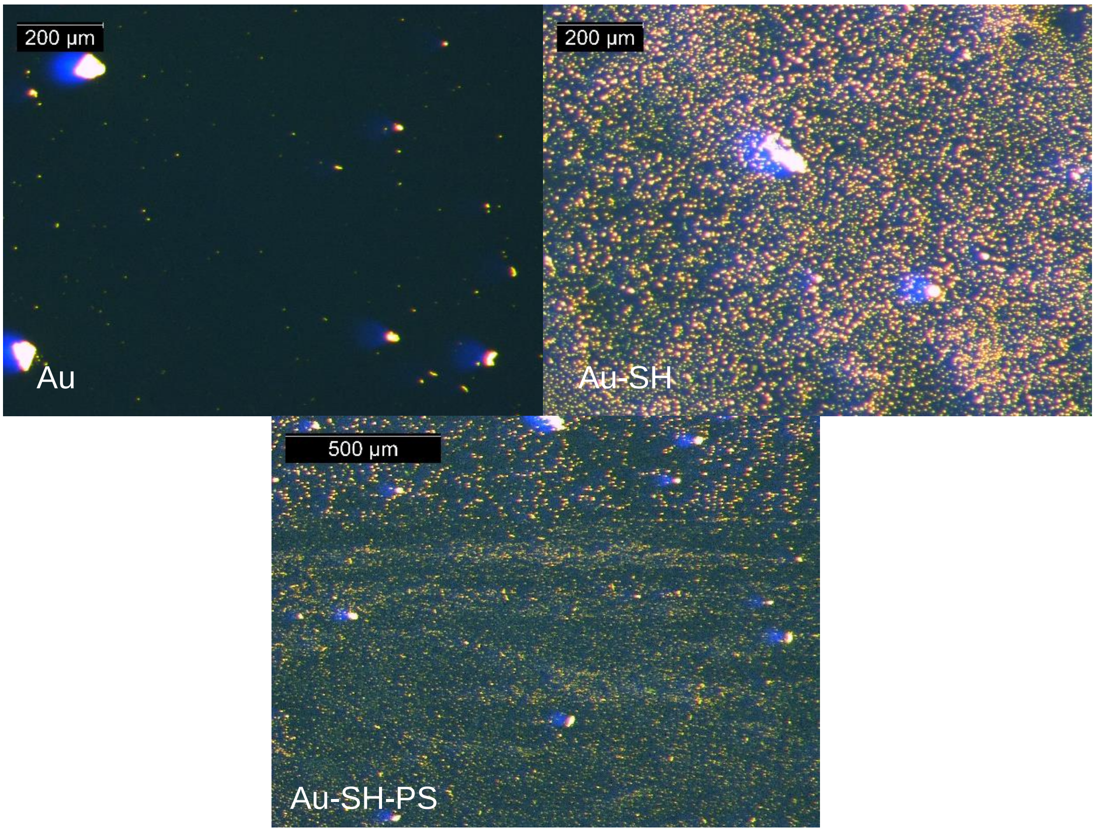

Figure 89: Optical microscopy images for gold chip 1. The images show the surface prior to thiol addition and then prior to PS layer addition.

Although all gold chips were prepared following the same experimental protocol, chips 1 and 2 differed from chips 3-6 in their formed layers appearance under the optical microscope. This is quite clearly observed when looking at the optical microscopy images for chip six shown in Figure 90, which have minimal blemishes on the surface. Overall, the combined use of SPR surface measurements and optical microscopy show agreement with one another when the key thickness parameters are assessed. This supports the conclusion that stable, ultrathin layers can be formed on the gold surfaces for further measurements including aqueous glycine solutions.

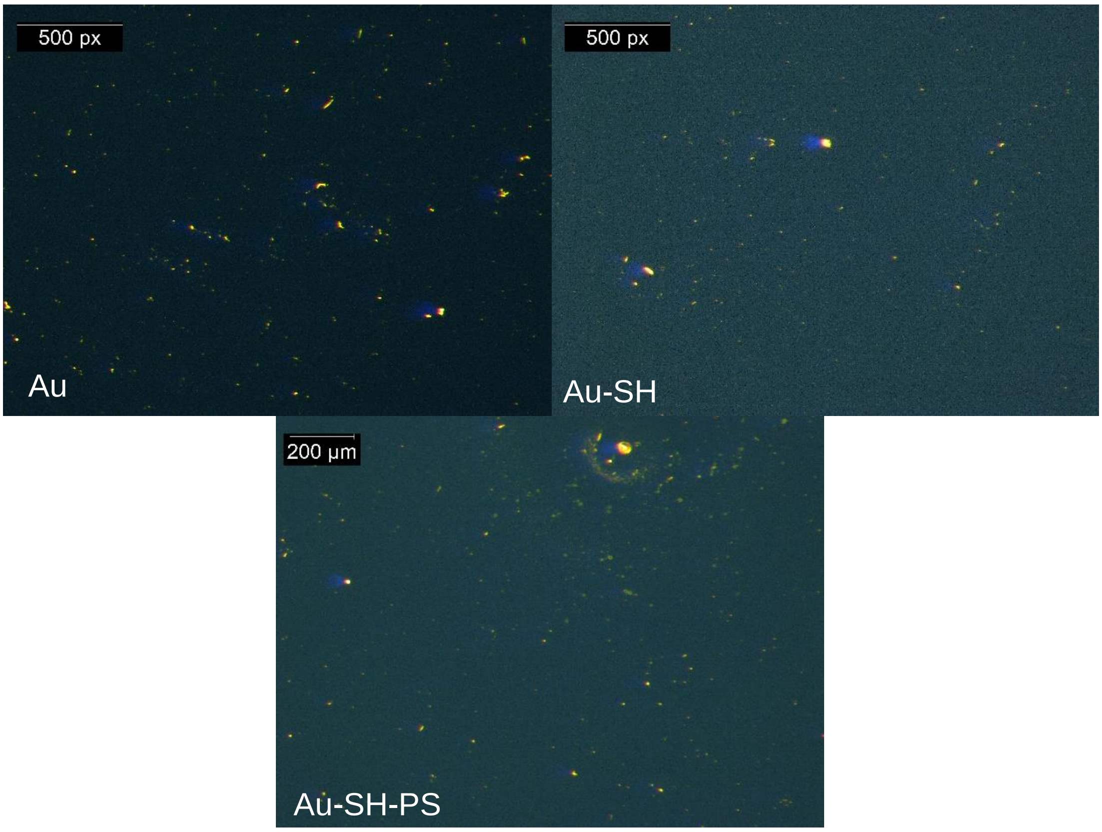

Figure 90: Optical microscopy images for gold chip 6. The images show the surface prior to thiol addition and then prior to polystyrene layer addition.

6.3.2 Raw Angular Reflectivity Measurements

As has been the case throughout this research, the key metric by which we can qualitatively confirm interfacial glycine concentration enhancement in the first instance is by first bulk refractive index matching aqueous glycine solutions to a solvent reference measurement and then comparing the respective coupling angle minima positions.

Figure 91 shows an SPR measurement of ethanol on the PS-coated Au surface compared against a refractive index matched aqueous glycine solution at 176 g/kg bulk solution concentration on gold chip 3. It was observed that the coupling angle minima are not aligned, indicating that the interfacial region permittivity exceeds that of the bulk solution. This is not an isolated observation, as assessment over a range of bulk glycine solution concentrations leads to the same observation.

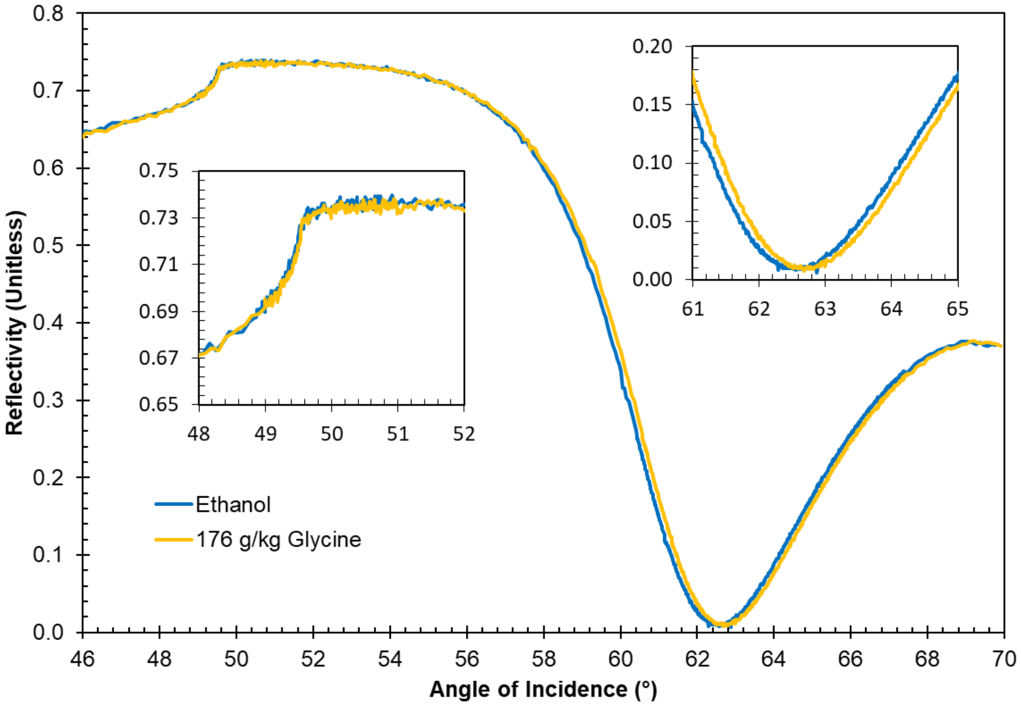

Figure 91: Comparison of a 176 g/kg aqueous glycine solution against a refractive index matched solvent reference measurement of ethanol on PS Coated Gold Chip 3. It can be seen that the bulk permittivity is equivalent by way of the equivalent critical angles for total internal reflection, yet the coupling angle minima are not equivalent – indicative of a localised concentration increase at the polystyrene-glycine solution interface.

6.3.3 SPR model generation for interfacial region permittivity determination

Representative SPR models were developed following qualitative assessment of coupling angle mismatches in order to determine the degree of interfacial region solution permittivity enhancement being observed with respect to the bulk solution. Results of data analysis using models for each polystyrene coated gold chip are shown in Figures 92-97.

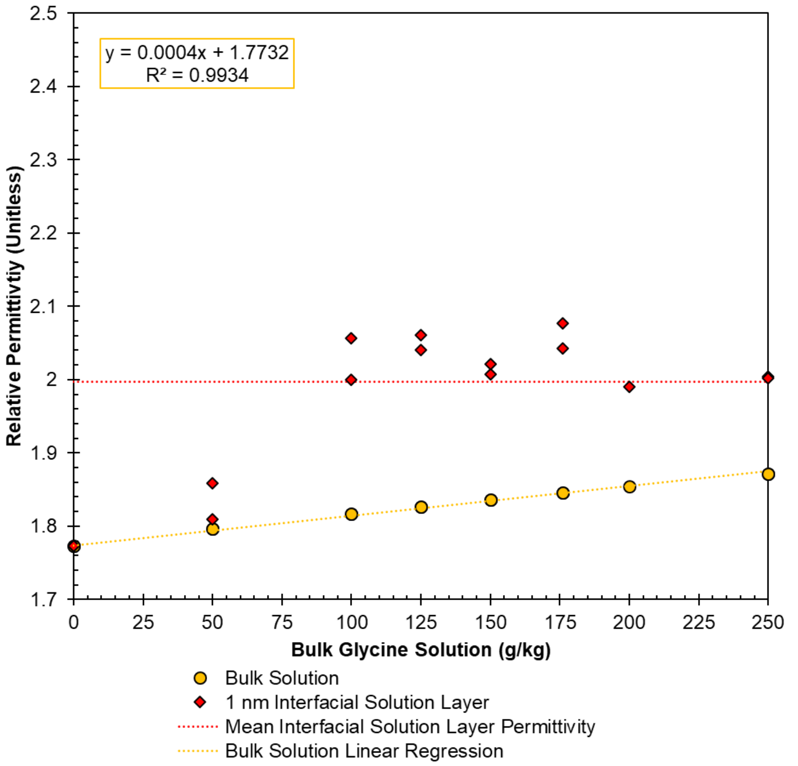

Figure 92: Chip 1, with a 46 nm gold layer and 7.25 nm thick PS layer.

Across all polystyrene coated gold chips, there is a degree of variation with respect to interfacial region permittivity on a given chip at the same bulk solution concentration. This was also observed when performing measurements of aqueous glycine and urea solutions on bare gold chips in chapters four and five, which was attributed to surface morphology and the way in which the gold layer formed during deposition upon the chip surface during gold chip preparation.

In the case of polystyrene coated chips, the observed variation is further influenced by the polystyrene layer formed on the gold surface, specifically how thick and uniformly coated it is on the surface. Regardless of this variation, the key observation was that, once more, the permittivity observed at the solid-liquid interface exceeds that of the bulk solution.

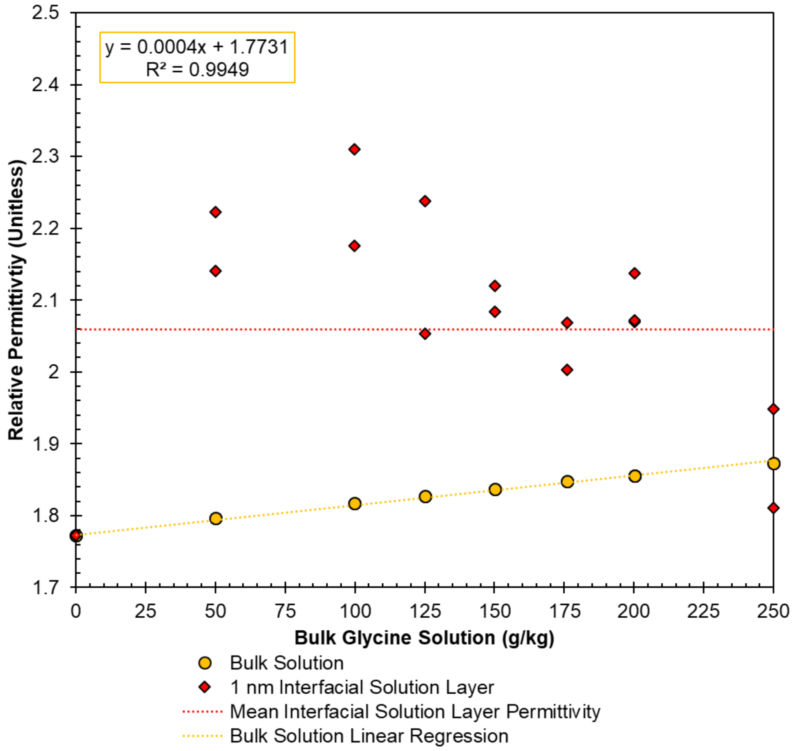

Figure 93: Chip 2, with a 46 nm gold layer and 8.70 nm thick PS layer.

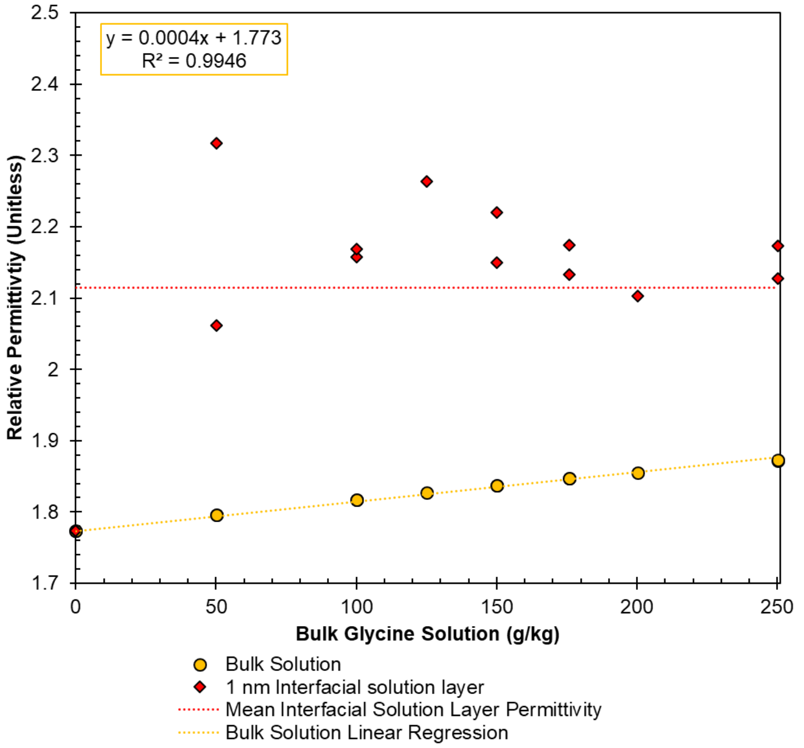

Figure 94: Chip 3, with a 46 nm gold layer and 8.68 nm thick PS layer.

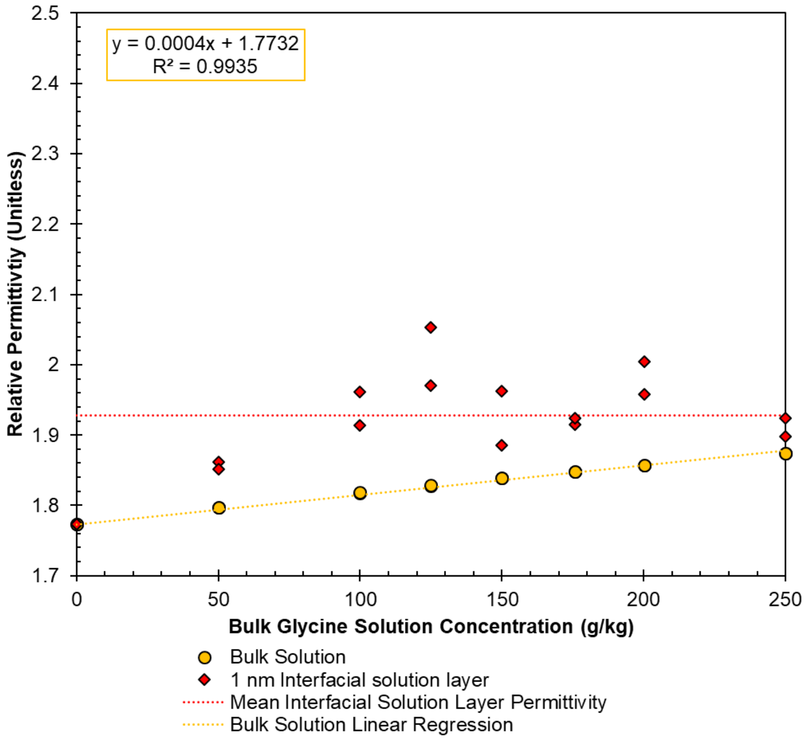

Figure 95: Chip 4, with a 46 nm gold layer and 7.99 nm thick PS layer.

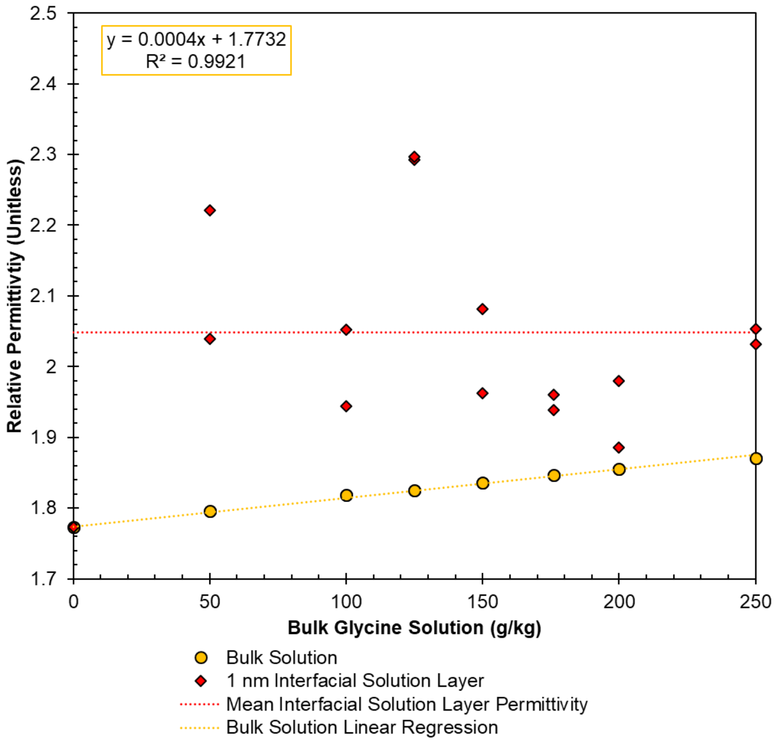

Figure 96: Chip 5, with a 59.5 nm gold layer and 14.235 nm thick PS layer.

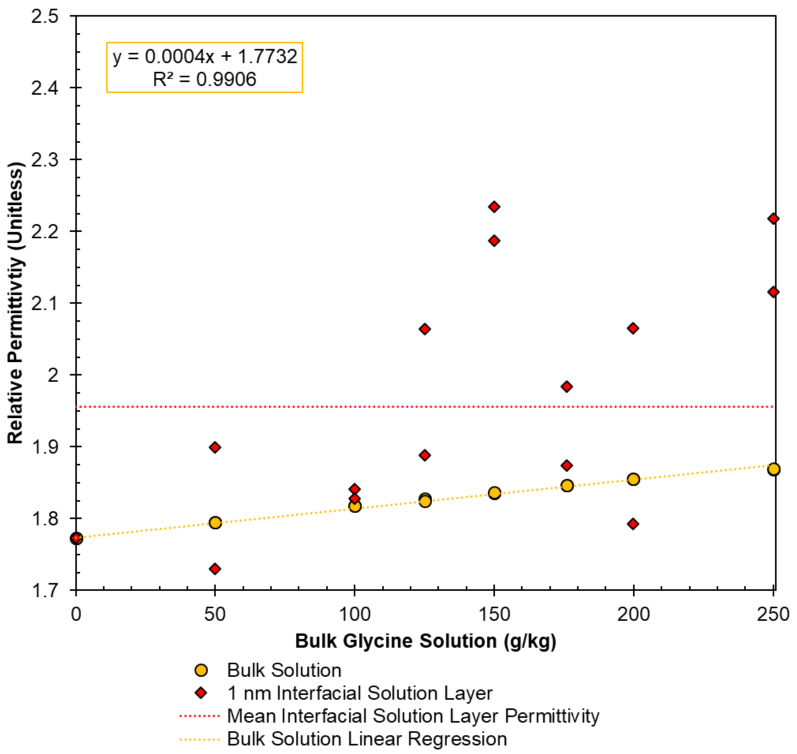

Figure 97: Chip 6, with a 57.5 nm gold layer and 13.52 nm thick PS layer.

It can be observed that the magnitude of the surface enhancement varies from chip to chip slightly but that there is a degree of uniformity to the magnitude of the slopes overall, something which was not observed on bare gold surfaces and which suggests that the polystyrene layer becomes saturated at low bulk glycine solution concentrations.

It is evident that the introduction of the polystyrene layer to the gold surface results in an increase in the magnitude of interfacial concentration enhancement when compared with those of bare gold chips. The precision of the bulk solution concentration measurements and the resultant permittivity values determined from SPR measurements means that there is no variation in the observed bulk solution permittivity measurements. This makes them a consistent foundation to support the observations made for the interfacial layer values determined.

This could suggest that the hydrophobicity of the polystyrene surface repels the water molecules and leads to an increase in glycine concentration localised at the solid-liquid interface, as observed in molecular simulations of such aqueous systems in contact with hydrophobic interfaces. [99]

Consistent with the analysis outlined in chapters four and five, chip to chip variability was also assessed in terms of the mean permittivity values observed at given aqueous glycine solutions across all polystyrene coated gold chips utilised. The results of this analysis are presented in Figure 98 below, with Table 24 highlighting the corresponding statistical analysis results.

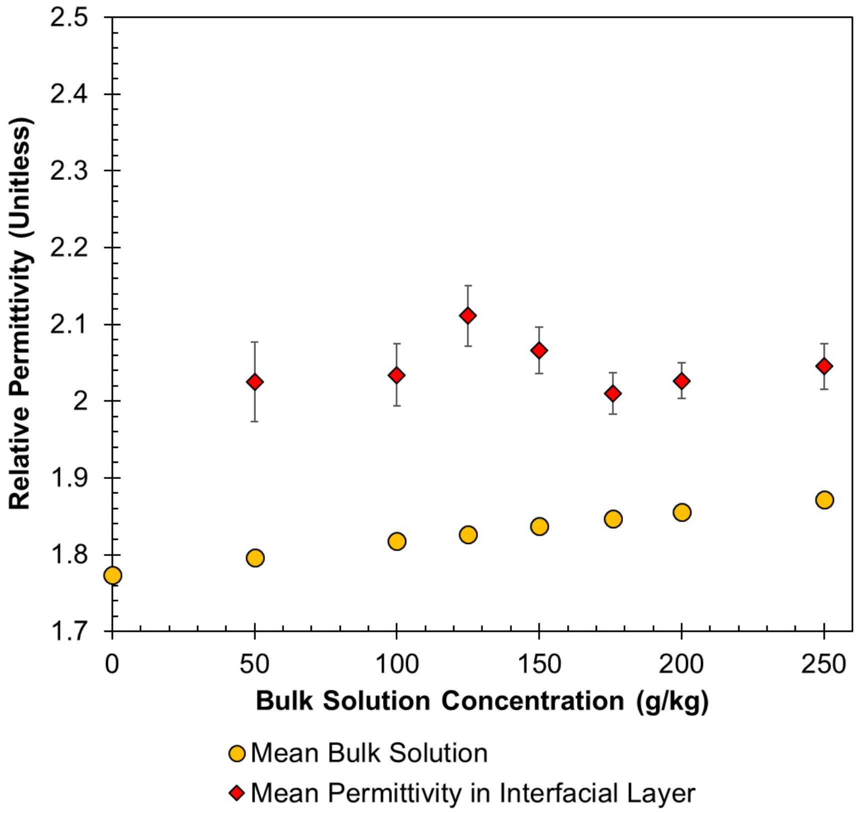

Figure 98: Mean bulk solution permittivity across the measured concentration range, along with the mean permittivity within the interfacial layer when L=1 nm. The error bars represent the standard error of the mean.

Table 24: Mean concentration, bulk solution permittivity, interfacial layer permittivity, standard deviation and standard error of the mean for measurements of aqueous glycine in contact with a polystyrene coated gold surface.

$\bar{X}$ Concentration (g/kg)	$\bar{X}$ Bulk Solution ε (Unitless)	$\bar{X}$ Interfacial Layer ε (Unitless)	σ Interfacial Layer	$\sigma_{\bar{X}}$ Interfacial Layer	n
0.000	1.773	1.773	0.000	0.000	12
50.003	1.797	2.026	0.172	0.052	11
99.967	1.817	2.034	0.141	0.041	12
125.043	1.827	2.111	0.132	0.040	11
149.992	1.837	2.066	0.105	0.030	12
175.887	1.847	2.010	0.092	0.027	12
200.010	1.855	2.027	0.072	0.023	10
250.015	1.872	2.045	0.099	0.030	11

In line with the results presented throughout this thesis, there is a clear trend of interfacial layer permittivity exceeding bulk solution permittivity across all solutions concentrations investigated on polystyrene coated gold chips, with the low standard errors highlighting the confidence which can be drawn from these results in the presence of the interfacial solution layer.

6.3.4 Relating interfacial region permittivity to concentration

The interfacial region permittivity observed across chips was then related to concentration through use of the Clausius Mossotti equation, the fundamental physical relationship used to estimate permittivity of highly concentrated glycine solutions in chapter four. Figure 99 below represents the relationship between glycine mass fraction and solution relative permittivity using the measurements of glycine solutions on polystyrene coated gold chips, similar to that outlined for bare gold surfaces in chapter 4.

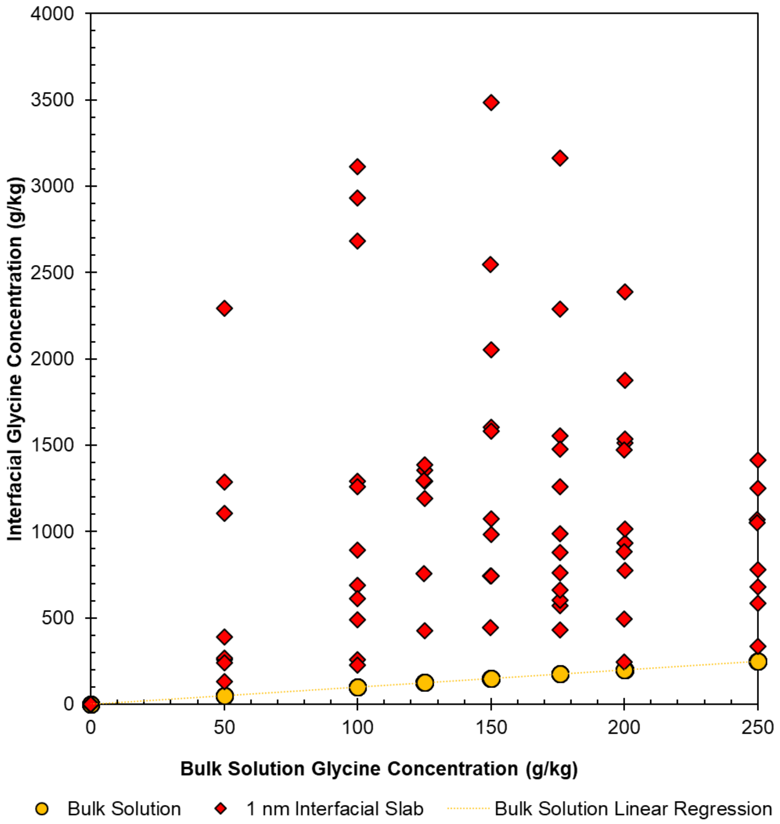

Figure 99: Interfacial region concentrations observed for all polystyrene coated gold chips in contact with aqueous glycine solutions at a range of bulk solution concentrations.

The results from SPR measurements, when analysed using their respective SPR models, had interfacial region concentrations of 2500 g/kg or below for the bare gold surface as discussed in chapter four. However, the introduction of a hydrophobic interface has led to an increase in mean interfacial region concentration across the glycine concentration range assessed. This can be rationalised as being the result of the hydrophobic polystyrene surface, as water would want to move away from the hydrophobic interface as much as possible. As such, glycine molecules would pull to the surface to fill that gap and thus justify the increased concentration enhancement observed within the interfacial solution layer.

6.3.5 Contact Angle Goniometry Measurements

Having confirmed with in situ SPR measurements that interfacial concentration enhancement of glycine at hydrophobic interface appears greater than for a bare gold chip surface, it was important to seek further insight with macroscale measurements. Contact angle goniometry was utilised as a means by which to investigate this upon a larger length scale.

6.3.5.1 Gold Chip Characterisation

Prior to contact angle measurements, each gold chip was characterised to determine their gold and chromium layer thicknesses using SPR spectroscopy. The four gold chips selected for polystyrene coating were then prepared in the same manner as was described in Section 6.3.1, whereby a dodecanethiol layer was first applied to the gold surface in order to produce a more uniformed polystyrene layer upon spin coating.

The resultant raw SPR spectra are shown in Figure 100 below, with the accompanying layer thicknesses given in Table 25. The chips appear stable, with sharp SPR coupling angle minima. Upon addition of thiol and polystyrene layers, the SPR reflectivity at coupling angle minima for chips E-H has not quite approached zero, which may indicate the presence of surface blemishes. In order to determine if this was the case, optical microscopy was utilised to gain more insight into whether this was a contributing factor.

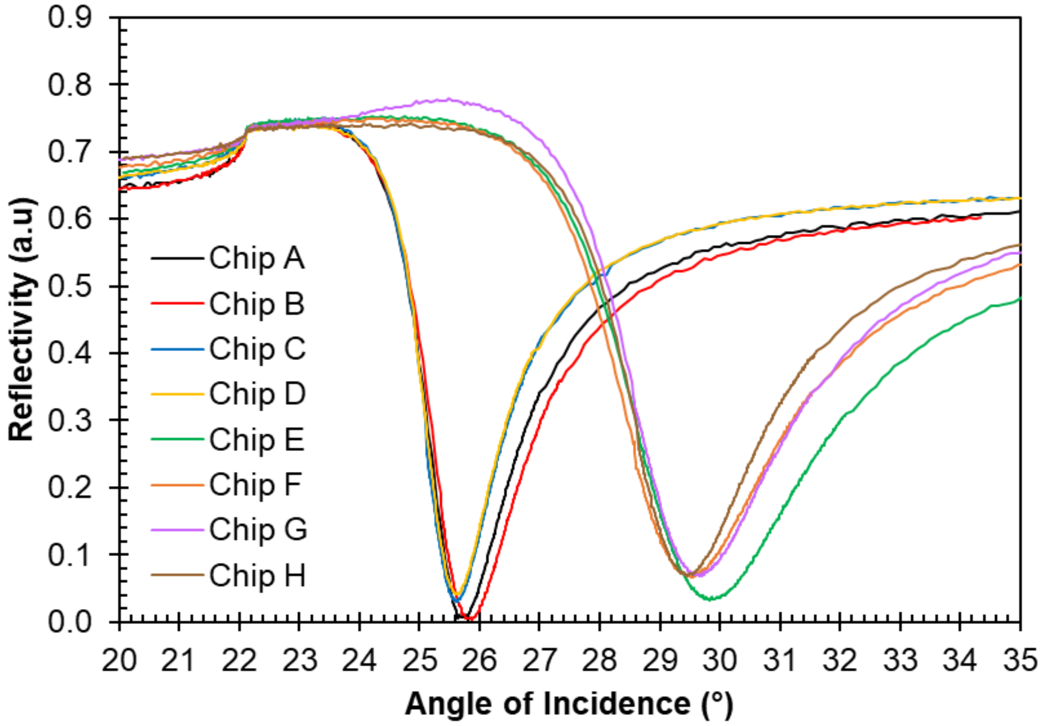

Figure 100: Raw SPR spectra for gold chips A-H utilised for contact angle measurements, where Chips A-D are bare gold and Chips E-H are PS coated.

Table 25: Corresponding chromium and gold layer thicknesses for chips A-H.

Chip	Cr Layer (nm)	Au Layer (nm)	SH Layer (nm)	PS Layer (nm)
A	0.8	47	0	0
B	0.8	47	0	0
C	0.7	48	0	0
D	0.7	48	0	0
E	0.7	48	1	15.98
F	0.7	48	1	15.62
G	0.7	48	1	16.10
H	0.7	48	1	16.07

Figure 101 shows microscopy images for bare gold chips A-D and Figure 102 shows microscopy images for polystyrene coated gold chips E-H. In the case of the bare gold chips, small blemishes and scratches are observed on the gold surface in the form of small black dots and lines. The chips had not been previously used and care was taken when handling the chips to ensure that the surfaces were as untouched as reasonably practicable.

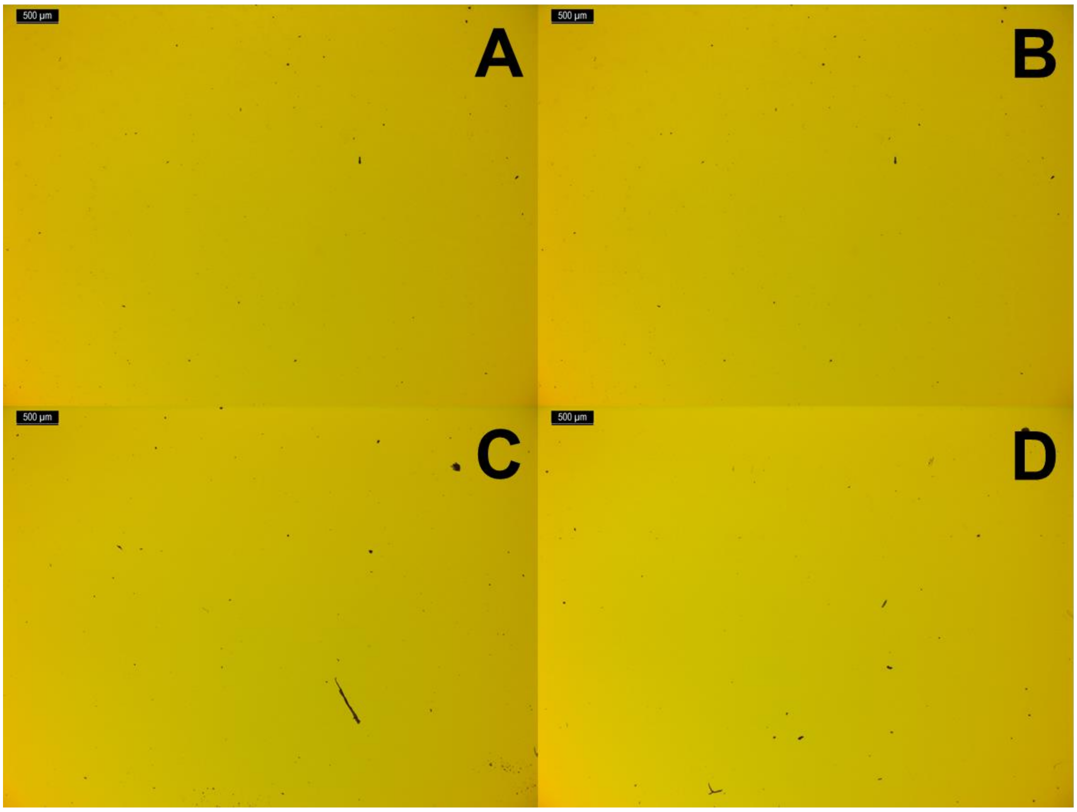

Figure 101: Optical microscopy imaging of bare gold chips A-D. The scale bar in the top left of each image denotes a length of 500 microns.

As such, the presence of such defects further emphasises the role such defects have in the degree of interfacial region permittivity variability from chip to chip which has been consistently highlighted throughout this research. Furthermore, the application of polymer layers onto surfaces will also be influenced by such crevices or scratches, as shown in Figure 102 for the microscopy of polystyrene coated chips E-H.

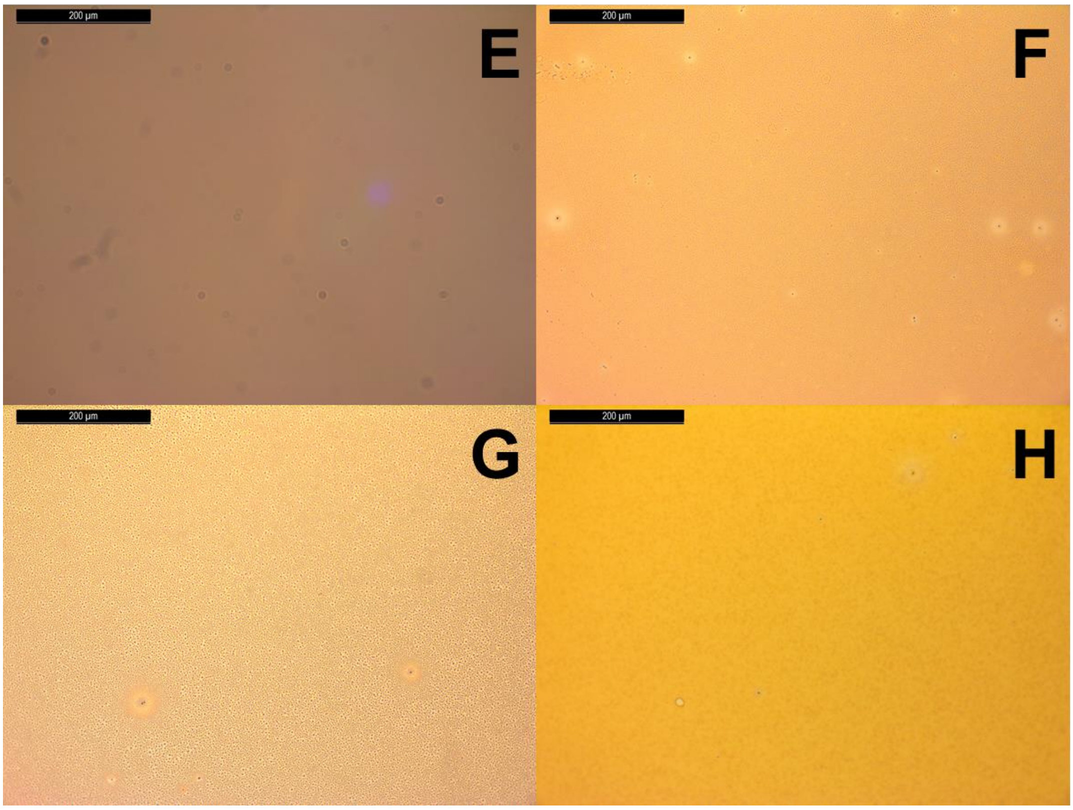

Figure 102: Optical microscopy imaging of polystyrene coated gold chips E-H. The scale bar in the top left of each image denotes a length of 200 microns.

Images E-H clearly show spots on the surface upon which polystyrene layers were then applied, and the influence they have on polystyrene layer formation. In order to minimise the effect of such defects on contact angle measurements, care was taken to select regions of each gold chip where minimal defects were present to ensure that external influences on the measurement were minimised.

6.3.5.2 Contact Angle Determination

Following characterisation of all chips intended for use in contact angle measurements, the contact angle measurements were performed following the protocol outlined in Section 6.2.4. The protocol was developed in an attempt to standardise the procedure used for all measurements, as contact angle measurements by nature are subject to variation and the influence of temperature, liquid flowrate or the volume of liquid injected onto the chip surface.

Figures 103 and 104 below show individual frames from individual video recordings made for the respective bare gold and polystyrene coated gold chips at the point where the static contact angle was defined. It should be noted that four repeated measurements where performed on each chip. The mean static contact angles are presented in Figure 105 and summarised in Table 26.

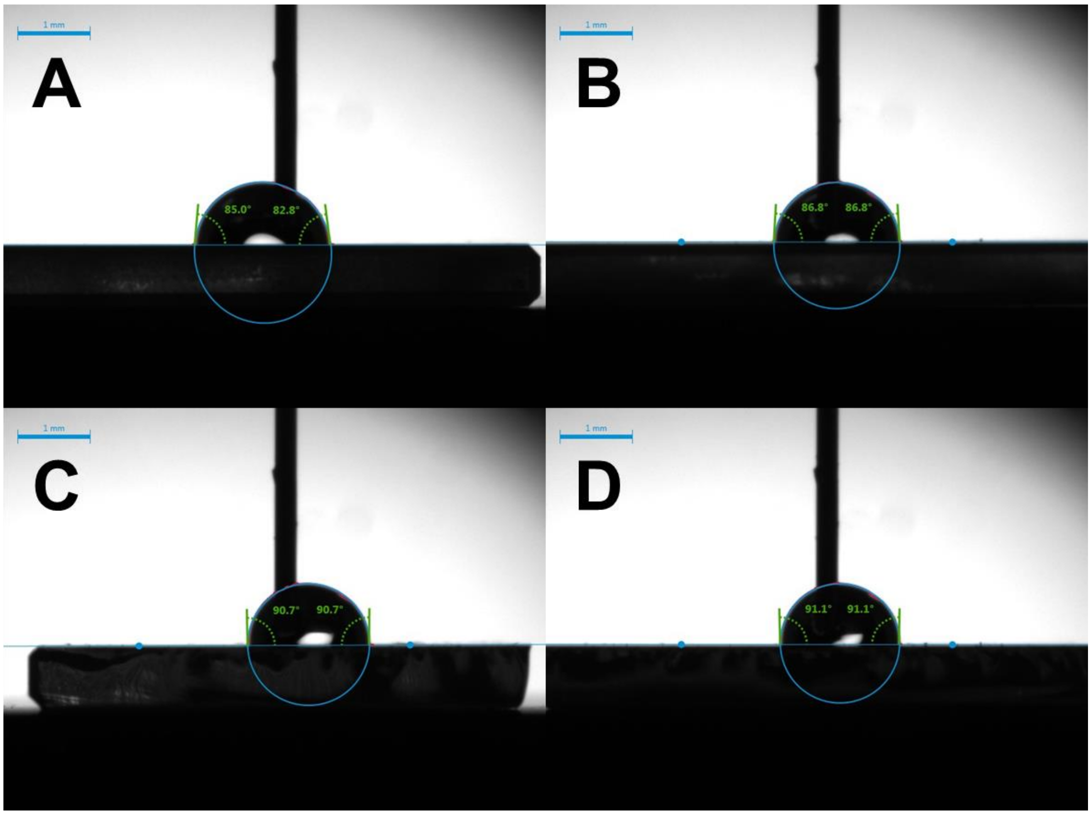

Figure 103: Static contact angles for individual measurements on bare gold chips at 0 (A), 100 (B), 176 (C) and 250 (D) g/kg aqueous glycine solution concentrations respectively.

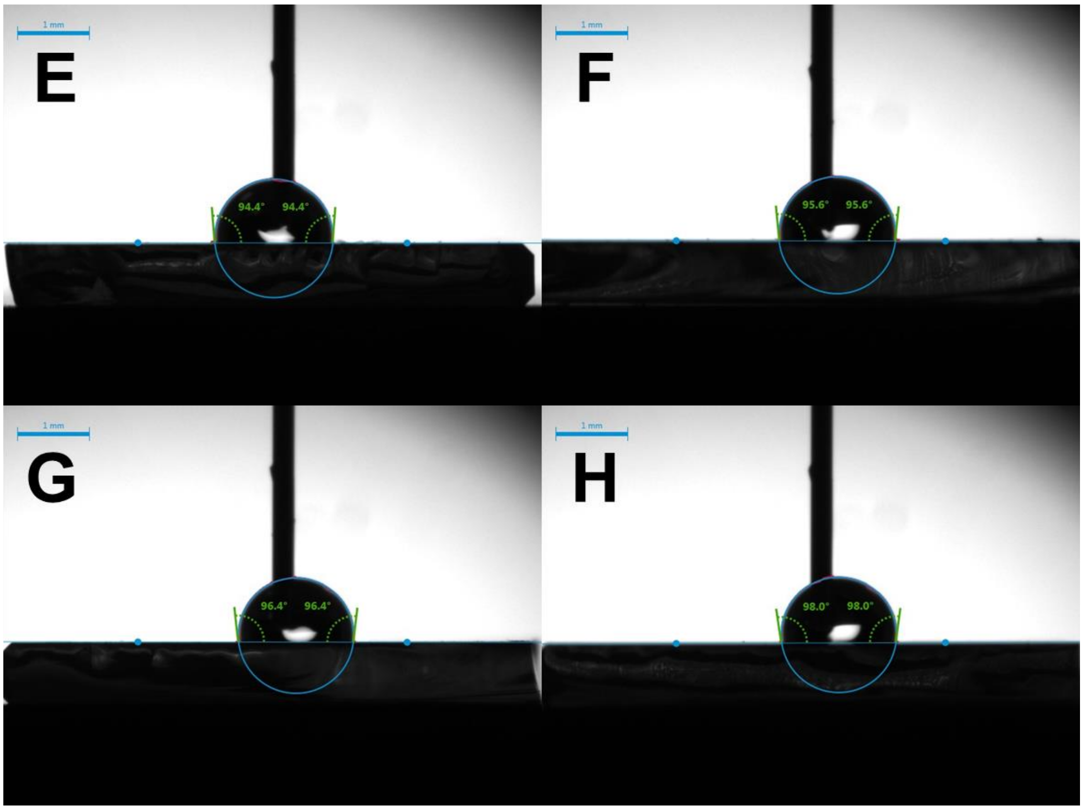

Figure 104: Static contact angles for individual measurements on PS coated gold chips at 0 (E), 100 (F), 176 (G) and 250 (H) g/kg aqueous glycine solution concentrations respectively.

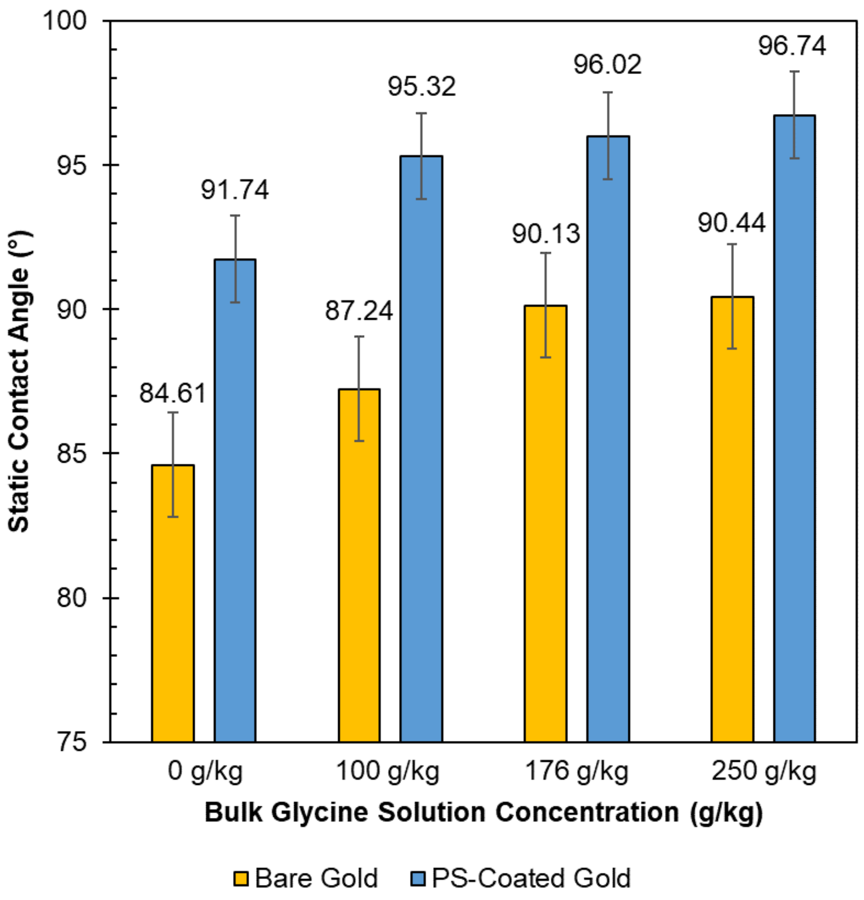

Figure 105: Mean static contact angles from four repeat measurements at each glycine solution concentration on each chip assessed. The error bar represents one standard deviation from the mean value.

Figure 105 shows that upon increasing the bulk glycine solution concentration, the mean static contact angle increases. This aligns with the expected behaviour of the solution on the respective surfaces, as the surface energy is higher due to the less significant attraction between the droplet and the surface. This is further emphasised in comparing the instance of bare gold chips with polystyrene coated gold chips, where the increased hydrophobicity of the polystyrene surface results in a higher static contact angle by comparison with those observed for the bare gold chips at the same bulk glycine solution concentration.

Table 26: Mean static contact angles from four repeat measurements at each glycine solution concentration on each chip assessed and the respective standard deviation from the mean.

Chip (Glycine Concentration Measured)	Mean Static Contact Angle (°)	Standard Deviation (°)
A (0 g/kg)	84.61	1.81
B (100 g/kg)	87.24	0.68
C (176 g/kg)	90.13	1.41
D (250 g/kg)	90.44	0.75
E (0 g/kg)	91.74	1.43
F (100 g/kg)	95.32	1.49
G (176 g/kg)	96.02	0.40
H (250 g/kg)	96.74	0.77

In addition to the measurement of the static contact angle, the advancing and receding contact angles were also determined on each chip assessed, as shown in Figure 106. The measurement of the dynamic contact angles provided a further means by which to verify the observations for the static contact angles, as well as providing a comparison to bare gold chips to further emphasise the markedly different interfacial behaviour being observed following addition of the polystyrene layer.

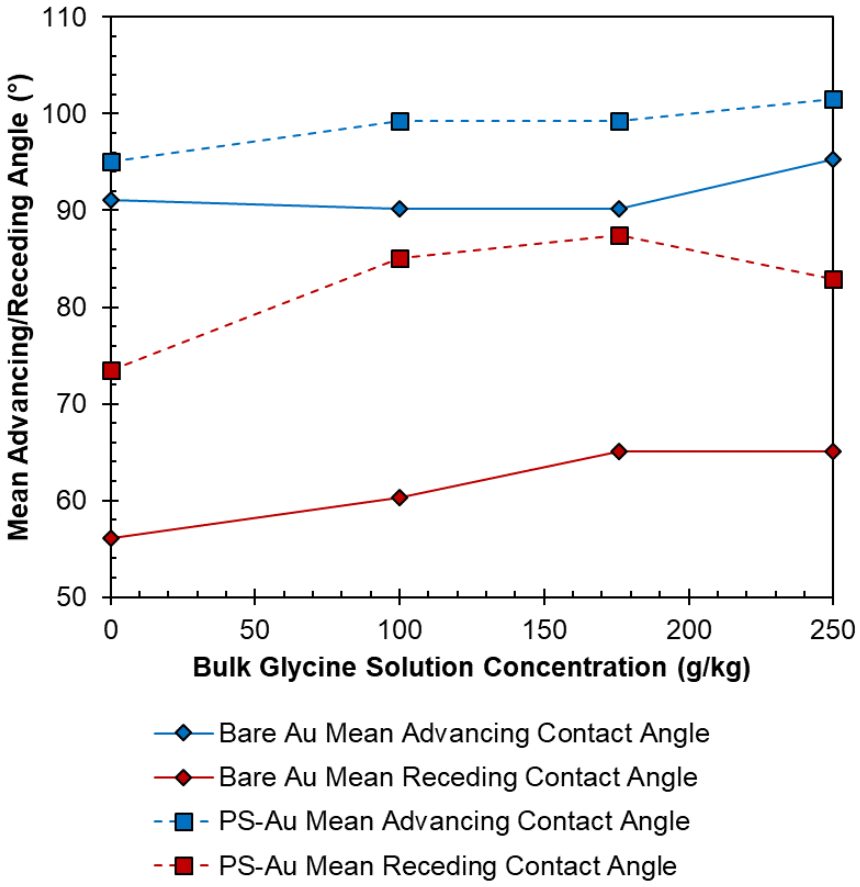

Figure 106: Mean advancing and receding contact angles for bare gold chips and polystyrene coated gold chips across the assessed bulk glycine solution concentration.

The higher angles obtained for the polystyrene surfaces relative to gold align with those of the static contact angle measurements obtained over the same acquisition period and therefore support the conclusion that the presence of a hydrophobic polystyrene layer has led to greater repulsion of the aqueous glycine solution at the solid-liquid interface when compared with a bare gold surface. The receding angles were however lower, and indicates that the polystyrene surfaces included a microscale roughness that pinned the movement of water drops. This could also have contributed to the higher advancing angles.

6.4 Conclusions

The work undertaken in this chapter has demonstrated the influence which the introduction of a hydrophobic interface has on interfacial concentration enhancement in aqueous glycine solutions investigated by in situ surface measurements.

Gold chips have been coated with ultrathin polystyrene layers and the procedure was optimised in order to produce chips with well defined, uniformed polymer layers. This was achieved through the addition of a thiol layer prior to polymer spin coating of the gold chip, which was shown to prevent de-wetting.

SPR measurements of pure component solvents, binary solvent mixtures and aqueous glycine solutions identified that the SPR coupling angle minima of reference solvent measurements were consistently lower than those of refractive index matched aqueous glycine solutions, which was also previously observed in chapter four. Through the implementation of representative SPR models, it was possible to quantify the interfacial region permittivity which was again higher than that in the bulk solution. It was found that while chip to chip variability was once again observed, the overall interfacial region permittivity values observed for the polystyrene coated chips were higher than those observed for bare gold chips in chapter four. The interfacial region permittivity was used to estimate the corresponding interfacial region concentration, which demonstrates the interfacial concentration enhancement in glycine solutions when in contact with a polystyrene surface.

This serves to highlight that when placed in contact with a hydrophobic interface, water molecules are being repelled at the interface, which leads to a localised concentration increase of glycine molecules larger than on a bare gold chip in the absence of polystyrene. These observations align with molecular simulations of glycine solutions in contact with hydrophobic interfaces and serves as the first direct experimental confirmation of such effects.

In order to assess how nanoscale interactions responsible for interfacial concentration enhancement relate to those which can be observed at the macroscale, contact angle measurements on bare gold chips and polystyrene coated gold chips using a range of glycine solution concentrations were performed. It was found that with increasing bulk glycine solution concentration, the contact angles increased as a result of the poorer affinity between the surface and the liquid droplet. Furthermore, the introduction of a polystyrene layer, when compared against measurements on bare gold chips, resulted in the increased hydrophobicity at the interface which led to an increase in the increased contact angles compared to those observed for bare gold chips.

7. Conclusions & Future Work

This thesis presents the investigation of solution behaviour at solution-solid interfaces within the context of heterogeneous crystal nucleation and the use of SPR measurements in order to experimentally capture interfacial concentration enhancement in solutions for the first time.

The key conclusions identified in each of the respective experimental chapter are summarised below, with recommendations for future work outlined thereafter. It is hoped that this work can serve as a link between molecular simulations and experimental measurements, while also serving as a foundation for future experimental investigations which can shed further light on this phenomenon.

7.1 Chapter Three

Chapter three involved the selection of pure solvents with refractive indexes that matched aqueous glycine and urea solutions for use in assessing how precisely key spectral features could be determined using the experimental setup refined for this work. Measurements of the solvents in contact with a bare glass prism (TIR reflectometry) and on gold chips (SPR spectroscopy) were performed and identified that the experimental setup was capable of a degree of sensitivity necessary for probing nanometre scale solution regions at solid-solution interfaces.

The resultant SPR spectra, when compared against a simulated response based on literature permittivity data at the same temperature, identified a mismatch between the two. This was found to be the result of literature permittivity data being captured at different laser light wavelengths or temperatures and served as an important confirmation of the role temperature and wavelength play in permittivity measurements, as well as the need to be aware of this influence when proceeding to the measurement of solutions.

7.2 Chapter Four

A comprehensive review of the literature identified that SPR spectroscopy had no prior application in the field of interfacial concentration measurements as it is typically applied to monitor interfacial phenomena in dilute solutions rather than small changes in highly concentrated solutions. Having identified in chapter three that the necessary sensitivity was achievable with this technique, an experimental workflow was developed for the measurement of pure solvents and binary solvents mixtures with permittivity matched aqueous glycine solutions.

If glycine solutions behaved as homogenous systems, it was expected that they would have identical SPR spectra to corresponding solvent reference measurements where the bulk refractive index of each liquid was equivalent. Such a scenario would align with assumptions made when using current heterogenous nucleation theories, whereby the local composition of the solution at the interface is assumed to be the same as in the bulk solution. This was found not to be the case, with the mismatch in SPR coupling angle minima indicative of a localised increase in solution concentration at the solid-liquid interface.

Qualitative confirmation of concentration enhancement was consistently observed and although the magnitude of this enhancement varies across different gold chips, it confirms predictions made by previous molecular simulations and provides a means by which to probe these effects. The ability to capture this effect in situ experimentally is a key novel contribution of this work, as it provides a link between predictions made through use of molecular dynamics simulations and real-world physical systems.

7.3 Chapter Five

The findings of chapter four were then applied to a different model system of interest, aqueous urea solutions. Urea has a markedly higher water solubility when compared with glycine and as a result, there are a wider range of pure solvents which can be utilised as solvent reference measurements to compare urea solutions against.

Application of the experimental workflow developed in chapter four led to the same outcome – a marked difference in the SPR coupling angle minima of solvent reference measurements when compared with the refractive index matched urea solution of interest. This serves to extend the findings of chapter four and to indicate that interfacial concentration enhancement at the solid-solution interface with respect to that of the bulk solution may be generally expected for a wide range of solution interfaces.

7.4 Chapter Six

Chapter six developed on the work of chapters four and five through surface measurements of aqueous glycine solutions in contact with polystyrene spin coated gold chips. The addition of a hydrophobic interface upon addition of ultrathin polystyrene layers led to an uplift in the magnitude of the interfacial concentration enhancement which was observed with respect to that seen in chapter four for bare gold chips. This observation indicated that the introduction of a hydrophobic interface leads to an additional repulsion of water molecules at the interface, thus facilitating a localised increase in glycine surface concentration with respect to the concentration within the bulk solution.

In order to further contextualise this observation, static, advancing and receding contact angle measurements were performed using bare gold and polystyrene coated gold chips in contact with aqueous glycine solutions of varying bulk solution concentration. This identified that with both increasing bulk glycine solution concentration and the introduction of a polystyrene layer to gold chips, the static, advancing and receding contact angles all increased due to the increased hydrophobicity of the surface and the reduction in the surface energy at the solid-liquid interface.

7.5 Future Work

It is hoped that the results presented in this thesis can form a basis from which further investigation can be undertaken to better understand the key drivers behind solution behaviour at interfaces and the role it plays in heterogeneous crystal nucleation. To achieve this, further work is required to build on this initial experimental confirmation of the effect to further investigate the key drivers at play.

One way with which to achieve this is through the assessment of further model systems on bare gold surfaces. The use of non-aqueous and mixed solvents and bulkier solute molecules would be the fruitful direction for further investigation. A further avenue from which to develop this research would be in the utilisation of a wide range of interfacial materials and surface chemistries in order to assess how this may impact the degree of interfacial concentration enhancement.

Use of a wider variety of spin coated polymers with varying degrees of hydrophobicity would serve as a further indicator of the degree to which such surfaces can influence solution behaviour at various interfaces and their subsequent effects on crystal nucleation. It is hoped that this work and that which follows from it can help to fill the gaps in current understanding of crystal nucleation at interfaces.

8. References

1. ter Horst, J.H., C. Schmidt, and J. Ulrich, *32 - Fundamentals of Industrial Crystallization*, in *Handbook of Crystal Growth (Second Edition)*, P. Rudolph, Editor. 2015, Elsevier: Boston. p. 1317-1349.
2. Wu, D.T., *Nucleation Theory*, in *Solid State Physics*, H. Ehrenreich and F. Spaepen, Editors. 1996, Academic Press. p. 37-187.
3. McGinty, J., et al., *CHAPTER 1 Nucleation and Crystal Growth in Continuous Crystallization*, in *The Handbook of Continuous Crystallization*. 2020, The Royal Society of Chemistry. p. 1-50.
4. Thakore, S.D., A. Sood, and A.K. Bansal, *Emerging role of primary heterogeneous nucleation in pharmaceutical crystallization.* Drug Development Research, 2020. **81**(1): p. 3-22.
5. Mullin, J.W., *Crystallization*. 4th ed.. ed, ed. Elsevier. 2001, Oxford Boston: Oxford Boston : Butterworth-Heinemann.
6. Kadam, S.S., H.J.M. Kramer, and J.H. ter Horst, *Combination of a Single Primary Nucleation Event and Secondary Nucleation in Crystallization Processes.* Crystal Growth & Design, 2011. **11**(4): p. 1271-1277.
7. Mastan, T.H., M. Lenka, and D. Sarkar, *Nucleation kinetics from metastable zone widths for sonocrystallization of L-phenylalanine.* Ultrasonics Sonochemistry, 2017. **36**: p. 497-506.

8. Rein ten Wolde, P. and D. Frenkel, *Homogeneous nucleation and the Ostwald step rule.* Physical Chemistry Chemical Physics, 1999. **1**(9): p. 2191-2196.
9. Erdemir, D., A.Y. Lee, and A.S. Myerson, *Nucleation of Crystals from Solution: Classical and Two-Step Models.* Accounts of Chemical Research, 2009. **42**(5): p. 621-629.
10. Jiang, Q. and M.D. Ward, *Crystallization under nanoscale confinement.* Chemical Society Reviews, 2014. **43**(7): p. 2066-2079.
11. Davey, R.J., S.L.M. Schroeder, and J.H. ter Horst, *Nucleation of Organic Crystals—A Molecular Perspective.* Angewandte Chemie International Edition, 2013. **52**(8): p. 2166-2179.
12. Artusio, F. and R. Pisano, *Surface-induced crystallization of pharmaceuticals and biopharmaceuticals: A review.* International Journal of Pharmaceutics, 2018. **547**(1): p. 190-208.
13. Shah, U.V., et al., *Heterogeneous nucleants for crystallogenesis and bioseparation.* Current Opinion in Chemical Engineering, 2015. **8**: p. 69-75.
14. Warzecha, M., et al., *Direct Observation of Templated Two-Step Nucleation Mechanism during Olanzapine Hydrate Formation.* Crystal Growth & Design, 2017. **17**(12): p. 6382-6393.
15. Diao, Y., et al., *Surface Design for Controlled Crystallization: The Role of Surface Chemistry and Nanoscale Pores in Heterogeneous Nucleation.* Langmuir, 2011. **27**(9): p. 5324-5334.

16. Verma, V., et al., *Dependence of Heterogeneous Nucleation on Hydrogen Bonding Lifetime and Complementarity.* Crystal Growth & Design, 2018. **18**(11): p. 7158-7172.

17. Di Profio, G., et al., *From Tailored Supports to Controlled Nucleation: Exploring Material Chemistry, Surface Nanostructure, and Wetting Regime Effects in Heterogeneous Nucleation of Organic Molecules.* Crystal Growth & Design, 2012. **12**(7): p. 3749-3757.

18. Curcio, E., et al., *Regulating Nucleation Kinetics through Molecular Interactions at the Polymer–Solute Interface.* Crystal Growth & Design, 2014. **14**(2): p. 678-686.

19. Zhang, C.-Y., et al., *An Investigation of the Effects of Self-Assembled Monolayers on Protein Crystallisation.* International Journal of Molecular Sciences, 2013. **14**(6): p. 12329-12345.

20. Boyes, M., et al., *Exploiting the Surface Properties of Graphene for Polymorph Selectivity.* ACS Nano, 2020. **14**(8): p. 10394-10401.

21. Gebauer, D., et al., *ON CLASSICAL AND NON-CLASSICAL VIEWS ON NUCLEATION.* American Journal of Science, 2018. **318**(9): p. 969-988.

22. Sear, R.P., *On the interpretation of quantitative experimental data on nucleation rates using classical nucleation theory.* Journal of Physical Chemistry B, 2006. **110**(43): p. 21944-21949.

23. Vekilov, P.G., *Nucleation.* Crystal Growth & Design, 2010. **10**(12): p. 5007-5019.

24. Vekilov, P.G., *The two-step mechanism of nucleation of crystals in solution.* Nanoscale, 2010. **2**(11): p. 2346-2357.

25. Karthika, S., T.K. Radhakrishnan, and P. Kalaichelvi, *A Review of Classical and Nonclassical Nucleation Theories.* Crystal Growth & Design, 2016. **16**(11): p. 6663-6681.

26. Vekilov, P.G., *Dense Liquid Precursor for the Nucleation of Ordered Solid Phases from Solution.* Crystal Growth & Design, 2004. **4**(4): p. 671-685.

27. McKechnie, D., et al., *Interfacial Concentration Effect Facilitates Heterogeneous Nucleation from Solution.* Journal of Physical Chemistry Letters, 2020. **11**(6): p. 2263-2271.

28. Jawor-Baczynska, A., J. Sefcik, and B.D. Moore, *250 nm Glycine-Rich Nanodroplets Are Formed on Dissolution of Glycine Crystals But Are Too Small To Provide Productive Nucleation Sites.* Crystal Growth & Design, 2013. **13**(2): p. 470-478.

29. Homola, J., S.S. Yee, and G. Gauglitz, *Surface plasmon resonance sensors: review.* Sensors and Actuators B: Chemical, 1999. **54**(1): p. 3-15.

30. Homola, J. *SENSORS BASED ON SPECTROSCOPY OF GUIDED WAVES*. 2006. Dordrecht: Springer Netherlands.

31. Bousiakou, L.G., et al., *Surface Enhanced Raman Spectroscopy for Molecular Identification- a Review on Surface Plasmon Resonance (SPR) and Localised Surface Plasmon Resonance (LSPR) in Optical Nanobiosensing.* Croatica Chemica Acta, 2019. **92**(4): p. 479-494.

32. Mol, N.J.d. and M.J.E. Fischer, *Surface plasmon resonance : methods and protocols / [internet resource]*. 1.. ed. 2010, New York: New York : Humana Press.

33. Wang, J., et al. *Surface Plasmon Resonance Sensors on Raman and Fluorescence Spectroscopy*. Sensors, 2017. **17**, DOI: 10.3390/s17122719.

34. Homola, J., *Surface plasmon resonance sensors for detection of chemical and biological species.* Chemical Reviews, 2008. **108**(2): p. 462-493.

35. Giessibl, F.J., *Advances in atomic force microscopy.* Reviews of Modern Physics, 2003. **75**(3): p. 949-983.

36. Dufrêne, Y.F., et al., *Imaging modes of atomic force microscopy for application in molecular and cell biology.* Nature Nanotechnology, 2017. **12**(4): p. 295-307.

37. Corporation, B. *Spectroscopic Ellipsometry*. 2025 [cited 2025 March]; Available from: https://www.bruker.com/en/products-and-solutions/test-and-measurement/ellipsometers-and-reflectometers/spectroscopic-ellipsometers.html.

38. Ltd, H. *Spectroscopic Ellipsometry: Basic Concepts*. 2025 [cited 2025 March]; Available from: https://www.horiba.com/gbr/scientific/technologies/spectroscopic-ellipsometry/spectroscopic-ellipsometry/.

39. Wee, A., X. Yin, and C.S. Tang, *Introduction to Spectroscopic Ellipsometry of Thin Film Materials: Instrumentation, Data Analysis, and Applications*. 2022.

40. Knoll, W., *Interfaces and thin films as seen by bound electromagnetic waves.* Annual Review of Physical Chemistry, 1998. **49**: p. 569-638.

41. Quigley, G.R., R.D. Harris, and J.S. Wilkinson, *Sensitivity enhancement of integrated optical sensors by use of thin high-index films.* Applied Optics, 1999. **38**(28): p. 6036-6039.

42. Knoll, W., et al., *Nanoporous thin films in optical waveguide spectroscopy for chemical analytics.* Analytical and Bioanalytical Chemistry, 2020. **412**(14): p. 3299-3315.

43. Becker, M.R., et al., *Waveguide optical properties of polystyrene doped with p-nitroaniline derivatives.* Optical Materials, 2010. **32**(11): p. 1526-1531.

44. Ma, H., A.K.Y. Jen, and L.R. Dalton, *Polymer-based optical waveguides: Materials, processing, and devices.* Advanced Materials, 2002. **14**(19): p. 1339-1365.

45. Hernandes, M.S. and L.R.P. Troncone, *Glycine as a neurotransmitter in the forebrain: a short review.* Journal of Neural Transmission, 2009. **116**(12): p. 1551-1560.

46. Razak, M.A., et al., *Multifarious Beneficial Effect of Nonessential Amino Acid, Glycine: A Review.* Oxid Med Cell Longev, 2017. **2017**: p. 1716701.

47. Weissbuch, I., et al., *Solvent Effect on Crystal Polymorphism: Why Addition of Methanol or Ethanol to Aqueous Solutions Induces the Precipitation of the Least Stable β Form of Glycine.* Angewandte Chemie International Edition, 2005. **44**(21): p. 3226-3229.
48. Boldyreva, E., *Glycine: The Gift that Keeps on Giving.* Israel Journal of Chemistry, 2021. **61**(11-12): p. 828-850.
49. Hughes, C.E. and K.D.M. Harris, *Direct observation of a transient polymorph during crystallization.* Chemical Communications, 2010. **46**(27): p. 4982-4984.
50. Towler, C.S., et al., *Impact of Molecular Speciation on Crystal Nucleation in Polymorphic Systems: The Conundrum of γ Glycine and Molecular 'Self Poisoning'.* Journal of the American Chemical Society, 2004. **126**(41): p. 13347-13353.
51. Lee, I.S., et al., *Concomitant Crystallization of Glycine on Patterned Substrates: The Effect of pH on the Polymorphic Outcome.* Crystal Growth & Design, 2008. **8**(1): p. 108-113.
52. Berliner, J.F.T., *Crystal Urea: Industrial Development and Properties.* Industrial & Engineering Chemistry, 1936. **28**(5): p. 517-522.
53. Hamidipour, M., N. Mostoufi, and R. Sotudeh-Gharebagh, *Modeling the synthesis section of an industrial urea plant.* Chemical Engineering Journal, 2005. **106**(3): p. 249-260.
54. Piaggi, P.M. and M. Parrinello, *Predicting polymorphism in molecular crystals using orientational entropy.* Proceedings of the National Academy of Sciences, 2018. **115**(41): p. 10251-10256.

55. Shang, C., X.-J. Zhang, and Z.-P. Liu, *Crystal phase transition of urea: what governs the reaction kinetics in molecular crystal phase transitions.* Physical Chemistry Chemical Physics, 2017. **19**(47): p. 32125-32131.

56. Patel, M.A., B. Nguyen, and K. Chadwick, *Predicting the Nucleation Induction Time Based on Preferred Intermolecular Interactions.* Crystal Growth & Design, 2017. **17**(9): p. 4613-4621.

57. Green, R.J., et al., *Surface plasmon resonance for real time in situ analysis of protein adsorption to polymer surfaces.* Biomaterials, 1997. **18**(5): p. 405-413.

58. vanDelden, C.J., et al., *Heparinization of gas plasma-modified polystyrene surfaces and the interactions of these surfaces with proteins studied with surface plasmon resonance.* Biomaterials, 1997. **18**(12): p. 845-852.

59. Zhu, X.M., et al., *Surface treatments for surface plasmon resonance biosensors.* Sensors and Actuators B: Chemical, 2002. **84**(2): p. 106-112.

60. Jung, L.S., et al., *Quantitative interpretation of the response of surface plasmon resonance sensors to adsorbed films.* Langmuir, 1998. **14**(19): p. 5636-5648.

61. Ekgasit, S., et al., *Influence of the Metal Film Thickness on the Sensitivity of Surface Plasmon Resonance Biosensors.* Applied Spectroscopy, 2005. **59**(5): p. 661-667.

62. Miyazaki, C.M., F.M. Shimizu, and M. Ferreira, *6 - Surface Plasmon Resonance (SPR) for Sensors and Biosensors*, in *Nanocharacterization Techniques*, A.L. Da Róz, et al., Editors. 2017, William Andrew Publishing. p. 183-200.

63. Shalabney, A. and I. Abdulhalim, *Sensitivity-enhancement methods for surface plasmon sensors.* Laser & Photonics Reviews, 2011. **5**(4): p. 571-606.

64. GmbH, R.T. *Winspall Data Analysis Software*. [cited 2021 February]; Website link to PDF file]. Available from: http://www.res-tec.de/downloads.html.

65. Soto, A., A. Arce, and M.K. Khoshkbarchi, *Effect of cation and anion of an electrolyte on apparent molar volume, isentropic compressibility and refractive index of glycine in aqueous solutions.* Biophysical Chemistry, 1999. **76**(1): p. 73-82.

66. Aldrich, S. *Physical Properties of Solvents*. Available from: https://www.sigmaaldrich.com/deepweb/assets/sigmaaldrich/marketing/global/documents/614/456/labbasics_pg144.pdf.

67. Aralaguppi, M.I., C.V. Jadar, and T.M. Aminabhavi, *Density, Viscosity, Refractive Index, and Speed of Sound in Binary Mixtures of Acrylonitrile with Methanol, Ethanol, Propan-1-ol, Butan-1-ol, Pentan-1-ol, Hexan-1-ol, Heptan-1-ol, and Butan-2-ol.* Journal of Chemical & Engineering Data, 1999. **44**(2): p. 216-221.

68. Iglesias, M., B. Orge, and J. Tojo, *Densities and Refractive Indices for Acetone + Methanol + 1-Propanol at 298.15 K.* Journal of Chemical & Engineering Data, 1996. **41**(2): p. 218-221.

69. Tilton, L.W.a.T., J.K, *Refractive Index and Dispersion of Distilled Water for Visible Radiation, at temperatures 0-60°C.* Journal of Research of the National Bureau of Standards, 1938. **20**: p. 419-477.

70. Ortega, J., *Densities and refractive indices of pure alcohols as a function of temperature.* Journal of Chemical & Engineering Data, 1982. **27**(3): p. 312-317.

71. Rodriguez, H., et al., *Apparent molar volume, isentropic compressibility, refractive index, and viscosity of DL-alanine in aqueous NaCl solutions.* Journal of Solution Chemistry, 2003. **32**(1): p. 53-63.

72. Kumari, L., et al., *Thermodynamic, spectroscopic and DFT studies of binary mixtures of poly(vinylpyrrolidone) (PVP) with ethanol, 1-propanol and 1-butanol.* Journal of Molecular Liquids, 2020. **299**.

73. O'Brien, R.N. and D. Quon, *Refractive index of some alcohols and saturated hydrocarbons at 6328 A.* Journal of Chemical & Engineering Data, 1968. **13**(4): p. 517-517.

74. Ikeda, R.M., R.E. Kepner, and A.D. Webb, *Densities, Refractive Indices, and Rotations of Mixtures of Active Amyl and Isoamyl Alcohols.* Analytical Chemistry, 1956. **28**(8): p. 1335-1336.

75. Resa, J.M., et al., *Densities, excess molar volumes, and refractive indices of ethyl acetate and aromatic hydrocarbon binary mixtures.* The Journal of Chemical Thermodynamics, 2002. **34**(7): p. 995-1004.

76. Aminabhavi, T.M., et al., *Densities, viscosities, and speeds of sound for diethylene glycol dimethyl ether + methyl acetate.* Journal of Chemical & Engineering Data, 1993. **38**(4): p. 540-541.

77. Stanley, E.M., *Refractive index of pure water for wavelength of 6328 Ang at high pressure and moderate temperatures.* Journal of Chemical & Engineering Data, 1971. **16**(4): p. 454-457.

78. Thormahlen, I., J. Straub, and U. Grigull, *REFRACTIVE-INDEX OF WATER AND ITS DEPENDENCE ON WAVELENGTH, TEMPERATURE, AND DENSITY.* Journal of Physical and Chemical Reference Data, 1985. **14**(4): p. 933-946.

79. Schiebener, P., et al., *REFRACTIVE-INDEX OF WATER AND STEAM AS FUNCTION OF WAVELENGTH, TEMPERATURE AND DENSITY.* Journal of Physical and Chemical Reference Data, 1990. **19**(3): p. 677-717.

80. Daimon, M. and A. Masumura, *Measurement of the refractive index of distilled water from the near-infrared region to the ultraviolet region.* Applied Optics, 2007. **46**(18): p. 3811-3820.

81. Shekaari, H. and F. Jebali, *Densities, Viscosities, Electrical Conductances, and Refractive Indices of Amino Acid plus Ionic Liquid (BMIm Br) Water Mixtures at 298.15 K.* Journal of Chemical and Engineering Data, 2010. **55**(7): p. 2517-2523.

82. Deosarkar, S., M.P. Pawar, and S.M. Deoraye, *Refractive index, molar refraction and polarizability of ciprofloxacin hydrochloride in aqueous-*

glycine solutions. International Journal of Chemical Sciences, 2015. **13**: p. 830-836.

83. Shekaari, H., M.T. Zafarani-Moattar, and S.N. Mirheydari, *Effect of 1-Butyl-3-methylimidazolium Ibuprofenate as an Active Pharmaceutical Ingredient Ionic Liquid (API-IL) on the Thermodynamic Properties of Glycine and L-Alanine in Aqueous Solutions at Different Temperatures.* Journal of Solution Chemistry, 2016. **45**(4): p. 624-663.
84. Vesga, M.J., et al., *Conundrum of γ glycine nucleation revisited: to stir or not to stir?* CrystEngComm, 2019. **21**(13): p. 2234-2243.
85. McKechnie, D., et al., *Interfacial concentration effect facilitates heterogeneous nucleation from solution.* J. Phys. Chem. Lett., 2020. **11**: p. 2263.
86. Acikbas, Y., et al., *Characterization of 1,7-dibromo-N,N'-(bicyclohexyl)-3,4:9,10-perylendiimide Langmuir–Blodgett film for organic vapor sensing application.* Applied Surface Science, 2015. **350**: p. 135-141.
87. Halay, E., et al., *Calix 4 arene-triazine conjugate intermediate: optical properties and gas sensing responses against aromatic hydrocarbons in Langmuir-Blodgett films.* Research on Chemical Intermediates, 2020. **46**(10): p. 4433-4445.
88. Patyar, P., G. Kaur, and T. Kaur, *Volumetric Investigations on Molecular Interactions of Glycine/l-alanine in Aqueous Citric Acid Solutions at Different Temperatures.* J Solution Chem, 2018. **47**(12): p. 2039-2067.

89. T. Sivanesan, V.N.a.S.P., *Non-linear optical properties of α-glycine single crystals by Z-Scan technique.* Indian Journal of Science and Technology, 2010. **2010**.

90. Guerin, S., et al., *Control of piezoelectricity in amino acids by supramolecular packing.* Nature Materials, 2018. **17**(2): p. 180-+.

91. Priya, N.S., *Solution growth of <i>γ</i>-glycine from cadmium sulphate as solvent for frequency doubling applications.* Materials Research Express, 2019. **6**(9): p. 095101.

92. Ashok Kumar, R., et al., *Crystal growth, optical and thermal studies of nonlinear optical γ-glycine single crystal grown from lithium nitrate.* Optik, 2012. **123**(5): p. 409-413.

93. Sivakumar, N., et al., *Synthesis, growth, spectral, electrical, mechanical and thermal characterization of a potential optical material: γ-glycine single crystal.* Optical Materials, 2018. **80**: p. 177-185.

94. Haynes, W.M., Lide, D.R, Bruno, T.J, *CRC Handbook of Chemistry and Physics (95th ed.)*. 95 ed. 2014, Boca Raton: CRC Press.

95. Warren, J.R. and J.A. Gordon, *On the Refractive Indices of Aqueous Solutions of Urea.* The Journal of Physical Chemistry, 1966. **70**(1): p. 297-300.

96. Krivacic, J.R. and D.W. Urry, *Ultraviolet refractive indices of aqueous solutions of urea and guanidine hydrochloride.* Analytical Chemistry, 1971. **43**(11): p. 1508-1510.

97. Lide, D.R., G.W.A. Milne, *Handbook of Data on Organic Compounds.* 3rd ed. Vol. 1. 1994, Boca Raton ,FL. : CRC Press, Inc.

98. Sultanova, N., S. Kasarova, and I. Nikolov, *Dispersion Properties of Optical Polymers.* ACTA PHYSICA POLONICA A, 2009. **116**: p. 585-587.

99. McKechnie, D., et al., *Tuning Interfacial Concentration Enhancement through Dispersion Interactions to Facilitate Heterogeneous Nucleation.* The Journal of Physical Chemistry C, 2022. **126**(38): p. 16387-16400.